Synthesis and Characterization of Amphiphilic Precision Glycomacromolecules

Inaugural-Dissertation

to obtain the academic degree

Doctor rerum naturalium (Dr. rer. nat.)

of the Faculty of Mathematics and Natural Sciences

of the Heinrich Heine University Düsseldorf

submitted by

Alexander Banger

from Essen

Düsseldorf, June 2022

Heinrich Heine Universität Düsseldorf

The work presented in this thesis was accomplished in a period between 01.04.2018 and 30.06.2021 at the Heinrich-Heine-Universität Düsseldorf in the Institute of Organic Chemistry and Macromolecular Chemistry under the supervision of Prof. Dr. Laura Hartmann, Department of Macromolecular Chemistry.

Printed with permission of the
Faculty of Mathematics and Natural Sciences of the
Heinrich Heine University of Düsseldorf

Supervisor: Prof. Dr. Laura Hartmann
Co-supervisor: Prof. Dr. Matthias Karg
Date of the oral examination: 22.11.2022

Declaration of authorship

I hereby declare that the thesis submitted is my own work without making use of impermissible aids, considering the “Rules on the Principles for Safeguarding Good Scientific Practice at Heinrich Heine University Düsseldorf”. All direct or indirect sources used are acknowledged in the bibliography as references. I further declare that I have not submitted this nor a similar thesis at any other examination board in order to obtain a degree.

_____

Alexander Banger Date

Für Oma

Table of content

List of publications

Parts of this thesis are already published or were presented on professional conferences.

Publications included in this work:

Synthesis and self-assembly of amphiphilic precision glycomacromolecules. A. Banger, J. Sindram, M. Otten, J. Kania, A. Strzelczyk, D. Wilms, S. Miletic, T. Marlovits, M. Karg and L. Hartmann, Polym. Chem., 2021, 12, 4795-4802.

Own contribution:
Collaborative project conceptualization with Laura Hartmann. Synthesis, purification and analysis of all building blocks and oligomers. CMC determination experiments using different fluorescence probes. Collaborative further analysis of micellar assemblies using DLS, TEM and AFM. Micellar crosslinking and analysis. Conduction of binding studies with lectins and bacteria and following interpretation. Collaborative writing of the manuscript.

Publications in preparation:

Amphiphilic glyco(oligoamidoamines) with AIE luminophores to visualize cluster formation in self-assembled systems. Tentative author list: A. Banger, P. Pasch, M. Otten, M. Karg, L. Hartmann

Own Contribution:
Collaborative project conceptualization with Laura Hartmann and Peter Pasch.. Fluorescence measurements and evaluation (CMC detection in LBB, fluorescence reduction experiments by adding a secondary non-AIE oligomer). Mixed micelle binding experiments with lectins and bacteria. Collaborative writing of the manuscript.

Presentations on Professional Conferences:

Alexander Banger, Mischa Baier, Jessica Kania, Julian Sindram, Matthias Karg and Laura Hartmann, “Self-assembly of Amphiphilic Precision Glycomacromolecules”, CRC 1208 Conference "Dynamics of Membrane Systems", March 12-14, 2019, Düsseldorf, Germany.

Alexander Banger, Peter Pasch, Marius Otten, Jens Voskuhl, Matthias Karg, Laura Hartmann, “Synthesis and Analysis of Amphiphilic Precision Glycomacromolecules”, 16th Zsigmondy Colloquium ("Soft Colloids"), March 09-11, 2020, Düsseldorf.

Alexander Banger, Julian Sindram, Marius Otten, Jessica Kania, Dimitri Wilms, Alexander Strzelczyk, Sean Miletic, Thomas Marlovits, Matthias Karg, Laura Hartmann, “Amphiphilic glycomacromolecules: self-assembly properties and lectin binding in dependence of their monomer sequence”, ACS Spring, April 05-16, 2021, virtual.

Abstract

Carbohydrates are ubiquitous, nearly every cell of eukaryotes and prokaryotes is covered in a layer of carbohydrates the so called “glycocalyx”. The counterpart to the glycocalyx are carbohydrate binding proteins, for example the class of lectins. Interactions of lectins with various carbohydrates have been identified to play a key role in many biological processes like cell communication and signal transduction processes. Additionally, being one of the first point of contacts, carbohydrates and lectins are associated with pathogen adhesion to host cells but have also been associated with various developmental stages of cancer. A single carbohydrate-lectin binding is usually weak, hence Nature presents carbohydrates in a multivalent fashion combining multiple weak binding events to create stronger binding. Using this concept of multivalency, significant advances towards so-called glycomimetics have been made. Recently, Hartmann and co-workers have described the usage of a stepwise assembly process of tailormade monomer building blocks onto a solid support obtaining sequence defined oligo(amido)amines scaffolds for the multivalent presentation of different carbohydrates. Such precision glycooligomers are considered a new class of glycomimetics as they now offer high structural control and variability, more closely mimicking natural multivalent carbohydrate constructs such as oligosaccharides or glycoproteins and glycolipids.

In this thesis, precision glycooligomers are extended by making them amphiphilic and thereby utilizing self-assembly as bottom approach for the synthesis of larger multivalent systems. Therefore, the synthesis of amphiphilic precision glycomacromolecules (APGs) is introduced, including the synthesis of novel building blocks, establishing design principles for APGs along with optimized synthetic protocols. In the second part, APG self-assembly and binding behavior is investigated and in the third part this approach is combined with AIE fluorophores for potential read-out of binding. Finally, alternative multivalent scaffold, active ester polymers are explored for combinations with precision glycooligomers.

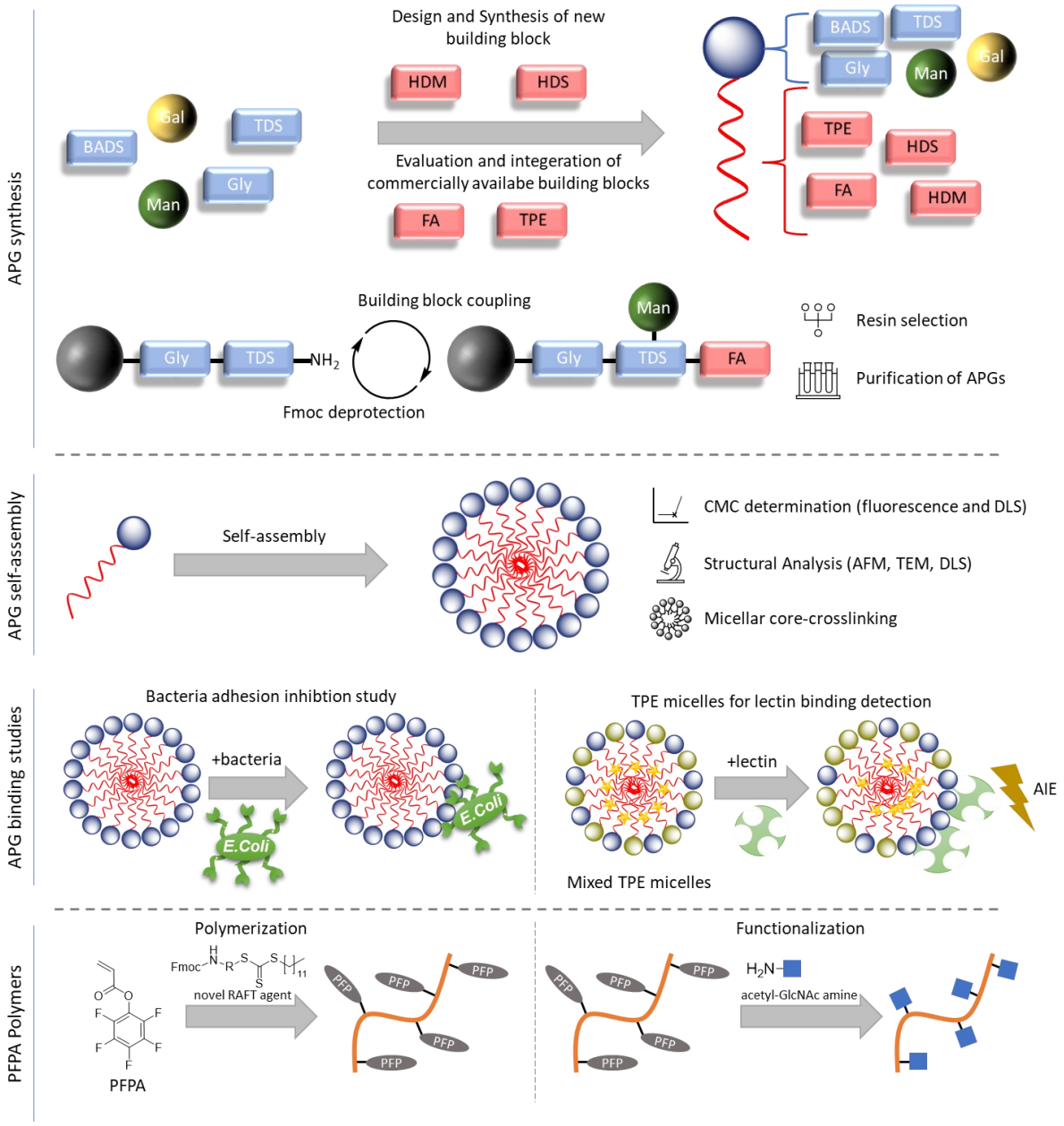

Figure 1. Schematic overview of the different projects described in this thesis.

In the first part of this thesis, the APG synthesis was successfully established and applied to derive a series of APGs for systematic structure-property correlation studies. As part of the synthesis, two novel hydrophobic building block suited for SPPoS were developed. Starting from hexamethylenediamine a synthesis was established, which allowed for the preparation of the alkyl spacing building block **h**examethylene**d**iamine coupled with **s**uccinic anhydride (HDS) and the alkene bearing **h**examethylene**d**iamine coupled with **m**aleic anhydride (HDM). These hydrophobic building blocks allowed to prolong the hydrophobic part of the APG and in the case of HDM also to introduce an alkene species, which was later used for micellar core-crosslinking. Here, three different strategies for micellar core-crosslinking were investigated

utilizing the new HDM building block. Additionally, fatty acids as terminal hydrophobic moieties were introduced to solid phase tool box. C_{10}, C_{12} and C_{15} fatty acids were attachable under standard coupling conditions to the APGs and were later shown to be sufficient to induce self-assembly in water.

Building on to the first part, a series of 8 APGs was systematically analyzed regarding their self-assembly characteristics by the means of CMC, micellar size and shape. The CMC can be readily tuned by the length of the terminal fatty acid with CMCs ranging from micromolar to millimolar. Subsequently, the shape and size of the micelle were assessed using DLS, AFM and TEM. Here it was shown, that depending on the number of hydrogen bonds available in the APG backbone, spherical as well as rodlike micelles were accessible which is in agreement with comparable structures based on peptide amphiphiles. Furthermore, crosslinking of micelles was achieved using the novel HDM building block. Crosslinked micelles were not only more stable during AFM and TEM analysis, but they could also withstand dilution below CMC and solvent changes from water to ethanol. Lastly, APGs were tested regarding their potential as inhibitors of bacterial adhesion of FimH bearing *E. coli*. Here, non-crosslinked APGs showed a better inhibition as crosslinked micelles. Surprisingly, for crosslinked micelles a cooperativity factor of 2 was determined compared to the cooperativity factor of close to 1 for the non-crosslinked micelles suggesting that despite a lower overall binding affinity the crosslinking improved the probability of a secondary binding event once the first binding is established.

In the third part of this thesis and based on preliminary studies by Peter Pasch, aggregation induced emission (AIE) dyes were integrated into the tail end of the APGs and their usage as clustering sensors was evaluated. For tetraphenylethylene containing APGs rod-like micelles were observed, whereas for carboxylated aromatic thioether luminophore containing APGs spherical micelles were detected. By combining AIE-APGs and commercial non-AIE, non-carbohydrate amphiphiles as well as non-AIE-APGs, so-called mixed micelles (micelles that are formed out of at least two different surfactants) experiments were conducted showing that the overall fluorescence of AIE-APG micelles can be reduced by adding a non-AIE containing APG. Subsequently, binding characteristics of these mixed micelle systems were investigated. As binding targets, the two tetrameric lectins Con A and GNA as well as the dimeric lectin LCA were employed. Titration of these lectins to the mixed micelles lead to a fluorescence increase

but with a more pronounced effect for the tetramers. This experiment showcased the future potential of utilizing mix micelles as sensors for clustering events.

In the last and fourth part of this thesis, polymers based on active esters as GAG mimetics for incorporation into hydrogels were developed. Therefore, a novel RAFT agent was synthesized bearing an Fmoc-protected terminal amine group allowing for later hydrogel integration. Polymerization with this RAFT agent showed good results in terms of dispersity but failed to reach polymer weights above 8000 g/mol. Furthermore, functionalization of the active ester polymer was readily accomplished and confirmed by ^{1}H-NMR, ^{19}F-NMR and H_2O-GPC.

Overall, the new concept as well as the synthesis of amphiphilic precision glycomacromolecules was established, thereby extending the field of peptide amphiphiles and other amide based amphiphiles. The approach allows for great synthetic flexibility due to the usage of tailormade building blocks, as demonstrated by the introduction of AIE units or the core-crosslinking of micelles. Additionally, as shown by initial binding experiments, APGs have great potential for various applications e.g., adhesion inhibitors or as multivalent binding partners in general. Furthermore, first insights regarding membrane clustering events were obtained using AIE-APGs.

1 Introduction

1.1 Carbohydrates

Carbohydrates have been, are and will be also in the future ubiquitous on this planet. They come in a broad variety ranging from the simple monomeric glucose to longer and more complex polysaccharides. With so many variations of carbohydrates, there are also manifold applications e.g., nutrition, structural raw material for textiles or recently increasingly as ligands in research (Figure 1).

Figure 1. Exemplary depiction of typical carbohydrate sources in your daily nutrition.

However, in research in particular, carbohydrates were for a long time regarded only as energy supply and storage, as they are not encoded into the genome. However, since Bennett first discovered that all cells are covered by a carbohydrate-containing material, or better known as the glycocalyx (“sweet husk”), more and more attention has shifted towards discovering further functions of carbohydrates in Nature (see Figure 2).[1]

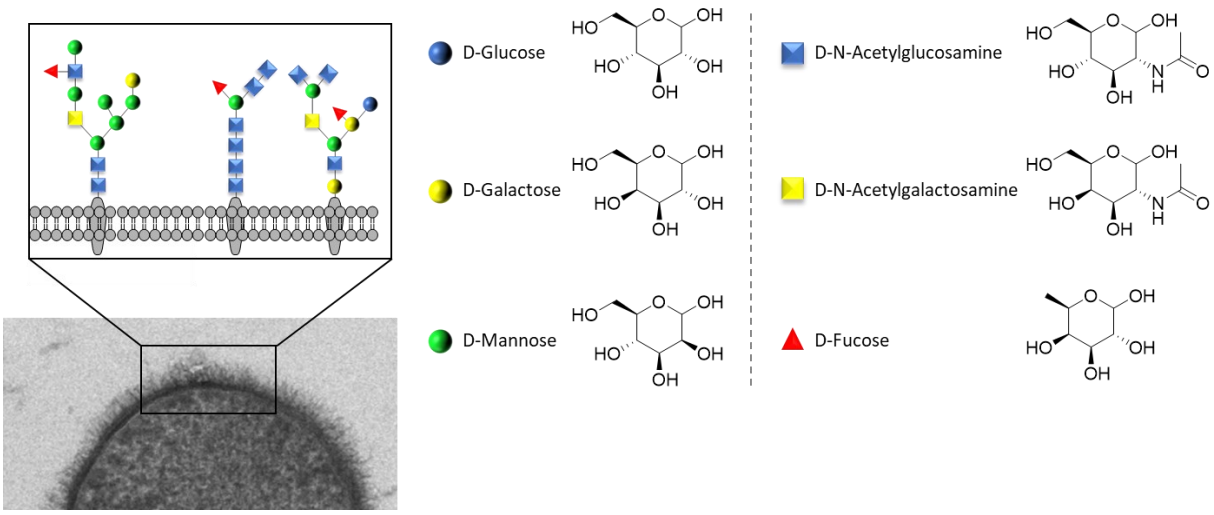

Figure 2. TEM image of a cell (taken by Allon Weiner, The Weizmann Institute of Science, Rehovot, Israel. 2006.) with a schematic illustration of the glycocalyx.

To this day, evidence has been found that carbohydrates play a decisive role in cell sociology such as cell communication, cell adhesion and signal transduction.[2-4] On top of that, research has shown that carbohydrates are also involved in pathogen recognition and cell infection e.g. bacteria or viruses but also cancer cells show anomalies in their interactions with carbohydrates.[5-8] When carbohydrate ligands are used to encode information, one of their main binding partners, the so-called lectins, are of significant importance. Those lectins are receptor proteins often located on the surface of a cell or pathogen, which specifically bind carbohydrates and are so specific in certain cases that they distinguish between α and β anomers. Anomers are nearly identical stereoisomers with the sole difference of the position of the anomeric carbon. For example, the lectin Concanavalin A (Con A) specifically binds the α-anomers of mannose (Man) and glucose, whereas it has tenfold lower binding affinity to the respective β-anomers.[9-11] Seeking to gain more knowledge about the function of carbohydrates and by doing do so enabling new ways to tackle infections or cancer, glycobiology has become an important topic of today's research.[12, 13]

1.1.1 Glycomimetics

Glycans by themselves are very diverse and are often found as glycan-conjugates including glycoproteins, proteoglycans, glycolipids and even the recently discovered glycoRNA.[14-16] The origin of this complexity are their monosaccharide building blocks, which can be linked to each other in many ways as every hydroxyl group of the carbohydrates can be used in the linkage.[17]

On top of that, additional complexity is added as the anomeric carbons can be present as equatorial or axial isomers at the anomeric center. To mimic these complex natural structures scientist have developed the concept of glycomimetics, which use artificial carbohydrate structures. On the one hand, glycomimetics are mostly easier to synthesize and they can be produced in larger quantities than their natural glycan. On the other hand, using multivalency or the introduction of e.g., aglycone motifs the avidity/affinity and potentially the selectivity compared to natural carbohydrate can be increased.[18]

A potential application of glycomimetics is their usage as drugs or in therapeutic agents. For example, in the bird flu pandemic the antiviral carbohydrate inspired drug Tamiflu was used to combat the virus (see Figure 3).[19] Tamiflu can be considered a sialic acid mimetic and serves as a viral neuraminidase inhibitor so that the virus is prevented from reproducing through budding.[20]

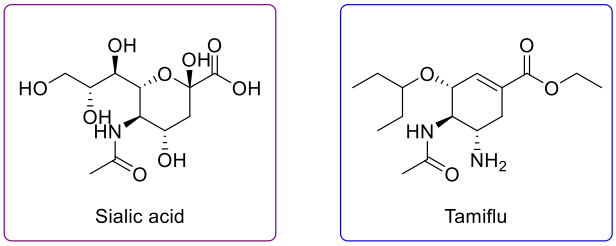

Figure 3. Sialic acid and its structurally related drug Tamiflu.

Additionally, not only monovalent but especially multivalent presentation of carbohydrates has been reported to be a potent strategy for drug candidates, mostly due to an increased specificity and avidity when compared to their monomeric counterparts.[21-24]

Furthermore, scientists use glycomimetics to simplify complex natural structures. As depicted in Figure 4 usually branched oligosaccharides are displayed on a cell surface, and it is generally thought that only most of the times only the terminal residue is crucial for any given binding event. The importance of the residual oligosaccharide scaffold is still not fully understood but it is assumed that they it serves a supporting role. Consequently, glycomimetics have been synthesized with the focus on the terminal carbohydrate moiety, thus allowing for simplifications as depicted in Figure 4.

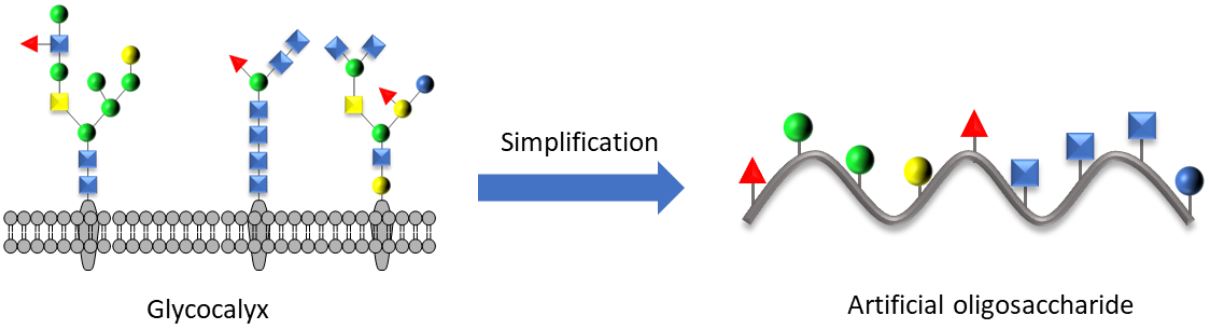

Figure 4. Schematic presentation of a simplified artificial glycocalyx, which only displays the terminal carbohydrate moieties.

The artificial scaffold can even be more simplified by only presenting one type of carbohydrate allowing to narrow down the importance of every carbohydrate presented, a so-called homomultivalent presentation. In recent years, many researchers have been working on glycomimetic with a special focus on the architecture but also on properties of the carbohydrate presenting scaffold. Different architectures e.g. linear, dendrimers, star shaped and brushes have been realized, while for the scaffold the influence of its length, rigidity, and hydrophobicity has been investigated.[25-31] Additionally, carbohydrates were attached onto nanoparticles or included into hydrogels trying to mimic at a smaller scale an entire cell with its glycocalyx.[32-34] Furthermore, accessing self-assembly also allows for the synthesis of complex 3D cell mimetics using glycolipids or block copolymers.[35-38]

In the next section, the underlying concept of multivalency and its consequences on binding shall be discussed.

1.1.2 Multivalency

The binding of a single carbohydrate to a receptor is relatively weak, hence Nature presents carbohydrates and/or receptors in a multivalent fashion to combine multiple weak binding events and create a strong attraction. A well-studied example is the binding of the viral membrane protein hemagglutinin to sialic acid derivatives. While the binding to a singular sialic acid is weak with a K_D value of around 2 mM, a multivalent presentation of sialic acids results in a K_D value of 0.3 µM.[39] Despite an increase in avidity and specificity, multivalent carbohydrate receptor binding events remain reversible. The four main mechanisms to consider in multivalent binding are receptor clustering, the chelate effect, statistical rebinding and steric shielding (Figure 5figure 5).

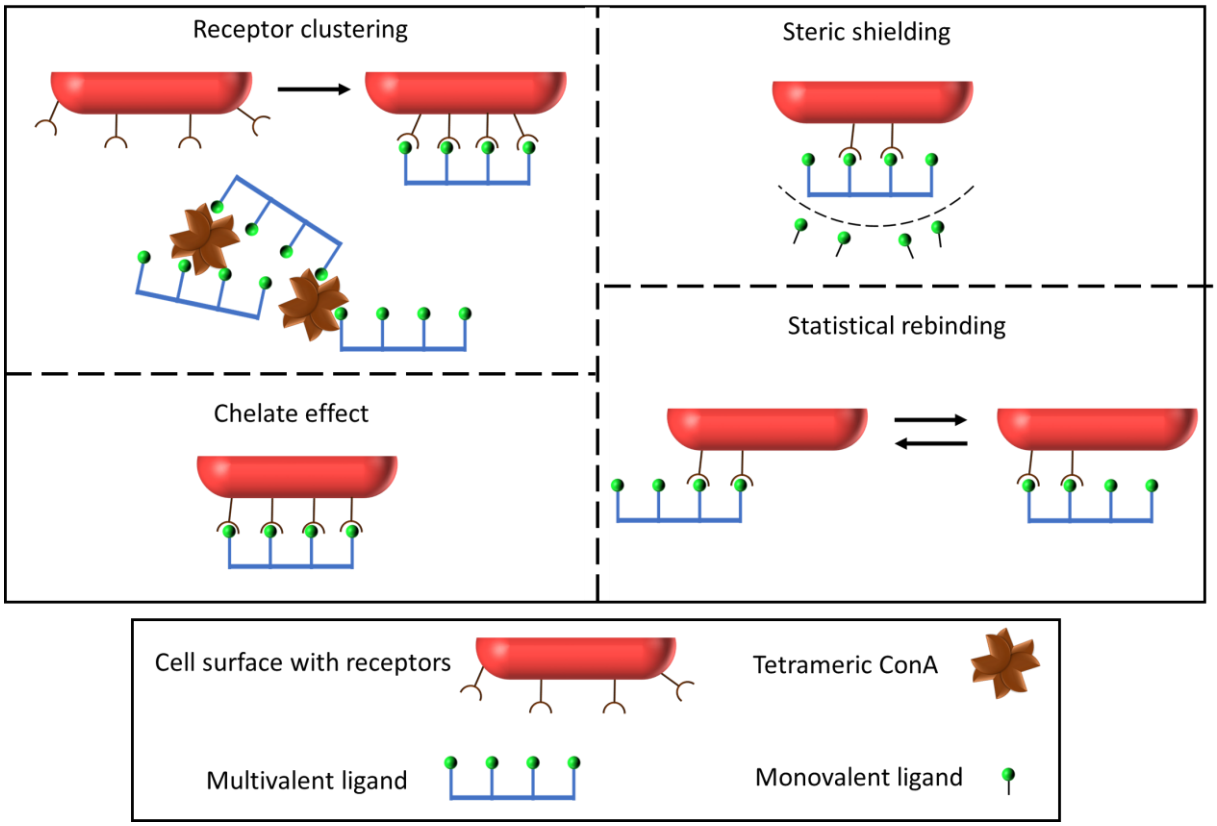

Figure 5. Schematic illustration of the four main mechanism relevant in mulitvalent ligand/receptor binding events (adapted from [40]).

Receptor clustering describes the phenomena when either a multivalent ligand induces a receptor clustering on a cell surface or when multiple multivalent receptors such as the tetrameric Con A bind to multiple multivalent ligands.[41, 42] In the latter case the receptors act similar to crosslinking agent for the multivalent ligand, which can potentially lead to precipitation of ligand-receptor complexes from solution. This ligand induced receptor clustering plays and important role in immune functions, growth factor signaling and neuronal cell communications.[43, 44]

While for the clustering multiple ligand molecules are involved, for the chelate effect only one multivalent ligand is involved. It describes the potential of a multivalent ligand to bind several carbohydrate binding domains (CRD) of one receptor, thus forming a chelate complex.[40] The chelate complex is generally more stable than a complex in which each binding site is occupied by a separate ligand. This increased stability can be explained through entropy considerations as the number of multivalent molecules in a chelate complex are less compared to monomeric ligands, thus less molecules are hindered to move freely in solution. In general, ligands binding to a receptor lose entropy by the meaning of rotational, transformational as well as conformational degrees of freedom.[24] However, for chelate binding it is assumed that the first

binding event pays the majority of the entropic loss, thus rendering the following binding events less 'expensive' in terms of entropy penalties. [21, 45]

Another important aspect is the so-called statistical rebinding. As mentioned earlier, the individual binding of a carbohydrate ligand with a receptor is highly reversible with high dissociation rates. However, for multivalent ligands a high concentration of unbound ligands is present in the proximity of the CRD, which can upon dissociation directly rebind to the CRD. This effect provides an apparent stronger binding for multivalent ligands.[46, 47]

The last mechanism is steric shielding and it considers the non-binding parts of a multivalent ligand, which can act as steric shields for the ligands that are bound to the receptor. This effect can prevent other ligands from interacting with the receptor, thus making a displacement of the bound ligand less likely. This steric shielding increases the overall binding affinity through stabilization and depends strongly on the size and type of the non-binding components of the ligand.[24, 48] For example a study by Jacobi et. al showed that PEGylated ligands have a significantly higher potential of inhibiting ligand-receptor interactions in comparison to their non-PEGylated counterparts.[49]

In an actual receptor-ligand interaction, these four multivalent effects do not occur separately. Even though research has been trying to understand correlations between structure and function, it is far from trivial to systematically study and in the next step to take advantage of multivalency using glycomimetics. One promising route could be the development of bottom-up assembled materials, which allow for the synthesis of big multivalent mimetics from relatively small and simple structures.

1.2 Self-assembly

The term self-assembly refers to processes of structure and pattern formation from individual elements that occur without any intervention. It covers not only the molecular level, as in the formation of cell membranes, but also on a macroscopic level like the formation of rafts by fire ants or a school of fish in the ocean.[50] There are mainly two types of self-assembly mechanisms: static and dynamic self-assembly. While structures following the static self-assembly form simply due to energy minimization, aggregates based on dynamic self-assembly require a continuous input of energy. The key difference is the need of a continuous energy input for the dynamic self-assembly in order to keep the system forcefully away from its equilibrium state. On the one hand, this makes the dynamic self-assembly harder to work with, because assemblies cannot be predicted based on energy calculation. But on the other hand, it also allows for structures that are not possible to achieve with static self-assembly. Not only the predictably, but also the feasibility of using assembled products in various environments (without continuous energy supply) makes static self-assembly more applicable. Common examples are surfactant micelles, block copolymer aggregates, nanofibers, and molecular crystals.[51-53] They find application in microelectronics and novel medicinal approaches e.g. drug delivery vehicles are widely employed in industry.[54-56]

The focus of the work described here lies on the assembly of amphiphilic molecules into micelles based on static self-assembly. The fundamental ideas and theories behind this concept will be explained in more detail.

1.2.1 Hydrophobic effect

The mechanistic effect responsible for spontaneous self-assembly is called the hydrophobic effect and it occurs when non-polar (or water-phobic) molecules or groups of molecules are present in aqueous solution.[57, 58] The effect is the cause of the formation of monolayers or phase separation but also of the self-assembly of lipid double layer or micelles. Despite controversial debates in the literature about the origins of this effect, the main theory describes the key driving force of the hydrophobic effect as entropy based.[59] A self-ordering or self-assembly that is entropy driven is counterintuitive at first, but a detailed discussion about the self-assembly process as depicted in Figure 6 provides an explanation.

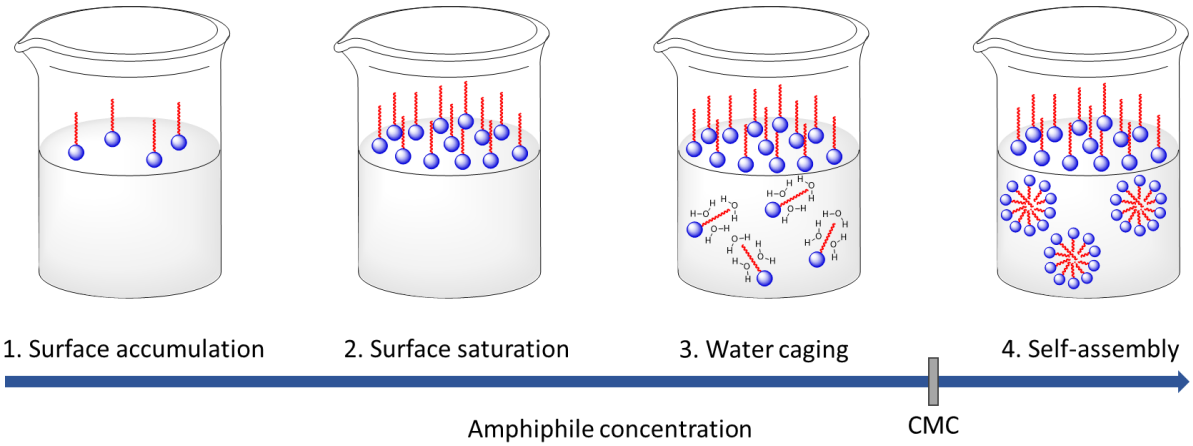

Figure 6. Stages of micellar self-assembly in water in dependence on the concentration.

As shown in Figure 6 the self-assembly process of an amphiphile in water depends on the concentration of the amphiphile. At first the amphiphilic molecules start to populate the water/air interface and the hydrocarbon tail sticking out of the water in order to reduce contact with it. In the second stage the surface gets saturated and every additional molecule cannot find space on the surface, thus it must remain in solution. When the third stage is reached the hydrogen bond network of the water molecules is disrupted and forces a reorientation of the water molecules in proximity to the amphiphile or rather in proximity of the hydrocarbon tail. The reorientation leads to a state where the water molecules form a cage like structure in order to minimize contact to the hydrocarbon tail and to reduce the disruption of its hydrogen bond network. Although the second law of thermodynamics states that the entropy of a closed system can never decrease, amphiphiles assemble into micelles over a specific concentration, the critical micelle concentration (CMC), as illustrated in Figure 6. Upon aggregation the amphiphiles lose entropy but the overall entropy of the system increases, due to the release of the water cage and the restoration of the water hydrogen bond network. The aggregation process can be described using Gibbs free energy equation.[60]

$$G(p,T) = H - TS \tag{1}$$

$$with\ G = Gibbs\ free\ energy\ \left[\frac{J}{mol}\right], p = pressure, T = temperature[K], H = enthalpy\left[\frac{J}{mol}\right]\ and\ S = entropy[\frac{J}{K * mol}]$$

As self-assembly is a spontaneous process without the need of an external energy supply, the Gibbs free energy of the process needs to be negative. Therefore, either the enthalpy, the entropy or both must be negative, to yield an exergonic process. For most amphiphiles the

enthalpy H is positive for the self-assembly at room temperature, thus the enthalpy is not the driver for the aggregation. Based on the aforementioned hydrophobic effect it is evident that upon self-assembly the systems entropy increases by the release of the water cage. This entropy gain outweighs the entropy loss, making the self-assembly process exergonic.

An even more detailed explanation of the thermodynamic model was developed by Tanford.[57] It describes the free energy change when an infinitely diluted amphiphile in water self-assembles into micelles.

$$\left(\frac{\Delta\mu^{\circ}{}_{g}}{kT}\right) = \left(\frac{\Delta\mu^{\circ}{}_{g}}{kT}\right)_{Transfer} + \left(\frac{\Delta\mu^{\circ}{}_{g}}{kT}\right)_{Interface} + \left(\frac{\Delta\mu^{\circ}{}_{g}}{kT}\right)_{Head} \qquad (2)$$

$$with\ k = Boltzman\ constant\ [\frac{J}{K}], T = temperature\ [K]\ and\ \Delta\mu^{\circ}{}_{g} = standard\ free\ energy$$

Three main terms need to considered for the change of the standard free energy, when self-assembly occurs. The first term describes the change in energy when a hydrocarbon-tail transfers from an unfavorable water medium to a more favorable oil-like medium in the core of the aggregate. The change of energy is negative and this contribution is the main driving force of the micellization process. The second term considers the remaining interaction of the hydrocarbon-tail within the assembly with water molecules and it is positive. The last term accounts for the head group repulsion, which contributes positively as the distance between the headgroups is reduced compared to their natural equilibrium state. The repulsion can be of steric or electrostatic nature, but electrostatic repulsion only occurs for charged headgroups. From Tanfords model the equilibrium area per molecule can be derived, which is an essential component in the considerations about the packing parameter proposed by Israelachvilli.[61] The next paragraph will highlight the potential and the limits of the packing parameter model.

1.2.2 Packing parameter

Based on the consideration around the hydrophobic effect it is possible to explain why self-assembly occurs, but it does not allow for any practical predictions concerning the single molecule and the associated self-assembled state. Micellar assemblies are very diverse and depending on their shape micelles can have different characteristics (see Figure 7). Comparing a spherical micelle with a lipid bilayer it is evident, that these assemblies can fulfil different

purposes. Lipid bilayers are incremental for cell membrane formation while spherical micelles are for example formed by commercial soaps. In drug applications today mainly, liposomes are used as they can reduce toxicity and increase accumulation at the target site. The sizing of liposomes is also a critical parameter, which can be controlled using various methods e.g., extrusion techniques.[62]

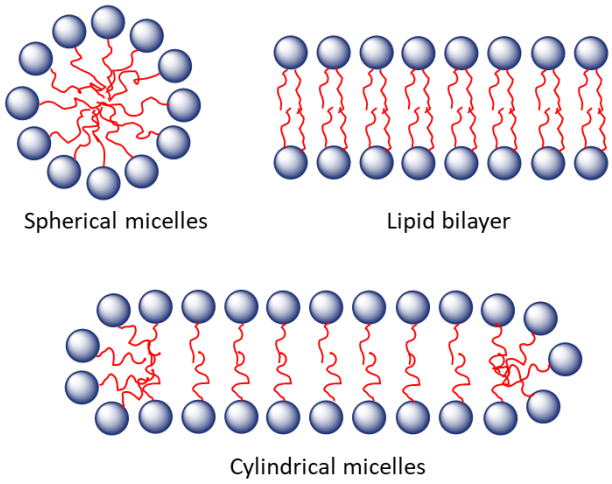

Figure 7. Typical examples of micellar assemblies.

Therefore, to match liposomes it is of interest to predict micellar shapes and sizes in order to unlock the full potential of self-assembly. In 1976 Israelachvilli developed a concept called the packing parameter, which allows for the prediction of the micellar shape based on considerations of the single amphiphilic molecule. His theory is based on a mix of thermodynamics, free energy and geometry considerations.[61] Israelachvilli has assigned critical packing shapes to specific threshold values of the packing parameter, which then lead in consequence to specific micellar assembly (see Table 1).

Table 1. Summary of the packing parameter, critical packing shape and the resulting micellar shape.

P_c	Critical packing shape	Expected micellar shape
$< \frac{1}{3}$	Cone	Spherical micelles
$\frac{1}{3} - \frac{1}{2}$	Truncated Cone	Cylindrical micelles
$\frac{1}{2} - 1$	Truncated Cone	Vesicles
~ 1	Cylinder	Planar bilayers
> 1	Wedge	Inverted micelles

The basic equation of the packing parameter is shown in Figure 8. As displayed, the parameters v_0 and l_0 represent the volume and the length of the surfactant hydrocarbon tail, respectively. For the majority of single tail amphiphiles the quotient of v_0 and l_0 is around 0.21 nm² and for double tail surfactants 0.42 nm². This simplification leads to the understanding that the packing parameter is only influenced by the equilibrium area per molecule, which is often equated to headgroup size.

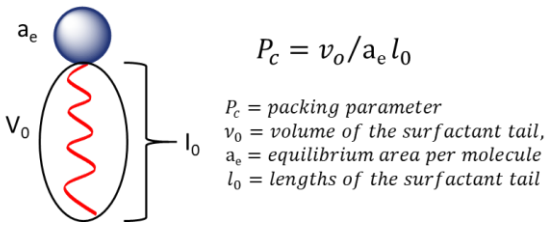

Figure 8. The packing parameter as introduced by Israelachvilli.

This holds true for some amphiphiles for example the non-ionic Brij which consist of a polyethyleneglycol (PEG) part (headgroup) and a polyethylene (PE) part (tail). If the PEG part is shortened, the headgroup size decreases, thus the packing parameter increases and if the threshold value of 1/3 is reached the micellar shape will change from a spherical micelle to a cylindrical micelle. However, for spherical ionic micelles, this simplification cannot be made, because as it was shown by Nagarajan that the tail has an influence on the ionic strength of the solution and thereby also the equilibrium area per molecule.[63] Additionally, applying the packing parameter in practice, it is rather difficult to determine the exact numerical values for all the parameters, therefore it is mostly used to roughly estimate which micellar shape can

be expected. Especially, when considering more complex amphiphiles e.g. division into head and tail group is not clear or when additional forces such as intermolecular hydrogen bonding are present, the model of the packing parameter becomes less suited.

1.3 Analytical methods for amphiphiles

For amphiphiles determination of the CMC is critical, as only after the CMC is reached micelles or other assemblies will be formed. This is then followed by an analysis of the formed micelles or assemblies with special focus on their shape, size and aggregation number.

1.3.1 CMC determination techniques

The main approaches used to determine the CMC are surface tensiometry, dynamic light scattering (DLS) and fluorescence spectroscopy.[64, 65] Surface tensiometry is by far the most common technique and it was invented Pierre Lecomte du Noüy, who is also the namesake of the du Noüy ring used in these measurements.[66] This method is based on the principle that the force required to lift a submerged ring from the water is directly correlated to the surface tension of the liquid. Other variants of the surface tensiometry use plates or rods instead of the du Noüy ring but follow the same basic principle. As described earlier in the paragraph 1.2.1 the hydrophobic effect, amphiphiles will first occupy the surface and by doing so the surface tension decreases. In practice a concentration series of the amphiphile is made and for every concentration the surface tension is measured. The CMC in this case is the point, at which the surface tension stops to decrease. The main advantages of this technique are that the instrumentation required is relatively cheap and no additives to the amphiphile solution need to be made. However, this method usually requires large sample amounts, as the ring or plate cannot be indefinitely reduced in size because the force to retract the ring becomes then too small to be measured for the attached scale.

Another non-invasive technique is DLS. The theory of DLS will be highlighted later (section 1.3.2.1) but the basic principle for CMC measurements revolves around the fact that the scattering intensity of an object increases with its size to the power of 6.[67] If now a concentration series of an amphiphile is measured, the scattering intensity is plotted against the concentration and the CMC is the point at which the scattering intensity markedly increases.[64] Furthermore, the high resolution of the DLS makes it suited to be used with small

sample amounts (in the mg range), but the high resolution is also its greatest disadvantage. This is especially true for small weak scattering particles as only the slightest amount of a contaminating particle e.g. dust can overshadow the sample's scattering signal. Possible ways to overcome this disadvantage is to use multiangle light scattering or a fitting method described by Ruf, which aims to eliminate the effect of dust.[68]

Another CMC determination technique with high resolution is fluorescence spectroscopy. In contrast to the before mentioned methods, the usage of fluorescence spectroscopy usually requires the addition of a reporter molecule to the sample solution, unless a sample is inherently fluorescent with a switchable nature that would be (de)activated upon micelle formation. Two of the most common fluorescence probes are pyrene and Nile red. Pyrene is well suited, because of its well defined five distinct vibrionic band peaks, which are strongly influenced by the hydrophobicity of the environment.[69-71] The ratio of the two vibronic bands vibronic bands (v_I at λ = 372 nm and v_{III} at λ =383 nm) has been shown to be especially sensitive to the polarity of the probes environment.[72] Unlike pyrene, Nile red is characterized by a pronounced solvatochromism and strong quantum yield dependency on its environment.[73, 74] The emission maximum shifts for example from 520 nm in heptane to 600 nm in acetone and simultaneously the quantum yield is reduced by a factor of 80.[75] Therefore, for Nile red both effects: the shift and the fluorescence intensity increase are suited to be used to determine the CMC. In general, when the measured sample starts to assemble into micelles both dyes will be incorporated inside the micelles and thereby the dye's environment changes from aqueous to a more hydrocarbon-dominated/-hydrophobic environment. The concentration is then plotted for pyrene against the I_1/I_3 ratio and for Nile red against the intensity or the blue shift of the emission maximum. The CMC can then be found as the intersection of the two linear fits as shown in Figure 9.

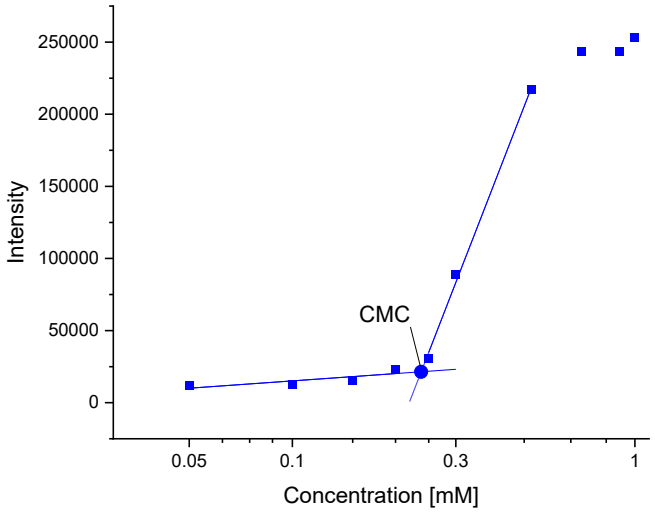

Figure 9. Schematic linear fits of typical CMC data.

1.3.2 Analytical methods to determine shape, size and aggregation number of self-assembled structures

Typical approaches to gain information beyond the CMC include the scattering techniques DLS, depolarized dynamic light scattering (DDLS), static light scattering (SLS) and also the image techniques atomic force microscopy (AFM), transmission electron microscopy (TEM) and transmission electron cryomicroscopy (cryo-TEM).

1.3.2.1 Scattering techniques

Using DLS not only the CMC but also the hydrodynamic radii, size distributions (dispersities) and aggregation effects can be determined.[76] The DLS itself measures the intensity fluctuations of the scattered light from the sample. These fluctuations are connected to the Brownian motions of the particles in the liquid medium and these in turn are dependent on the particle size as larger particles move more slowly than smaller ones. In order to gain information from the DLS data, those intensity fluctuations are converted into an autocorrelation function.[77] This function is then fitted using either the cumulant method or the Contin algorithm. These fits allow for the determination of the relaxation rates $\bar{\Gamma}$, which can be used to calculate the translational diffusion coefficient (D_t) as seen in equation 3.

$$D_t = \frac{\bar{\Gamma}}{q^2} \qquad (3)$$

$$with\ D_t = translational\ diffuson\ coefficient\ [\frac{m^2}{s}], \bar{\Gamma} = relaxation\ rate\ [s^{-1}]\ and$$

$$q = scattering\ vector\ [m^{-2}]$$

Following, the hydrodynamic radius (R_H) can be determined using D_t and the Stokes-Einstein relation (see equation 4).

$$R_H = \frac{kT}{6\pi\eta D_t} \qquad (4)$$

$$with\ k = Boltzman\ constant\ \left[\frac{J}{K}\right], T = temperature\ [K], \eta = viscosity\ [Pa * s],$$

$$and\ R_H = hydrodynamic\ radius\ [m]$$

One important point is that the hydrodynamic radius is only an approximation. As the Stokes-Einstein approximation is built upon a solid sphere model, it works well for spherical samples but is not suited for other sample shapes like rods or discs.[78] This is due to the fact, that for anisotropic samples not only the translational diffusion but also the rotational diffusion contributes to the measured intensity fluctuations. In a DLS setup this rotational diffusion is superimposed by the translational diffusion, which makes it impossible to determine the rotational diffusion (D_r).[79] In order to determine the rotational diffusion, DDLS is employed, which allows to isolate the contribution of the rotation to the scattering fluctuations. The setup for DDLS is similar to the DLS but instead of only one polarizer directly after the laser, there is a second polarizer between the sample and the detector. The polarizers are arranged in a crossed setup, which means that no light meets the detector unless the polarization of the light is changed. Only rotational movements change the polarization of the light and thereby the signal measured by detector can be solely attributed to the rotational diffusion. Fitting of these data leads to the rotational diffusion coefficient, which then can be used to calculate the dimensions of the anisotropic particle for example using the approach presented by De La Torre and Tirado for rodlike particles.[80, 81]

Furthermore, additional information about the particle in terms of the molecular weight, radius of gyration and the second viral coefficient can be gained using SLS. Most of the time multi-angle light scattering (MALS) is used as for all particles that are bigger than the Raleigh criteria (wavelength scattered light divided by 20), an angular dependency of the scattering can be found. Omitting this angular observation, would result in big errors. Furthermore, the option to determine the molecular weight using SLS is of particular importance when

considering micelles, as it is directly associated to the aggregation number.[82] One possible route is the MALS analysis of a concentration series of particle with a subsequent Zimm plot.[83, 84]

1.3.3 Microscopy techniques

TEM and AFM offer a direct route to determine the size and shape of a micelle. While AFM relies on the scanning of a surface with a cantilever, TEM is based on the interactions of the sample with an electron beam.[85, 86] Both techniques allow for ultra-high resolution images in a sub-nanometer range to be generated, which makes them suited to be used in the investigation of micelles. However, the usual analytical set-up of both techniques requires a dry and solvent free sample, which is in particular challenging for micelles as the self-assembly only takes place in solution. To circumvent this shortcoming, special preparation techniques can be employed like the spin coating method, which uniformly spreads the sample and also allows for a rapid evaporation, thereby better persevering the micellar structure. Under certain circumstance, both methods can also be used to measure samples in solution.[87, 88] AFM measurements in solution are highly depended on the rigidity and size of the sample and especially for soft micelles this experimental setup is fragile. In contrast, for cryo-TEM measurements, the sample solution is snap-frozen in liquid ethane and then again examined using electron beam.

1.4 Types of amphiphiles

The term “amphiphile” is based on the Greek terms amphis (both) and philos (loving) describing a molecule which has hydrophilic and hydrophobic properties. Amphiphiles or surfactants (surface active agents) are omnipresent and indispensable as they are not only used to form cell membranes but also in various applications ranging from washing to emulsifiers e.g. mayonnaise.[89, 90] In general, amphiphiles are classified either by their origin (biological or synthetic), their headgroup (cationic, anionic, amphoteric or non-ionic) or their size (low or high molecular weight). In Figure 10 three typical amphiphiles are categorized by their size. While small commercial amphiphiles like sodium dodecyl sulphate (SDS) and also some block copolymers are produced in a megaton fashion, whereas the majority of block copolymers and peptide amphiphiles (PAs) are more an academic niche but with an increasing number of commercial applications.[91, 92] The next paragraphs will shortly highlight peptide amphiphiles and block copolymers as they are the most relevant to the amphiphiles prepared in this thesis.

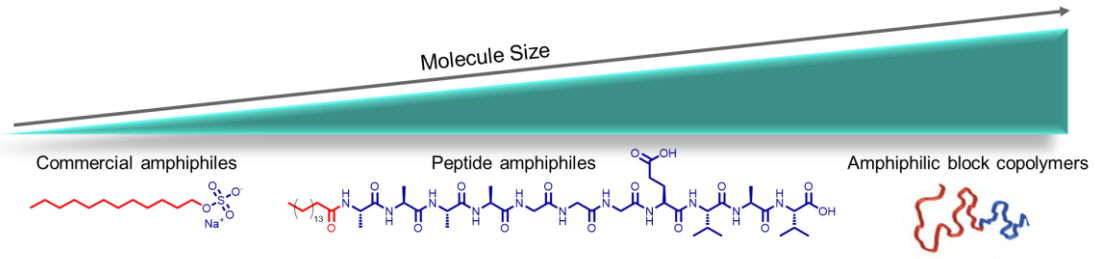

Figure 10. Three typical amphiphile groups categorized by their size.

1.4.1 Amphiphilic block copolymers

Since Szwarc prepared the first block copolymer of styrene and isoprene using living anionic polymerization, the interest and applications of block copolymer have been increasingly high.[93] Shortly after Szwarc´s studies, the first amphiphilic block copolymers that self-assembled into micelles were reported.[94] Amphiphilic diblock copolymers usually consist of a hydrophilic water soluble block (akin to the headgroup) and a hydrophobic water insoluble block (akin to the tail part). They are also able to self-assemble above the CMC, also often called in this context critical aggregation concentrations (CAC). However, in contrast to smaller amphiphiles, most block copolymers cannot be simply dissolved in water in order to achieve self-assembly. Specific preparations techniques e.g. dialysis are needed in order to switch slowly from an organic solvent like dimethyl sulfoxide (DMSO) or dimethyl formamide (DMF)

to aqueous solutions.[95] This slowly transition leads to the collapse/coalescence of the hydrophobic blocks and ultimately to a similar self-assembly process as described earlier for low molecular weight amphiphiles.[96] Furthermore, a novel approach called polymerization induced self-assembly (PISA) introduced by Armes et al. allows to skip the step of slowly exchanging the solvent to induce micelle formation. In PISA, a polymer that is soluble in a solvent (usually water) is grown with an increasingly hydrophobic content and at certain block size self-assembly can occur to a range of morphologies.[97-99] In general, the advantages of polymeric micelles (PMs) when compared to smaller amphiphiles are their greater stability of aggregates, lower CMC and potentially longer retention times due to their larger size. Additionally, amphiphilic diblock copolymers can be readily tuned in order to form a wide range of micelle morphologies.[100-102] Simply following the theory of the packing parameter, the size of the headgroup can be altered by varying the repeating units of the hydrophilic monomer, which in turn results in different assembly morphologies (see Figure 11).

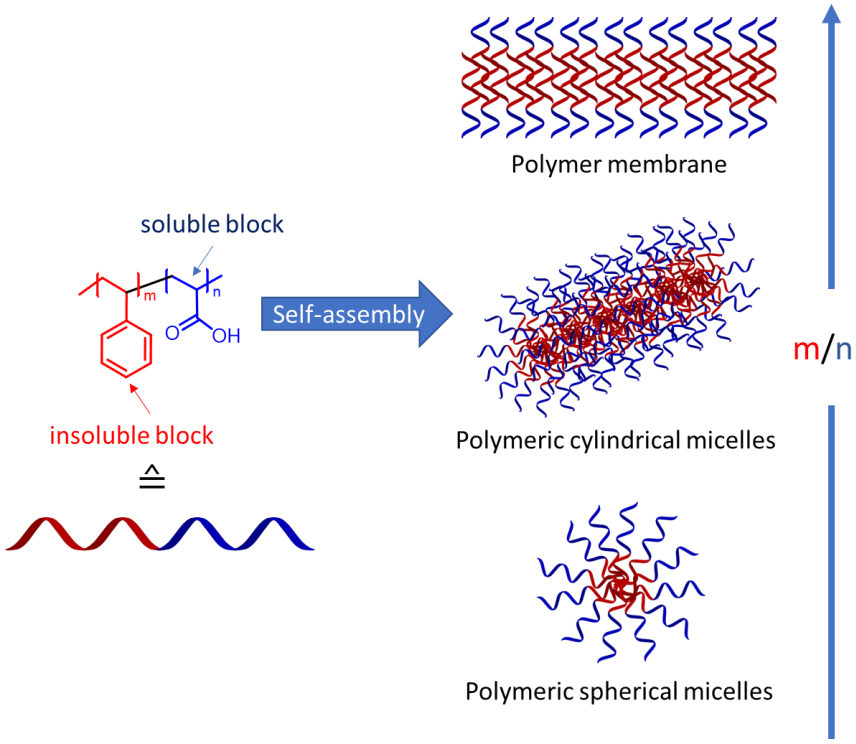

Figure 11. Schematic illustration of possible aggregates formed by polystyrene-block-poly(acrylic acid) in dependence of the polymer composition (adapted from [103]).

Amphiphilic block copolymers are used in various industrial applications such as the usage of alkylene oxide based block copolymers as stabilizers, surfactant and gelators.[104] More recently, applications in the field of drug and gene delivery have emerged.[105, 106] For example

a formulation of paclitaxel with polymeric micelles (Genexol®PM) was FDA approved due to its reduced toxicity and improved solubility of paclitaxel.[107]

1.4.2 Peptide amphiphiles

Peptide-based amphiphiles contain distinct hydrophilic and hydrophobic region. The hydrophilic region consists made of a peptide sequence while the hydrophobic part is either also peptide-based or a hydrophobic lipid alkyl chain can be utilized. In 1995 PAs were described for the first time by the group of Matthew Tirrell.[108] They employed solid phase synthesis to gain access to PAs with a double alkyl-chain, similar to phospholipids. Following the synthesis, they investigated the monolayer formation capabilities at the water/air interface, but they did not include any other experiments regarding their self-assembly behavior. Only six years after Tirrell, Stupps and coworkers reported a PA which self-assembled into fiber-like structures.[109] That PA had four key structural features for the headgroup and one key structural feature for the tail group as displayed in Figure 12.

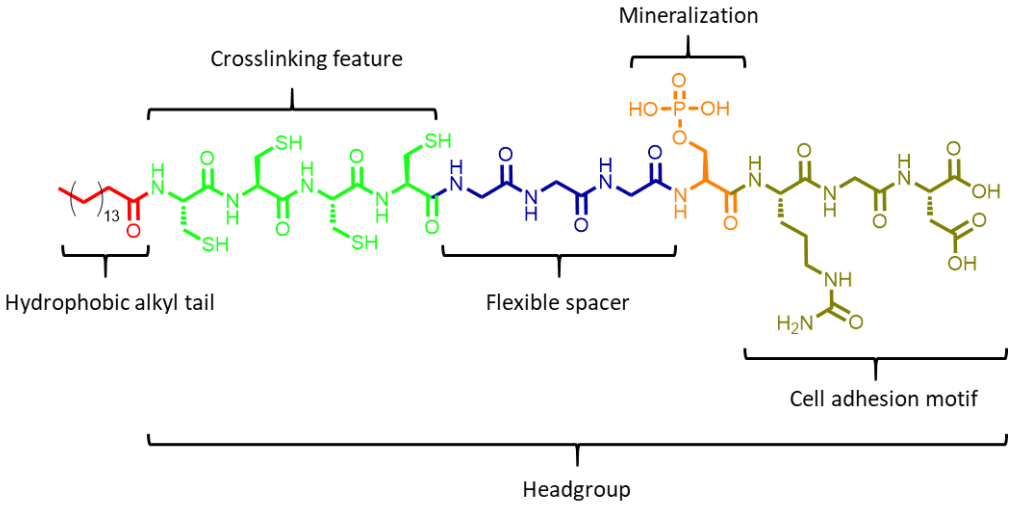

Figure 12. First reported fiber forming peptide amphiphile as reported by Stupp et al.

Most amphiphiles would be expected to assemble into spherical micelles but these PAs assembled into rods, which was unexpected due to the relatively large headgroup (see 1.3.2 Packing Parameter).

However, they found evidence of ß sheets and α helices in the assembled aggregates, most likely originating from the many amide bonds in the molecule. This led them to the hypothesis that this intermolecular hydrogen bonding and the resulting secondary structures could be the reason behind the fiber formation.

In a latter systematic study conducted by Hartgerink, this hypothesis was tested by systematically reducing the amount of amide bonds present in a PA by exchanging glycine units with sarcosine.[110]

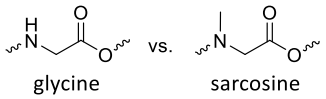

Figure 13. Comparison of built-in glycine (capable of hydrogen bonding) and sarcosine (not capable of hydrogen bonding).

They could provide evidence that below a certain threshold of amide bonds, mainly spherical micelles were formed instead of rods. Additionally, it was shown that amide bonds in proximity to a hydrocarbon tail have a more pronounced effect on the assembly of rods than amide bonds closer to the headgroup. Another publication by Stupp et al. has shed further light on the assembly behavior of PAs with the consideration of energy landscapes of the supramolecular assemblies.[111]

As the understanding of PAs has deepened, many applications have evolved. Due to their similarity to natural peptides most of the applications have been focused on medicine including biosensing, bioimaging, and drug delivery.[112-114] A key feature which was often highlighted is the synthetic flexibility of the PAs allowing for the tailoring and adaption of the structure to the targeted application. When used as carriers for drugs or vaccines, the guest host interactions can be tuned but also the overall size of the micelles.[115, 116] Furthermore, bioactive motifs such as Arg-Gly-Asp (RGD), carbohydrates etc. can be easily introduced, which allow when combined with a release mechanism e.g. pH controlled for smart drug delivery.[117] The advantages PAs and other sequence-defined systems are derived from the flexibility offered by solid-phase synthesis, in the next section solid-phase synthesis shall be discussed and a range of materials will be highlighted.

1.5 Solid Phase Synthesis

As effortlessly as Nature synthesizes monodisperse sequence defined peptides, chemists have struggled for a long time to achieve similar results in the lab. The common approach for peptide synthesis relied on standard solution phase chemistry pioneered by Fischer, which required extensive purification after each amino acid coupling and was very low yielding.[118] In 1963 Merrifield revolutionized the way peptides were and are synthesized by establishing the concept of solid phase peptide synthesis (SPPS).[119] It not only accelerated the speed of the synthesis but also allowed for longer peptide sequences with higher yields while having fewer side and termination reactions compared to the solution phase peptide synthesis.

1.5.1 Solid Phase Synthesis by Merrifield

Merrifield's early studies on peptide growth factors, rendered the need of sequence defined peptides and ultimately led to the development of the solid phase peptide synthesis.[119, 120] The idea was to use an insoluble solid support on which the peptide chain can grow and after each coupling the solid support can be washed, eliminating unnecessary, extensive intermediary purifications such as chromatography or recrystallization. As a solid support material, Merrifield used porous beads made from cross-linked polystyrene (PS) with divinylbenzene (DVB).

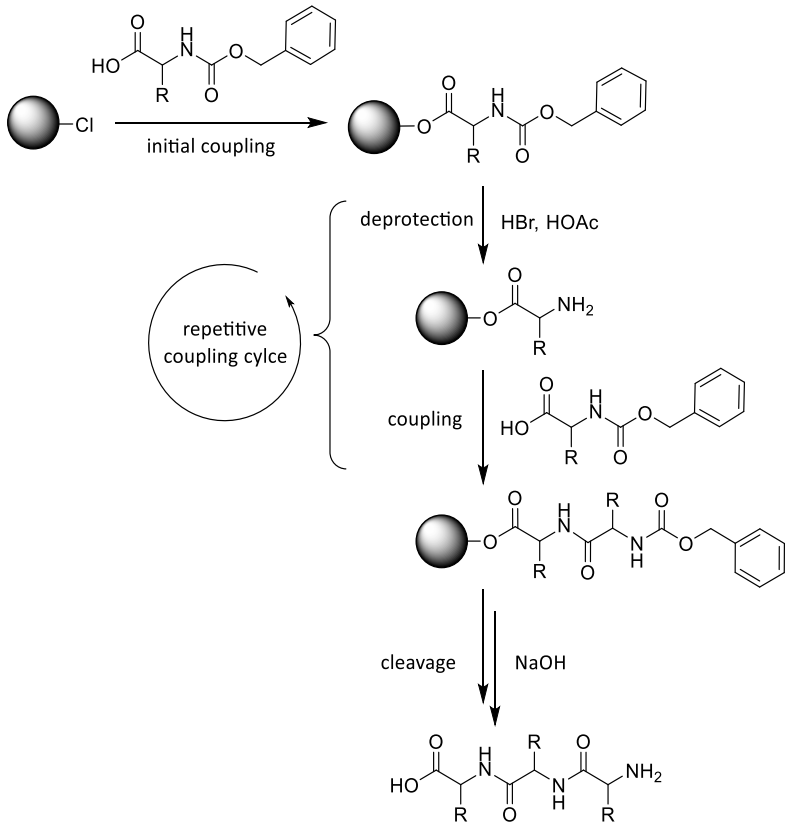

Figure 14. Scheme of the early SPS developed by Merrifield (adapted from [119]).

The polystyrene beads were chloromethylated in order to allow for an initial amino acid coupling and also for a later cleavage of the final peptide. In Figure 14 the early synthetic scheme of the SPS is displayed. During the solid phase synthesis only N-terminal protected amino acids are utilized to avoid multi-coupling and other possible side reactions. The first amino acid is attached covalently to the beads at the carboxyl end and subsequently the peptide is elongated following, the repetitive coupling cycle: consisting of N-terminal deprotection and coupling. Repetition of these two steps is required for every amino acid in a target peptide sequence. In the last step the finished peptide is cleaved off the solid support and, if necessary, subjected to further purifications. Already in 1963 Merrifield realized that the SPS had the potential to revolutionize peptide chemistry, especially when automatization could be achieved.[119] Hereafter, the advances and improvements realized for today's SPS are presented.

1.5.2 Modern Solid Phase Synthesis

Based on the classic SPS developed by Merrifield et al. many improvements have been realized in the fields of solid phase resins, protecting groups and coupling reagents. The next paragraphs will highlight the most common examples in each field.

1.5.2.1 Solid Phase Resins and Linkers

With the manifold requirements the solid support needs to meet, in order to be suitable for a synthesis, many different resins have been developed. Thus, it is necessary to carefully evaluate, which resin fits best for a given synthesis. Characteristics to consider are swelling properties, cleavage orthogonality, chemical stability as well as loading capacities. In general, loading of a resin refers to how many moles (or millimoles) of a given peptide can be synthesized per unit of resin (typically it is denoted in the range 0.1 - 1.4 mmol/g). In Figure 15 three of the most common resins are displayed. to this day, PS resins crosslinked with DVB remain the most popular and widely employed resins, due to their low cost and stability. PS resins exhibit good reaction rates and swelling properties in non-polar solvents, which allow for the reaction sites located inside of the PS network to be made accessible. However, PS resins readily collapse in more polar solvents, thus as an improvement PEG grafted PS resins were developed. [121, 122]

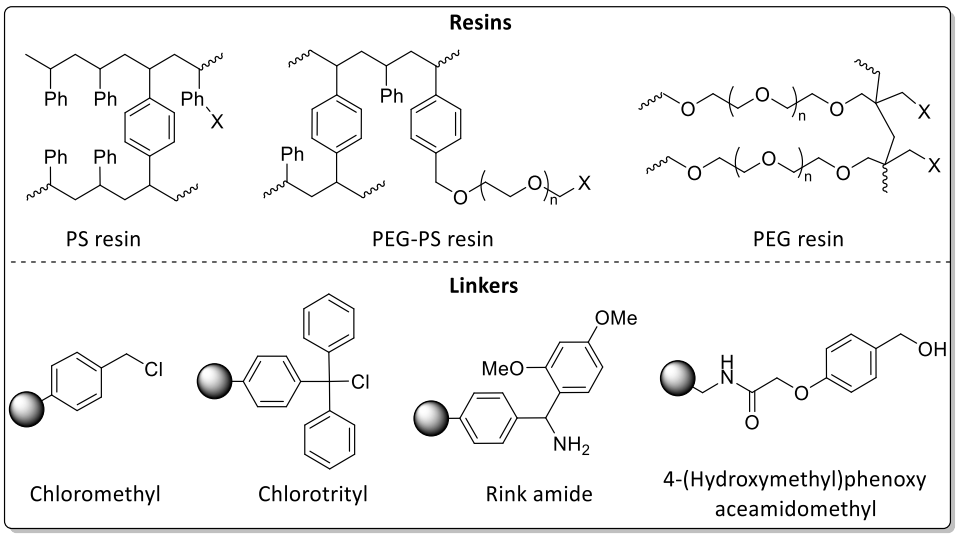

Figure 15. Overview of the most common resins and linkers for SPS.

These resins contain about 60-70% of PEG, hence the overall properties of the resin are dominated by the PEG content, which allows for sufficient swelling in polar solvents e.g. DMF.[123, 124] Additionally, the PEG linkers ensures that the reaction site behaves kinetically as in solution, instead of in a gel type state encountered for the PS resins.[125] Going one step

further, Meldal et al. and Cote independently developed a resin solely based on PEG.[126, 127] These resins combine the good swelling characteristics of PEG-grafted resins with the chemical stability of the PS resins, so that compared to PEG grafted resins no PEG leaching occurs during cleavage. PEG resins have been shown to be especially useful for long hydrophobic peptides, that were hitherto only accessible through ligation or recombinant techniques.[128, 129]

Not only the resin but also the linkers, connecting the solid support and the initial molecule, are key factors in SPS. Linkers can be differentiated by their attachment site N or C terminal, cleavage conditions and resulting end group of the released structure after cleavage. Four prominent examples of linkers are displayed in Figure 15. Comparing the Rink amide and the 4-(Hydroxymethyl)phenoxy aceamidomethyl (HMPA) linker, the previously mentioned differences among linkers can be seen. The Rink amide only allows for C terminal attachment, while the HMPA linker allows for both C and N terminal attachment. Additionally, cleavage from the Rink amide is only achieved with extremely acidic e.g. 95% trifluoroacetic acid (TFA) in DCM, where the HMPA allows for milder acidic and even basic conditions.[130, 131] In general, the most common linkers are acid labile and cleavage from the resin is released with TFA ranging from 1 to 95 vol%. However, until today a broad variety of alternative linkers have been developed allowing researchers to choose from a range of cleavage conditions such as acidic, basic, reductive, oxidative or even UV irradiation.[132-134]

1.5.2.2 Protecting Groups and Coupling Reagents

As solid phase synthesis is a stepwise procedure with repeating cycles of deprotection and coupling, it is crucial that both steps are quantitative, otherwise impurities will add up resulting in a highly impure mixture and for longer peptides target structures might even not be isolable.

Already, Merrifield made use of the carbodiimide coupling reagent *N,N'*-dicyclohexylcarbodiimide (DCC) developed by Sheehan and Hess (see figure 16).[135] Activation by DCC relies on the formation of an active O-acyl isourea intermediate, which than can be attacked by a resin bound primary amine releasing an urea derivative, whilst forming an amide bond. However, carbodiimide-mediated coupling suffers side reactions, such as rearrangements to stable N-acyl urea compounds or racemizations.[136] The rearrangements can be considerably reduced by cooling the carboxylic acid and the coupling reagent to 0°C before introducing a nucleophilic amine. Furthermore, the addition of a nucleophile that

reacts faster than the competing acyl transfer and produces an active intermediate that is still able to couple with the amine also prevents the side reactions. Nowadays, there are a variety of high performance coupling reagents such as the phosphonium salt benzotriazol-1-yl-oxy-tris-(pyrrolidino)-phosphonium hexafluorophosphate (PyBOP) or the uronium salt 2-(1H-Benzotriazol-1-yl)-1,1,3,3-tetramethyluronium-hexafluorophosphat (HBTU), which have been optimized to minimize side reactions and racemization.[137, 138]

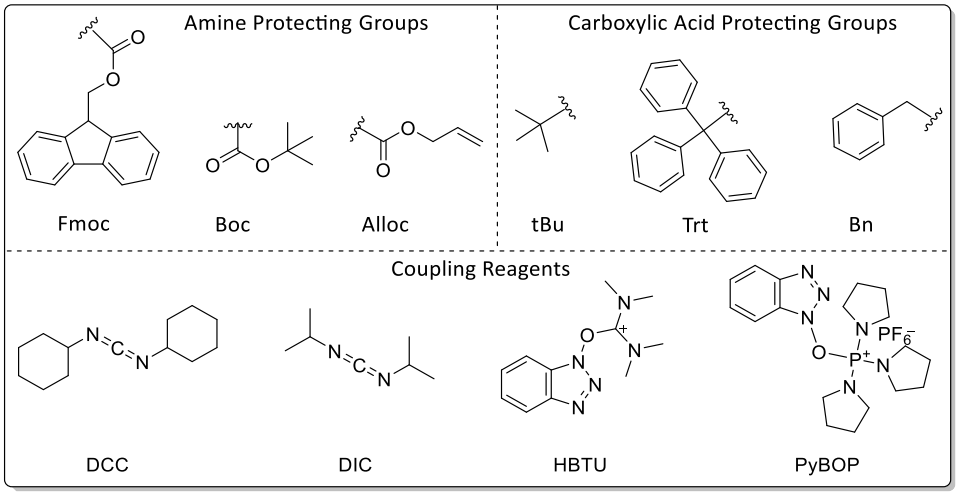

Figure 16. Exemplary structures of the most common protecting groups and coupling agents.

On the other side, protecting groups (PGs) are an essential part of SPS as they inhibit multi-coupling, and the production of faulty sequences, whilst allowing for new architectures e.g. branched structures to be synthesized.[139] PGs should be stable during the reaction and ideally facile to introduce/remove from the target functional group before/after the reaction in-solution and on-resin, respectively. Generally, PGs can be divided into amine and carboxylic acid PGs (see Figure 16). The standard procedure today relies on fluorenyl methoxycarbonyl (Fmoc) chemistry combined with acid labile linkers as Fmoc can be cleaved under mild basic conditions using secondary amines such as piperidine, so that limited product loss occurs while deprotecting. Furthermore, the half-life of Fmoc in 20% piperidine solution (pH = 12-13) is six seconds allowing for an efficient and fast deprotection, which is essential during the automated synthesis of longer peptide sequences as the overall synthesis time can be drastically reduced compared to the carbobenzoxy group used by Merrifield.[140, 141] Concerning the synthesis of complex peptides, orthogonal PGs need to be employed. Orthogonality in this context, means that PGs can be cleaved off individually from one another. The allyloxycarbonyl (Alloc) PG is well suited to be used together with many PGs for example Fmoc,

tert-butyloxycarbonyl (Boc) and tert-butyl (tBu) as Alloc is stable under acidic as well as basic conditions and is only cleaved upon exposure to palladium species.[142]

1.5.3 Solid Phase Polymer Synthesis

Following the Merrifield concept of the SPS for peptides, SPS approaches for the synthesis of nucleic acids and carbohydrates emerged.[143, 144] Parallel fully automated peptide synthesizers had grown out of their infancy and with that enabled scientists to cancel out mistakes during synthesis and by operating these synthesizes 24/7 longer sequences became feasibly accessible. In 2001, Seeberger and colleagues succeeded for the first time to transfer this fully automated process onto the synthesis of oligosaccharides.[145] With the clear aim to develop a new synthesis towards sequence-defined macromolecules, Hartmann et al. introduced the solid phase synthesis of alternating condensation reactions of diamine and dicarboxylates resulting in monodisperse poly(amidoamine)s (PAA).[146] This method gave access to fully synthetic monodisperse and sequence-defined oligoamidoamine structures that would not be accessible by classical polymerization methods such as polycondensations. While not requiring any PGs, this method was partially restricted in possibilities of architectural variations or introduction of side chain functionalities. Therefore, an alternative method based on PG chemistry was introduced to allow the usage of tailor-made bi- or multi-functional building blocks allowing for more synthetic freedom.[22] Each building block presents a free carboxylic acid and a protected amine group, most of the time Fmoc as temporary protecting group, thus allowing for fully automated assembly by standard peptide coupling protocols. The building blocks, so far developed, can be divided into two subcategories, functional building blocks, which allow for the introduction of ligands in the sidechain and spacing building block. An overview of the most utilized building blocks is provided in figure 17.

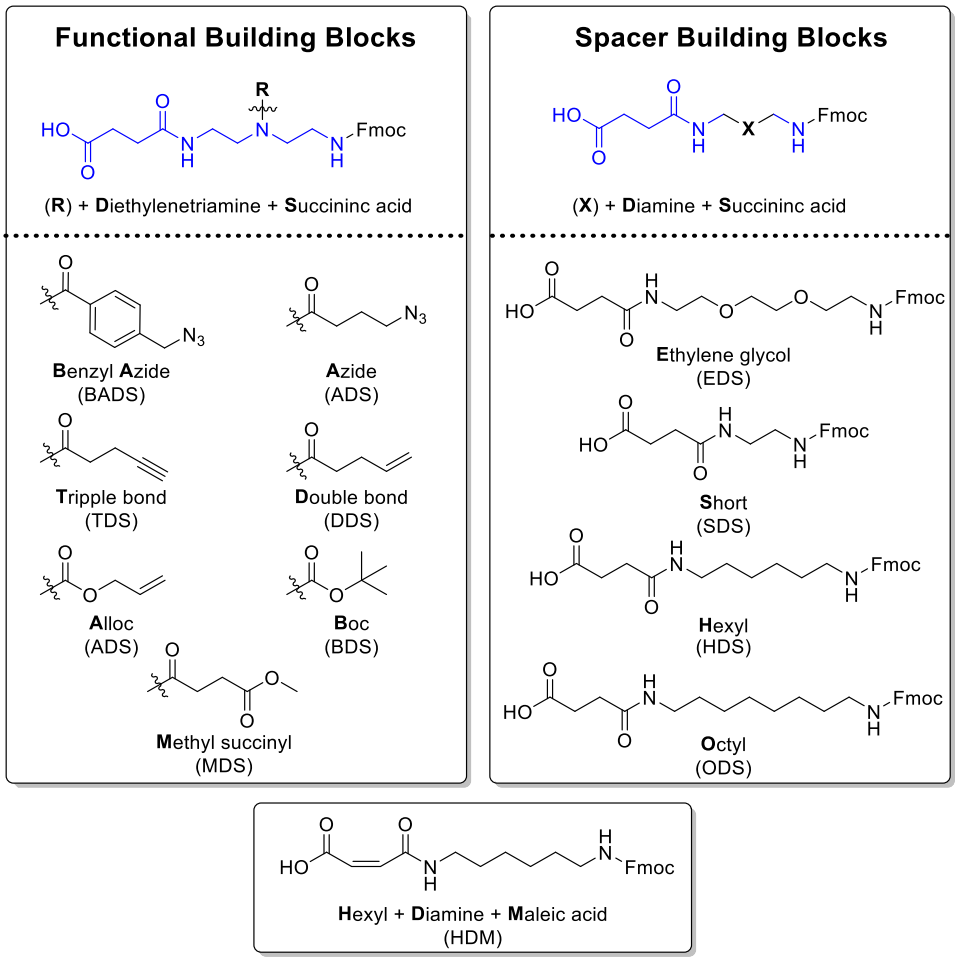

Figure 17. Overview of the building block library from the Hartmann lab.[22, 29, 131, 147-150]

The synthetic approach for today's solid phase polymer synthesis (SPPoS), carried out in the Hartmann Lab, is visualized in Figure 17. In short, as a first step the carboxyl moiety of the initial building block is coupled to an amine functionalized resin (here shown with a Rink amide linker). While coupling, the amine group of the building block remains protected, thus preventing side reactions. After the initial coupling and after every coupling and deprotection step the resin is washed thoroughly to clear excess reagents and to prevent faulty sequences. Subsequently, the PG (in this case Fmoc) is cleaved off the terminal amino group using piperidine. Following deprotection and resin washing, the next building block is coupled. This two-step coupling cycle consisting of deprotection and coupling can be repeated until the desired sequence is obtained. Additionally, when building blocks like **t**riple bond functionalized **d**iethylenetriamine coupled with **s**uccinic anhydride (TDS) or **b**enzyl **a**zide functionalized **d**iethylenetriamine coupled with **s**uccinic anhydride (BADS), which carry a functional side chain, are coupled, it is possible to conjugate ligands to the oligo(amidoamine) backbone. In figure 18 the conjugation of α-Man-azide to the backbone via copper(I)-

catalyzed azide-alkyne cycloaddition (CuAAC) is depicted.[151] This reaction is a catalyzed variation of the Huisgen 1,3-dipolar cycloaddition where a 1,3-dipole (azide component) reacts with a dipolarophile (alkyne component), which gives exclusively the 1,4-isomer whereas the non-catalyzed Huisgen reaction gives a mixture of both the 1,4 and 1,5-isomers.[152] The reaction belongs to the family of "Click reactions", which are characterized as one-pot reactions with high yields, while producing only minimal and inoffensive byproducts.[153] Those characteristics make the reaction optimal for the introduction of ligands to assembled oligomers, so the final product remains monodisperse. Lastly, the final oligomer is cleaved from the resin using a cleavage reagent (in this case TFA). Cleavage conditions and the resulting end termini depend on the linker and resin used for the synthesis.

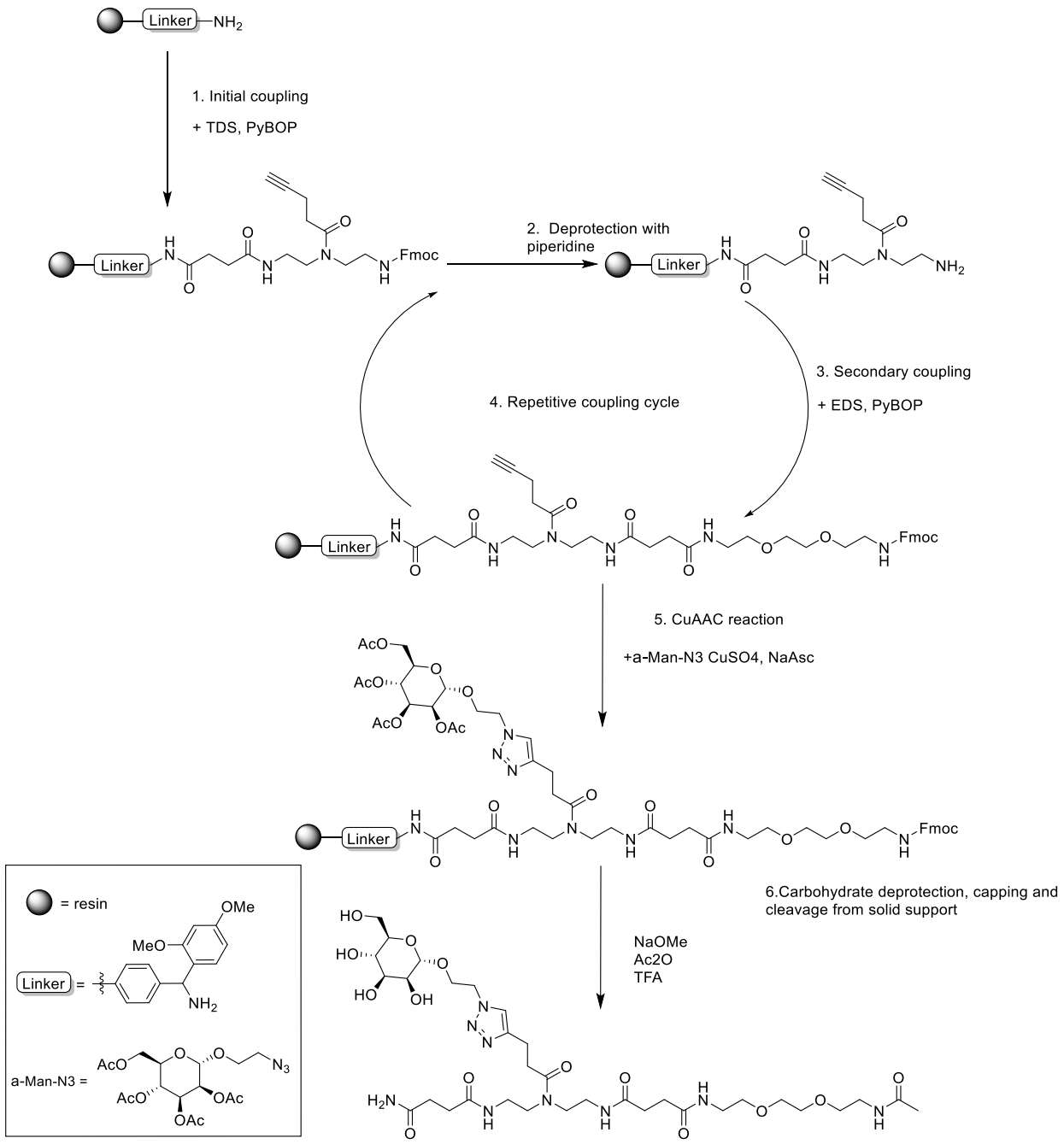

Figure 18. Exemplary SPPoS with the tailor-made building blocks TDS and EDS and subsequent CuAAC coupling of Man-azide.

2 Aims and Outline

The interaction of carbohydrates and carbohydrate-recognizing proteins such as lectins is of great importance in many biological processes such as cell communication and signal transduction processes. Additionally, carbohydrate-protein-interactions are associated with pathogen adhesion to host cells and are crucial in many developmental stages of cancer cells.[1, 154, 155] These interactions rarely take place between a single receptor and single ligand but are rather based on multivalent interactions of multiple carbohydrates and proteins simultaneously. Using this multivalent approach Nature increases the overall affinity/avidity of these binding events. Therefore, multivalency is also one of the main principles in developing glycan mimetics – artificial structures mimicking the carbohydrates' biological activity – e.g. when attaching multiple copies of a carbohydrate to a polymeric scaffold. In contrast to the high definition of their natural analogues, such synthetic glycan mimetics are often less defined with limited control over a monomer sequence and dispersity. To overcome this limitation, the Hartmann lab has made use of a stepwise assembly process of single monomer building blocks onto a solid support giving access to monodisperse, sequence-defined glycooligo(amidoamines) or so-called precision glycomacromolecules. A remaining disadvantage of this approach is its limitation in terms of molecular size/chain length and is thus not suited to be used to synthesize larger, polyvalent structures. In order to overcome this limitation, this thesis explores self-assembly strategies by first creating amphiphilic precision glycomacromolecules by solid phase synthesis, maintaining high structural control, that can then self-aggregate into micellar assemblies thereby resulting in larger, higher valent glycoassemblies. Such glycoassemblies can also be considered as simplified cell mimetics, they could find therapeutic application e.g., in antiadhesion therapy or be used for drug delivery, or a combination thereof.

Overall, the goal of this thesis is to develop a solid phase synthesis-based approach to access amphiphilic precision glycomacromolecules (APGs). Once the synthetic procedure is established, a series of APGs will be synthesized and studied regarding structure-self-assembly relationships and dependencies. Therefore, a range of spectroscopic techniques will be employed including fluorescence spectroscopy and dynamic light scattering to determine the CMC, the size and the shape of the micelles. Additionally, different microscopic techniques

e.g., atomic force, light and electron microscopy will be used to analyse self-assembled micelles. Having thoroughly investigated the APGs structure after self-assembly, the biological profile of APGs when interacting with lectins and bacteria shall be investigated, in particular examining potential inhibition characteristics.

In the second part of this thesis the building block library for amphiphilic precision glycomacromolecules will be extended by evaluation of two aggregation induced emission dyes (AIE) as hydrophobic tail components for APGs. In this joined project, three APGs containing different AIE dyes were synthesized and provided by Peter Pasch. In this thesis these AIE-APGs are characterized in terms of their self-assembly behavior and potential use as sensors to measure lectin binding.

The fourth part of this thesis will explore an alternative route to create larger, polyvalent glycomimetics employing controlled radical polymerization to derive poly(active ester) derivatives suitable for conjugation with precision glycomacromolecules. Therefore, a novel change transfer agent will be synthesized and used for the polymerization of an active ester monomer. Following, the active ester polymer will be functionalized with carbohydrates and analyzed regarding the size and number of carbohydrate units.

3 Results and Discussion

3.1 Amphiphilic precision glycomacromolecules

Over the years, the Hartmann lab has gained a lot of expertise regarding the synthesis of multivalent carbohydrate presenting structures. Usually they are synthesized employing SPPoS for shorter structures or combined with polymerization techniques to gain access to higher-molecular weight structures. In this thesis a new approach based around the novel class of APGs was developed. These relatively short APGs can be synthesized using SPPoS but allow for the bottom-up assembly of big multivalent structures. Combining the precision of solid-phase chemistry with a comprehensive building block library, this thesis aimed for amphiphile art (see Figure 19).

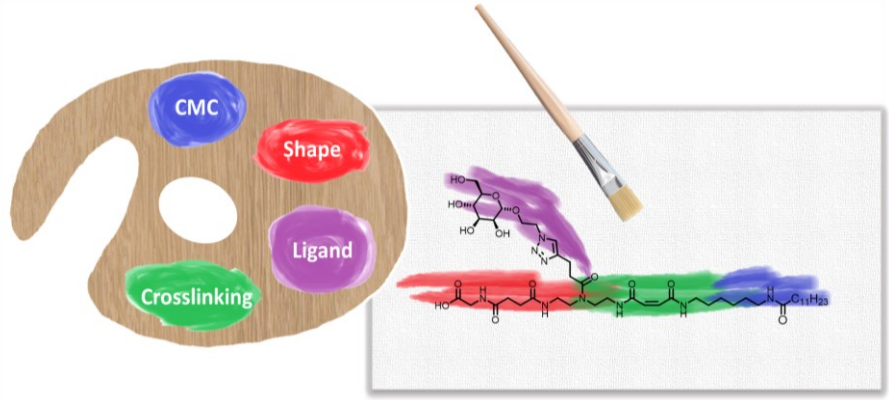

Figure 19. Amphiphile art (reproduced from [131], published by the Royal Society of Chemistry).

The upcoming section will highlight the basic concept of the design, synthesis, analysis and crosslinking of APGs.

3.1.1 Choice of building blocks and design of APGs

One of the first steps in the thesis was to establish a general concept about the structural composition of the APGs. For that the building block library from the Hartmann lab as well as many commercially available building blocks, were evaluated regarding their usage in an APG. The evaluation was mainly focussed on two points:

1. Can the building block be classified as hydrophilic or hydrophobic?

2. Which additional function can the building block add to the APG?

For conventional amphiphiles, e.g. surfactants like SDS or block copolymers like polystyrene-block-poly(acrylic acid), these criteria seem unnecessary, because their head and tail group can be easily distinguished and their components can be readily classified as hydrophilic or hydrophobic. However, for APGs this is more complex as a building block can be intrinsically hydrophobic but is used as a part of the headgroup, e.g. the functional building blocks TDS and BADS are used in the headgroup but are by themselves hydrophobic. Therefore, the first criterion should rather be:
Can the building block be used to generate a hydrophilic headgroup or a hydrophobic tail?
The second criterion was equally important and played a key role in the design of the new HDM building block, which was envisioned to be used for micellar core crosslinking (see chapter 3.1.2). Based on this evaluation of functionality, a range of building blocks were chosen to be tested as part of the head or tail group in APGs.

For the headgroup the functional building blocks TDS and BADS were chosen as they carry a functional side chain, which can be used to introduce carbohydrate ligands via CuAAC reaction (see Figure 20).[148] As carbohydrate ligands Man azide, propargyl Man and galactose (Gal) azide were chosen. Although being stereoisomers, Gal and Man exhibit vastly different binding properties towards lectins or pathogens like FimH expressing bacteria.[10, 11, 156] Therefore, this carbohydrate pair is particularly suitable for joint use, as one carbohydrate binds and the other can act as negative control. The structural similarity of Gal and Man makes them especially useful for amphiphilic structures as any larger alterations of the structure will also result in different self-assembly properties. Additionally, a terminal glycine unit was used to introduce a negative charge in the headgroup part of the APGs. The possibility of introducing a negative charge, increased not only the synthetic flexibility to access charged amphiphiles but also allowed for more colloidal stable APGs.

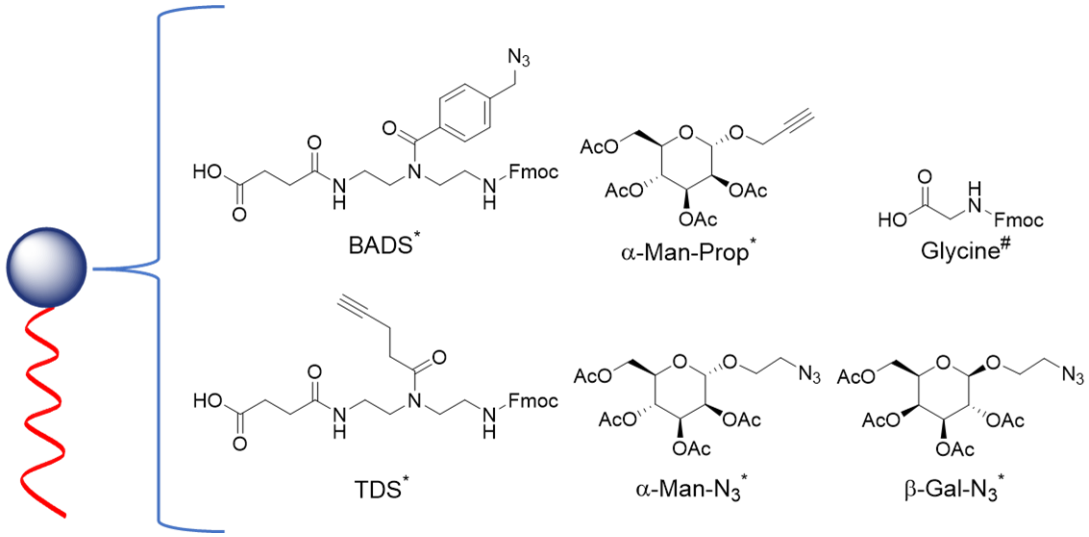

Figure 20. Building blocks used to generate a hydrophilic headgroup.[22, 148] All building blocks were either synthesized following previously reported procedures, bought commercially in the highest available purity# or developed as part of this thesis+.[22, 131, 148, 149, 157, 158]*

For the tail group the two new building blocks **h**examethylene**d**iamine coupled with **s**uccinic anhydride (HDS) and **h**examethylene**d**iamine coupled with **m**aleic anhydride (HDM) were developed (see Figure 21) (detailed synthesis is displayed in chapter 3.1.2). HDS was used as a hydrophobic spacer building block whereas the HDM building block additionally introduces a polymerizable moiety into the main chain of the APG. Furthermore, commercially available 4-(Fmoc-amino)benzoic acid was utilized as an aromatic, hydrophobic building block. Aromatic moieties are known to increase the rigidity of self-assembled structures, hence this building block was chosen to investigate its effect on the APGs.[159, 160] Moreover, six different fatty acids ranging from C_6 to C_{20} were employed as terminal hydrophobic building blocks (see section 3.1.3.1). Additionally, two AIE dyes, carboxylated aromatic thioether luminophore (CATE) and tetraphenylethylene (TPE), were investigated regarding their usage as tail group in a collaboration with Jun.-Prof. Jens Voskuhl and Peter Pasch.[157, 161] They are not only hydrophobic and aromatic but when these dyes are hindered in their free rotation they start to fluoresce.[162] This potential intrinsic sensor was reasoned to be potentially useful in determining self-assembly characteristics and binding characteristics of such AIE-containing APGs (see chapter 3.2). Lastly, **a**zide-functionalized **d**iethylenetriamine coupled with **s**uccinic anhydride (ADS) was used to allow introduction of alkyne-functionalized TPE as a terminal tail moiety.[149]

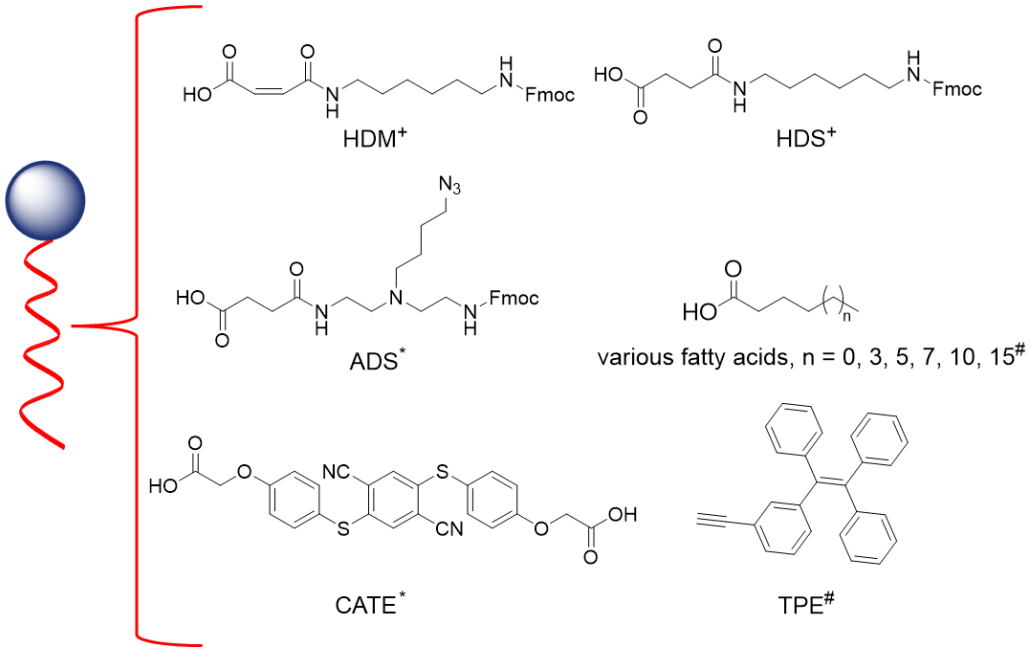

Figure 21. Building blocks utilized to generate a hydrophobic tail.[131, 149, 157](All building blocks were either synthesized following previously reported procedures, bought commercially in the highest available purity# or developed as part of this thesis.[22, 131, 148, 149, 157, 158])*

Based on this building block selection, basic design restrictions for the APGs were developed as the aimed amphiphilicity for the APGs requires a balanced composition of hydrophilic headgroup and hydrophobic tail building blocks. For all APGs the headgroup should consist of at least one functional building block with a carbohydrate unit attached to it, which ensures hydrophilicity but also biological activity. The hydrophobic part should consist for one sample set of at least one fatty acid and for the other set of exactly one AIE fluorophore. Following these guidelines, a series of APGs was synthesized and studied. The next subchapter will describe the detailed the synthesis of the new building blocks HDM and HDS and will highlight specific challenges for crosslinkable building blocks.

3.1.2 Design and synthesis of new functional hydrophobic building blocks

For the synthesis of APGs, three new hydrophobic building blocks were envisioned, with two of them bearing a crosslinking feature. Chemical crosslinking of the micelles should give the opportunity to lock APGs in their micellar structures. As the self-assembly process is dynamic and dependent on many factors such as concentration, solvent and temperature, having the option to fix the micellar structure can facilitate the analysis but also can serve useful in later applications.

Inspired by the already established spacing building blocks, succinylated 2,2'-(ethylenedioxy)bis(ethylamine) (EDS) and recently developed 4-((8-aminooctyl)amino)-4-oxobutanoic acid (ODS), three new building blocks were designed. [22, 29] In Figure 22 the three new hexamethylendiamine based building blocks are displayed.

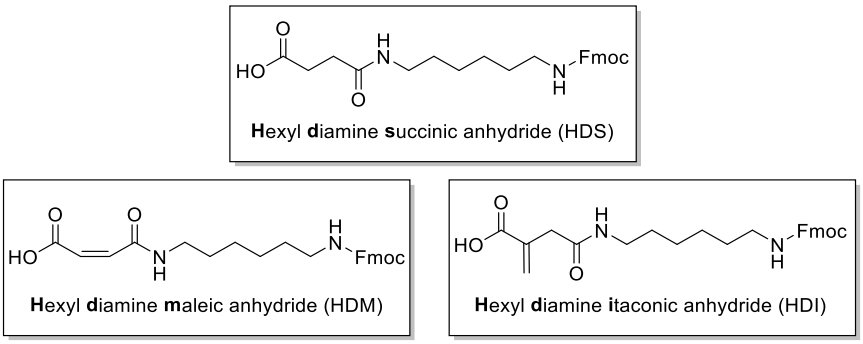

Figure 22. The three new building block HDS, HDM and HDI.

The first building block HDS, is a shorter derivative of ODS and serves as a hydrophobic alkyl spacer (see Figure 23).

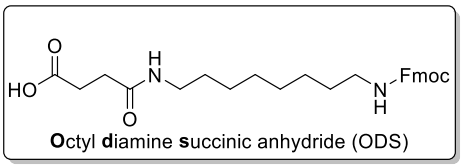

Figure 23. The hydrophobic spacing building block ODS.[29]

Hexamethylene was used instead of octamethylene as for ODS it was reported that coupling efficiency under standard conditions (DMF, 20 eq N,N - Diisopropylethylamine (DIPEA) and 4.9 eq PyBOP) was only around 70%.[29] This relatively low coupling efficiency is most likely due to the hydrophobicity of the building block and the resulting solubility problems in DMF. Compared to ODS, HDS coupled with an efficiency of >98% under standard conditions, which negates the need of double couplings.[163] The other two building blocks were also derived from a **h**examethylene**d**iamine core coupled with **m**aleic anhydride (HDM) or with **i**taconic anhydride (HDI). These hydrophobic spacers additionally introduce an alkene

moiety into the main chain, which allows for the introduction of a polymerizable unit into the structure of the hydrophobic part of the amphiphiles. It was envisaged this could allow for post assembly functionalization e.g. biomolecular conjugations via thiol-ene chemistry or allow for core crosslinking of self-assembled structures similar to what has been done with polymeric micelles.[164, 165] This will be further discussed in section 3.1.5. Furthermore, the main difference between HDM and HDI lies in the electron richness of the alkene moiety. For HDM the double bond can be considered electron poor as the carbonyl groups in proximity have an electron-withdrawing effect. In comparison, the double bond of HDI is less electron deficient as it is further away from the carbonyl groups. These differences could allow a wider variety of reaction types, for example the Michael addition, which favors electron poor alkenes.[164] In addition, an increasingly important factor is environmental friendliness of the chemistry, which also divides HDM and HDI. While maleic acid is mainly produced using conventional methods starting from petroleum, it is possible to produce itaconic acid biotechnologically from renewable ressources, specifically by fermentation of carbohydrates using fungi.[166]

Favorably, both alkene moieties are compatible with the standard reaction conditions of the SPS, thus no disruptive side reactions like unwanted side chain couplings or spontaneous polymerization originating from these moieties are expected. All building blocks share the same synthetic procedure until the coupling of the anhydride component (see Scheme 1). In a first step, excess of hexamethylenediamine (**1**) was asymmetrically protected using tritylchloride (Trt-Cl). The excess of (**1**) ensures that only the asymmetrically protected product (**2**) is formed and not the double protected unwanted derivative. Subsequent, in order to remove residual unprotected hexamethylenediamine the mixture was washed with bicarbonate solution, giving a nearly quantitative yield to product (**2**). In the next step the remaining primary amine of product (**2**) was protected using Fmoc-Cl following the optimized reaction conditions for the EDS and TDS building block.[22] After recrystallization product (**3**) could be isolated in high purities with an average yield of 60%. The final step for the synthesis of the intermediate (**4**), was the deprotecting of the trityl group using TFA. Deprotection could be followed by TLC and significant color changes (red/orange to yellowish) of the reaction mixture. After completion, the reaction mixture was precipitated and dried in vacuo. Altogether, compound (**4**) was isolated in an overall yield of 50% and high purities as analyzed by reverse phase high-performance liquid chromatography (RP-HPLC) and proton nuclear magnetic resonance spectroscopy (^{1}H-NMR) spectroscopy (see Experimental Section and

Appendix for further details on the synthesis and analysis as well as spectra of the final product).[131]

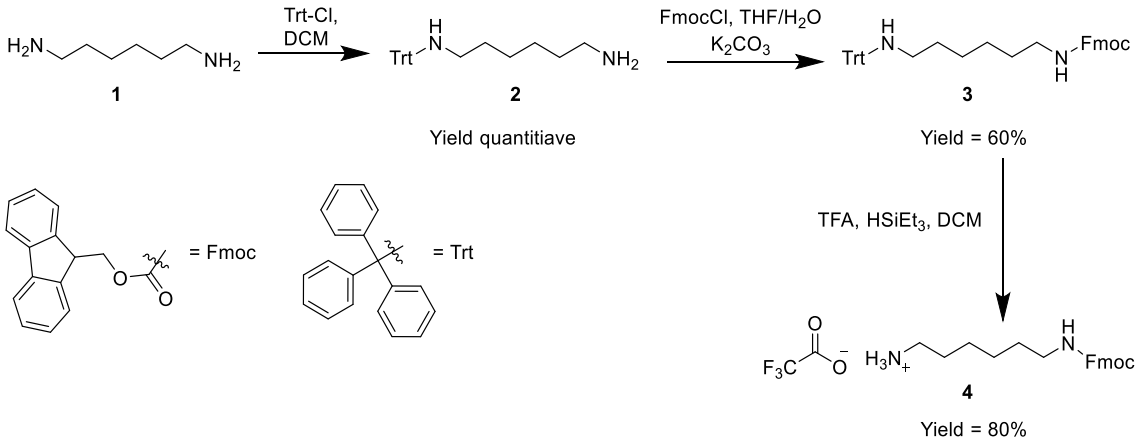

Scheme 1. Synthetic route for the intermediate structure synthesis

For the synthesis of HDS, compound **4** could be reacted with succinic anhydride following the optimized procedure for TDS and EDS reported in the literature.[22] However, following the same protocol for both maleic and itaconic anhydride, side reactions were observed, indicated by an almost instantaneous color change of the solution and a precipitate forming after several minutes of stirring. Most likely this precipitate is derived from the homopolymerization of maleic acid or itaconic acid. Braun and Pomakis showed in 1973, that maleic acid can homopolymerize in the presence of pyridine and to some degree also in the presence of triethylamine.[167] They postulated that the homopolymerisation of maleic acid is initiated through a charge-transfer complex of maleic acid and an nucleophilic organic base. In this process, the organic base is incorporated at the end of the polymer chain. NMR analysis of the precipitate revealed a clear polymer backbone signal and also a shift for some of the vinylic protons, which is expected for a polymer (see Appendix 1). Further evidence that this process also occurred in the present reaction is provided by mass spectroscopic analysis of the crude reaction mixture (see Scheme 2).

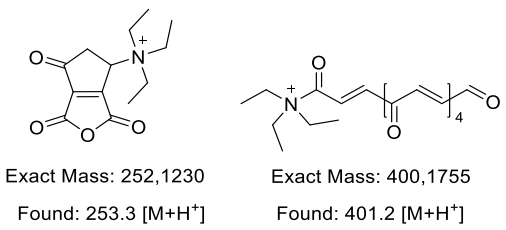

*Scheme 2. Side products of the reaction from compound **4** with maleic acid upon the addition of triethylamine observed via mass spectroscopy.*

Two triethylamine adducts could be assigned to the observed masses, which are both likely products of the polymerization as described earlier. One approach trying to prevent homopolymerisation, was to exchange triethylamine with different organic bases like DIPEA and 1,8-Diazabicyclo[5.4.0]undec-7-ene (DBU). However, homopolymerization still occurred with every base. Therefore, a new coupling protocol was developed, which starts by mixing compound **4** and a twofold excess of triethylamine. This mixture was then stirred for two hours in order to fully deprotonate compound **4**. Following, this mixture was added slowly over a period of several hours to a dilute solution of maleic or itaconic anhydride. Using this approach, no side reactions in form of polymerization were detected. Most likely, this is due to the fact that never a critical concentration of the organic base was reached to induce the charge-transfer complex. However, the yields following this route were significantly lower than for the synthesis of HDS. Additionally, for HDI always a mixture of the two possible isomers were obtained, which is due to that itaconic anhydride is, unlike maleic or succinic anhydride, asymmetric. Isomers could not be separated by recrystallization nor column chromatography, thus HDI was not used further as a building block for APGs in this thesis. Nevertheless, HDM and HDS were synthesized in high purities >99% and were characterized using RP-HPLC, ^{1}H-NMR and carbon nuclear magnetic resonance spectroscopy (^{13}C-NMR) (see section 5.3.1). The next subchapter will describe the synthesis of APGs, specifically highlighting important adaptions of solid phase synthesis protocols towards the efficient synthesis of amphiphilic structures.

3.1.3 Synthetics of APGs

3.1.3.1 Fatty acids as hydrophobic building blocks

An essential part in this work was the introduction of saturated fatty acids to the building block library of solid phase polymer synthesis. For that, fatty acids ranging from C_6 to C_{20} were investigated regarding their usage as SPS building blocks and their ability to induce self-assembly e.g. via micelle formation. All fatty acids except the C_{20} chain were readily soluble in the common SPS solvents (dichloromethane (DCM) and DMF) and showed quantitative coupling (examples of APGs bearing C_{10}, C_{12} and C_{15} can be found in in section 3.1.3.3). Only C_{20} fatty acid did not dissolve in DMF or DCM as tested by Jessica Kania in her master thesis, which makes it incompatible with the standard coupling procedure.[168] Further solvent testing (e.g. acetonitrile and ether) as well as using activation reagents variations (e.g. diisopropylcarbodiimid, Hydroxybenzotriazole (HOBt) and DCC) were not successful rendering the C_{15} fatty acid the longest aliphatic linear chain length compatible with standard conditions (DMF, DIPEA and PyBOP mixture). Moreover, fatty acids can only be used as terminal building blocks as they only have one functional moiety. However, when used, it makes the capping step unnecessary, which is often performed for terminal dimer building block in order to convert the residual free amine to an amide via acetic anhydride.

As will be shown in section *3.1.4 Analysis of APGs self-assembly behaviors*, APGs derived from fatty acids with 6 to 8 carbons showed no self-assembly behavior in concentration up to 10 mM and were therefore not used further in the synthesis of APGs (data not included). The concentration maximum of 10 mM was set as the regular synthesis batch performed in this thesis was yielding around 0.06 mmol of APG, thus making higher concentrations not feasible. Furthermore, all other fatty acids readily induced self-assembly and could be used to tune the CMC of the APGs.

3.1.3.2 Resins and yield

The choice of the right solid phase (resin) is crucial for the success of a solid-phase synthesis, because it determines compatible solvents, cleavage conditions, protecting group strategy, coupling strategy, the residual group upon cleavage and to some extend also the yield. For the main part of the APG synthesis the resins displayed in Scheme 3 were used.

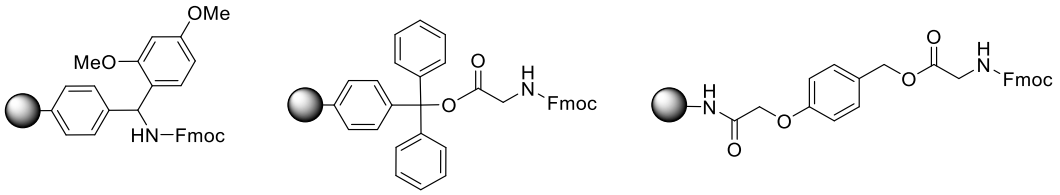

TentaGel S Ram TentaGel S TRT TentaGel R HMPA

Scheme 3. Different resins for the synthesis of APGs.

On the one hand, the commonality of these resin is that they are all TentaGel® resins, which are PEG grafted PS resin. This type of resin was chosen as it exhibits superior swelling properties. This is especially important for amphiphilic substances, as TentaGel® resins allow the use of solvents with different polarities during the coupling. On the other hand, the primary differences of these resins are the linkers, which influences the end group and cleavage conditions. Cleavage of the S Ram resin generates an amide while the other two resins are glycine pre-loaded and will yield a free carboxylic acid. Therefore, synthesis on the S Ram resin results in non-ionic APGs (if the APG has no other charged groups), whereas the synthesis on the other resins produces ionic APGs with a terminal carboxylic group. Synthesis was carried following previously established protocols of the Hartmann group (see Scheme 4).[29]

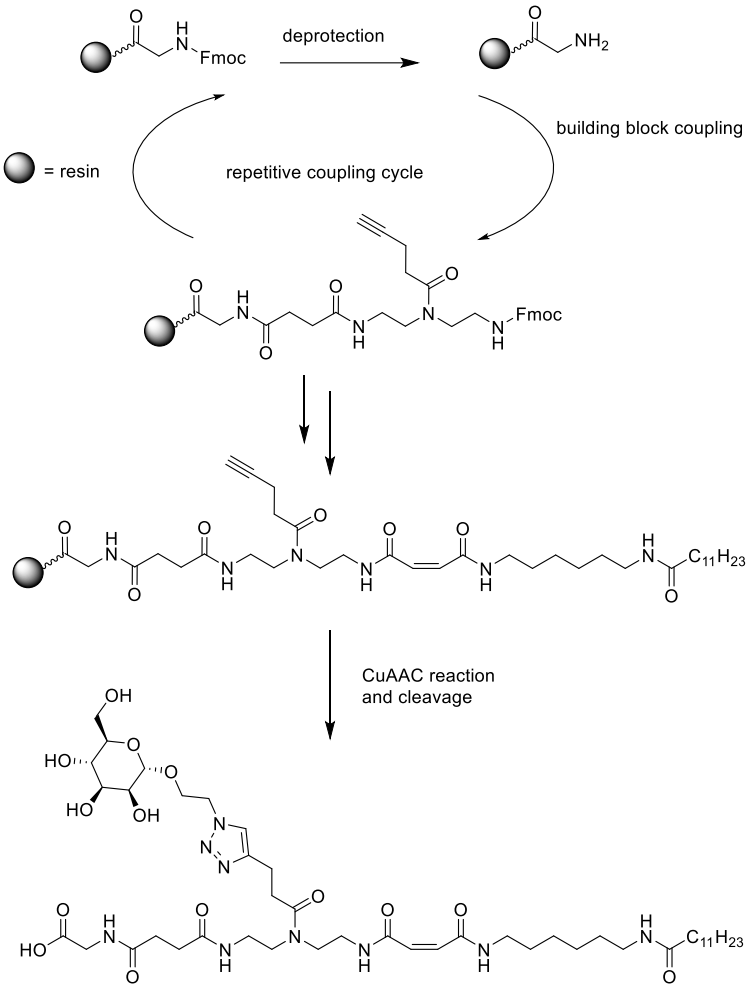

*Scheme 4. Solid polymer synthesis exemplary shown for APG **1**. (adapted from [131])*

Table 2 provides an overview of the used cleavage conditions and achieved yields of AGP **1** (TentaGel® S TRT) and APG **5** (TentaGel® S Ram) with the respective resin.

Table 2. Overview of the yields achieved with the different resins.

Resin	Cleavage condition	Yield range[a] [%]
TentaGel® S Ram	95% TFA, 2.5% TIPS*, 2.5% DCM	75 - 90
TentaGel® S TRT	0.05 M NaOH	8 - 32
TentaGel® R HMPA	0.05 M NaOH	60 - 90

*Triisopropylamine (TIPS), [a] Yield determined by weighing after freeze drying and either precipation (S Ram) or dialysis (S TRT and R HMPA)

Contrary to the manufacturer's suggested acidic cleavage condition, the glycine preloaded resins were cleaved using 0.05 M NaOH.[131] Using this approach, the cleavage of the final APG

and the deprotection of the acetylated carbohydrate moiety could be combined in one step, which allowed for an overall faster synthetic procedure. However, regardless of whether acidic or alkaline cleavage conditions were used, yields for the TentaGel® S TRT were always very low. Possible causes could be that the trityl linker is prone to be cleaved during either coupling or deprotection, which is supported by the fact that the yields for longer structures e.g. divalent or trivalent structures were especially low, marking the lower end of the yield range as shown in Table 2. As the building blocks used for the synthesis are quite laborious and expensive, low yielding syntheses are problematic. Therefore, different resins were tested and with the TentaGel® R HMPA, a resin was found, which showed nearly identical characteristic to the TentaGel® S TRT but with significantly higher yields, up to 90%.

Typically, oligomers are isolated after cleavage from the resin by precipitation in cold diethylether. Such direct precipitation mostly failed for ionic APGs. In general, purifying APGs and also other amphiphilic substances is not trivial as they are soluble in a wide range of solvents, which inhibits the use of solvent extraction for purification. On top of that, these molecules can aggregate in water, which interferes with the usage of water based chromatographic techniques such as preparative HPLC or GPC.

Considering APGs, two main isolating pathways were found and used in this thesis. The first pathway employs dialysis against water directly after cleavage and subsequent freeze drying, which produced clean products (>90% relative purity determined by RP-HPLC) with good yields (>60% final APG). However, this route was limited to APGs with a molecular weight above 1 kDa and also the dialysis tubes were not stable against TFA, so that exclusively APGs synthesized on the TentaGel® S TRT and R HMPA were isolated this way. The second pathway followed a more traditional peptide purification route, which included concentration of the cleavage solution, diluting with ether and subsequent cooling until precipitation. For most APGs both routes could be used, but the dialysis pathway gave cleaner products (always >90 % relative purity measured by RP-HPLC).

3.1.3.3 Synthesis of first APG library

With the building block platform, optimized resin choice and purification pathway at hand, eight APGs were synthesized and analyzed regarding their amphiphilic behavior (see Figure 24).

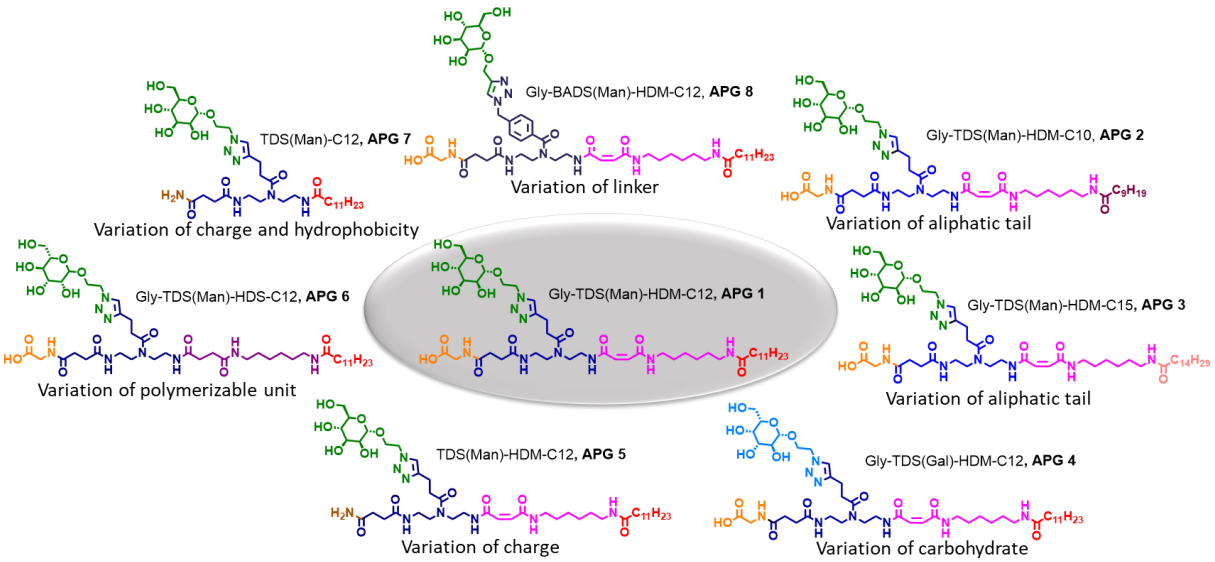

*Figure 24. Overview of the first APG library (APG **1** - **8**) (reproduced from [131], published by the Royal Society of Chemistry).*

The modular SPPoS approach allowed to systematically add and remove building blocks into the APG to determine the impact of specific building blocks on the characteristics of the APG. The first three APGs (APG **1** – APG **3**) were synthesized to examine the influence of different chain lengths of the terminal fatty acid. The overall structure was kept the same for all three APGs, consisting of glycine, a Man moiety coupled to the functional TDS building block, a hydrophobic HDM building block and as terminal component the respective fatty acid ranging from C_{10} to C_{15}.

The other 5 APGs (APG **4** - **8)** were based on APG **1** with different alterations to the head and/or tail group, but with the commonalty that all had a terminal C_{12} fatty acid. For APG **4** the tail was kept but Gal was attached to TDS instead of Man. Even though Gal and Man are stereoisomers they exhibit different properties especially considering their specificity to lectins. By omitting the glycine moiety for APG **5** another head group alteration was realized, which resulted in a non-ionic APG allowing to test the limits of this approach regarding solubility and stability. For APG **6** the hydrophobic building block HDM was exchanged with HDS, thus allowing to compare APGs with and without polymerizable moieties. Another non-ionic APG was realized with APG **7** but in comparison to APG **5** not only glycine was omitted but also the hydrophobic tail was shortened by removing the HDM building block. Lastly, for APG **8** the functional building block TDS was exchanged with BADS, which bears an aromatic linker instead of an aliphatic linker, allowing to test the influence of an aromatic feature in the APG structure towards its self-assembly characteristics. Synthesis of all APGs were performed

following the approach presented in 3.1.3.2 and with purities of above 90%. Structures were verified using ^{1}H-NMR, HPLC-MS and HR-ESI (see Figure 52-Figure 75).[131]

3.1.4 Analysis of APGs self-assembly behavior

Following the successful synthesis, AGPs were tested regarding their ability to self-assemble into micelles. The established experimental cascade revolved around a first quick foam test followed by CMC determination via fluorescence and finally analyses of the micellar shape and size by DLS, AFM and TEM.

The initial test for every APGs was the so called “foam test” and was rather simple and did not require instrumentation. The test consisted of dissolving APG in water and subsequent vigorous shaking of the vessel. If the APG is surface active, foam formation will be observed, which is a first qualitatively indication that the APG might self-assemble (see Figure 25).

Figure 25. A successful "foam test".

3.1.4.1 CMC measurements of the first APG library

Subsequently, for all APGs the CMC was measured, which is a critical characteristic as only above the CMC spontaneous formation of micelles occurs. For CMC measurements the most common methods are surface tension, fluorescence spectroscopy and DLS (see Introduction chapter). Due to the limited sample amounts, in this thesis mostly fluorescence spectroscopy was used for CMC determination.

As fluorescence probe, Nile red was employed instead of the more frequently used probe pyrene, because all APGs showed intrinsic fluorescence overlapping with the fluorescence of pyrene (370 to 400 nm) (Figure 86 - Figure 89).[72, 74] Using Nile red not only the problem with the intrinsic fluorescence of APGs was solved as it fluoresces in the region of 640 nm (emission maximum) but also the analysis of the data was simplified (Figure 90 and Figure 91). With pyrene, usually the ratio of the two vibronic bands (v_I at λ = 372 nm and v_{III} at λ =383 nm) is

used, while with Nile red simply the fluorescence intensity can be used. This is due to the fact that Nile red is highly solvatochromic and its fluorescence drastically increases in hydrophobic environments, in this case upon solvation inside the micelles.[75] The Nile red approach was optimized using a microplate reader, thus allowing for CMC determination of multiple APGs in one microplate in a 10 minute time frame. After data collection, the CMC is determined as the cross-section between the linear fits of the stagnant part and the exponential part (see Figure 26).

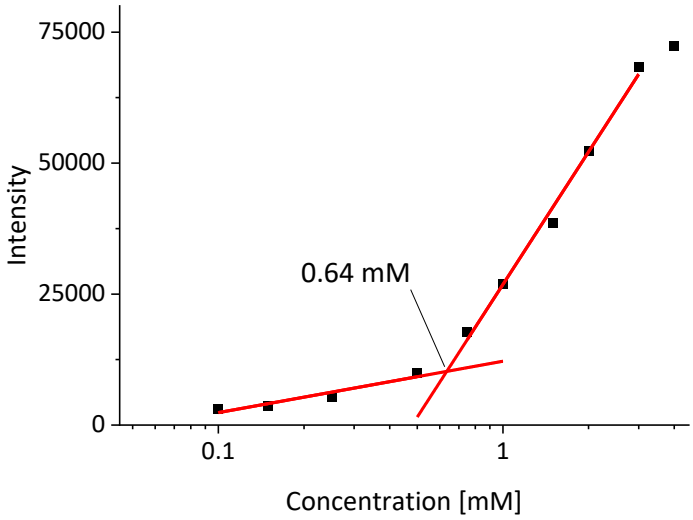

*Figure 26. A typical fitted CMC curve of APG **1**.*

Summarized data of all CMC experiments in MQ and phosphate-buffered saline (PBS) is displayed in Table 3. Experiments in PBS were carried out to evaluate the CMC of APGs in a high salt environment as for many biological assays solutions with a high salt content are necessary e.g., for lectin assays lectin binding buffer (LBB) or for bacteria assays PBS is used.

Table 3. Overview of the determined CMCs for all APGs in MQ and PBS.

Oligomer	CMC in MQ [mM]	CMC in PBS buffer [mM]
APG **1**	0.64 ± 0.07[a]	0.59 ± 0.01[a]
APG **2**	3.41 ± 0.08[a]	n.m.[b]
APG **3**	0.15 ± 0.01[a]	0.06 ± 0.004[a]
APG **4**	0.68 ± 0.07[a]	0.63 ± 0.07[a]
APG **5**	precipitation	precipitation
APG **6**	1.81 ± 0.02[a]	0.49 ± 0.001[a]
APG **7**	1.70 ± 0.19[a]	1.98 ± 0.02[a]
APG **8**	0.33 ± 0.01[a]	0.30 ± 0.01[a]

[a] error values represent standard deviations; [b] n.m. = not measured

In general, the CMC values of APGs seem to be higher than for PAs of similar length.[169-171] This could be caused by the usage of the tailormade building blocks, which could provide more steric repulsion than their natural counterparts (amino acids) and thereby leading to higher CMCs. Nevertheless, general reported trends still hold true for APGs, as APGs with longer fatty acids showed a lower CMC (0.15 mM for APG **3**) than APGs with shorter fatty acids (3.42 mM for APG **2**).[172] Furthermore, for the non-ionic APG **5** no CMC could be determined as it precipitated in minutes after dissolving. In contrast to APG **5**, for APG **7** a CMC of 1.7 mM could be determined but for this APG not only the glycine was omitted but also the hydrophobic HDM building block. This showcases the importance of the right balance of hydrophilic and hydrophobic components in an APG especially if no charges are present in the structure.

Additionally, comparing the CMC of APG **1** and APG **8** the exchange of TDS with BADS and thereby exchanging the aliphatic linker (TDS) to an aromatic linker (BADS) lead to an CMC reduction by the factor of 2 from 0.64 mM for APG **1** to 0.33 mM for APG **8** (see Table 3). This could be due to several factors. One cause could be the increased hydrophobicity of APG 8 as the BADS building block is more hydrophobic than the TDS building block. Another cause could be that with BADS the potential of π-π stacking was introduced, which in turn could positively influence the micelle formation, thus lowering the CMC.

As all of the APGs are aimed at to be used in biologicals assays, CMCs were also determined in PBS buffer. Literature suggest that for ionic/charged amphiphiles the steric repulsion between the head group gets reduced with increasing ion concentration in water, thus

lowering the CMC of charged amphiphiles in ionic solutions.[173] In accordance with the literature for all charged APGs a decreased CMC was measured (see Table 3). However, for the non-ionic APG **7** the CMC increased. In general, non-ionic surfactants are not influenced by changes in the ion concentration but rather by temperature changes. Potentially, different ambient temperatures of the experiments, as the MQ and PBS experiments were carried out month apart from each other, could be the cause of this increased CMC.

3.1.4.2 Analysis of size and shape of first APG library

With the CMC at hand, APGs were investigated regarding their micellar shape and size. Therefore, multiangle DLS as well as AFM and TEM experiments were performed in collaboration with Julian Sindram, Marius Otten, Dimitri Wilms, Alexander Strzelczyk, Sean Miletic, Matthias Karg and Thomas C. Marlovits. While AFM and TEM experiments only allow analysis of dried micelles, multiangle DLS experiments allowed to analyse micelles in solution. First multiangle dynamic light scattering and multiangle depolarized dynamic light scattering experiments were performed for APG **1**, APG **7** and APG **8**. In general, from the DLS data the translational diffusion coefficient (D_t) can be derived using the linear relationship shown in equation 3 (see introduction). With the D_t at hand and employing the Stokes-Einstein equation (see equation 4), the hydrodynamic radius can be calculated. However, this holds only true for spheres and not for any other aggregate shape. For other shapes it is important to also derive the rotational diffusion coefficient (D_r), which allows then, using different equation for different shapes, to calculate the aspect ratio. Therefore, DDLS is employed to derive the D_r from the distinct positive offset of the relaxation rates using equation 5.

$$\bar{\Gamma} = D_t * q^2 + 6D_r \qquad (5)$$

$$D_r = rotational\ diffusicon\ coefficient$$

In Figure 27 fitted data for APG **8** a) DLS and b) DDLS is shown and in Table 4 all scattering data is displayed.

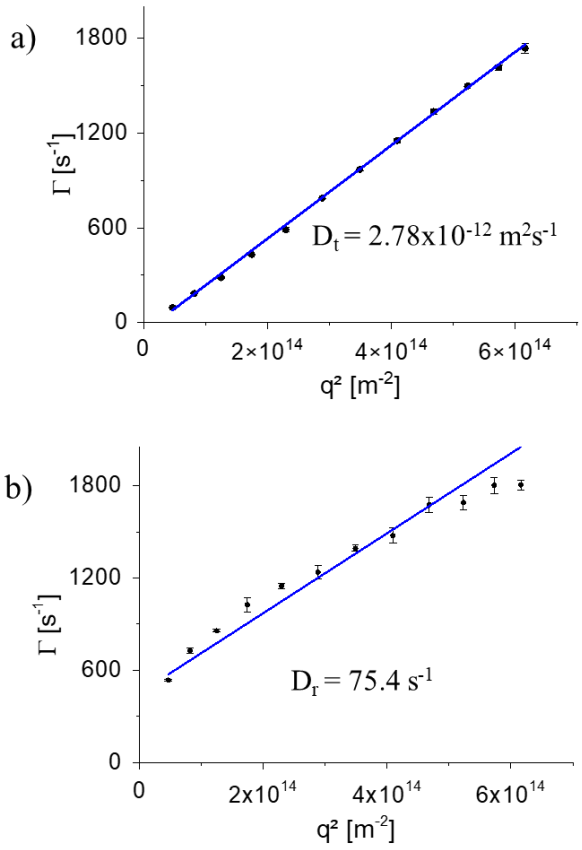

Figure 27. Fitted light scattering data for APG 8; a) DLS and b) DDLS (reproduced from [131], published by the Royal Society of Chemistry).

Surprisingly, for all APGs expect APG **7**, strong signals in the DDLS experiments were recorded, suggesting that only APG **7** self-assembles into spherical aggregates. In literature, for most single tail surfactants, mostly spherical micelles are reported, if not the conditions are altered e.g. by increasing the ion concentration.[174] However, for peptide amphiphiles Hartgerink et. al showed that depending on the number of possible hydrogen bonds in the peptide amphiphile structure, both spherical and rod like shaped micelles are accessible.[110] This is most likely due to the intermolecular interaction of the hydrogen bonds forming secondary structures such as β-sheets, which in turn favor rod like assemblies. As APGs are similar to peptide amphiphiles, the oligoamidoamine scaffold can potentially undergo similar interactions and form secondary structures. Supporting this hypothesis is the fact that the only spherical micelles forming APG (APG **7**), has the least amount of amide bonds with only three amide bonds compared to the five amide bonds of APG **1** and **8**.

*Table 4. Overview of the scattering data for APG **1**, **7** and **8**.*

Oligomer	D_t	R_H [nm]	D_r	L [nm]	r [nm]
APG **1**	$3.99x10^{-12}$	61.6	n.e.[b]	n.e.[b]	n.e.[b]
APG **7**	$3.97x10^{-12}$	61.9	n.m.[c]	n.m.[c]	n.m.[c]
APG **8**	$2.78x10^{-12}$	88.3	75.4	460	24.4

Based on the DLS data a hydrodynamic radius of 61.6 nm was determined for APG **7**, which is compared to other single tail surfactants like SDS or peptide amphiphiles relatively large (see Table 4).[110, 175] For APG **1** and APG **8** an approach proposed by Garcia de la Torre et al. was applied to calculate the length and the radius of the rod like micelles. However, as the correlation function revealed a significant polydispersity for APG **1** meaning that a mix of micelles with drastically differing aspect ratios was present, no calculation could be performed for APG **1**. In contrast, for APG **8** the micelles were more uniform, potentially due to the introduced aromatic motif of the linker of APG **8**. This is supported by literature as it was shown for other amphiphiles, that the introduction of an aromatic moiety inside the amphiphile structure increases the interactions between the headgroups of the micelles, resulting in more stiff and uniform micelles.[176] APG **8** cylindrical micelles were calculated to be in average 460 nm long and 24 nm in radius. Further verification of size and shape was performed using AFM and TEM (see Figure 28).

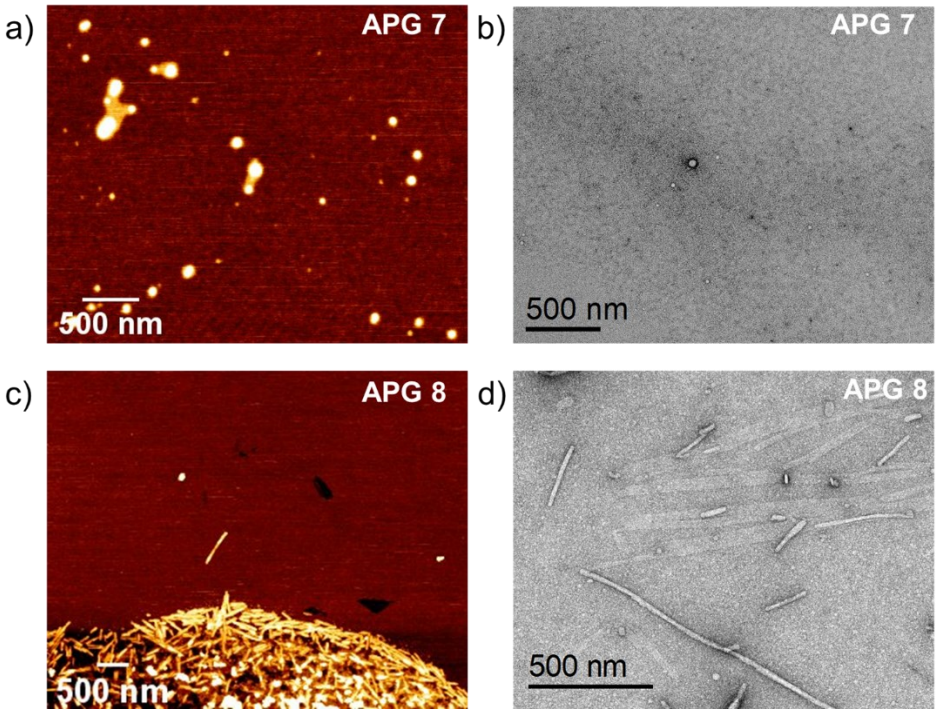

*Figure 28. AFM images (a,c) and TEM images (b,d) of APG **7** and APG 8 (reproduced from [131], published by the Royal Society of Chemistry).*

AFM and TEM experiments confirmed the results from the light scattering regarding the shape but showed different results regarding the size. For APG **7** AFM experiments showed spherical micelles with an average diameter of 92 nm and a height of 12 nm. TEM revealed generally smaller sizes averaging at 51 nm but with a wider range of diameters observed, spanning from 18 to 127 nm. For APG **8** TEM showed polydisperse, cylindrical micelles with lengths ranging from 60 nm to 1100 nm and an average core width of 17 nm. AFM produced comparable results, albeit with a lower dispersion than TEM. Most likely the origin of these size differences, between light scattering and AFM/TEM, is the fact that the latter two were both performed in a dry state and not in solution as the light scattering. Adding to this point is also the relatively low height measured in AFM, suggesting that the micelles are flattened.

Furthermore, especially for the imaging techniques many samples needed to be measured as it was found that during sample preparation micelles were prone to disintegrate. Therefore, it was important to have the option to crosslink micelles, thus fixing them in their current state and thereby allowing for a simpler sample preparation and improved images. The following paragraph will discuss different crosslinking techniques employed in this thesis.

3.1.5 Micellar core-crosslinking of APGs

This paragraph will highlight the possibilities of micellar core-crosslinking of APGs using three different approaches: radical polymerization, Michael addition and polymerization via 1,4-addition reaction.

For the radical polymerization and the Michael addition approach, APGs containing the novel HDM building block were used as it introduces an alkene moiety in the main chain of the hydrophobic tail. Furthermore, the crosslinking needs to be performed in water and should only take place inside the micellar core so that the micellar structure remains intact upon crosslinking. To ensure that, only initiators and crosslinking agents that are hydrophobic were considered, so that these reagents are only solubilized inside the micellar core.

For the free radical crosslinking three different crosslinking agents and two different initiators were tested with APG **1** as a sample compound (see Figure 29).

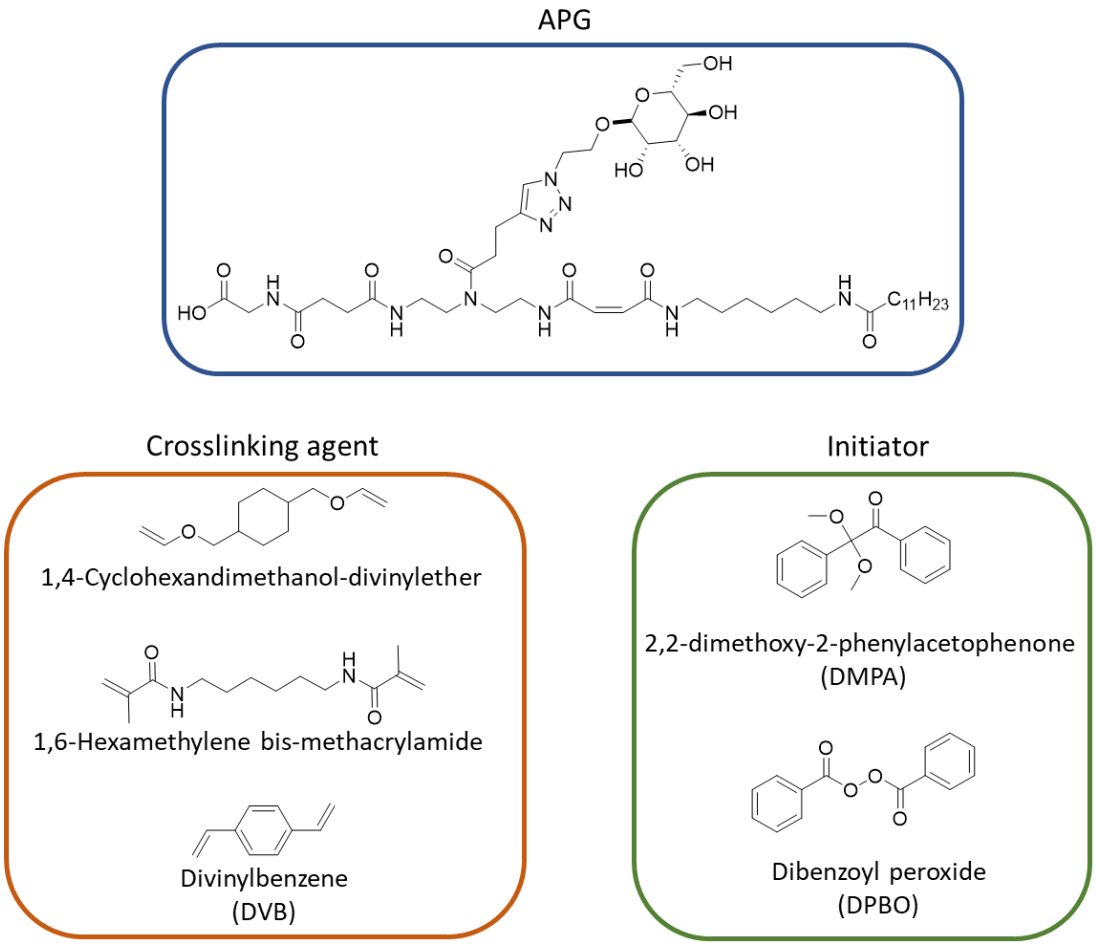

Figure 29. APG, crosslinking agents and initiators used for the micellar core-crosslinking.

For the initiators one photo (DMPA) and one thermal initiator (DBPO) were tested. However, after the first trials it was evident that the thermal initiator was not suited for APG crosslinking as it was very low yielding and most of the times no crosslinked APGs could be isolated. These

low yields could be due to a disruption of the intermolecular hydrogen bond network of the APGs and a subsequent disbanding of the micelles caused by the high temperatures (70 – 90°C) employed. Additionally, all prior characterization of the micelles was performed at 25°C, which would have made direct comparison of the crosslinked and non-crosslinked micelles difficult.

For the crosslinking agents, the rational was to test whether the different electron density of the alkene moiety makes a difference during crosslinking. Furthermore, 1,6-hexamethylene bis-methacrylamide in particular was chosen due to its structural similarity to the HDM building block. Overall, all crosslinking agents in combination with DMPA were able to achieve micellar core-crosslinking. However, the yields of crosslinked APG derived using these crosslinking agents were drastically different (see Table 5). Yields were determined by weighing the crosslinked APG after purification of the reaction mixture by extensive dialysis and subsequent freeze drying.

Table 5. Overview of the different yields of crosslinked APG per crosslinking agent.

Crosslinking agent	Yield range [%]
1,4-Cyclohexandimethanol-divinylether	<3%*
1,6-hexamethylene bis-methacrylamide	<3%*
Divinylbenzene	15-25%

*Weight loss of reaction vessel during freeze drying was greater than the yield.

Differences in yields could be due to the previously discussed electron density of the alkene bonds but also due to the higher hydrophobicity of DVB compared to the other agents. Most likely is the hydrophobicity the determining factor as crosslinking can only happen upon solubilization of the crosslinking agent inside the micelles.

The final procedure included 1 eq of APG with 0.2 eq of DVB and 0.04 eq of DMPA and an irradiation of one hour withr a medium pressure mercury lamp (see Figure 30). Subsequently, the final product was dialyzed in a mixture of 1:1 water and EtOH using a weight cut-off of 3.5 kDa, in order to exclude all non-crosslinked APGs and left-over reagents.

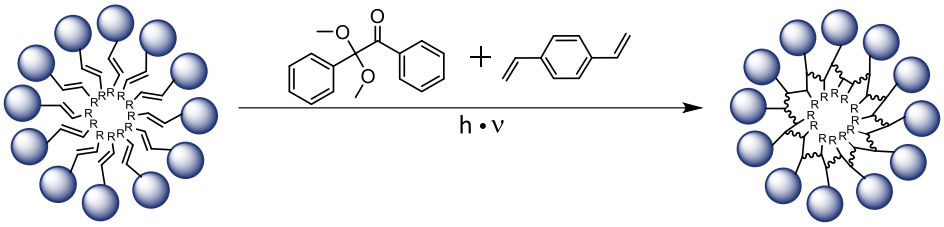

Figure 30. Schematic overview of the final crosslinking procedure employing DVB and DMPA (reproduced from [131], published by the Royal Society of Chemistry).

Verification that indeed micelles had been crosslinked and their original shape was preserved was performed using DLS, AFM and TEM. For the DLS experiments, non-crosslinked and crosslinked micelles were dissolved in a water ethanol mixture 1:1, which is known for destroying micellar assemblies. These experiments showed qualitatively that for the crosslinked micelles aggregates were still present, while for the non-crosslinked micelles only unimers were found (see Figure 99). However, these experiments did not yield information about the perseverance of the original micelle shape. For that, crosslinked APG **8** micelles were analyzed using TEM, which showed for preparations from H_2O and EtOH that the micellar structure was preserved (see Figure 31). Additionally, it was found that the core width of the crosslinked micelles was reduced from 17 to 14 nm, which could be due to a compactization of the micelle structure upon crosslinking.

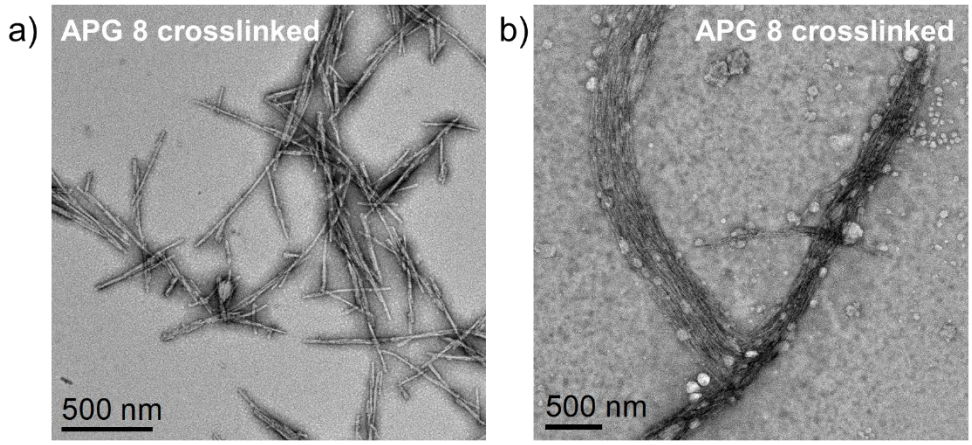

*Figure 31. TEM images of crosslinked APG **8** prepared from H_2O (a) and EtOH (b) (reproduced from [131], published by the Royal Society of Chemistry).*

The second crosslinking possibility for AGPs using a Michael addition approach was first explored by Jessica Kania as part of her master thesis.[168] As already pointed out the alkene moiety of the HDM building block is electron-deficient, which makes it ideal to be used as a Michael acceptor.[164] It was found that the HDM building block readily reacts within minutes with various thiols under dimethylphenylphosphine catalysis. However, since APGs used

contained only one HDM building block, this Michael addition led to precipitation of Michael adducts instead of crosslinking the whole micelle. Future experiments should be focused on APGs with at least two HDM units combined with a multivalent thiol compound such as pentaerythritol tetrakis(3-mercaptopropionate).

Another possible crosslinking alternative was the use of diacetylene containing fatty acids (the following experiments were conducted by Dominik Scholz as part of his research internship supervised by Alexander Banger). This approach is especially interesting as no further additives are required to crosslink micelles. Crosslinking can be simply induced by UV-irradiation or a thermal stimulus. One example of these fatty acids is the 10,12-tricosadiynoic acid (TCDA). APGs with terminal TCDA were easily accessible using the standard coupling protocol, which was surprising as APGs with a C_{20} saturated fatty acid were not obtainable. Two model APGs were synthesized and could be isolated in good yields and purities (see Figure 32 and Appendix 2 – Appendix 5).[131]

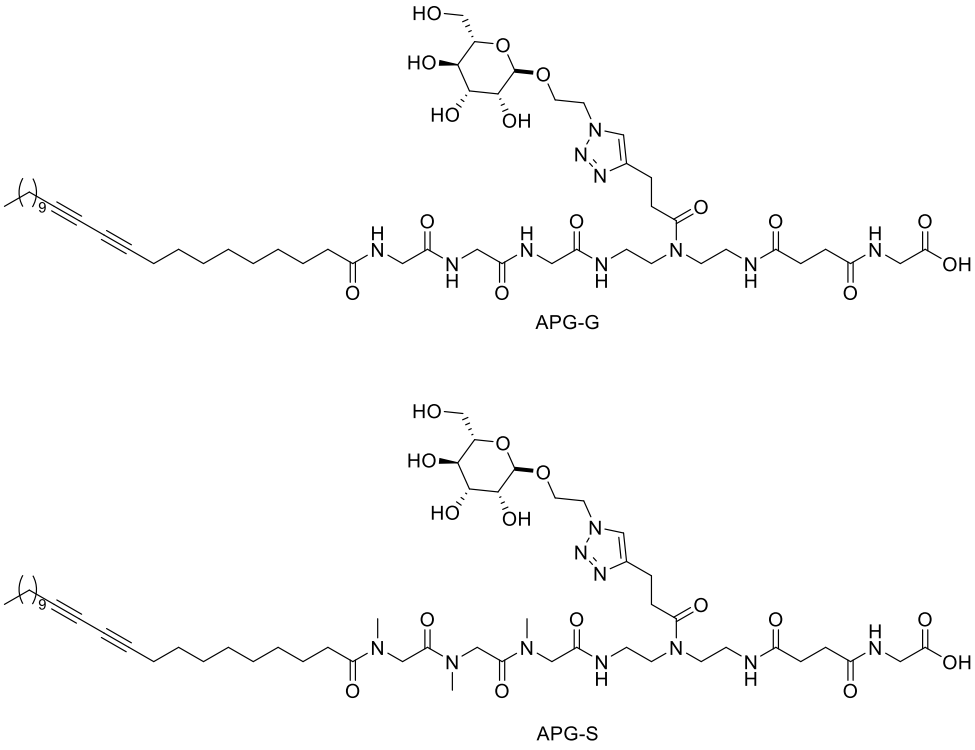

*Figure 32. The two model APGs (APG-**G** and APG-**S**) containing TCDA as hydrophobic tail.*

Both APGs are built up nearly identical with the main difference that APG-**G** contains three glycine units in the main chain, whereas APG-**S** contains three sarcosine units in the main chain. Prior to crosslinking, CMCs were determined using the optimized Nile red approach.[131] With the TCDA tail CMCs between 4.1 µM (APG-**G**) and 5.5 µM (APG-**S**) were determined (see Appendix 6 and Appendix 7). First crosslinking experiments via simple UV irradiation with

these model APGs showed promising results as the crosslinked APG micelles did not change in size compared to the non-crosslinked APG micelles and the crosslinked micelles were also stable in pure EtOH (see Appendix 8). Furthermore, crosslinking induces a color change of the micelles as a conjugated π system is generated inside the hydrophobic micellar core. This color change could later be useful, for example to localize micelles in cell studies.

Following synthesis, analysis of self-assembly characteristics and crosslinking the next step of this thesis was to assess the biological activity of APGs. The next section will present first results regarding the binding characteristics of APGs.

3.1.6 Initial bioassays of first the APG library

The commonalty of all APGs is their headgroup carbohydrate motifs, which in theory should allow for interactions with any form of carbohydrate binding entity e.g., proteins, bacteria, or cells. As a first proof of concept experiment the interaction of APGs with the model lectin Con A were studied (experiments were conducted in collaboration with Dimitri Wilms). Con A is a tetrameric lectin derived from the jack bean plant, which binds specifically to α-D-Man and α-D-glucose.[9, 177] Many literature examples have shown that mixing Con A with structures, that present Man or glucose in a multivalent fashion, results in aggregation.[178] For the experiments in this thesis, rhodamine labeled Con A was employed, which allowed to directly evaluate aggregation employing a fluorescence microscope. In Figure 33 the results of mixing rhodamine labelled Con A with APG **8** is shown. Here it was clearly evident that APG **8** was able to form aggregates with Con A, which was the first evidence that the carbohydrate motifs of the APGs are still available for protein recognition.

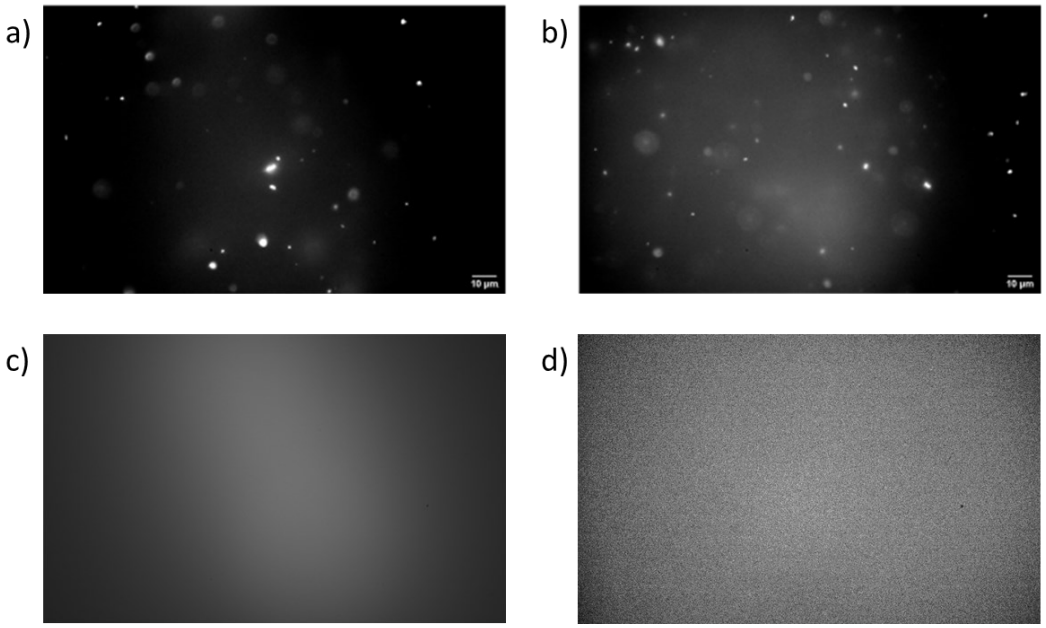

*Figure 33. Fluorescence microscope image of a) & b) APG **8** incubated with rhodamine conjugated Con A, c) pure APG **8** in solution, d) pure rhodamine conjugated Con A in solution (post edited with ImageJ) (reproduced from [131], published by the Royal Society of Chemistry).*

Following this initial experiment, APGs were tested for binding towards a more complex system, specifically *E. coli* bacteria. To cause an infection, many bacterial species, including *E. coli*, must adhere to a target cells.[179] As a result, these species present specific adhesive organelles, which allow them to bind for example onto the glycocalyx of cells. For *E. coli* these organelles are type 1 fimbriae (FimH) presenting an α-D-mannopyranoside-specific lectin at the tip of the organelle.[180, 181] In order to gauge the binding efficacy of APGs, an experimental setup from Lindhorst was adapted employing a GFP expressing *E. coli* strain bound onto a mannan coated surface (these experiments were conducted in collaboration with Dimitri Wilms).[182] Using this setup, the binding or rather inhibition of the APGs towards the *E. coli* can be measured using the difference of total fluorescence before and after incubating the *E. coli* with APGs. Plotting this fluorescence difference for an APG concentration series, allows to determine IC_{50}-values, which represent the half-maximum inhibitory concentration.

For all Man containing APGs (APG **1**,**3**, **6**, **7**, **8** and crosslinked APG **8**) sigmoidal inhibition curves were obtained, which allowed to derive the according IC_{50} values. In Table 6 the results of the inhibition experiments are summarized.

Table 6. Summary of the determined IC_{50} values for selected APGs.

Oligomer	IC_{50}-value [µM]
APG **1**	61 ± 20
APG **3**	503 ± 125
APG **4**	no inhibition
APG **6**	222 ± 21
APG **7**	135 ± 81
APG **8**	63 ± 11
Oligomer	IC_{50}-value [µg/ml][a]
APG **8**	64 ± 11
Crosslinked APG **8**	253 ± 27

[a]For crosslinked APG **8** IC_{50} values can only be determined in [µg/ml], for direct comparison, IC_{50} value of APG **8** is given in the same unit.

Overall, all APGs except APG **4**, which is the only Gal containing APG, showed inhibition in the µM range. Indicating that the inhibitory effect of APGs is based on specific binding events rather than on unspecific binding e.g. from the backbone towards the *E. Coli*. Except for APG **3**, all APGs have IC_{50} values lower than their corresponding CMC. As a result, most likely most APGs interact with the bacteria as single molecules rather than as micellar assemblies (see Figure 34).

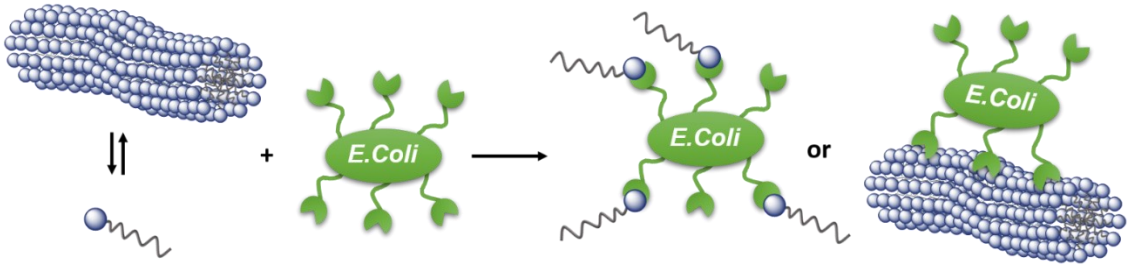

Figure 34. Schematic representation of single molecule vs, micellar assembly binding towards an E. Coli (reproduced from [131], published by the Royal Society of Chemistry)

Supporting this hypothesis is the finding that APG **3** has a significantly higher IC_{50} than its structural analogue APG **1**. This could be due to its significantly lower CMC, so that APG **3** first assembles into micelles before interacting with the bacteria, thus lowering the effective concentration of Man ligands available for FimH binding and inhibition. Adding to the point is

the comparison of APG **8** and crosslinked APG **8**, which shows the same trend, as the crosslinked APG **8** has a higher IC_{50} than the non-crosslinked APG **8**. Furthermore, for crosslinked APG **8** a cooperativity factor of 2 determined, indicating a cooperative binding behavior. For all other APGs, also for APG **3**, a cooperativity of 1 or less was calculated, which is typical for FimH binding.[183] This could indicate that the gained rigidity through crosslinking increases the cooperativity but decreases the overall IC_{50} value as the inhibition becomes less efficient per Man.

3.2 Detection of lectin clustering in self-assembled glycomimetics by aggregation induced emission

In the previous chapter, the binding behavior of APGs towards lectins and bacteria was investigated and not only did APGs show significant binding but also signs of clustering were observed. Clustering is a form of a multivalent binding mode, in which one multivalent ligand interacts with several protein receptors that are brought into close proximity through this so-called clustering event.[42, 184] In Nature such clustering not only occurs in solution but also on a membrane, e.g. when the proteins are membrane-bound. This is indeed highly relevant, for example for the phosphorylation of proteins by tyrosine kinase, which makes an important contribution to signal conduction.[185] Especially this form of membrane clustering is difficult to observe and usually relies on methods like fluorescence resonance energy transfer or fluorescence photoactivation localization microscopy.[186-188] Another option to observe this form of clustering could be the use of AIE luminophores. In contrast to fluorophores like fluorescein, AIE luminophores do not or only very little fluoresce when solubilized but upon aggregation, either in solid state or upon binding e.g. to a protein, the fluorescence signal increases significantly.[161] This emission behavior is attributed to the restriction of internal rotation and/or vibration of the luminophore within the aggregated molecules or molecular complex (ligand-receptor).[189]

For this work, the aim was to combine AIE luminophores and APGs to create simple mimetics of glycan-functionalized membranes to study clustering. The underlying hypothesis was that AIE-containing APGs are still able to self-assemble into micellar structures, where upon assembly the incorporated AIE dyes should start to fluoresce.

In a first step, Peter Pasch introduced AIE luminophores into the hydrophobic part of the APGs during solid phase assembly and synthesized in total three AIE containing APGs (**Man**-**T**PE-**O**ligomer (**MTO**), **Gal**-**T**PE-**O**ligomer (**GTO)** and **Man**-**C**ATE-**O**ligomer (**MCO**) (see Figure 35).

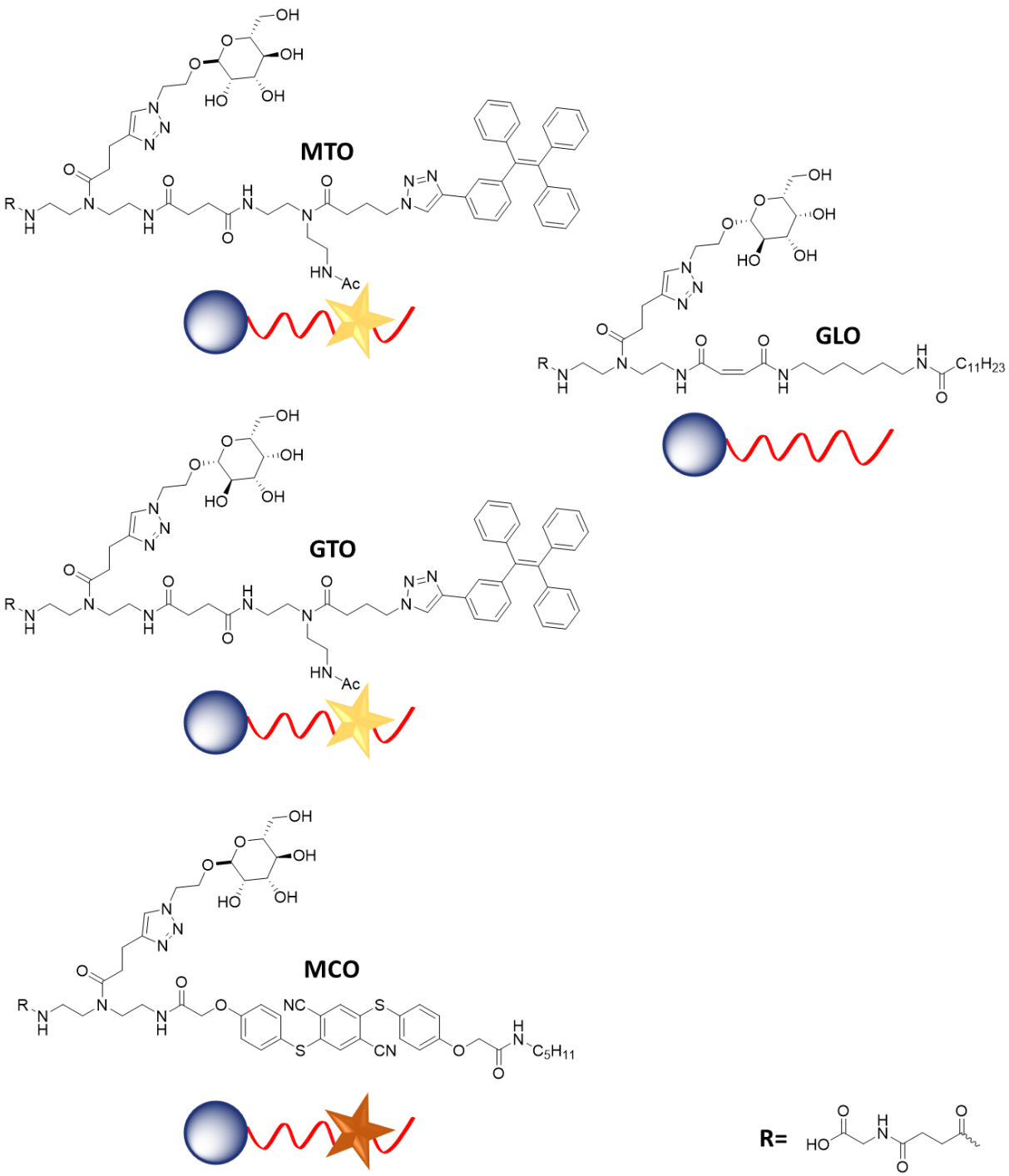

*Figure 35. Overview of the three AIE-APGs (**MTO**, **GTO** and **MCO**) and the non-AIE containing APG (**GLO**). TPE is shown as a yellow and CATE as a bronze star.*

With these molecules at hand, he determined the CMC of all three AIE-APGs in water using the intrinsic AIE effect (see Table 7), which was a first confirmation of the hypothesis that AIE-APGs are still able to self-assemble.

Additionally, as part of this thesis, the CMCs in lectin binding buffer (LBB) were measured (see Table 7). LBB is the typical buffer for lectin binding studies containing Hepes, sodium chloride as well as divalent cations such as calcium and manganese required for binding to C-

type lectins such as Con A. As all AIE-APGs are ionic, it was expected and confirmed that the CMC values in LBB are lower than in water. The higher ion concentration of the buffer leads to decreased head group repulsion, which in turn results in lower CMC values. However, although a CMC could be measured for **MCO**, it was prone to precipitation after more than 1 hour in solution, which is why it could not be used in the later binding studies.

Table 7. CMC of AIE-APGs in water and LBB determined by AIE.

Structure	CMC in MQ [µM]	CMC in LBB [µM]
MTO	73 ± 6[1]	46 ± 1
GTO	64 ± 4[1]	51 ± 3
MCO	100 ± 8[1]	96 ± 5
GLO	630 ± 70[2]	n.m.

[1]CMCs were determined by Peter Pasch, [2]According to literature[131], n.m. = not measured

To further verify that indeed micelles are formed upon solubilization of AIE-APGs, samples were characterized by AFM and TEM. TEM measurements of **MTO** only showed large aggregates (see Appendix 9). Potentially this is due to the high number of aromatics in the backbone, which are prone to π-π-stacking. When using a drop coating technique, the drying process leads to high local concentration of the APG, which in turn can result in these large aggregated structures rather than the visualization of single assemblies. Therefore, for AFM measurements, an adapted spin coating procedure was applied. Figure 36 shows AFM images for **MTO** micelles and **MCO** micelles prepared from aqueous solutions.

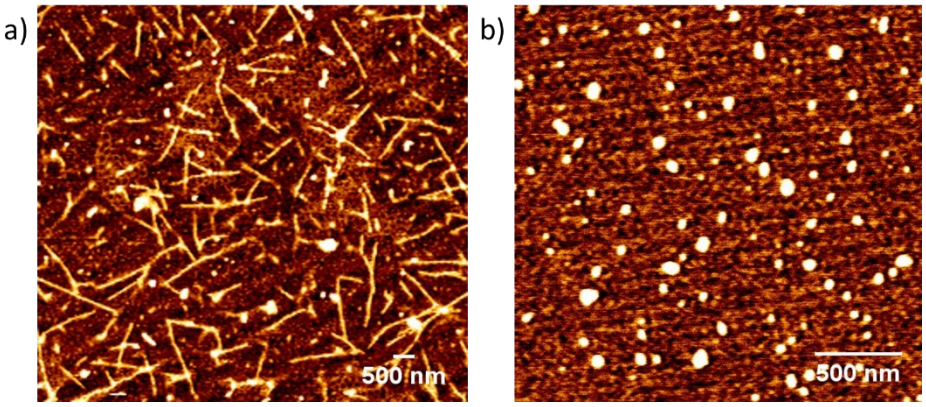

Figure 36. AFM images of a) **MTO** micelles (300 µM in water) and b) **MCO** micelles (300 µM in water).

Interestingly, for **MTO** rod like micelles were observed compared to the spherical micelles of **MCO**. This nicely correlates with the previous results in this work (see section 3.2), where it was shown that depending on the number of amide hydrogen bonds spherical as well as rod like micelles were accessible. Most likely AIE-APGs and non-AIE-APGs behave similar and their shape is affected by the number of available amide hydrogen bonds so that a certain number of amide hydrogen bonds are necessary to form rod like micelles. Comparing the number of available amide hydrogen bonds, **MTO** has five while **MCO** has only four, which could explain the different shapes.

With this data at hand, the next step was to test the potential of AIE-APGs as clustering sensors. However, as the AIE containing APGs self-assemble and thereby fluoresce, they cannot be directly used as clustering sensors. To employ AIE-APGs as sensors, the fluorescence of the starting material must be low and only upon addition e.g. of a lectin that leads to clustering of the carbohydrate-containing head groups and thereby to close proximity of the AIE attached to those head groups, fluorescence should be measurable. Therefore, the use of mixed micelles systems was investigated (Figure 37).

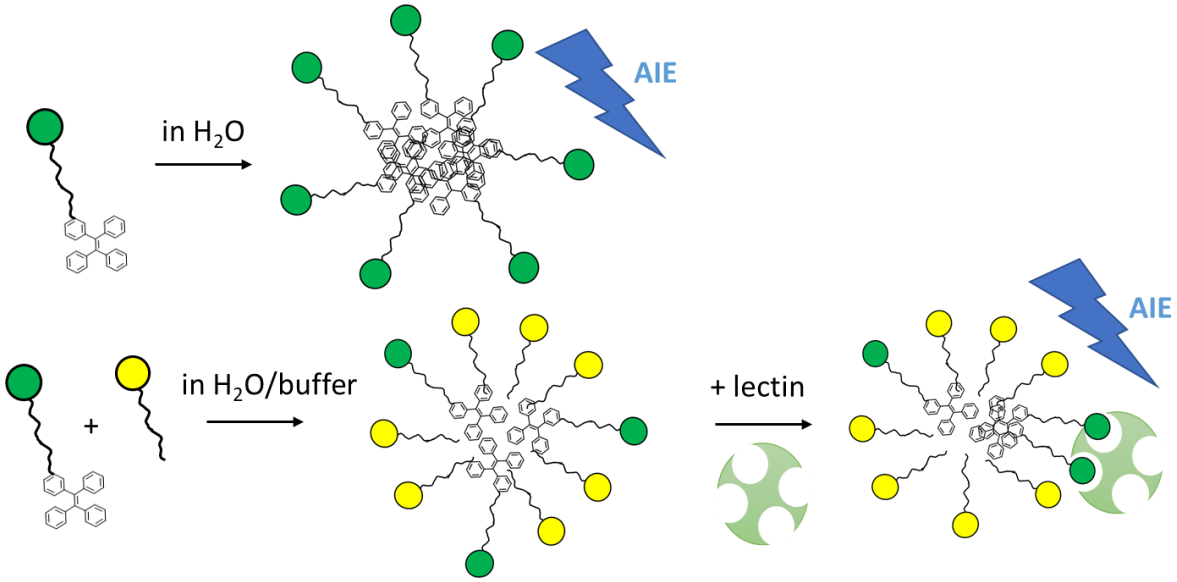

Figure 37. AIE-APG micelles starting to fluoresce upon self-assembly and AIE-APG mixed micelles starting to fluoresce upon lectin binding.

First preliminary experiments performed by Peter Pasch showed that using the non-fluorescent, non-carbohydrate containing surfactant SDS, it was possible to reduce the fluorescence of mixed micelles containing **MTO** and SDS up to 97% compared to pure **MTO** micelles.

Following, in this thesis, SDS was exchanged with **GLO**, which is an APG similar in structure to the AIE-APGs but bears Gal instead of Man and contains no AIE dye (see Figure 38).

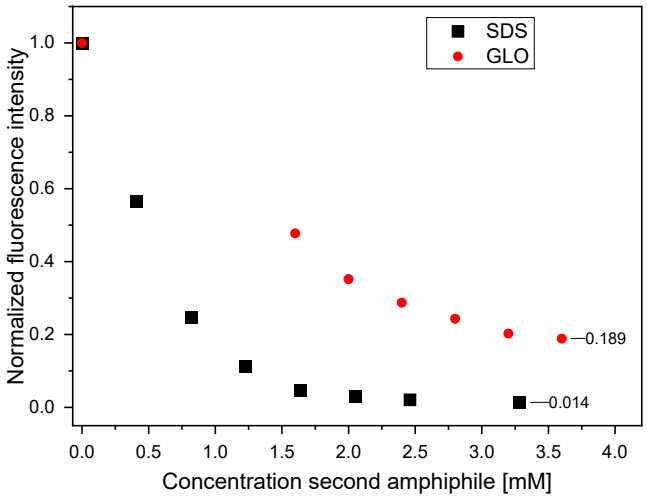

*Figure 38. Fluorescence reduction for a solution of 300 µM **MTO** in water by addition of SDS (performed by Peter Pasch) or **GLO** (triplicates, λ_{ex} = 340 nm, λ_{em} = 457 nm).*

With the addition of **GLO** the fluorescence could also be reduced but it was less potent than SDS. In general, the reduction of fluorescence of these mixed micelle systems is most likely based on reduced intermolecular interactions and motion restrictions of the luminophores within the hydrophobic core of the assembly, e.g. through reduced π-π-stacking.

Moreover, it is known for similar charged ionic amphiphiles that they form stable mixed micelles, here two anionic amphiphiles are mixed, thus stable mixed micelles are expected.[190] Additionally, the CMC of such systems heavily depends on the ratio of the employed amphiphiles and it is important to know the CMC as the latter binding studies need to be performed above the CMC. Based on the previous data, a ratio of 1:20 (**MTO** to **GLO**) was chosen and CMC studies for these mixed micelles using the intrinsic AIE and the reporter dye Nile red were conducted. Both experiments showed a CMC with 170 µM for the intrinsic AIE and 235 µM for Nile red (see Appendix 9 and Appendix 10). Based on these findings a concentration of 1.05 mM for the mixed micelles was chosen in the following binding studies.

Lectin binding studies were performed using mixed micelles containing the Man and AIE bearing APG **MTO** together with the Gal bearing non-AIE-APG **GLO**. As Man-recognizing lectins of different affinities and valencies, tetrameric Con A, tetrameric Galanthus nivalis lectin (GNA) and dimeric Lens culinaris lectin or agglutinin (LCA) were chosen.

Readily prepared mixed micelles were incubated with lectins at different concentrations for two hours and fluorescence as well as turbidity was detected. Additionally, 10 ppm of PEG were added to the samples in order to prevent the lectins from sticking to the polypropylene surface of the wellplates as reported by Liu et al.[191] The ratio between the observed emission of the mixed micelle system (E_0) and the emission detected for the mixture with the according lectins (E) is evaluated. Values for $E/E_0 = 1$ show no AIE effect, values > 1 show an increase in emission, which is attributed to the AIE effect.

First, as control experiment, mixed micelles bearing APGs **GTO** and **GLO** were incubated with the different lectins at the highest concentration (4 µM) in order to exclude any non-specific binding. As expected, no or only slight fluorescence changes were observed for all lectins tested (see Table 8). Additionally, no turbidity increase was detected for all three lectins.

Table 8. Overview of the fluorescence and turbidity data of GTO/GLO (1:20, 1.05 mM overall concentration) mixed micelles incubated with 4 µM of different lectins for 2 h. Turbidity is corrected against a mixed micelles blank with no lectin addition.

Lectin	Corrected Turbidity	Fluorescence E/E_0
Con A	0.015	0.973
GNA	-0.005	1.08
LCA	0.005	0.994

By replacing **GTO** with **MTO**, now a binding carbohydrate was introduced, which allows for interaction with the different lectins. The underlying hypothesis is that through multivalent binding of the lectins with multiple AIE-APGs presenting a binding carbohydrate, clustering takes place within the micellar assembly that should lead to AIE (or AIE fluorescence) (see Figure 37). Especially for higher valent lectins and at higher concentrations additional clustering of multiple micelles can be expected. In order to follow such clustering, turbidity was measured alongside fluorescence (see Figure 39).

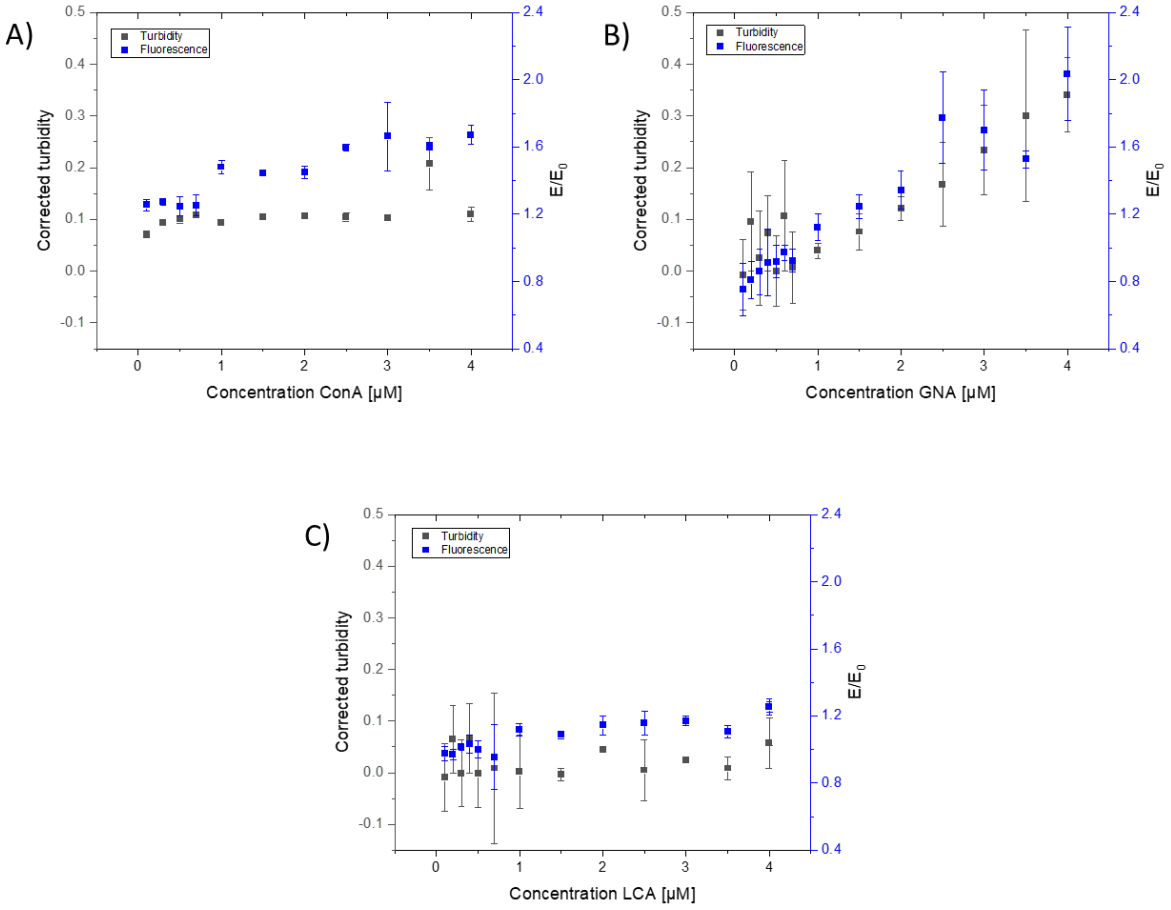

Figure 39. Change in emission (E/E_0) (blue) and turbidity (black) data of the lectin binding assay of mixed micelles consisting of 50 µM MTO 1 mM GLO. Fluorescence is measured at λ_{ex} = 340 nm and λ_{em} = 457 nm. Turbidity of the solution is measured at 450 nm. Either the emission changes of the ratio E = final emission to E_0 = start E or the turbidity changes are plotted against the concentration of the respective lectin. A) Con A titration, B) GNA titration and C) LCA titration.

Both tetrameric lectins, Con A and GNA, lead to a more pronounced increase of the emission in comparison to dimeric LCA. Even if corrected for the number of carbohydrate recognition sites, the effect for Con A and GNA remains stronger. This could be first evidence, that the tetrameric lectins are capable to induce a rearrangement of the amphiphiles inside the micelle. However, for all lectins but especially for GNA it seems that the fluorescence increase is directly correlated to an increase of the turbidity of the solution. The increased turbidity is most likely due to the lectins being able to crosslink several micelles, thereby forming big clusters, which in turn precipitate. Since for all lectins turbidity was detected even at the lower end of the concentration range, it is unclear at this point which part of the fluorescence increase is due to rearrangement of the micelles and which part is due to precipitation. In order to reduce the possibility of precipitation and focus on the clustering by

rearrangement of APGs within the micellar assembly, additional binding studies were started using microprinted Con A surfaces in cooperation with Jonas Rickhoff from the Ravoo lab at the University Münster. The advantage of the microstructured surfaces lies in the contrast between functionalized and non-functionalized areas, allowing to distinguish between selective binding to the lectin and non-selective binding to the glass surface. Due to time constraints these experiments are not part of this thesis.

While in the previous sections the focus lied on APGs, which presented carbohydrates in a multivalent fashion through self-assembly, the following section will focus on a more classical approach of multivalent presentation, namely polymers.

3.3 Polymers and hydrogels to mimic the ECM

This subchapter describes the development and synthesis of functional polymers suited for the integration into hydrogels. The underlying ideas are based on a collaboration with the working group of Prof. Kumacheva from Toronto, Canada. Her group has been working on cellulose nanocrystals (CNCs) and their use as hydrogels.[192-196] CNCs are composed of nanosized cellulose fibrils, which can have several microns in length and have a diameter in the nanometer range. CNCs can be readily surface functionalized using an oxidation procedure, yielding an aldehyde functionalized surface. Combining these CNCs with gelatin, denatured collagen presenting many primary amines, hydrogels can be prepared.[193, 197] These hydrogels have not only a fibrilic structure but are also bio-adhesive, due to the several RGD units within the gelatin.[198, 199] Based on these characteristics the hydrogels are well suited to mimic the extracellular matrix (ECM). Especially concerning cancer research, ECM mimicking hydrogels are of increased importance as they allow for the cultivation of cancer spheroids inside of them. Cancer spheroids in comparison to 2D cancer cell cultures are much more similar to cancer cells in patients, thus experimental data can be easier transferred from cell studies to clinical applications. However, until today the cultivation of primary cancer cell spheroid in CNC hydrogels remains challenging, possibly due to the lack of carbohydrates, which are omnipresent in the real ECM in the form of glycosaminoglycans. Therefore, the novel concept displayed in Figure 40 was developed, which aims at the introduction of carbohydrate-presenting polymers (glycopolymers) onto the CNC surface.

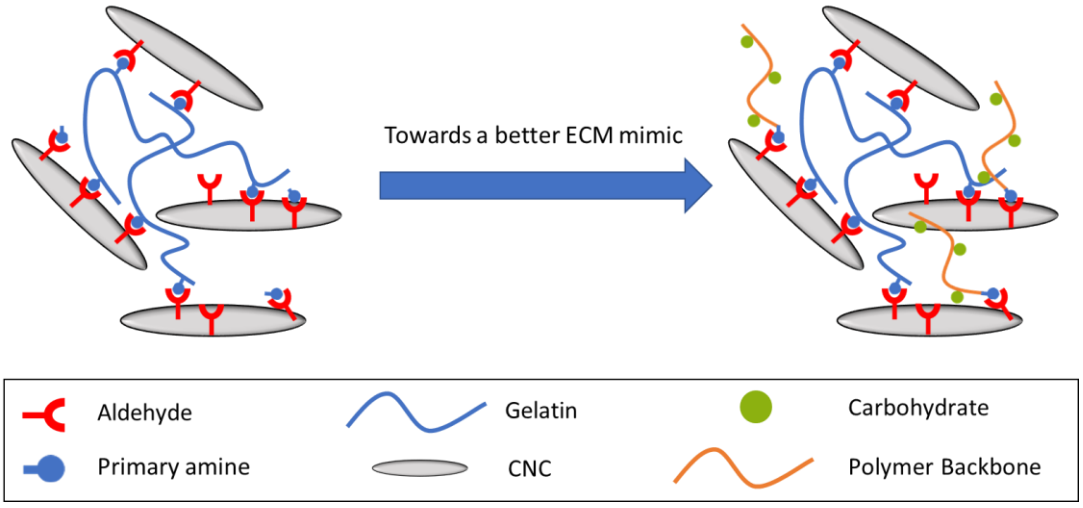

Figure 40. Concept of CNC hydrogels combined with carbohydrate-presenting polymers.

Suitable glycopolymers ideally have a narrow size distribution, which is crucial for reproducibility, can present differenty types of carbohydrates and bear exactly one terminal primary amine for the chain-endattachment onto the CNC.

3.3.1 Polymer selection

In general, two synthetic routes can give access to the targeted glycopolymers: synthesis of a carbohydrate monomer and subsequent polymerization, or synthesis of a precursor polymer that allows for post polymerization functionalization with carbohydrates. Post polymerization strategies offer more synthetic flexibility as they allow to gain access to a precursor polymer that can then easily be functionalized with various carbohydrates, whereas for the first approach for every carbohydrate a new monomer must be synthesized. Therefore, the active ester polymer poly(pentafluorophenyl acrylate) (p(PFPA)) was chosen as precursor polymer. This polymer, as introduced by Theato and co-workers, has been successfully used for the efficient attachment of various amine-containing species.[25, 200, 201] Compared to other active esters like N-(methacryloyloxy)succinimide, the p(PFPA) is superior as it combines a good solubility in organic solvents as well as hydrolysis stability.[202, 203] Based on literature protocols and further optimization by Ali Balasini as part of his master thesis, the synthesis of pentafluorophenyl acrylate (**5**) was carried out from pentafluorophenol and acryloyl chloride (Scheme 5).[204, 205]

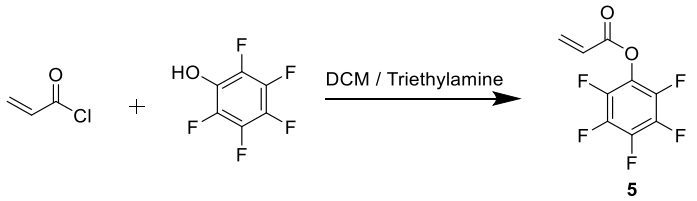

Scheme 5. Synthesis of pentafluorophenol acrylate.

Since it was required for the final polymer to have a narrow size distribution, reversible addition−fragmentation chain-transfer (RAFT) polymerization was chosen as polymerization method. Additionally, the final polymer needs to have one primary amine in order to allow for the attachment onto the CNC. However, since the active ester is very reactive towards amines, it is necessary to first fully convert the active ester and in a next step introduce a free amine group to the polymer. A possible route is the use of the commercially available and azide bearing CTA 2-(dodecylthiocarbonothioylthio)-2-methylpropionic acid 3-azido-1-propanol ester. Following polymerization and functionalization of the polymer (exchanging all active

ester moieties with a carbohydrate), the terminal azide, which is inert regarding the polymerization conditions, can then be reduced to an amine, for example employing the Staudinger reduction. In general, a mild reduction reaction is required in order to not reduce the carbohydrate side chains.

In Scheme 6 the performed polymerization is shown with optimized reaction conditions adopted from the prior work of Fadi Shamout.[25]

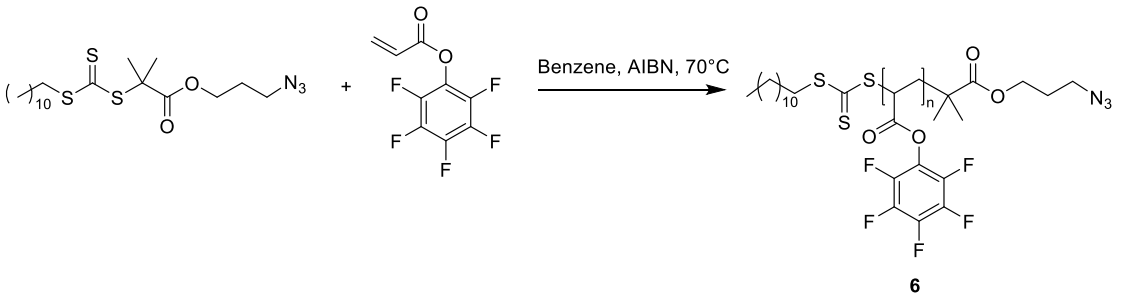

Scheme 6. Synthetic scheme of the polymerization of 2-(dodecylthiocarbonothioylthio)-2-methylpropionic acid 3-azido-1-propanol ester and pentafluorophenyl acrylate.

Polymerization was performed several times and GPC analysis showed dispersities between 1.2 and 1.6, which are higher than expected for a controlled radical polymerization via the RAFT mechanism. Potentially, the azide can undergo an azide-alkene cycloaddition with the pentafluorophenyl acrylate as shown by Díez-González et al.[206] Any form of alteration or reaction of the CTA changes its polymerization characteristics and therefore could be the reason for the unexpectedly high dispersity. A potential cycloaddition side reaction was supported by IR analysis of the CTA before and after stirring it with pentafluorophenyl acrylate (see Figure 41). In general, the azide peaks for the asymmetric and symmetric stretching can be found in the frequency regions of 2162-2095 and 1258-1206 cm^{-1}, respectively. The azide peak of the CTA completely disappeared already after 5 minutes at room temperature (see Figure 41). This confirms that already at room temperature the azide of the CTA can undergo side reactions with the pentafluorophenyl acrylate.

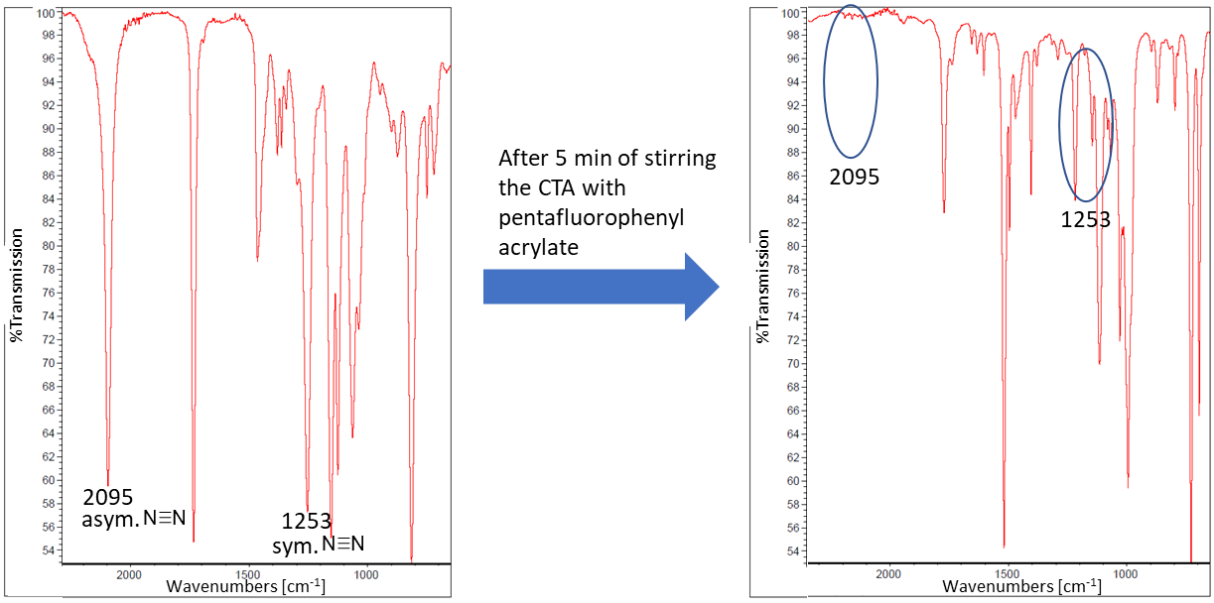

Figure 41. IR-Spectra of the CTA (left) and the mixture of CTA and pentafluorophenyl acrylate (ratio 1:50) after 5 minutes of stirring.

Therefore, this synthetic route was discarded and new approach based on a novel RAFT agent was pursued. In the following the synthesis of this novel RAFT agent will be discussed.

3.3.2 Synthesis of a novel RAFT agent

The challenge of this part of the work is based on the fact that the active ester monomers react with free amines but also a free amine is needed for the coupling to the CNC. Therefore, it is not possible to simply reduce the azide before the polymerization as any free amine would directly react with the active ester. For this reason, a novel RAFT agent (CTA-prot, **8**) containing a protected amine moiety was designed, allowing for an on demand deprotection of the primary amine. The two-step synthetic approach is shown in in Scheme 7.

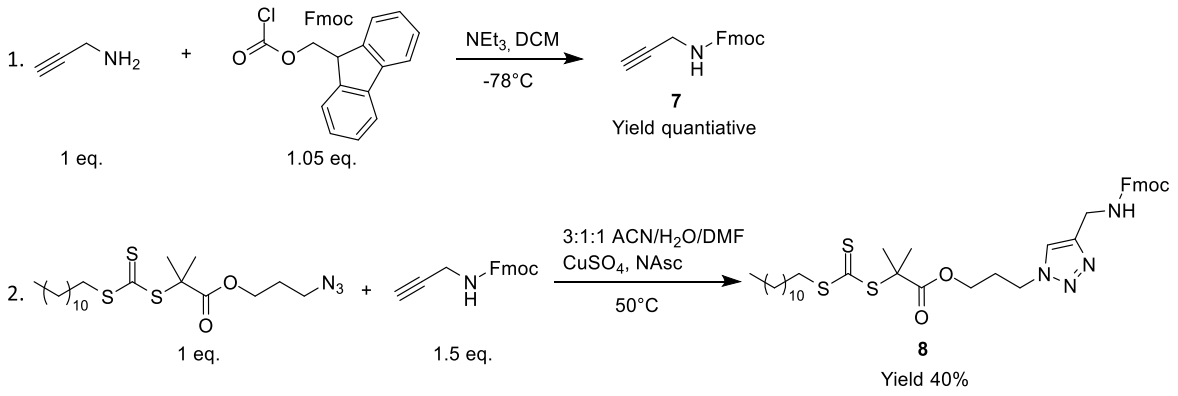

*Scheme 7. Synthetic procedure for the new RAFT reagent (**8**).*

In the first step, propargylamine was protected using Fmoc-chloride, following a similar synthetic procedure as used for the solid phase building blocks.[22] Subsequently, Fmoc-propargylamine and the azide CTA were clicked employing CuAAC. For this click reaction a solvent mixture of water, DMF and ACN and temperatures of 50°C were required to prevent precipitation of any educts or copper salts. After 24h, the reaction mixture was concentrated in vacuum and the product was isolated using column chromatography. The final CTA-prot was characterized by ^{1}H-NMR and HR-ESI mass spectroscopy (see Figure 42 and Appendix 12). In the NMR spectrum the characteristic signals for the Fmoc-protection group as well as for the triazole moiety can be found in the low field between 7.3 and 7.8 ppm. Furthermore, MS results are in good accordance with the theoretical values as the calculated mass for CTA-prot is 724.3151 g/mol and the mass found for the hydrogen adduct is 725.3216 g/mol.

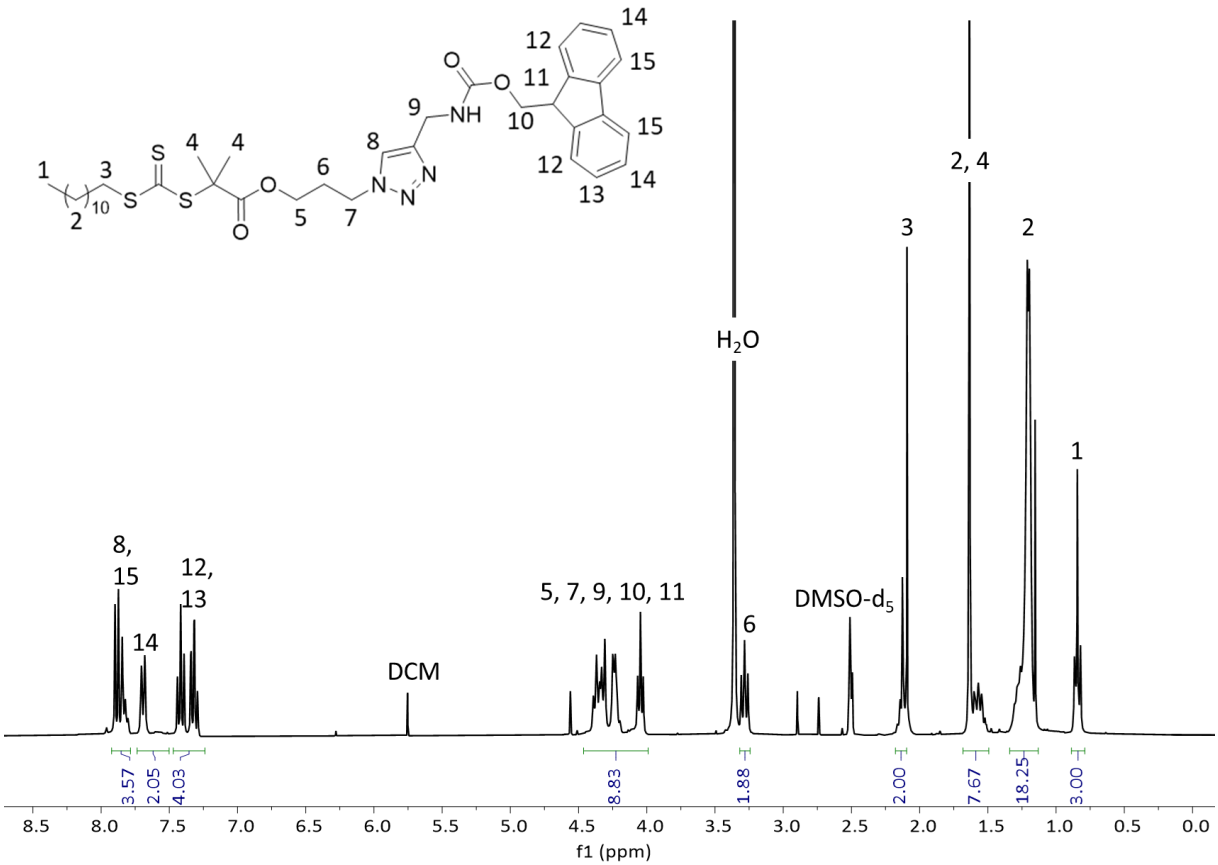

Figure 42. ^{1}H-NMR spectrum of the novel CTA-prot recorded in DMSO-d_6 at 600 MHz. The individual protons are assigned by number.

3.3.3 RAFT-polymerization of pentafluorophenyl acrylate with the novel CTA-prot

Following the successful synthesis of the novel CTA-prot, several polymerizations using the active ester monomer were performed in order to study the polymerization characterises of this CTA.

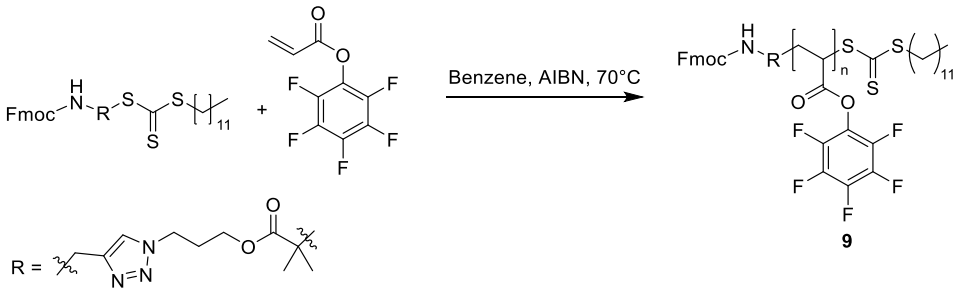

Scheme 8. Polymerization of pentafluorophenyl acrylate with CTA-prot.

The aim was to synthesize polymers with different length to test the influence of the polymer length in the later hydrogel application. In theory, for a RAFT polymerization the molecular weight of a polymer can be estimated using equation 6.[207]

$$M_{n,th} = \frac{[M]_0 * p * M_M}{[CTA]_0} + M_{CTA} \qquad (6)$$

$$with\ M_{n,th} = theoretical\ number\ average\ molar\ mass,$$

$$[M]_0 = initial\ monomer\ concentration, p = monomer\ conversion,$$

$$M_M = molar\ mass\ of\ the\ monomer, [CTA]_0 = initial\ CTA\ concentration,$$

$$M_{CTA} = molar\ mass\ of\ the\ CTA$$

For longer polymerization times the equation can be further simplified by assuming that the conversion is close to 100%. Therefore, the molecular weight can be estimated by only multiplying the ratio of the used CTA to the monomer by the monomer mass plus the mass of the CTA. In Table 9 the monomer CTA ratios, theoretical as well as measured values for the number average molar mass are compiled.

Overall, it becomes apparent that the measured values are not in accordance with the expected values. The overall polymerization rate seems rather slow when compared to other known RAFT polymerizations. Reaction times of 6 hours are usually enough to reach completion and here only a conversion of about 50% is achieved. Compared to the commercially available CTAs, the CTA-prot is larger and more sterically demanding, which could be one of the reasons for the low polymerization rate.

Table 9. Overview of polymerizations of CTA-prot with pentafluorophenyl acrylate at 70°C and AIBN as initiator (I) (Polymerizations were performed by Ali Balasini).

Sample	Ratio (M : CTA : I)	Duration [hours]	Expected $\overline{Mn}$ [g/mol]	Measured $\overline{Mn}$ [g/mol]*	Đ	P_n GPC
10	50 : 1 : 0,1	6	12625	6476	1.11	24
11	100 : 1 : 0,1	6	24525	7933	1.10	30
12	50 : 1 : 0,1	18	12625	6571	1.35	24
13	100 : 1 : 0,1	18	24525	8211	1.85	31

*measured using THF-GPC, $\overline{Mn}$ and Đ are averaged based on the values from the two detectors (UV and RI).

Additionally, it was not possible to achieve a high molecular weight polymers (>10kDA) while keeping the dispersity low. Ratios as well as polymerization times were increased, but higher polymer weight was always accommodated with a high dispersity. Similar high dispersities were observed using the commercially available azide bearing CTA, which was caused by side reactions of the azide with the monomer. Here one possible cause could also be based on another side reaction, due to a thermal cleavage of the Fmoc protecting group and a subsequent reaction of the primary amine with the active ester component of the monomer. Literature has shown that a thermal cleavage of Fmoc is possible and can occur quantitatively already within 15 minutes at 120°C.[208] During polymerization the temperature is only 70°C, but it seems for reactions times longer than 6 hours this could be enough to at least partially cleave Fmoc. Nevertheless, precursor polymer **10** was further analysed using NMR spectroscopy and used in the subsequent functionalization steps (see Figure 43).

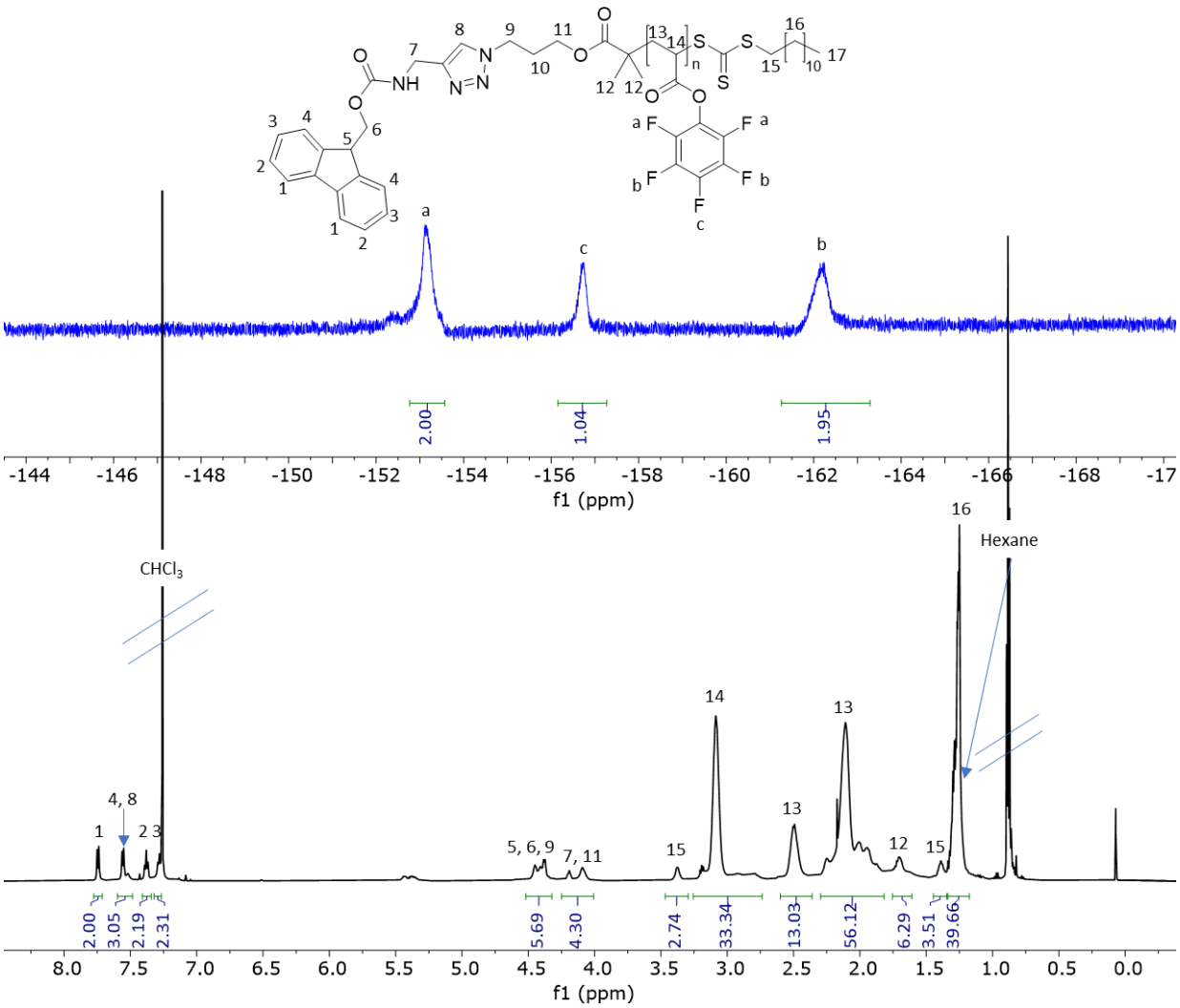

*Figure 43. ^{1}H-NMR (black) and ^{19}F-NMR (blue) of the precursor polymer **10** in $CDCl_3$ measured at 600 MHz.*

All expected signals were found and could be assigned. Characteristic signals are the three signals in the ^{19}F-NMR confirming the presence of the pentafluorophenyl group and also the signals for the Fmoc and the triazole moiety were found. However, from the NMR a P_n of 33 was calculated, which stands in slight contrast to the P_n of 24 determined by GPC. The following section addresses the functionalization of polymer **10**.

3.3.4 Functionalization of pentafluorophenyl ester polymers containing the novel CTA-prot

The last and final step of this project was to functionalize the polymers introducing carbohydrate side chains in order to mimic glycosaminoglycans (GAGs) as component of the ECM. Natural GAGs are long polysaccharides consisting of a uronic acid and an amino carbohydrate repeating unit.[209] One representative is hyaluronic acid (HA), known for its involvement in cell proliferation and migration.[210, 211] HA is based on the disaccharide repeating unit composed of D-glucuronic acid and N-acetyl-D-glucosamine.[212] For this work, the most occurring carbohydrate in the ECM, namely N-acetyl-D-glucosamine (GlcNAc), was chosen as side chain in the polymers. Different functionalized GlcNAc derivatives are well established in the Hartmann working group.[213] For comparison, polymers were also functionalized with ethanolamine, which will later serve as a negative control in the hydrogel experiments. Scheme 9 shows the synthetic pathway for the functionalization of the active ester polymer with ethanolamine (P-AE, **14**) and GlcNAc (P-AG, **15**).

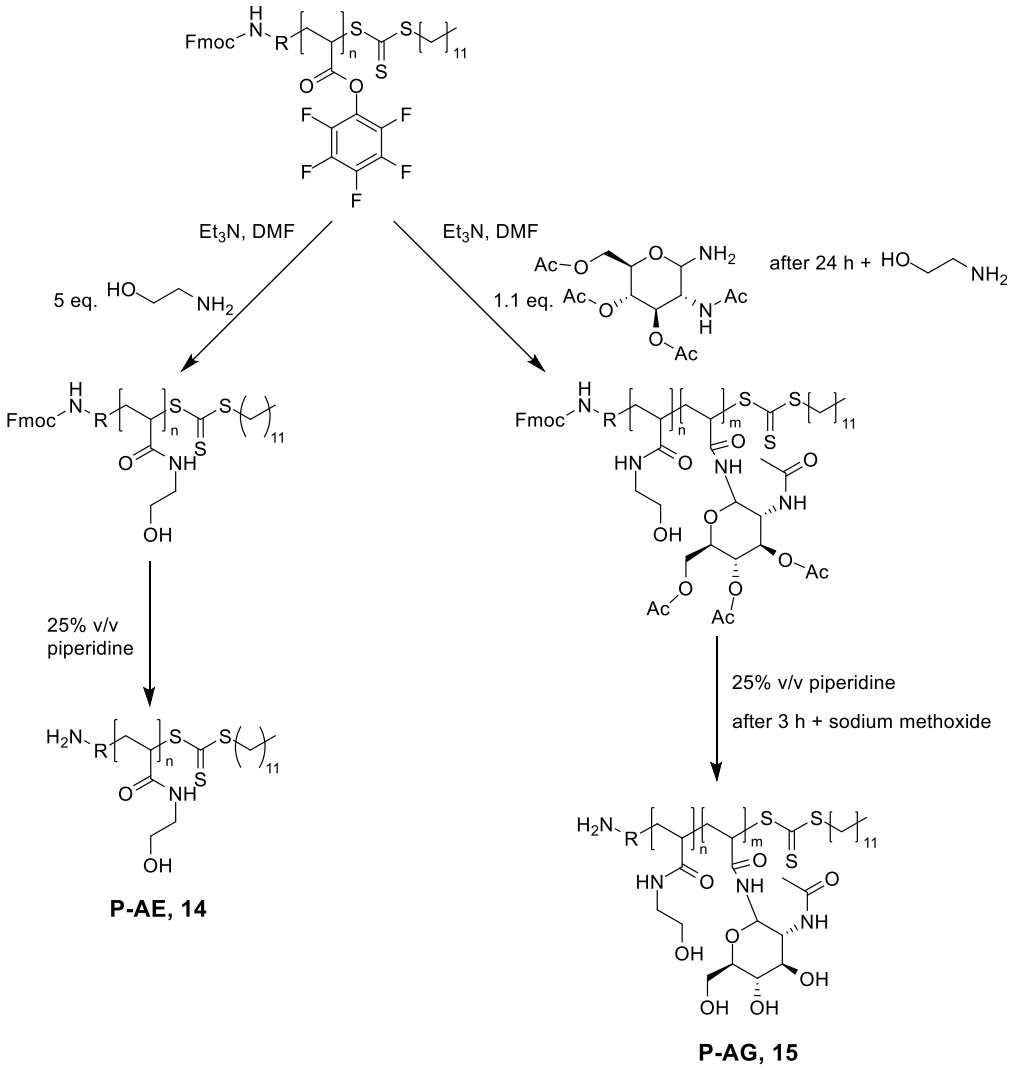

Scheme 9. Multi step synthesis of the functionalization of the active ester polymer with ethanol amine and amino-GlcNAc.

Following the shown route, P-AE could be readily synthesized. In short, the active ester polymer was solved in DMF and was stirred with a 5-fold excess of ethanolamine at 40°C for 24 hours. In order to deprotect the terminal amine group, piperidine was added until a final concentration of 25% v/v was reached and the solution was stirred for an additional 3 hours. The final product was then precipitated in acetone and purified further by dialysis in water. After freeze drying the colorless product was isolated in a 60% yield and further analyzed by ^{1}H-NMR, ^{19}F-NMR and H_2O-GPC. Figure 44 shows in blue the ^{19}F-NMR and in black the ^{1}H-NMR for P-AE. Since no signal was detected in the ^{19}F-NMR, it can be assumed that all pentaflurophenyl groups have been exchanged with ethanolamine. Furthermore, the ^{1}H-NMR shows no signals for the Fmoc groups, which confirms the deprotection of the primary amine. Additionally, a qualitative amine test using ninhydrin was also positive, reassuring the presence of a free terminal amine group. Furthermore, the calculated P_n from the ^{1}H-NMR is

24, which is in good accordance to the previously determined P_n for the precursor polymer using THF-GPC. However, the P_n for P-AE derived from the H_2O-GPC deviates with a value of 36. Most likely, the true value of P_n is somewhere in between.

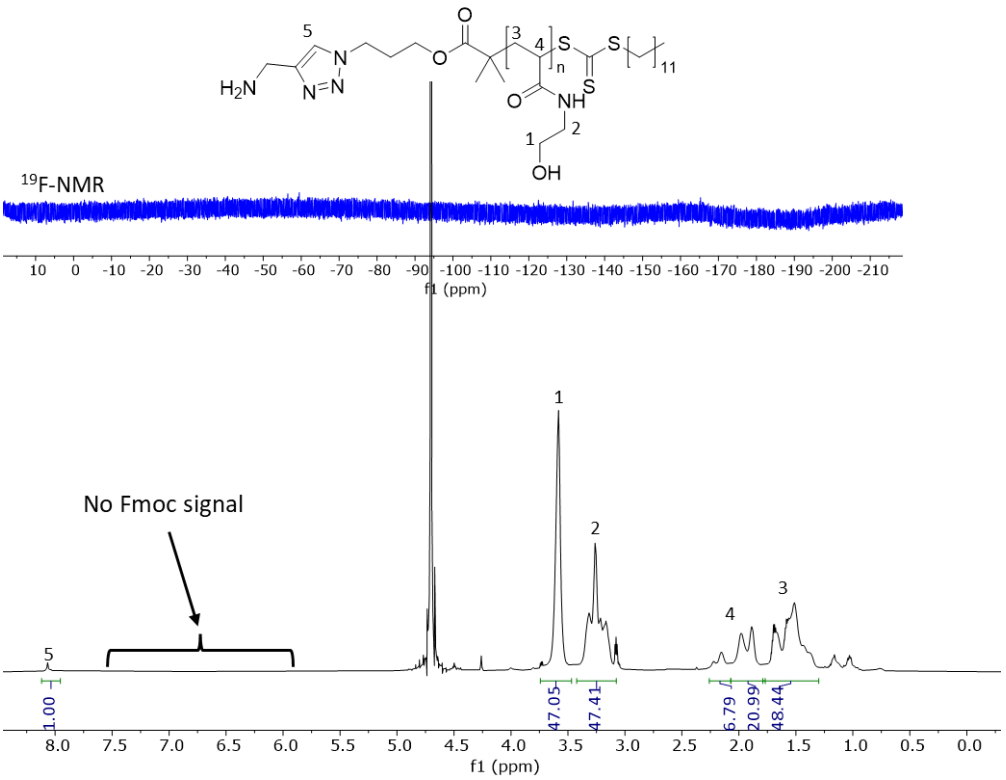

Figure 44. ^{1}H-NMR (black) and ^{19}F-NMR (blue) of P-AE in D_2O measured at 600 MHz.

After the successful synthesis of P-AE, in a first approach to synthesize P-AG, the precursor polymer was functionalized using 2-acetamido-2-deoxy-β-D-glucopyranosylamine. However, after minutes of stirring the reaction mixture became cloudy. Nevertheless, the reaction mixture was treated the same way as the for P-AE and was also purified using dialysis. Following, H_2O-GPC analysis showed a bimodal distribution data from the light scattering detector with one peak in the range of 200 kDa (see Appendix 17). Most likely, not only the terminal amine but also the hydroxyl groups of the carbohydrates are able to react with the active ester, which results in crosslinking of multiple polymer chains. This finding stands in contrast to the finding of Fadi Shamout who showed, although not for GlcNAc but for Man, that no crosslinking of the polymer occurred.[214] For the next synthesis, the path as shown in Scheme 9 was followed, which employed the 3,4,6-tri-O-acetyl-β-D-GlcNAc amine. This 3,4,6-tri-O-acetyl-β-D-GlcNAc amine was derived from the commercially available 3,4,6-tri-O-acetyl-β-D-GlcNAc azide using a palladium catalyzed reduction with hydrogen.[215]

Using the 3,4,6-tri-O-acetyl-β-D-GlcNAc amine no cloudiness was observed. Following 18 hours of stirring, excess of aminoethanol was added to ensure that every active ester group is reacted. After additional 18 hours of stirring, piperidine was added to cleave off the Fmoc group. Subsequently, sodium methoxide was added to cleave of the acetyl groups from the carbohydrates. Finally, the product was precipitated in acetone and purified further by dialysis in water. After freeze drying the colorless product was isolated in a 15% yield and was further analyzed by ^{1}H-NMR, ^{19}F-NMR and H_2O-GPC.

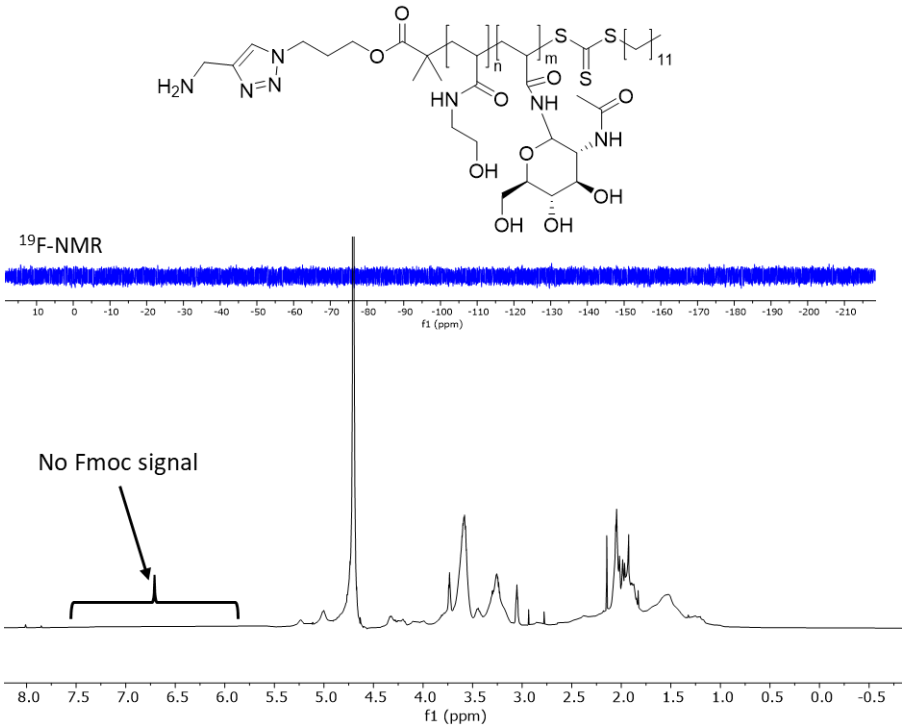

Figure 45. ^{1}H-NMR (black) and ^{19}F-NMR (blue) of P-AG in D_2O measured at 600 MHz.

Similar to the P-AE, for P-AG no signal in the ^{19}F-NMR could be detected, which indicates full conversion of the pentaflurophenyl groups. The ^{1}H-NMR showed a strong baseline distortion, thus it was only used to qualitatively check for the absence of Fmoc and presence of carbohydrate signals. As for the P-AE, for the P-AG the qualitative amine test was also positive, providing further evidence that the Fmoc moiety has been cleaved off. Following H_2O-GPC analysis resulted in a M_n of 7300 g/mol. Determination of the exact composition of the final P-AG was challenging, as the ^{1}H-NMR could only be used as a qualitative confirmation of the reaction and additionally the final polymer has potentially two different repeating units (ethanolamine repeating unit and GlcNAc repeating unit). However, with the results from ^{19}F-NMR it can be assumed that all pentaflurophenyl groups have been exchanged, thus the P_n from P-AG should be equal to the P_n of the precursor polymer. Therefore, to gauge the

polymer composition, the M_n for P-AG determined via H_2O-GPC (7300 g/mol) and the two P_n from the precursor polymer ($P_{n\text{-}NMR}$= 33, $P_{n\text{-}GPC}$=24) were used to calculate possible polymer compositions.

First the molecular mass of the deprotected CTA is subtracted from the M_n value (see equation 7).

$$7300\ \text{g/mol} - 502\ \text{g/mol} = 6798\ \text{g/mol} \qquad (7)$$

Following the compositions are calculated for $P_{n\text{-}NMR}$= 33, $P_{n\text{-}GPC}$=24. For that, two simple equations are set up, which can be solved for x (see equation 8 and 9).

$$P_{n\text{-}NMR}: 6798\ \text{g/mol} = 276.3*x + 117.1\ (33-x) \qquad (8)$$

$$P_{n\text{-}GPC}: 6798\ \text{g/mol} = 276.3*x + 117.1\ (24-x) \qquad (9)$$

The equations incorporate the molecular mass of each repeating unit, being 276.3 g/mol for the GlcNAc repeating unit and 117.1 g/mol for the ethanolamine repeating unit. Solving the equations, two compositions can be derived, which are summarized in Table 10.

Table 10. Possible structural composition of the final P-AG polymer based on precursor P_n and P-AG M_n.

P_n precursor polymer	GlcNAc units	Ethanolamine units
24 (GPC)	24	0
33 (NMR)	19	14

Overall, a polymer with at least 19 units of GlcNAc was synthesized. However, all the functionalization experiments were performed at a small scale resulting in around 20 mg of final polymer. Several tries upscaling this synthesis to a gram scale failed. Functionalization of the polymer with 3,4,6-tri-O-acetyl-β-D-GlcNAc amine always resulted in a dark brown solution and after workup using dialysis practically no substance was left. Using ethanolamine, this problem did not occur. Possible reasons are that the precursor polymer **10** degraded over time while storing or that the reaction volume was not increased enough, thus leading to concentration driven side reactions like the degradation of the 3,4,6-tri-O-acetyl-β-D-GlcNAc

amine similar to a Maillard reaction.[216] If repeated in the future, the precursor polymer should be prepared freshly and the solvent volume should be increased.

4 Conclusion and outlook

The concept as well as the synthesis of amphiphilic precision glycomacromolecules was established in this thesis. Based on the SPPoS, new building blocks and cleaving strategies were developed, which allowed for in depth investigation of the correlation between building block composition of the APGs and their respective self-assembly behavior. Building upon first findings, the synthetic flexibility of the SPPoS was used to introduce AIE moieties to the APGs, thus creating a form of an amphiphilic biosensor for clustering events. Additionally, APGs were subjected to binding studies against bacteria and lectins, showing the potential of multivalent presentation of ligands through self-assembly. Lastly, an approach towards the usage of controlled radical polymerization to derive poly(active ester) derivatives suitable for conjugation with precision glycomacromolecules was developed.

In the first part of this thesis, the APG concept based on the previously established SPPoS approach from the Hartmann lab was developed. First, design principles for APGs were detailed based around the tailor-made building blocks from the Hartmann lab. However, for the hydrophobic tail part of the APGs, building blocks were lacking, therefore three novel hydrophobic building block suited for SPPoS were developed. For the building blocks starting from hexamethylenediamine a synthesis was developed, which allowed for the preparation of the alkyl spacing building block HDS, the alkene bearing HDM building block and the non-published HDI building block. These hydrophobic building blocks allowed to prolong the hydrophobic part of the APG and in the case of HDM also to introduce an alkene species, which was used for micellar core-crosslinking. Comparing these building blocks to already existing building blocks like ODS based on octamethylenediamine, it is evident that with a hexamethylenediamine backbone the balancing of hydrophobic properties to coupling efficiency is superior.[29, 131] Following, the coupling of fatty acids with different length was established and their ability to induce self-assembly was evaluated. Results showed that fatty acids between C_{10} and C_{15} were attachable under standard coupling conditions and were sufficient to induce self-assembly. With that it was demonstrated that not only peptides but also tailormade oligo(amido)amines are suited for fatty acid coupling and thus made the new class of amphiphiles, APGs, accessible.

Next the synthesis of APGs was optimized on the basis of yield, feasibility and purity. Results showed that for charged APGs the yields were significantly higher using a TentaGel® R HMPA resin than a TentaGel® S TRT resin. Additionally, a novel mild alkaline cleavage was developed for the TentaGel® HMPA and S TRT resin, allowing for a first time for a quantitative cleavage of the APG off the resin and a simultaneous deprotection of carbohydrate ligands. Using this combination of resin and cleavage procedure resources in terms of time and materials can be saved compared to the usual cleaving procedures. Furthermore, a custom fitted experimental cascade for the analysis of the self-assembly characteristic of APGs was established.
Lastly, three different strategies for micellar core-crosslinking were investigated. First a radical crosslinking approach was followed and for that different crosslinking agents and initiator were compared in terms of yield and perseverance of the micellar structure. These experiments yielded the optimized synthetic crosslinking procedure, which was used and in the second part of this thesis. Following, a Michael addition approach was explored using the HDM building block as an electron-deficient alkene donor and various thiols as crosslinking agents. Using dimethylphenylphosphine catalysis the reaction took place within minutes, but no crosslinking was achieved as the sample APG only contained one HDM building block, which only allowed for a bridging between two APG molecules. Lastly, the use of diacetylene containing fatty acids as terminal hydrophobic groups and crosslinking agents combined were investigated. Here, initial experiments showed promising results as the micellar core-crosslinking was fast, did not require any additive and also induced a color change of the solution. Again similar results were reported for PAs, showing the kinship between APGs and PAs once more.[217]

Following, the APG concept was put to use and a series of in total 8 APGs were synthesized exchanging one building block at a time to investigate the influence of each individual building block on the APG overall characteristics. Following the synthesis, self-assembly characteristics of APGs were determined by the means of CMC, micellar size and shape. It was shown that the CMC can be readily tuned with the length of the terminal fatty acid with CMCs ranging from 0.15 mM for pentadecanoic acid variants to 3.41 mM for decanoic acid variants. Subsequent, the shape and size of the micelle were assessed using DLS, AFM and TEM. Interestingly most of the investigated APGs formed rod-like micelles and not as most other single tail surfactants spherical micelles. Probably the reasoning for this is similar to the

findings of Hartgerink et al., who showed that for peptide based amphiphiles similar to APGs, the rod-like assemblies originate from the hydrogen bonds of the amides groups within the main chain of the amphiphiles.[110] Supporting this hypothesis, a reduction of amide bonds in the APG backbone as for APG 7 resulted in formation of spherical micelles. Furthermore, for APG 8 it could be shown that the incorporated HDM building block is suited for micellar core-crosslinking. Crosslinked micelles were not only easier to prepare for AFM and TEM, but they could also withstand dilution below CMC and solvent changes from water to ethanol. Lastly, APGs were tested regarding their potential as inhibitors of bacterial adhesion of FimH bearing *E. coli*. Non-crosslinked APGs showed inhibition in the range of 61 to 222 µM and the crosslinked micelle had an IC_{50}-value of 253 µM. This means that in general the crosslinked micelles were worse inhibitors, even though the crosslinked micelles were thought to inhibit better through the multivalent presentation of Man. Most likely this is due to the fact that many Man ligands remain unused as inhibitors on the micelle's surface, thus increasing the overall IC_{50}-value. However, for crosslinked micelles a positive cooperativity factor of 2 was recorded, which shows that the binding to the bacteria profited either from the shape or the rigidity of the crosslinked micelles. To further these insights, in a future experiment a series of crosslinked APG micelles (spherical and rod-like) should be synthesized and subjected to the same binding study.

In the second part of this thesis, the integration of AIE dyes into APGs and their potential as sensors for clustering was evaluated. Initial experiments were performed by Peter Pasch, in which he synthesized three AIE containing APGs including full characterization and first AIE and CMC experiments. Building upon his work, further CMC studies in LBB were conducted with values ranging from 46 µM for MTO to 96 µM for MCO. Subsequently, AIE-APGs were subjected to AFM and TEM measurement. Similar TEM sample preparation as for the non-AIE APGs lead to images of big and clustered aggregates with no clear micellar structure visible. Most likely the high number of aromatic moieties and the associated π stacking is the reason of this large aggregate formation upon drying. However, for a peptide amphiphile with 7 TPE moieties a drop coating technique could be applied for TEM microscopy.[218] Therefore, potentially the combination of a carbohydrate, which is known to interact with aromatic compounds, with the TPE moiety lead to these large aggregates for the AIE-APGs.[219] For AFM samples a mild spin-coating was used, which allowed to image the micelles. For TPE containing

APGs rod-like micelles were observed, whereas for CATE containing APGs spherical micelles were detected. Next, the use of AIE-APGs as sensors was evaluated. In a first step, mixed micelles experiments were conducted with the aim to decrease the fluorescence in a reversible manner so that upon binding to a target the fluorescence can be re-established. As secondary amphiphile the non-AIE containing APG GLO was used and a reduction of 81% was reached. Subsequently, the binding characteristic of mixed micelles containing AIE-APG and GLO were investigated. As binding targets, the two tetrameric lectins Con A and GNA as well as the dimeric lectin LCA were employed. Titration of these lectins to the mixed micelles lead to a fluorescence increase across the board with a more pronounced effect for the tetramers. However, this assay was performed in solution and the fluorescence increase was always accompanied by an increase of the turbidity of the solution. Therefore, to distinguish if the fluorescence increase is based upon a rearrangement inside the micelles or based on the precipitation of AIE-APG lectin complexes, further experiments with Con A functionalized microstructured surfaces were started.

In the last part of this thesis, polymers as GAG mimetics for incorporation into hydrogels were developed. Synthesis was based on RAFT polymerization of the active ester monomer PFPA and the following exchange of the active ester moieties by amine functionalized GlcNAc. Initial RAFT polymerizations using an azide bearing commercially available CTA were not successful, most likely due to a cycloaddition side reaction of initiator and monomer.[206] Therefore, a novel RAFT agent was synthesized based on the azide CTA but functionalized so that it bears an Fmoc-protected terminal amine group. This CTA allowed for a terminal amine, which can be used to attach the polymer to CNCs, without interfering with the post-polymerization functionalization. Polymerization with this CTA-prot showed good results in terms of dispersity but failed to reach higher polymer weights than 8000 g/mol. Following the functionalization of the active ester polymer with aminoethanol and amino-GlcNAc was readily accomplished and confirmed by ^{1}H-NMR, ^{19}F-NMR and H_2O-GPC. Colorimetric tests with ninhydrin as well as ^{1}H-NMR analysis provided evidence that a free terminal amine is present in the polymer. Initial experiments by our collaboration partners trying to attach these polymers to CNCs and subsequently built-up hydrogels showed promising results, but as the scale up of these polymers failed, no further experiments could be performed.

In the future, the potential of heteromultivalent micelles should be considered. They could be used as a simple but closely related cell glycocalyx model as the detailed interaction of carbohydrate binding proteins to the glycocalyx is yet not fully understood.[33, 35]This could be in particular interesting as the APG approach offers great flexibility in terms of overall composition but also allows for tuning the rigidity of the micelles by using one of the described crosslinking routes. First experiments in this thesis showed that heteromultivalent mixed micelles could be readily formed simply by mixing APGs with different carbohydrates e.g. Man and Gal. This could be extended by subjecting crosslinked and non-crosslinked heteromultivalent mixed micelles to studies towards a glycocalyx cell model. Additionally, future experiments dedicated towards smart drug delivery could be pursued. One of the main drawbacks of many drug carriers systems is their toxicity.[220] Earlier studies with other poly(amidoamine)s and similar oligomers from the Hartmann lab showed no cell toxicity, which is a first indication that APGs might also be non-toxic.[221, 222] Additionally, the APG platform is flexible and allows to be custom fitted to each application, which is required for smart drug delivery. Combining this with the beforementioned heteromultivalent approach targeting could be optimized as literature has shown that the binding to a certain receptor can be maximized by incorporating non-binding carbohydrates.[223] First experiments should be focused around the solubilization characteristics of the APG, in order to evaluate how much payload (drugs) the APGs are capable of solubilizing. Proof of concept experiments were already presented in this thesis using the fluorescence reporter dyes pyrene and Nile red. In a next step the different crosslinking options could be further developed towards the goal of reversible crosslinking, which would allow to release payload only at the targeted location. For example, the usage of an acid labile acetal based crosslinking agent as reported by Fréchet et al. could be utilized for core-crosslinking of micelles and to unload cargo upon pH change e.g. cell entry of the APG micelles.[224]

5 Experimental Part

5.1 Materials and instrumentation

5.1.1 Materials

All chemicals were commercially available. The resins Fmoc-AA-TentaGel® S TRT loading 0.21 mmol/g, Fmoc-AA-TentaGel® R HMPA loading 0.021 mmol/g, Tentagel® S RAM loading 0.24 mmol/g were bought from RAPP Polymers. Trifluoroacetic acid 99%, diethylenetriamine 99%, hexamethylendiamine 98%, ethyltrifluoroacetate 99%, triisopropylsilane 99%, maleic acid 99%, sodium L-ascorbate, 2,2-dimethoxy-2-phenylacetophenone (DMPA) 99%, α-D-Man 99%, Dodecylthiocarbonothioylthio)-2-methylpropionic acid 3-azido-1-propanolester 98%, Nile red for microscopy, pyrene 99%, propargylamine 98, deuterated Methanol (MeOD), dimethylsulfoxide (DMSO-d_6), deuterated water (D_2O) and chloroform ($CDCl_3$) were bought from Sigma-Aldrich. 9-Fluorenylmethyl chloroformate, piperidine 99%, Lauric acid 99%, DIPEA 98%, Divinylbenzene for synthesis, Sodium Hydroxide for analysis were bought from Merck. Copper(II) sulfate 98% pure anhydrous, Piperidine 99% from Acros. Rhodamine labeled Con A was bought from vector laboratories. D-(+)-Gal (pure) were purchased from AppliChem. PyBOP (Benzotriazol-1-yloxy)tripyrrolidinophosphonium hexafluorophosphate >98% was bought from Carbosynth. Decanoic acid 99% was bought from J&K. Pentadecanoic acid 99%, Acryloyl chloride 96% was bought from Alfa Aesar. Pentafluorophenyl 98% was bought from BLD Pharmatech ltd. 3,4,6-tri-O-acetyl-β-D-GlcNAc azide 99% was bought from GLYCON Biochemicals. The chemicals were, if not mentioned otherwise used without further purification. HPLC grade solvents were used throughout all reactions.

5.1.2 Instrumentation

Nuclear magnetic resonance spectroscopy

^{1}H-NMR and ^{13}C-NMR measurements were performed using a Bruker Avance III 300 and Bruker Avance III 600 spectrometer operating at 300 MHz and 600 MHz for the ^{1}H NMR and at 75 MHz and 150 MHz for the ^{13}C-NMR at room temperature if not otherwise noted. The signals of the incompletetly deuterated solvents were used as internal standard. The spin multiplicities were abbreviated with s (singlet), d (doublet), t (triplet) and m (multiplet). The

chemical shifts (δ) were stated in parts per million (ppm) and coupling constants (*J)* were stated in hertz (Hz). For data analysis MestReNova 10.0.2 was used.

Mass spectroscopy

HR-MS (ESI) spectra were recorded on an Ion-Trap-API Finningan LCQ Deca (Thermo Quest) mass spectrometer. Ionization was carried out by electrospray ionization. All samples were measured in concentration of 1 mg/ml.

Reversed Phase High Pressure Liquid Chromatography coupled with ESI Mass Spectrometry

RP-HPLC-MS was carried out on an Agilent 1260 Infinity instrument coupled to a variable wavelength detector (VWD) and a 6120 Quadrupole LC/MS containing an Electrospray Ionization (ESI) source (operation mode positive and negative, m/z range from 200 to 2000). A MZ-AquaPerfect C18 (3.0 × 50 mm, 3 µm) RP column from Mz-Analysentechnik GmbH was used with a flow rate of 0.4 ml/min at 25 °C. As eluent system water/acetonitrile containing 0.1% formic acid was applied.

Thin layer chromatography

Thin layer chromatography (TLC) was performed on silicia gel coated aluminium sheets from Merk (60 F_{254} 0.25mm). The detection was carried out via UV irradtion and with a ninhydrin staining followed by heating or an iodine chamber.

Freeze drying

Samples were dissolved in water, frozen with liquid nitrogen and then freeze dried with an Alpha 1-4 LD plus instrument from Martin Christ Freeze Dryers GmbH.

Fluorescence spectroscopy

The fluorescence measurements were conducted using the FLS980 Fluorometer from Edinburgh Instruments and with a CLARIOstar plate reader from BMG Labtech.

Fluorescence microscopy

An inverted microscope (Olympus IX73, Japan) equipped with an Olympus 60× NA 1.35 oil-immersion objective (Olympus, Japan), and a CMOS camera (DMK 33UX174L, the Imaging Source, Germany) was used for the fluorescence microscopy.

Light scattering

For the light scattering measurements, a 3D LS Spectrometer from LS Instruments (Fribourg, Switzerland) was used in 2D pseudo cross-correlation operation. The instrument is equipped with a HeNe laser as light source (max. output power of 35 mW at λ = 632.8 nm). A quartz vet filled with decalin serves as temperature and refractive index matching bath. The setup is equipped with two Glan-Thompson prisms (extinction ratio of 10^{-6}), one in front of the sample and one in front of the detector. For depolarized dynamic light scattering (DDLS) measurements, the prism in front of the detector was turned by 90° and finely adjusted until minimal scattering intensity was detected using an isotropic scatterer. Analysis of the data were carried out using the cumulant method after Frisken.

Atomic force microscopy

For the AFM measurements a NanoWizard II from JPK instruments was used. The data was analyzed using JPKSPM analysis Software.

Electron Microscopy

Transmission electron microscopy was performed on a JEOL JEM-2100Plus operating in bright-field mode at 80 kV acceleration voltage. Images were analyzed using GMS 3.

UV-lamp

A TQ150 Hg medium pressure UV lamp from Heraeus Nobellight GmbH with a quartz glass immersion and cooling tube from Peschl Ultraviolet GmbH was used for micelle crosslinking

5.2 General Methods

Solid phase synthesis

For the solid phase assembly, a Fmoc Gly TentaGel® R Trt resin (prefunctionalised) with a loading of 0.21 mmol/g and a TentaGel® S RAM resin with a loading of 0.22 mmol/g was used as a solid support for the synthesis. The reactions were carried out on a scale between 0.05 and 0.20 mmol. As reaction vessels, polypropylene syringes with a porous polypropylene frit at the bottom were used. Before the first reaction step the resin was swollen two times for 15 minutes with DCM and then the solvent was changed to dimethylformamide (DMF) by washing the resin multiple times with DMF.

Solid phase building block and sugar synthesis

Solids phase building blocks as well as sugar azides were synthesized according to literature.[22, 158] However, during sugar synthesis additional precaution is required as with 2-bromoethanol and 2-chloroethanol, two highly toxic substances are used.

General Coupling protocol

The deprotection of the primary amine was performed with a solution of 25% piperidine in DMF two times, once for 5 and once for 15 minutes. Therefore at least 5 ml of the solution were added to the reaction vessel. Afterwards, the resin was washed at least 10 times with DMF. Then the coupling was performed by dissolving 5 equivalents of the used building block and 4.9 of PyBOP in 1 to 2 ml DMF (depending on the batch size) and 20 equivalents of DIPEA were added. The whole solution was vortexed to ensure complete dissolution. Afterwards, the solution was added to the reaction vessel and shaken for 1 hour. Then the mixture was washed five times with DMF and the coupling protocol is repeated, or the compound is cleaved of the solid support.

CuAAC protocol for solid phase copper mediated azide-alkyne cycloaddition

The CuAAC reaction was performed with 3 equivalents of the alkyne sugar regarding the azide groups on the backbone. Furthermore, 12 mg of copper sulfate and 12 mg of sodium ascorbate were used for all sugars except for sialic acid. For sialic acid the amount was increased to 50 mg of each compound because of its complexing properties. The sugar was solved in DMF and the other two compounds in water, so that the final ratio was 2 equivalents

DMF and 1 equivalents water. Then all solutions were added to the reactions vessel and shaken for 24 h. Afterwards, the resin was washed with water and DMF several times. Also, the resin was washed with a solution of dithiocarbamate order to remove the remaining copper ions.

Sugar deprotection and cleavage from solid support

For the glycine loaded resin the sugar moiety was deprotected and at the same time the oligomer was cleaved off the resin using 0.05 M NaOH.

For the S RAM resin the sugar was deprotected using 0.05 M NaOMe two times for 20 minutes. Cleavage was achieved with a solution of 95% TFA, 2.5% DCM and 2.5 % TIPS (*v/v*). The cleavage solution was precipated in ether, centrifuged, dried and dialysed against MQ Water (100-500 MWCO).

Core-crosslinking of the micelles

A stock solution of DVB (1 mg/ml) and DMPA (12.8 mg/ml) in DCM was prepared. Then 100 µL of the DVB and 10 µL DMPA stock solution was added to a falcon tube. The DCM was allowed to evaporate over a Nitrogen-flow. Following a solution of 4 mg oligomer dissolved in 0.8 ml ultrapure water (approximately 5 mM) was added to the falcon tube. The reaction mixture was shaken until all compounds were dissolved. Subsequently, the solution was degassed with argon for at least 20 minutes, transferred to a quartz reactor, sealed with Parafilm and immediately irradiated with a mercury lamp. Afterwards, the solution was purified in a dialysis tube MWCO 3.5 kDa in deionized water/ethanol 1:1 (*v/v*) (three solvent switches) followed by three solvent switches with deionized water.

AFM imaging

AFM experiments were conducted for the non-crosslinked micelles and for the crosslinked micelles. For the AFM experiments glass, silicon and mica surfaces were used. Prior to their usage glass and silicon surfaces were cleaned following a RCA-cleaning protocol. Samples were applied via drop or spin coating. AFM imaging was performed in air and the NanoWizard II was used in tapping mode. Commercial silicon probes were used with a nominal force constant of 7 n/m at a resonance frequency of about 155 kHz.

TEM imaging

7 microliters of the respective aqueous sample dispersion were applied to continuous carbon grids for 1 minute. After blotting, grids were placed on a drop of 3% uranyl acetate solution and immediately blotted. Then the grid was placed again on a drop of 3% uranyl acetate solution, this time for 30 seconds. After blotting the grid was dried for 20 minutes.

Fluorescence binding study

A rhodamine labeled Con A stock solution of 1mg/ml was prepared in lectin binding buffer (10 mM Hepes, 50 mM NaCl, 1 mM $MnCl_2$, 1 mM $CaCl_2$, pH 7.4). 1 µL of this solution was added to a solution of 5 mM APG 8 also in LBB. This mixture was incubated for 30 minutes and afterwards directly measured with a fluorescence Microscope.

Bacteria adhesion assay

The assay was adapted from literature. [182] In short black 96-well plates were coated with mannan solution (1.5 mg/ml) in carbonate buffer and dried in an incubator at 37°C overnight. The plate was washed three times with PBST (PBS + 0.05 % Tween 20) and blocked with 5% BSA in PBS for 2 hours. The plate is washed again three time with PBST and once with PBS. This was followed by adding the oligomer solutions and then the bacteria (*E. coli* PKL1162)s (2 mg/ml). The plate was incubated for 4.5 hours at 37°C with a closed lid. Plates were washed three times with PBS and then filled up with PBS 100µl/well. Finally, fluorescence intensity was measured with a Clariostar plate reader at 485 nm excitation and 535 nm emission.

Lectin binding study for AIE APGs

Mixed micelles consisting of AIE-APG and the non-AIE-APG with a ratio of 1/20 were readily and then incubated with lectins at different concentrations for two hours and fluorescence as well as turbidity was detected. Additionally, 10 ppm of PEG were added to prevent the lectins from sticking to the polypropylene surface of the wellplates as reported by Liu et al.[191]

5.3 Analytical Data

5.3.1 Synthesis of HDM:

The newly developed building block HDM was synthesized in a four-step procedure similar to the synthesis of EDS[22]. The overall yield of the synthesis was 10%.

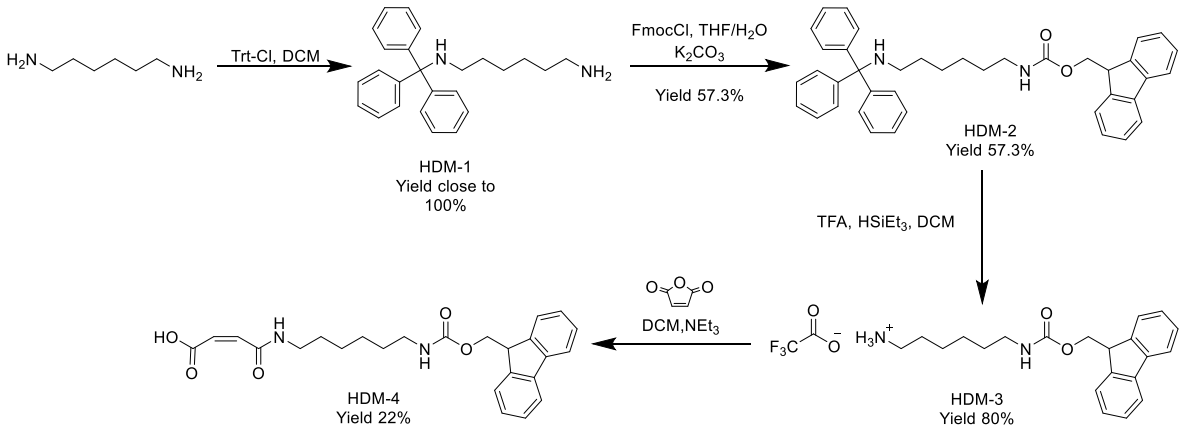

Figure 46. Overview of the synthesis of the HDM building block.

<u>*N*[1]-tritylhexane-1,6-diamine, **HDM-1**</u>

50 g (430 mmol) hexamethylenediamine was dissolved in 400 ml DCM. Then 24 g (86 mmol) tritylchloride was dissolved in 200 ml DCM and added drop wise over a period of 2 h to the ice-cooled solution of hexamethylenediamine while being stirred. After the addition, the mixture was allowed to reach RT and stirred for additional 2 h. The organic solution was concentrated to 200 ml in vacuo and washed three times with 100 ml sat. aqueous sodium bicarbonate solution. Then the solution was dried over $MgSO_4$, filtered and concentrated in vacuo and dried in high vacuo to give a yellowish oil. The product was used in the next step without further purifications.

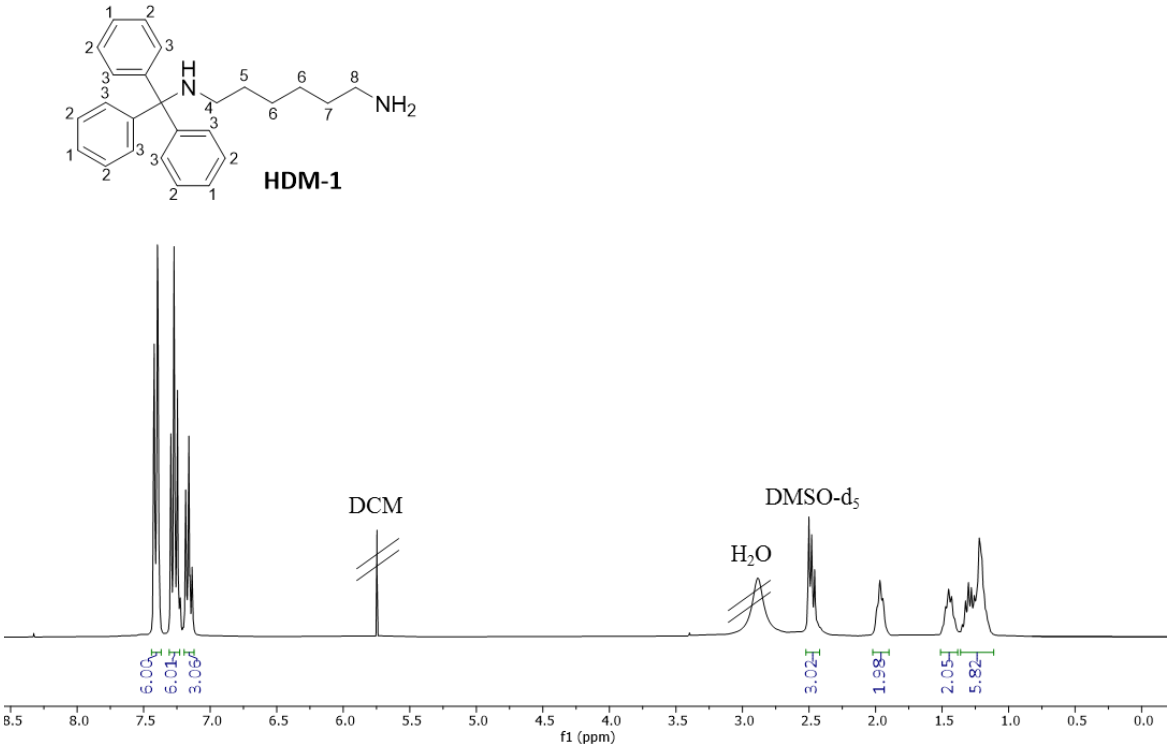

Figure 47. ^{1}H-NMR spectrum of HDM-1 recorded in DMSO-d6. The individual protons are assigned by number.

^{1}H NMR (300 MHz, DMSO-d_6): δ (ppm) 7.45 – 7.36 (m, 6H, 2), 7.32 – 7.21 (m, 6H, 3), 7.20 – 7.11 (m, 3H, 1), 2.54 – 2.41 (m, 2H, overlap with DMSO signal, 8), 2.01 – 1.91 (m, 2H, 4), 1.52 – 1.38 (m, 2H, 7), 1.36 – 1.12 (m, 6H, 5, 6).

ESI-MS for HDM 1 (Monoisotopic mass: 358.2 g/mol): Found 359.3 g/mol, $M+H]^{+}$.

(9H-fluoren-9-yl)methyl (6-(tritylamino)hexyl)carbamate, **HDM-2**

All of HDM-1 was dissolved in one portion in a mixture of 29.7 g (215 mmol) K_2CO_3 and 100 ml deionized water. Then 300 ml of THF were added (ratio of H_2O to THF = 1:3, *v/v*) and after that FmocCl was added in one portion under rigorous stirring. The reaction progress was monitored by TLC (EtOAc:nHex = 1:1, *v/v*). After complete conversion, 100 ml of EtOAc were added to the mixture. Finally, the aqueous phase was extracted twice with EtOAc (2 x 100 ml). Afterwards the organic phase was washed with brine, dried over $MgSO_4$ and concentrated in vacuo. The gel type product was recrystallized from Et_2O. 22.3 g (49.29 mmol, 57.3 %) of the pure product were obtained as a fine white powder.

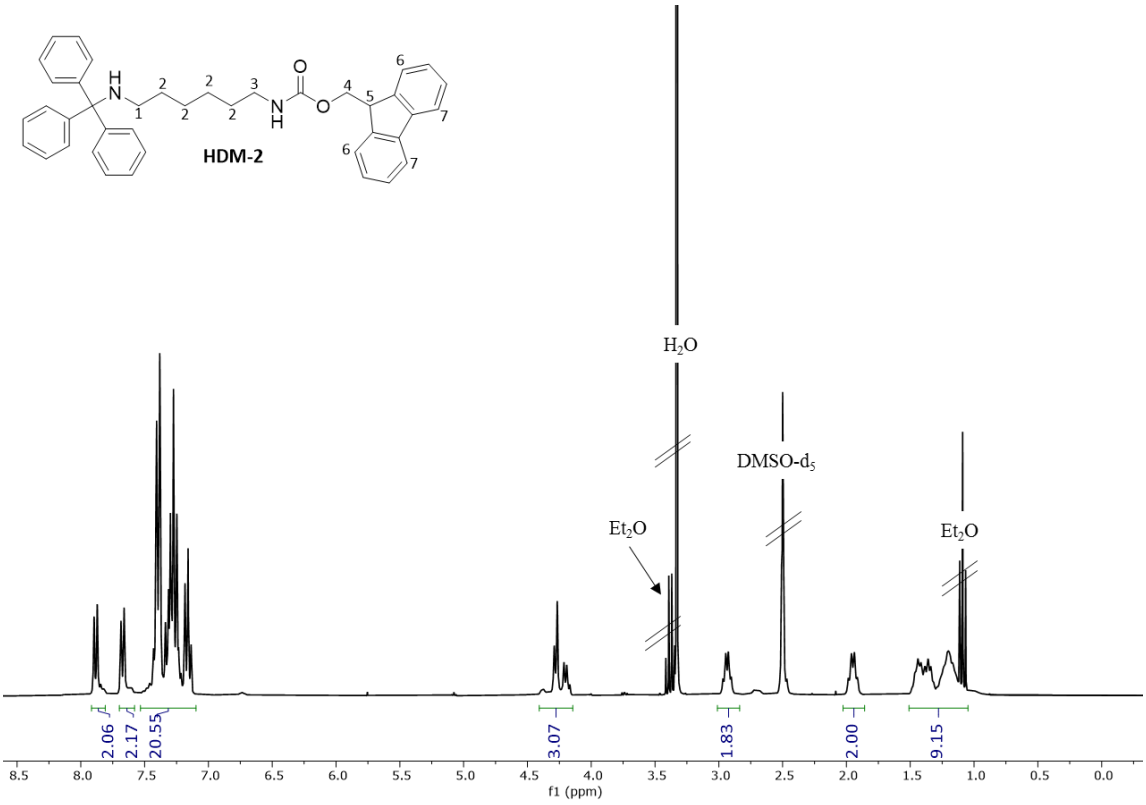

Figure 48. [1]H-NMR spectrum of HDM-2 recorded in DMSO-d6. The individual protons are assigned by number.

^{1}H NMR (300 MHz, DMSO-d_6): δ (ppm) 7.88 (d, *J* = 7.4 Hz, 2H, 7), 7.67 (d, *J* = 7.4 Hz, 2H, 6), 7.51 – 7.11 (m, 20H, rest of the aromatic protons), 4.41 – 4.16 (m, 3H, 4, 5), 3.04 – 2.85 (m, 2H, 3), 2.03 – 1.86 (m, 2H, 1), 1.53 – 1.06 (m, 8H (overlap with Et_2O rest)).

ESI-MS for HDM 2 (Monoisotopic mass: 580.3 g/mol): Found 581.3 g/mol, $[M+H]^+$.

RP-HPLC (linear gradient from 5-95% acetonitrile in water in 30 min at 25°C): t_R = 10.48 min. Determined relative purity: 96.1%

6-((((9H-fluoren-9-yl)methoxy)carbonyl)amino)hexan-1-ammonium 2,2,2-trifluoroacetate, **HDM-3**

22.3 g (49.29 mmol) of HDM-2 were dissolved in a mixture of 100 ml DCM and 10 ml triethylsilane, before 20 ml trifluoroacetic acid was added carefully while stirring at moderate speed. The reaction is exothermal and was cooled to room temperature. The reaction turned yellow to orange while adding TFA and turned clear again after complete conversion. The reaction progress was controlled with TLC (EtOAc:*n*-Hexan = 1:1, *v/v*) using ninhydrin staining to confirm complete conversion. The mixture was precipitated into 200 ml diethyl ether and a gel type product was formed. After complete precipitation of the product (usually in the fridge overnight) all solvents were decanted off and the residue was dried in vacuo. 18 g (40 mmol) were isolated, which corresponded to a yield of 80 %.

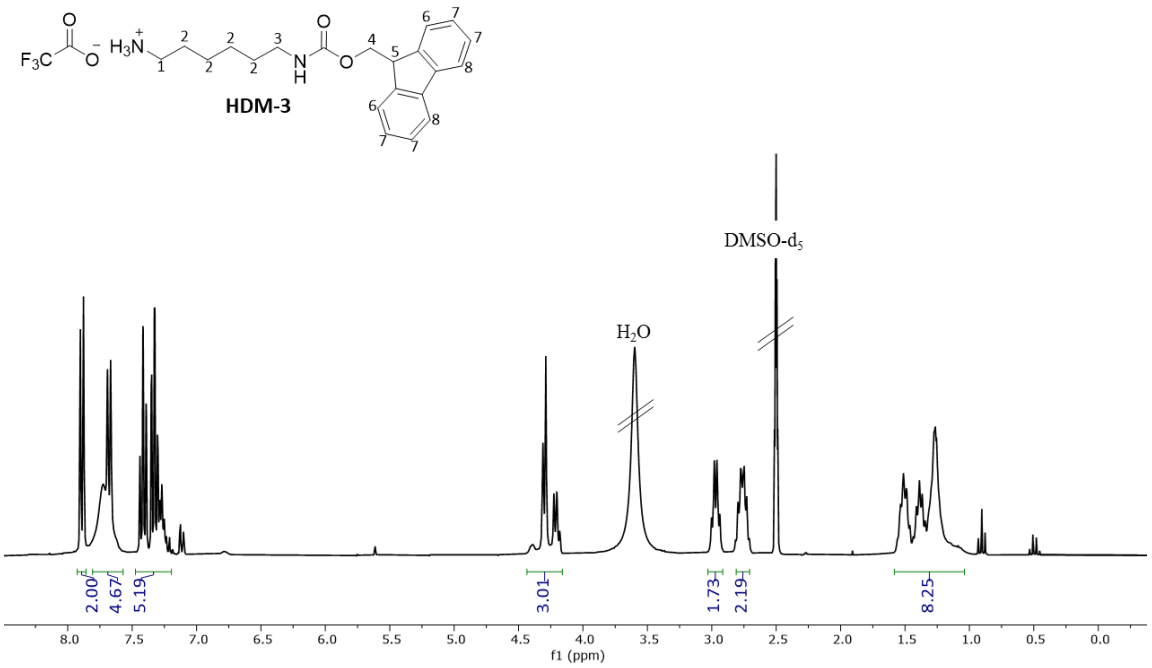

Figure 49. ^{1}H-NMR spectrum of HDM-3 recorded in DMSO-d6. The individual protons are assigned by number.

^{1}H NMR (300 MHz, DMSO-d_6): δ (ppm) 7.89 (d, J = 7.3 Hz, 2H, 8), 7.82 – 7.61 (m, 2H, 6(overlap with the amine signal)), 7.46 – 7.21 (m, 5H, 7), 4.43 – 4.16 (m, 3H, 4, 5), 3.04 – 2.91 (m, 2H, 1), 2.85 – 2.67 (m, 2H, 3), 1.60 – 1.04 (m, 8H, 2).

ESI-MS for HDM 3 (Monoisotopic mass: 339.2 g/mol): Found 340.3 g/mol, $[M+H]^+$.

RP-HPLC (linear gradient from 5-95% acetonitrile in water in 30 min at 25°C): t_R = 1.25 min. Determined relative purity: 94%

(Z)-4-((6-((((9H-fluoren-9-yl)methoxy)carbonyl)amino)hexyl)amino)-4-oxobut-2-enoic acid, **HDM-4**

10 g (22.1 mmol) of HDM-3 was dissolved in 80 ml DCM and 5 ml of triethylamine was added. The solution was stirred for two hours. In the meantime, a solution of maleic anhydride was prepared by dissolving 1.9 g in 100 ml of DCM. After two hours the solution of HDM-3 was slowly added via a dropping funnel to the maleic anhydride solution over a period of four hours. Note that the mixture of will not dissolve completely, but by adding it to the maleic anhydride solution it will dissolve. Additionally, the usage of the dropping funnel is essential as maleic anhydride is prone to polymerization (solution will turn red upon polymerization). Finally, all solvents were removed in vacuo, the resulting foam was dissolved in 200 ml of EtOAc and as much 0.2 g/ml citric acid solution was added until PH 3-4 was reached. The aqueous layer was than extracted three times (3x 100 ml) with EtOAc, the combined organic phases were dried over $MgSO_4$ and concentrated in vacuo. The raw product was recrystallized from EtOAc and 2.08 g (4.8 mmol, 22 %) of the pure product was obtained as a fine white powder.

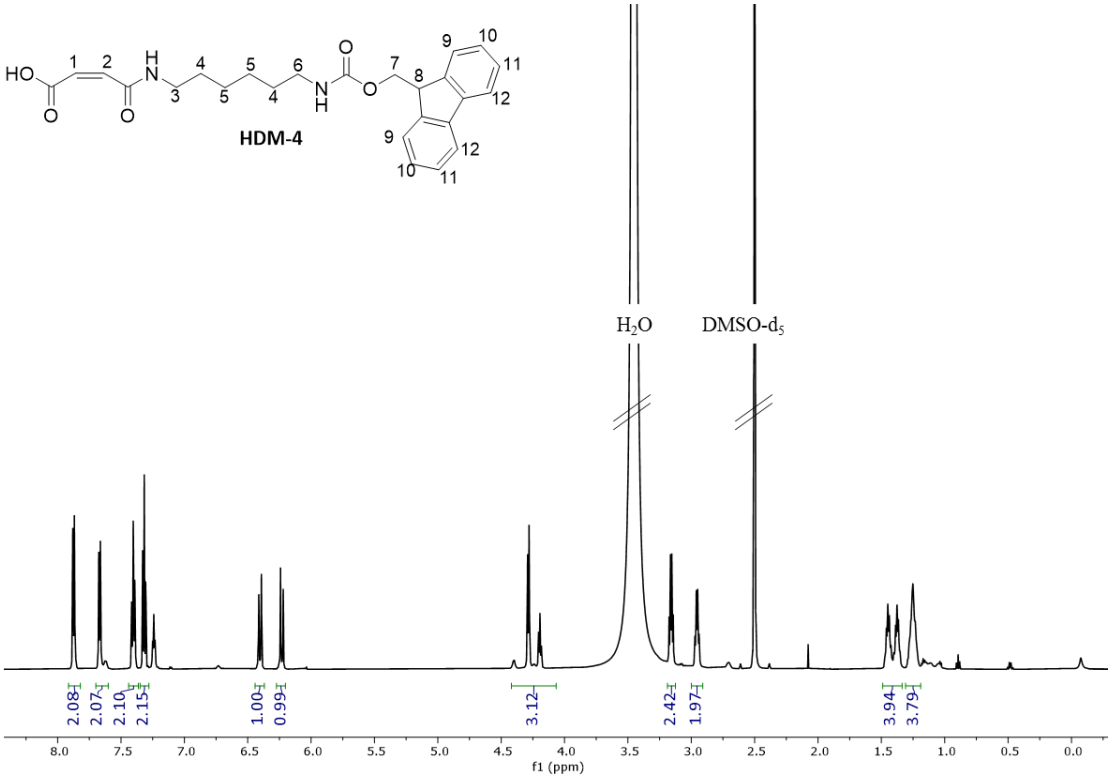

Figure 50. [1]H-NMR spectrum of HDM-4 recorded in DMSO-d6. The individual protons are assigned by number.

^{1}H NMR (600 MHz, DMSO-d_6): δ (ppm) 7.87 (d, J = 7.5 Hz, 2H, 12), 7.67 (d, J = 7.5 Hz, 2H, 9), 7.40 (t, J = 7.4 Hz, 2H, 11), 7.34 – 7.29 (m, 2H, 10), 6.40 (d, J = 12.6 Hz, 1H, 1), 6.23 (d, J =

12.5 Hz, 1H, 1), 4.32 – 4.16 (m, 3H, 7, 8), 3.16 (q, J = 6.7 Hz, 2H, 3 (overlap with residual solvent signal)), 2.96 (q, J = 6.6 Hz, 2H, 6), 1.49 – 1.34 (m, 4H, 4), 1.29 – 1.20 (m, 4H, 5).

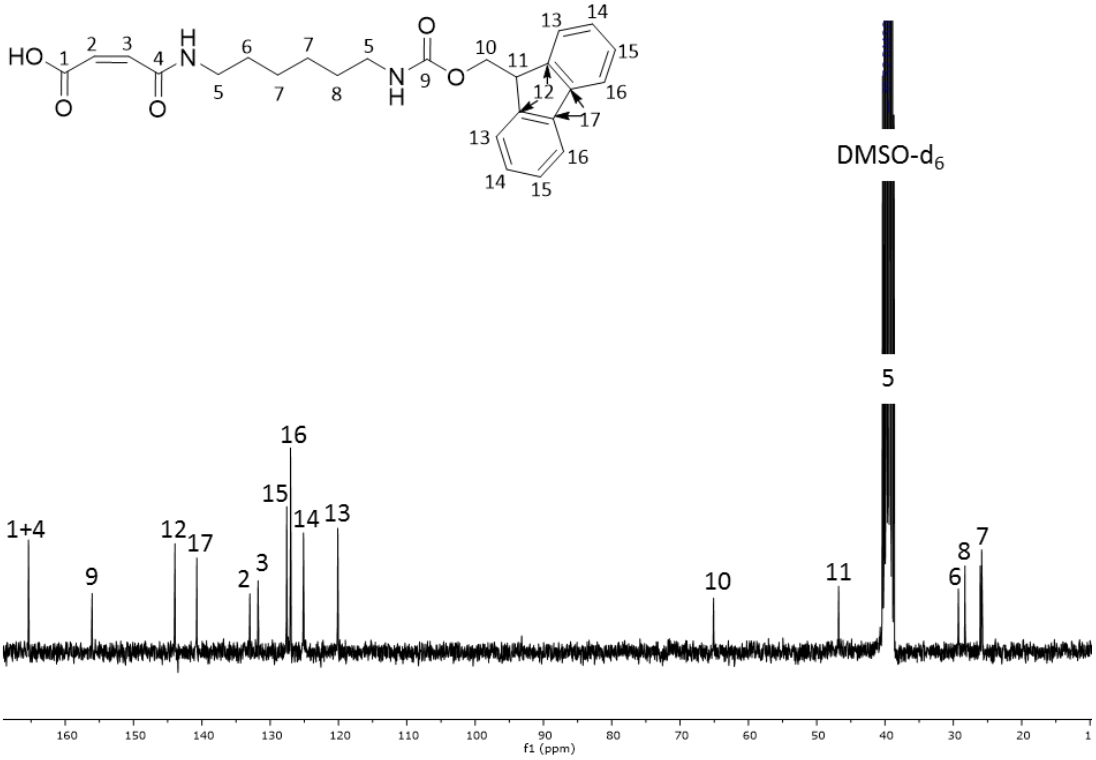

Figure 51. ^{13}C-NMR spectrum of HDM-4 recorded in DMSO-d6. The individual carbons are assigned by number.

^{13}C-NMR (75 MHz, DMSO): δ (ppm) 165.28 (C-1, C-4), 156.03 (C-9), 143.90 (C-12), 140.70 (C-17), 132.94 (C-2), 131.73 (C-3), 127.54 (C-15), 126.98 (C-16), 125.08 (C-14), 120.07 (C-13), 65.07 (C-10), 46.75 (C-11), 29.23 (C-6), 28.27 (C-8), 25.81 (C-7).

ESI-MS for HDM 4 (Monoisotopic mass: 436.2 g/mol): Found 437.2 g/mol, $[M+H]^+$.

RP-HPLC (linear gradient from 5-95% acetonitrile in water in 30 min at 25°C): t_R = 19.89 min.

Determined relative purity: 97%

Elementary analyses:

Table 11. Result of the elementary analyses of the new building block HDM

	Theoretical value	Analytical result
%C	68.79	68.40
%N	6.42	6.33
%H	6.47	6.47

4-((6-((((9H-fluoren-9-yl)methoxy)carbonyl)amino)hexyl)amino)-4-oxobutanoic acid **HDS-4**

10 g (22.1 mmol) of HDM-3 was dissolved in 200 ml DCM and 5 ml of triethylamine was added. Following 2.4 g (24.3 mmol) succinic anhydride was added at once and the solution was stirred overnight. Finally, all solvents were removed in vacuo, the resulting foam was dissolved in 200 ml of EtOAc and as much 0.2 g/ml citric acid solution was added until PH 3-4 was reached. The aqueous layer was than extracted three times (3x 100 ml) with EtOAc, the combined organic phases were dried over $MgSO_4$ and concentrated in vacuo. The raw product was recrystallized from EtOAc and 2.08 g (4.8 mmol, 22 %) of the pure product was obtained as a fine white powder.

^{1}H NMR (600 MHz, DMSO): δ (ppm) 7.87 (d, *J* = 7.5 Hz, 2H), 7.67 (d, *J* = 7.5 Hz, 2H), 7.40 (t, *J* = 7.4 Hz, 2H), 7.32 (t, *J* = 7.4, 2H), 4.28 (d, *J* = 6.9 Hz, 2H), 4.19 (t, *J* = 6.9 Hz, 1H), 2.99 (t, *J* = 7.0 Hz, 2H), 2.94 (t, *J* = 7.0 Hz, 2H), 2.41 (t, *J* = 7.0 Hz, 2H), 2.28 (t, *J* = 7.0 Hz, 2H), 1.39 – 1.19 (m, 8H).

ESI-MS for HDS 4 (Monoisotopic mass: 438.2 g/mol): Found 439.2 g/mol, $[M+H]^+$.

RP-HPLC (linear gradient from 5-95% acetonitrile in water in 30 min at 25°C): t_R = 17.5 min. Determined relative purity: 99%

5.3.2 Synthesis of APG library

Table 12. Overview of the yields and relative purities of the synthesized APGs

APG	Average Yield[1]	Relative Purity[2]
1	29%	>90%
2	22%	>90%
3	35%	>90%
4	32%	>90%
5	65%	>90%
6	30%	>95%
7	45%	>90%
8	34%	>95%[1]

[1]average yields of, [2]as determined by integration, [3]purified using preparative HPLC

APG **2**, Gly-TDS(Man)-HDM-C10

The integral for the multiplet between 3.9 – 2.9 is larger than expected, due to a baseline increase which is derived through the self-assembly nature of the material and an overlap with the solvent. In order to suppress the baseline increase as much as possible a solvent mixture of D_2O and CD_3OD was used. Furthermore, the integral for the alkene moiety of the HDM building block is decreased. Potentially this is due to the acidic nature of the alkene protons and that the protons are exchanged with deuterium, thus decreasing the integral.

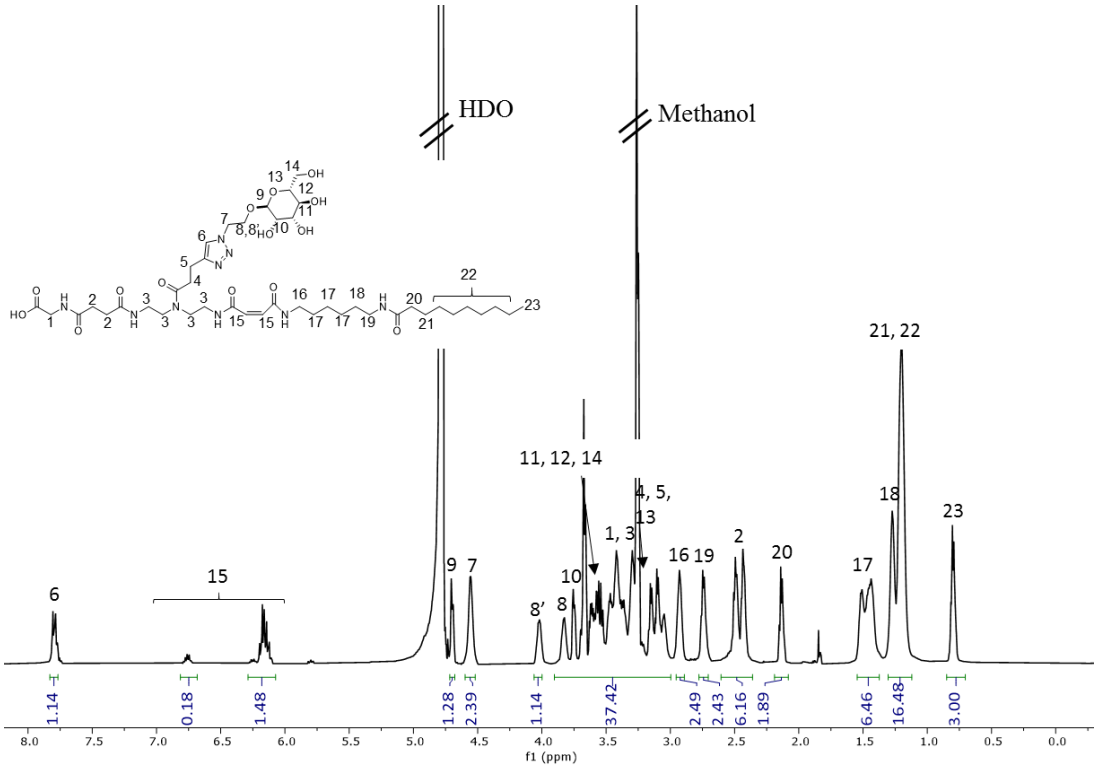

Figure 52. ^{1}H-NMR spectrum APG **2** recorded in D_2O/CD_3OD mixture. The individual protons are assigned by number.

^{1}H NMR (600 MHz, D_2O, CD_3OD): δ (ppm) 7.79 (m, 6), 6.76 – 6.04 (m, 15), 4.75 – 4.64 (m, 9), 4.61 – 4.44 (m, 7), 4.11 – 3.97 (m, 8'), 3.94 – 2.99, (m, 1, 3, 4, 5, 8, 10, 11, 12, 13, 14), 2.96 – 2.89 (m, 16), 2.82 – 2.67 (m, 19), 2.52 – 2.41 (m, 2), 2.19 – 2.09 (m, 20), 1.54 – 1.37 (m, 17), 1.30 – 1.12 (m, 18, 21, 22), 0.88 – 0.69 (m, 23).

HR-ESI-MS for $C_{45}H_{77}N_9O_{14}$. (Exact monoisotopic mass 939.5277): $[M+2H]^{2+}$ calcd. 470.7711, found 470.7715, mass accuracy -0.7 ppm.

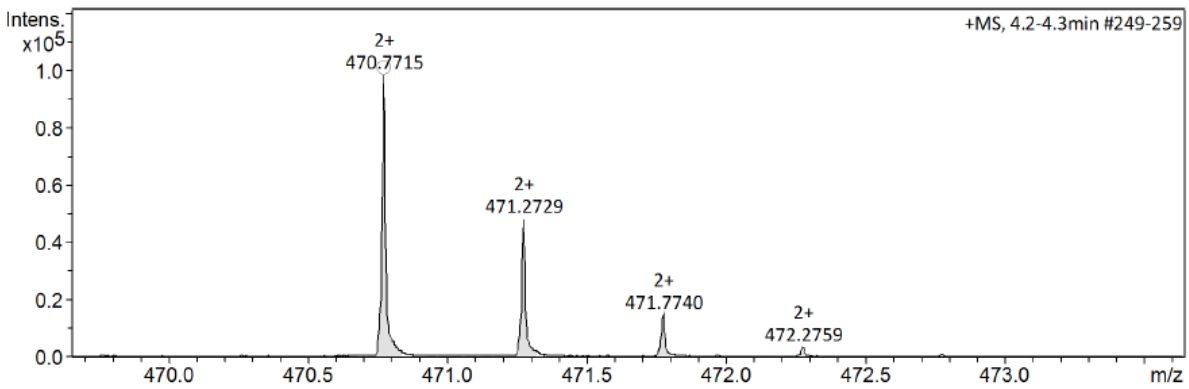

Figure 53. HR-ESI-MS of APG 2, recorded in positive mode.

RP-HPLC (linear gradient from 0 - 100% eluent B in 30 min at 25 °C): t_R = 14.25 min. Determined relative purity: >90% (Peak at t_r=14.25 and 14.65 have the same mass (data not shown) and are probably isomers caused by the HDM building block).

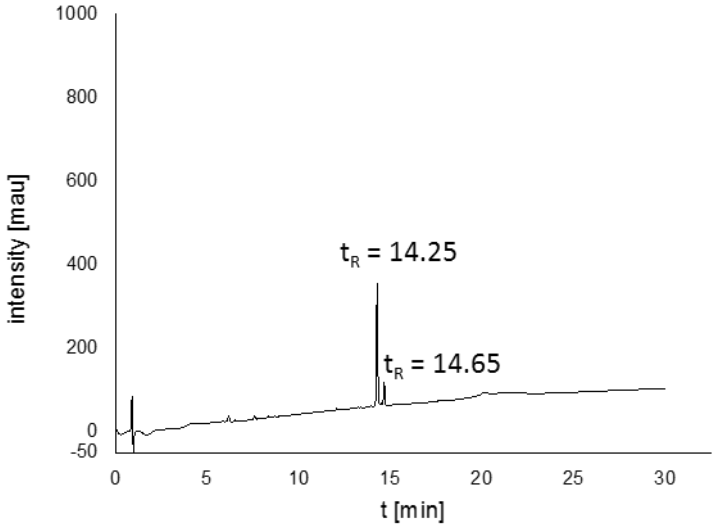

Figure 54. RP-HPLC of APG **2** (linear gradient from 5-95% acetonitrile in water in 30 min at 25°C).

APG **1**, Gly-TDS(MAN)-HDM-C12

The integral for the multiplets between 3.94 – 3.48 is larger than expected, due to a baseline increase which is derived through the self-assembly nature of the material. Furthermore, the integral for the alkene moiety of the HDM building block is decreased. Potentially this is due to the acidic nature of the alkene protons and that the protons are exchanged with deuterium, thus decreasing the integral. Additionally, this NMR measurement was performed at 50°C.

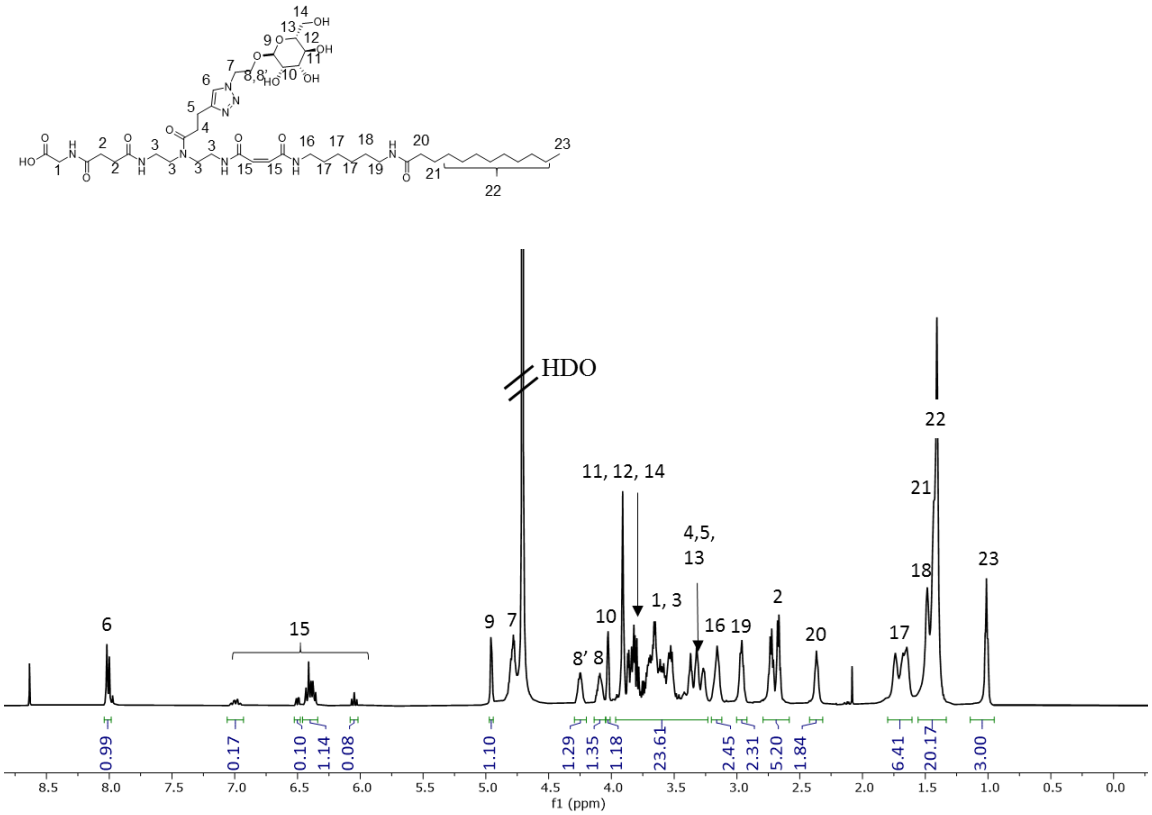

Figure 55. ^{1}H-NMR spectrum APG **1** recorded in D_2O. The individual protons are assigned by number.

^{1}H NMR (600 MHz, D_2O) δ 8.05 – 7.96 (m, 6), 7.05 – 6.02 (m, 15), 4.98 – 4.94 (m, 9), 4.83 – 4.74 (m, 7), 4.28 – 4.21 (m, 8'), 4.14 – 4.06 (m, 8), 4.06 – 4.01 (m, 10), 3.94 – 3.23 (m, 1, 3, 4, 5, 13, 11, 12, 14), 3.20 – 3.11 (m, 16), 3.01 – 2.91 (m, 19), 2.78 – 2.62 (m, 2), 2.41 – 2.32 (m, 20), 1.78 – 1.61 (m, 17), 1.54 – 1.38 (m, 18, 21, 22), 1.14 – 0.95 (m, 23).

HR-ESI-MS for $C_{45}H_{77}N_9O_{14}$. (Exact monoisotopic mass 967.5590): $[M+2H]^{2+}$ calcd. 484.7868, found 484.7872, mass accuracy -0.9 ppm.

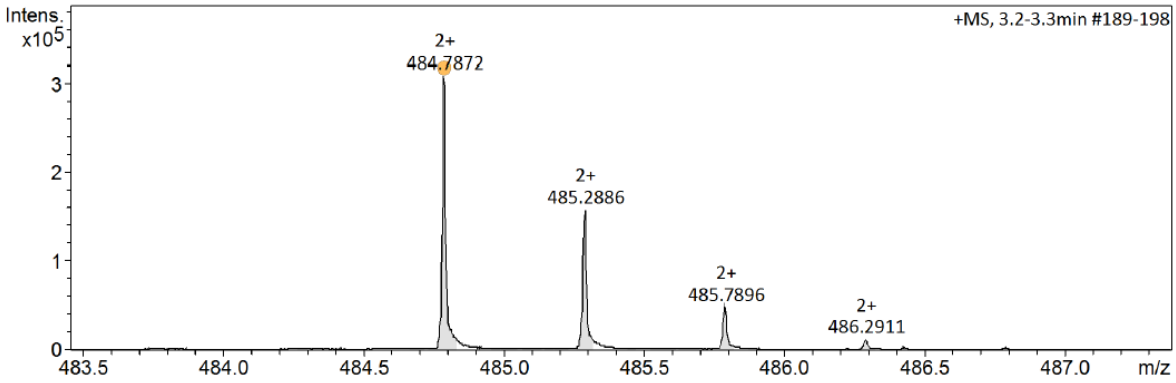

Figure 56. HR-ESI-MS of APG 1, recorded in positive mode.

RP-HPLC (linear gradient from 0 - 100% eluent B in 30 min at 25 °C): t_R = 17.0 min. Determined relative purity: >90% (Peak at t_r=17.0 and 17.3 have the same mass (data not shown) and are probably isomers caused by the HDM building block).

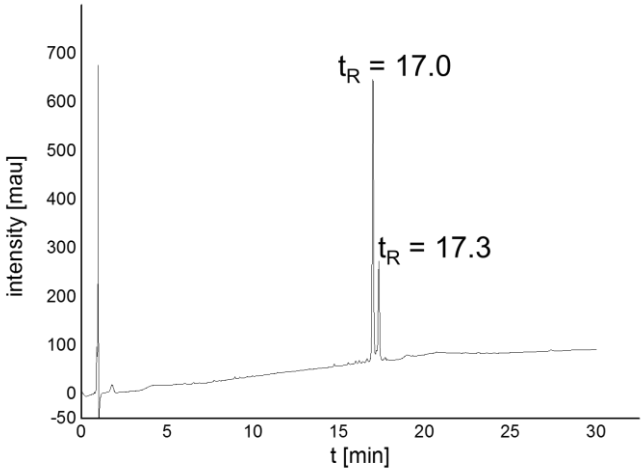

Figure 57. RP-HPLC of APG **1** (linear gradient from 5-95% acetonitrile in water in 30 min at 25°C).

APG **3**, Gly-TDS(MAN)-HDM-C15

The anomeric proton of Man (9) could not be integrated in ^{1}HNMR due to the overlaying signal from the residual water signal. An unidentified signal was detected with a chemical shift of δ 3.694 (s) ppm. The integral for the multiplets between 3.73 – 3.21 is larger than expected, due to a baseline increase which is derived through the self-assembly nature of the material. In order to suppress the baseline increase as much as possible a solvent mixture of D_2O and CD_3OD was used. Furthermore, the integral for the alkene moiety of the HDM building block is decreased. Potentially this is due to the acidic nature of the alkene protons and that the protons are exchanged with deuterium, thus decreasing the integral.

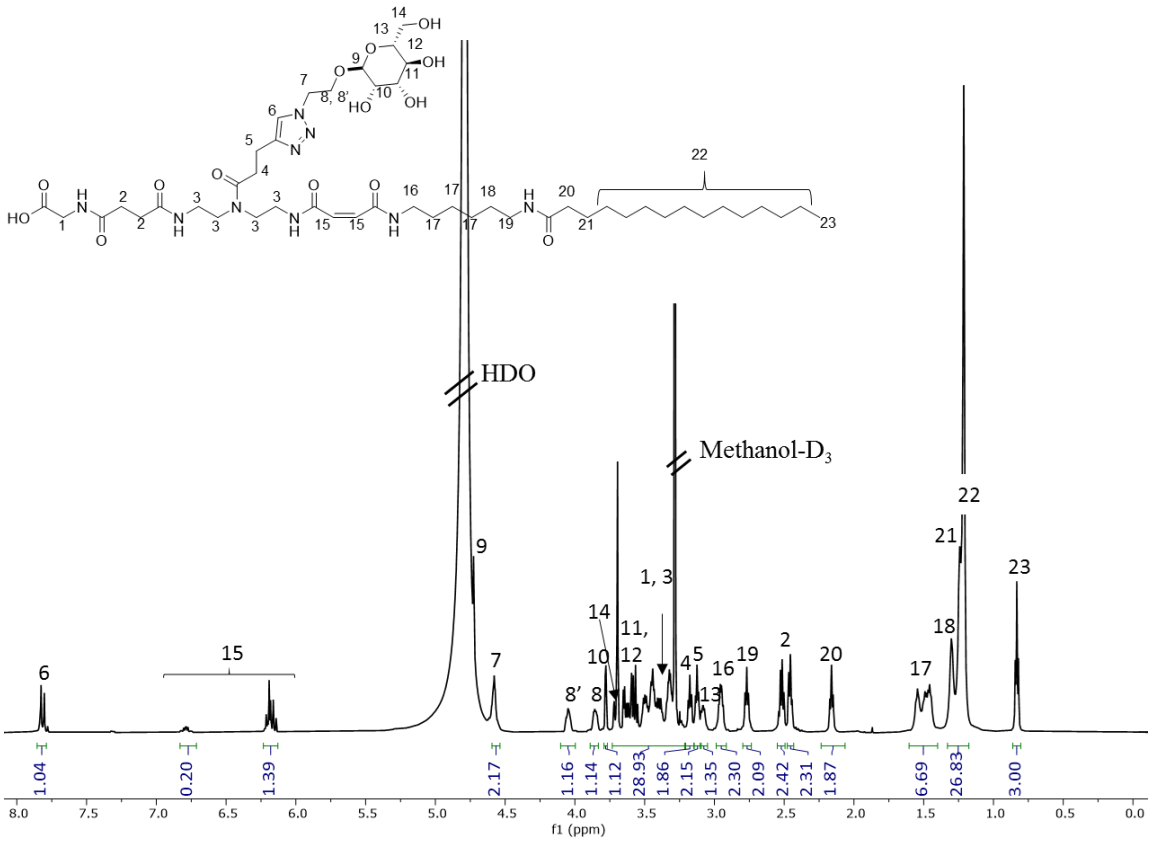

*Figure 58. ^{1}H-NMR spectrum APG **3** recorded in D_2O/CD_3OD mixture. The individual protons are assigned by number.*

^{1}H NMR (600 MHz, Deuterium Oxide, CD_3OD) δ 7.95 – 7.66 (m, 7), 6.8 – 6.13 (m, 15), 4.75 – 4.65 (m, 9), 4.61 – 4.53 (m, 7), 4.08 – 4.02 (m, 8'), 3.89 – 3.83 (m, 8), 3.80 – 3.76 (m, 10), 3.73 – 3.21 (m, 1, 3, 11, 12, 14), 3.18 (t, *J* = 7.1 Hz, 6), 3.12 (t, *J* = 6.8 Hz, 5), 3.10 – 3.05 (m, 1H, 13), 3.01 – 2.87 (m, 16), 2.77 (t, *J* = 7.4 Hz, 2H, 19), 2.58 – 2.39 (m, 2), 2.16 (t, *J* = 7.2 Hz, 20), 1.58 – 1.41 (m, 17), 1.34 – 1.17 (m, 18, 21, 22), 0.83 (t, *J* = 7.0 Hz, 23).

HR-ESI-MS for $C_{48}H_{83}N_9O_{14}$ (Exact monoisotopic mass 1009.6059): $[M+2H]^{2+}$ calcd. 505.8103, found 505.8101, mass accuracy 0.3 ppm.

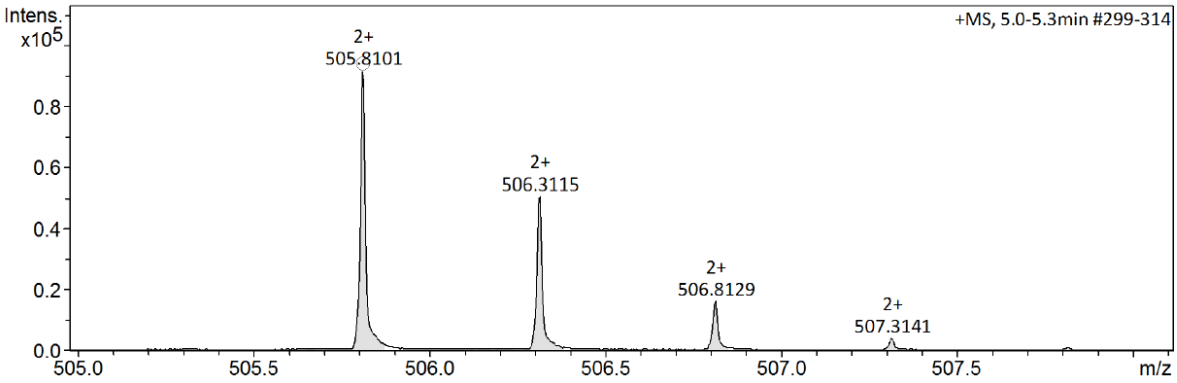

Figure 59. HR-ESI-MS of APG **3**, recorded in positive mode.

RP-HPLC (linear gradient from 0 - 100% eluent B in 30 min at 25 °C): t_r = 20.58. Determined relative purity: >90% (Peak at t_r=20.58 and 20.91 have the same mass (data not shown) and are probably isomers caused by the HDM building block).

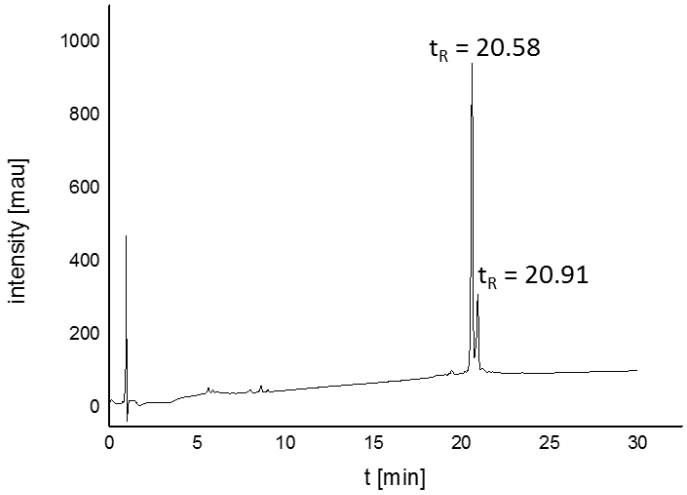

*Figure 60. RP-HPLC of APG **3** (linear gradient from 5-95% acetonitrile in water in 30 min at 25°C).*

APG **4**, Gly-TDS(Gal)-HDM-C12

The anomeric proton of Gal (9) could not be integrated in ^{1}HNMR due to the overlaying signal from the residual water signal. In order to suppress the baseline increase as much as possible a solvent mixture of D_2O and CD_3OD was used. Furthermore, the integral for the alkene moiety of the HDM building block is decreased. Potentially this is due to the acidic nature of the alkene protons and that the protons are exchanged with deuterium, thus decreasing the integral.

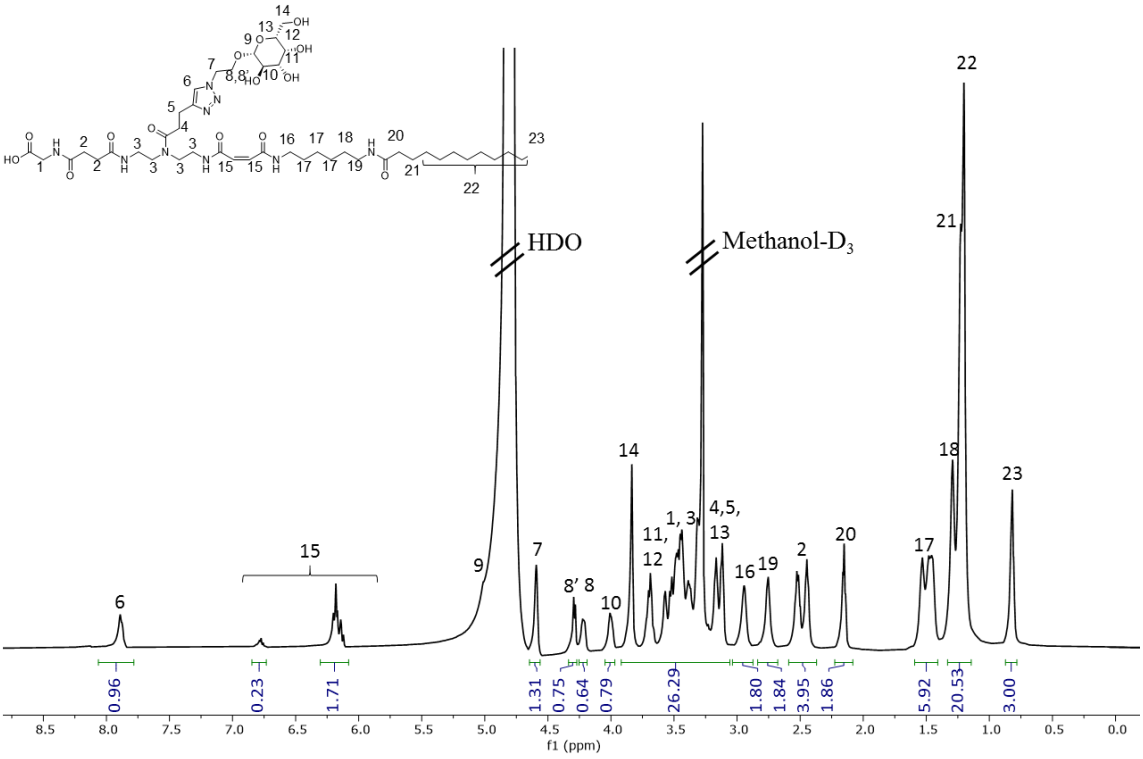

*Figure 61. ^{1}H-NMR spectrum APG **4** recorded in D_2O/CD_3OD mixture. The individual protons are assigned by number.*

^{1}H NMR (600 MHz, Deuterium Oxide, CD_3OD) δ 8.01 – 7.81 (m, 6), 6.86– 6.10 (m, 15), 4.65 – 4.55 (m, 7), 4.35 – 4.18 (m, 8', 8), 4.07 – 3.94 (m, 10), 3.90 – 3.07 (m, 1, 3, 4, 5, 11, 12, 13, 14), 3.03 – 2.87 (m, 16), 2.84 – 2.68 (m, 19), 2.59 – 2.37 (m, 2), 2.23 – 2.08 (m, 20), 1.59 – 1.41 (m, 17), 1.36 – 1.14 (m, 18, 21, 22), 0.82 (t, J = 6.9 Hz, 23).

HR-ESI-MS for $C_{45}H_{77}N_9O_{14}$ (Exact monoisotopic mass 967.5590): $[M+2H]^{2+}$ calcd. 484.7868, found 484.7872, mass accuracy -0.6 ppm.

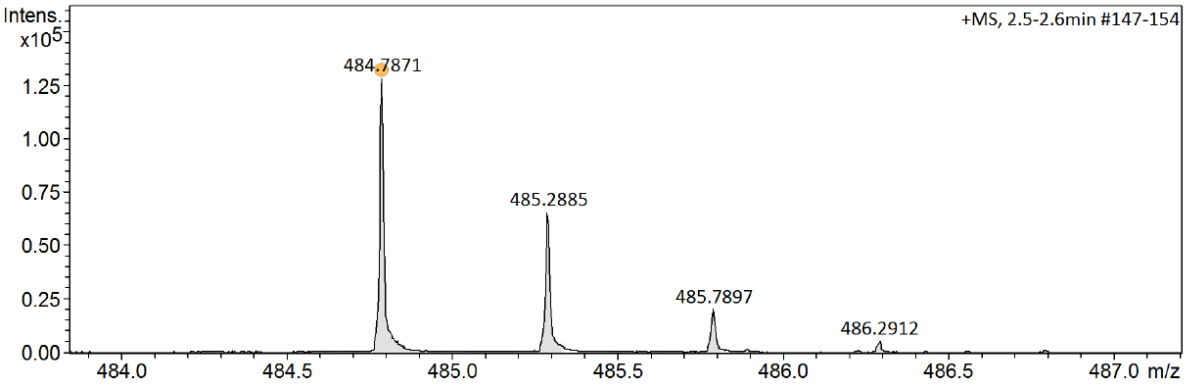

*Figure 62. HR-ESI-MS of APG **4**, recorded in positive mode.*

RP-HPLC (linear gradient from 0 - 100% eluent B in 30 min at 25 °C): t_R = 16.43 min. Determined relative purity: >90% (Peak at t_r=16.43 and 16.8 have the same mass (data not shown) and are probably isomers caused by the HDM building block).

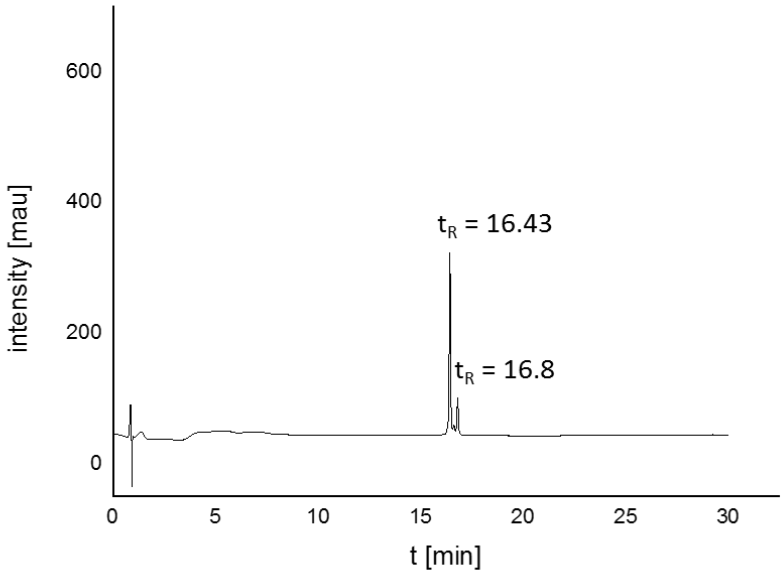

Figure 63. RP-HPLC of APG **4** (linear gradient from 5-95% acetonitrile in water in 30 min at 25°C).

APG **5**, TDS(Man)-HDM-C12

The anomeric proton of Man (9) could not be integrated in ^{1}HNMR due to the overlaying signal from the residual water signal. The same applies for signal 7. The integral for the multiplets between 4.03 – 3.30 is larger than expected, due to a baseline increase which is derived through the self-assembly nature of the material. In order to suppress the baseline increase as much as possible a solvent mixture of D_2O and CD_3OD was used. Furthermore, the integral for the alkene moiety of the HDM building block is decreased. Potentially this is due to the acidic nature of the alkene protons and that the protons are exchanged with deuterium, thus decreasing the integral.

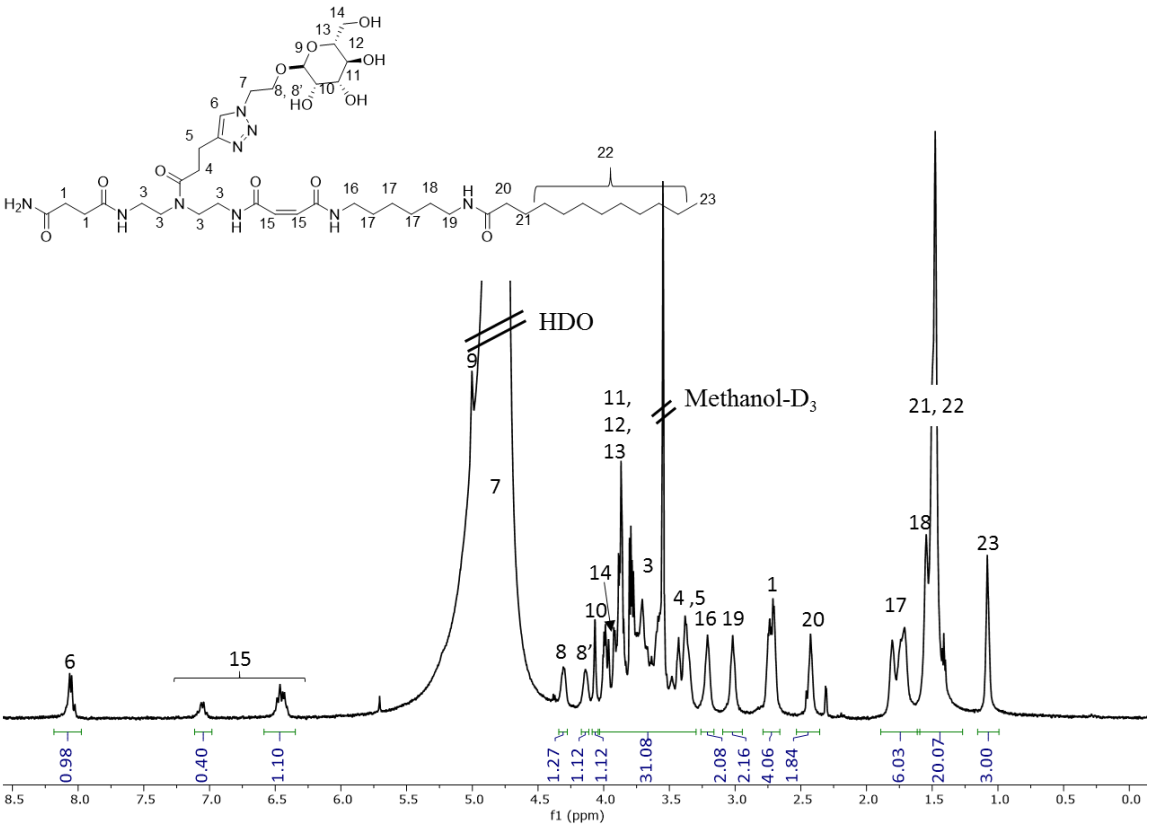

*Figure 64. ^{1}H-NMR spectrum APG **5** recorded in D_2O/CD_3OD mixture. The individual protons are assigned by number.*

^{1}H NMR (600 MHz, D_2O, CD_3OD) δ 8.12 – 8.00 (m, 6), 7.12 – 6.39 (m, 15), 4.37 – 4.28 (m, 1H, 8), 4.19 – 4.10 (m, 1H, 8'), 4.10 – 4.04 (m, 10), 4.03 – 3.3 (m, 3, 4, 5, 11, 12, 13, 14), 3.26 – 3.16 (m, 16), 3.07 – 2.95 (m, 19), 2.77 – 2.67 (m, 1), 2.51 – 2.38 (m, 20), 1.88 – 1.65 (m, 17), 1.60 – 1.33 (m, 18, 21, 22), 1.13 – 1.00 (m, 3H, 22).

HR-ESI-MS for $C_{43}H_{75}N_9O_{12}$ (Exact monoisotopic mass 909,5535): $[M+2H]^{2+}$ calcd. 455.7840, found 455.7845, mass accuracy -1.1 ppm.

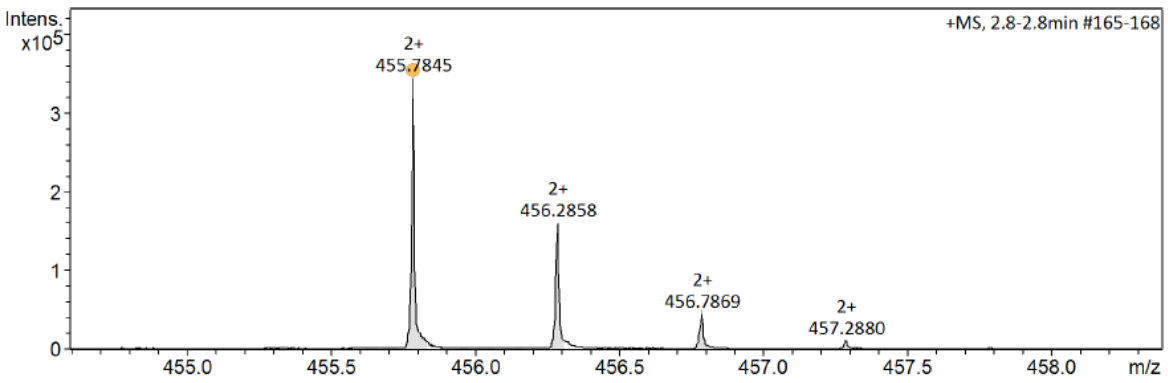

*Figure 65. HR-ESI-MS of APG **5**, recorded in positive mode.*

RP-HPLC (linear gradient from 0 - 100% eluent B in 30 min at 25 °C): t_r = 17.18. Determined relative purity: >90% (Peak at t_r=17.18 and 17.5 have the same mass (data not shown) and are probably isomers caused by the HDM building block).

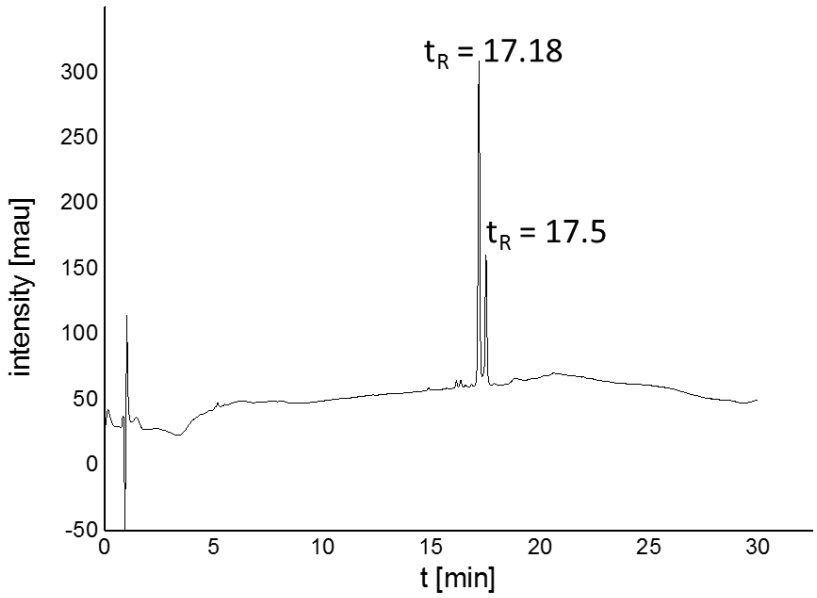

*Figure 66. RP-HPLC of APG **5** (linear gradient from 5-95% acetonitrile in water in 30 min at 25°C).*

APG **6**, Gly-TDS(Man)-HDS-C12

The anomeric proton of Man (9) could not be integrated in ^{1}HNMR due to the overlaying signal from the residual water signal. The integral for the multiplets between 3.97 – 3.32 is larger than expected, due to a baseline increase which is derived through the self-assembly nature of the material. In order to suppress the baseline increase as much as possible a solvent mixture of D_2O and CD_3OD was used.

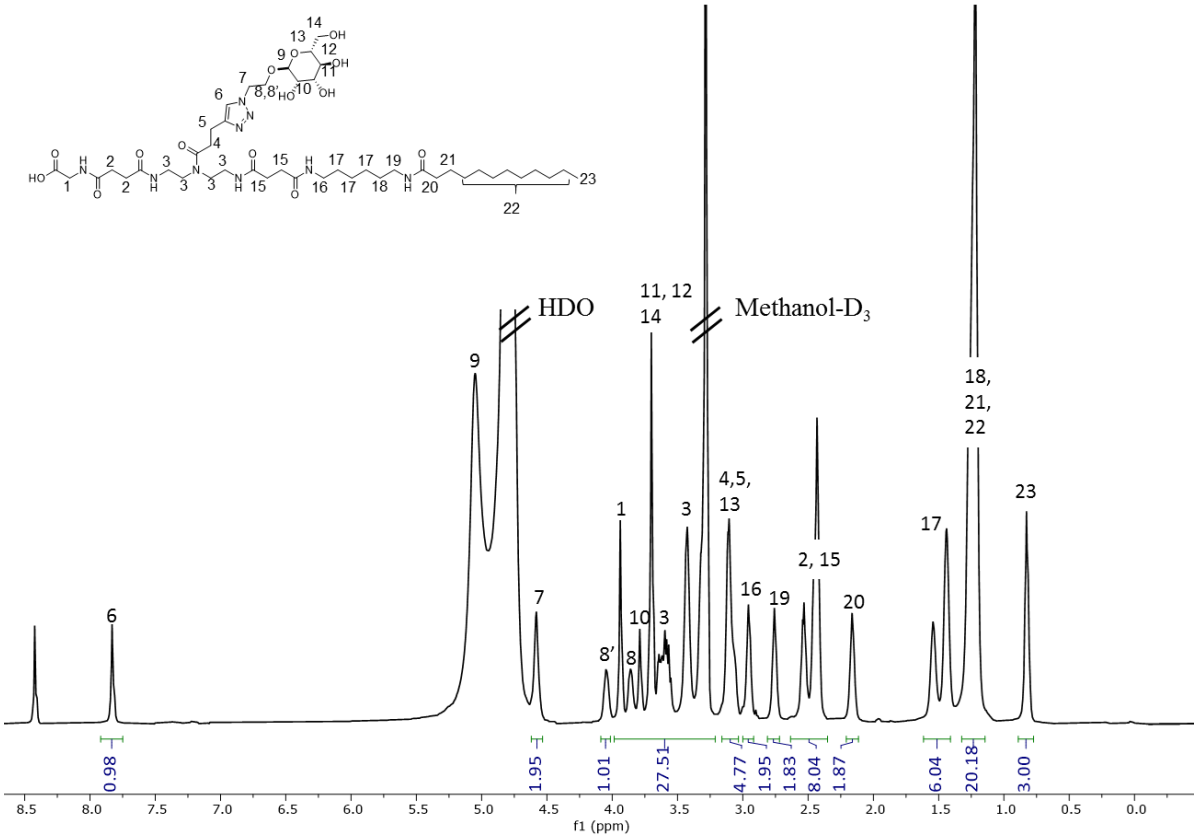

*Figure 67. ^{1}H-NMR spectrum APG **6** recorded in D_2O/CD_3OD mixture. The individual protons are assigned by number.*

^{1}H NMR (600 MHz, D_2O, CD_3OD) δ 7.86 – 7.80 (m, 6), 4.63 – 4.55 (m, 7), 4.08 – 4.01 (m, 8´), 3.97 – 3.32 (m, 1, 3, 10, 11, 12, 14), 3.15 – 3.04 (m, 4, 5, 13), 3.00 – 2.90 (m, 16), 2.83 – 2.66 (m, 19), 2.58 – 2.39 (m, 2, 15), 2.24 – 2.07 (m, 20), 1.61 – 1.37 (m, 17), 1.23 (m, 18, 21, 22), 0.89 – 0.75 (m, 23).

HR-ESI-MS for $C_{45}H_{79}N_9O_{14}$ (Exact monoisotopic mass 969,5746): $[M+2H]^{2+}$ calcd. 485.7946, found 485.7945, mass accuracy 0.1 ppm.

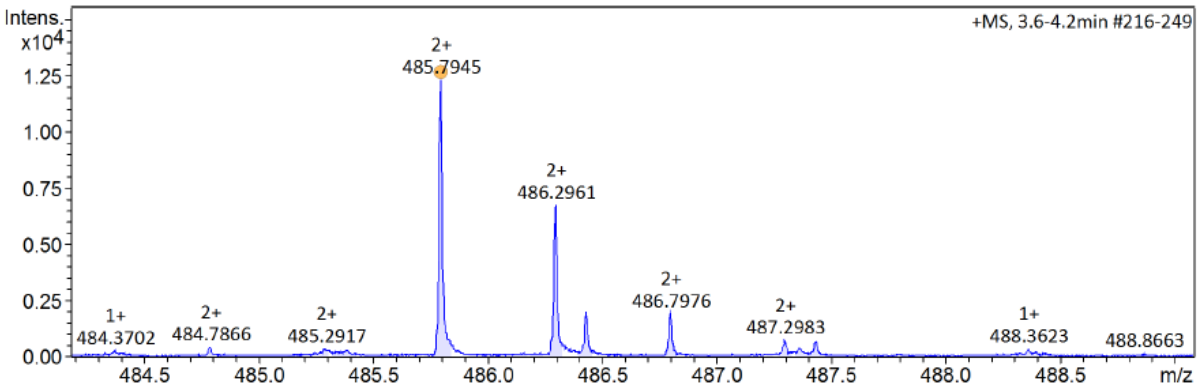

*Figure 68. HR-ESI-MS of APG **6** recorded in positive mode.*

RP-HPLC (linear gradient from 0 - 100% eluent B in 30 min at 25 °C): t_R = 16.75 min. Determined relative purity: >90%.

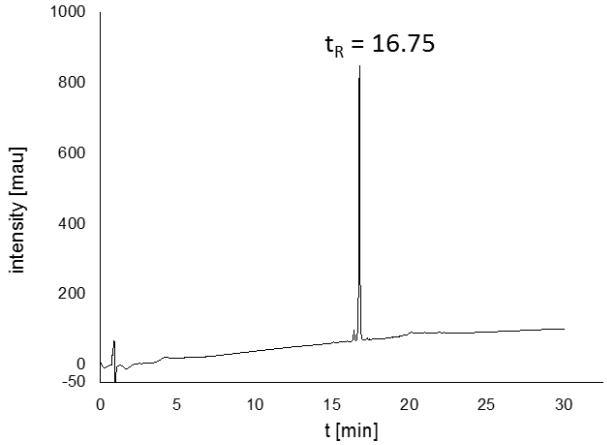

*Figure 69. -HPLC of APG **6** (linear gradient from 5-95% acetonitrile in water in 30 min at 25°C).*

APG **7,** TDS(Man)-C12

The anomeric proton of Man (9) could not be integrated in ^{1}HNMR due to the overlaying signal from the residual water signal. An unidentified signal was detected with a chemical shift of δ 5.42 (s) ppm. The integral for the multiple between 3.72 – 3.23 is larger than expected, due to a baseline increase which is derived through the self-assembly nature of the material and an overlap with the solvent signal. In order to suppress the baseline increase as much as possible a solvent mixture of D_2O and CD_3OD was used.

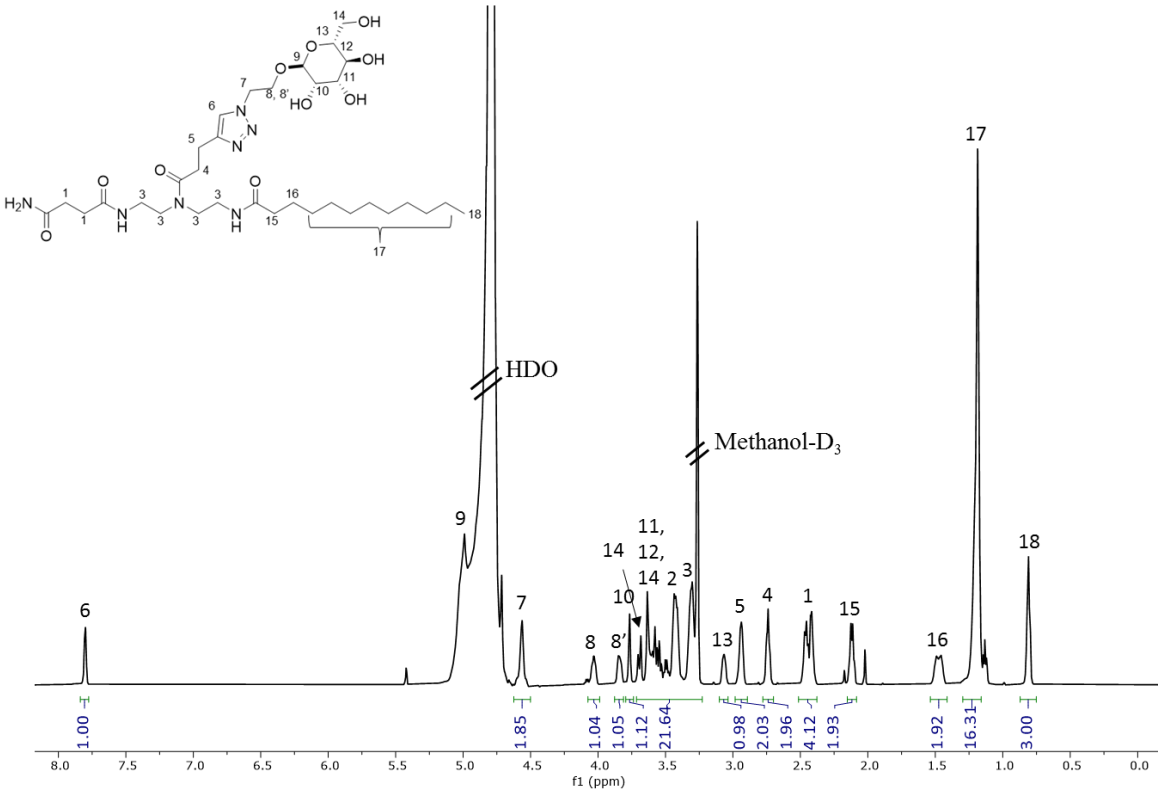

*Figure 70. ^{1}H-NMR spectrum APG **7** recorded in D_2O/CD_3OD mixture. The individual protons are assigned by number.*

^{1}H NMR (600 MHz, D_2O, CD_3OD) δ 7.83 – 7.78 (m, 6), 4.61 – 4.52 (m, 7), 4.08 – 4.00 (m, 8), 3.88 – 3.80 (m, 8'), 3.79 – 3.74 (m, 10), 3.72 – 3.23 (m, 2, 3, 10, 11, 12, 14), 3.09 – 3.05 (m, 13), 2.96 – 2.90 (m, 5), 2.74 (t, *J* = 7.4 Hz, 4), 2.51 – 2.33 (m, 1), 2.16 – 2.07 (m, 15), 1.56 – 1.41 (m, 16), 1.28 – 1.11 (m, 17), 0.87 – 0.75 (m, 18).

HR-ESI-MS for $C_{33}H_{59}N_7O_{10}$ (Exact monoisotopic mass 713.4323): $[M+H]^+$ calcd. 714.4396, found 714.4390, mass accuracy 0.8 ppm.

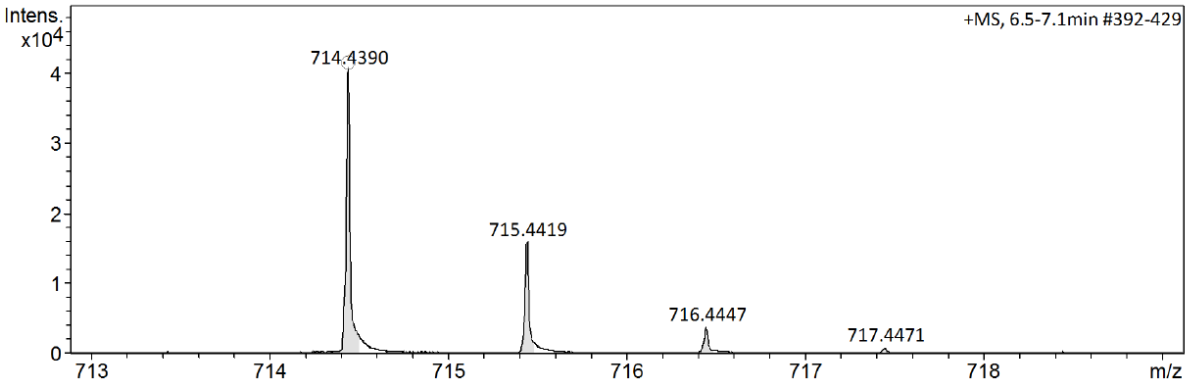

*Figure 71. HR-ESI-MS of APG **7**, recorded in positive mode.*

RP-HPLC (linear gradient from 0 - 100% eluent B in 30 min at 25 °C): tR = 15.71 min. Determined relative purity: >90%.

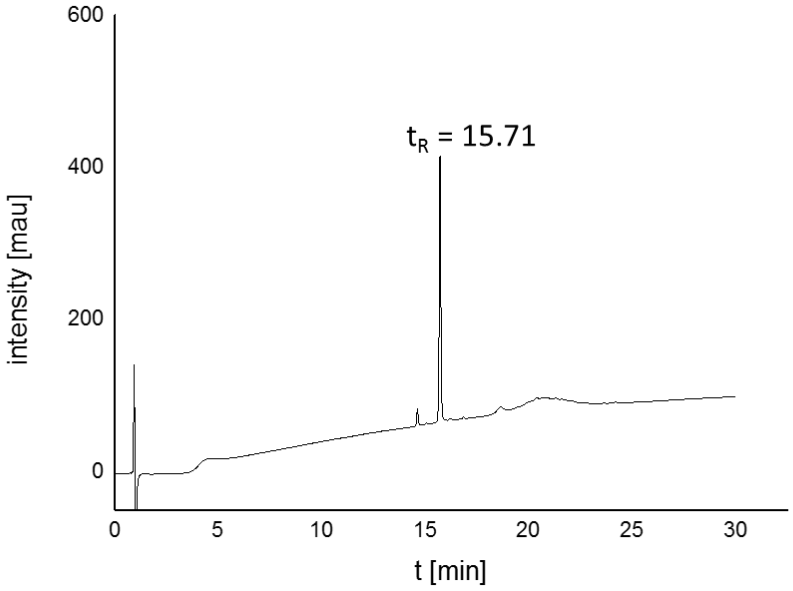

*Figure 72. RP-HPLC of APG **7** (linear gradient from 5-95% acetonitrile in water in 30 min at 25°C).*

APG **8**, Gly-BADS(Man)-HDM-C12

The anomeric proton of Man (8) could not be integrated in ^{1}HNMR due to the overlaying signal from the residual water signal. The integral for the multiple between 4.01 – 2.99 is larger than expected, due to a baseline increase which is derived through the self-assembly nature of the material. In order to suppress the baseline increase as much as possible a solvent mixture of D_2O and CD_3OD was used. Furthermore, the integral for the alkene moiety of the HDM building block is decreased. Potentially this is due to the acidic nature of the alkene protons and that the protons are exchanged with deuterium, thus decreasing the integral.

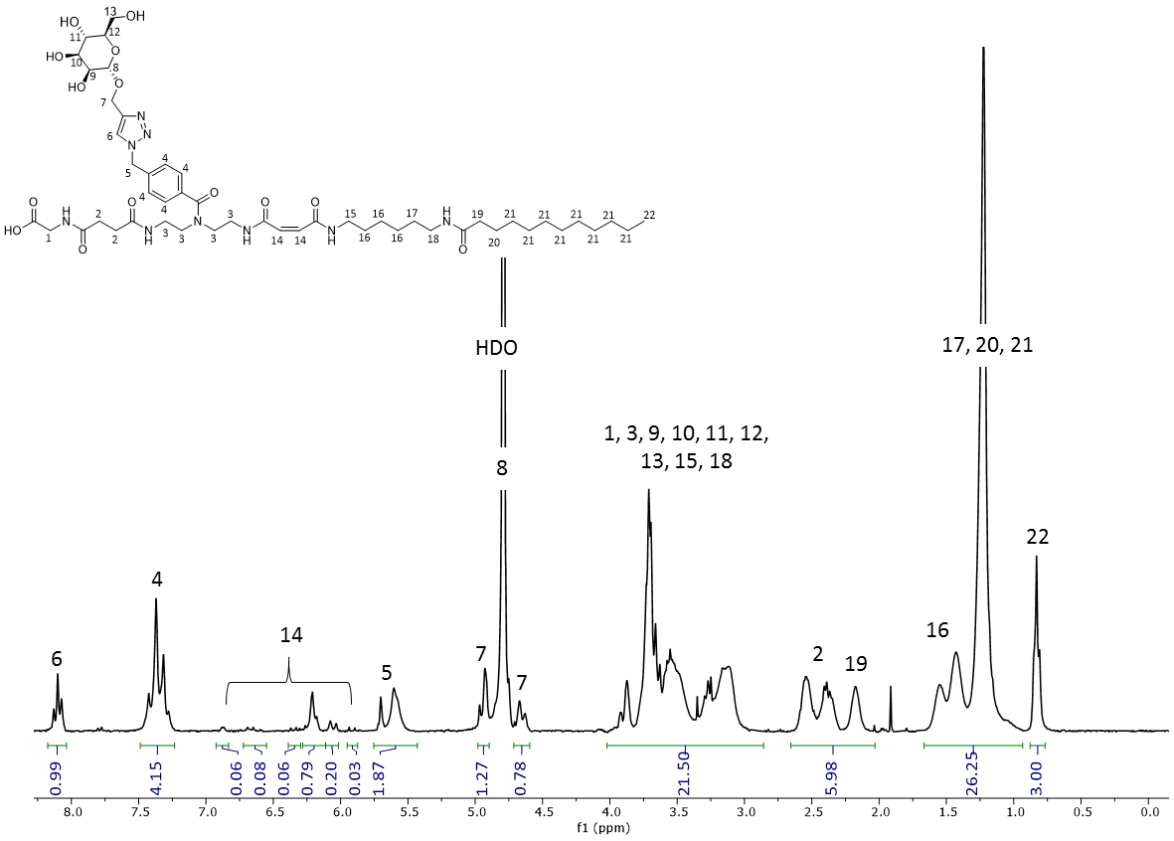

*Figure 73. ^{1}H-NMR spectrum APG **8** recorded in D_2O/CD_3OD mixture. The individual protons are assigned by number.*

^{1}H NMR (300 MHz, D_2O): δ (ppm) 8.17 – 8.03 (m, 6), 7.51 – 7.21 (m, 4), 6.89 – 5.85 (m, 14), 5.74 – 5.47 (m, 5), 4.99 – 4.89 (m, 7), 4.70 – 4.60 (m, 7), 4.01 – 2.99 (m, 1, 3, 9, 10, 11, 12, 13, 15, 18), 2.66 – 2.03 (m, 2, 20), 1.67 – 0.93 (m, 16, 17, 20, 21), 0.88 – 0.79 (m, 22).

HR-ESI-MS for $C_{49}H_{77}N_9O_{14}$. (Exact monoisotopic mass 1015,5590): $[M+2H]^{2+}$ calcd. 508.7868, found 508.7869, mass accuracy -0.2 ppm.

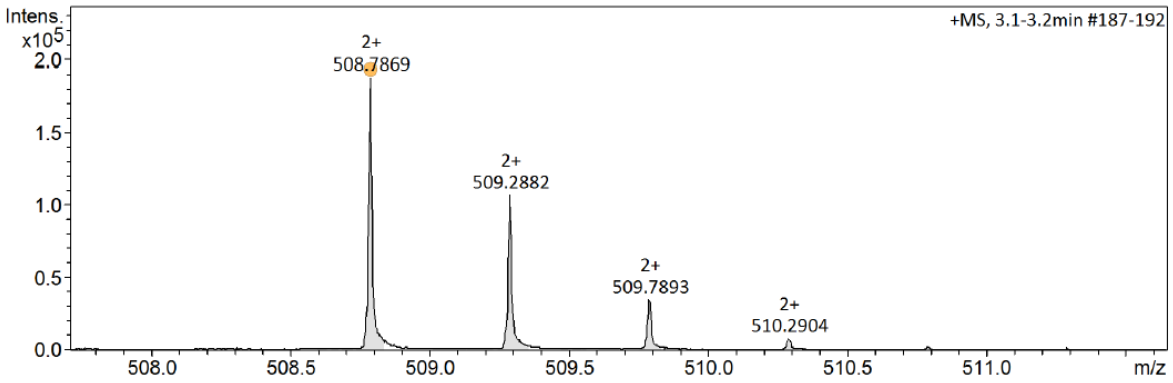

*Figure 74. HR-ESI-MS of APG **8**, recorded in positive mode.*

RP-HPLC (linear gradient from 0 - 100% eluent B in 30 min at 25 °C): t_r = 16.5. Determined relative purity: >90%.

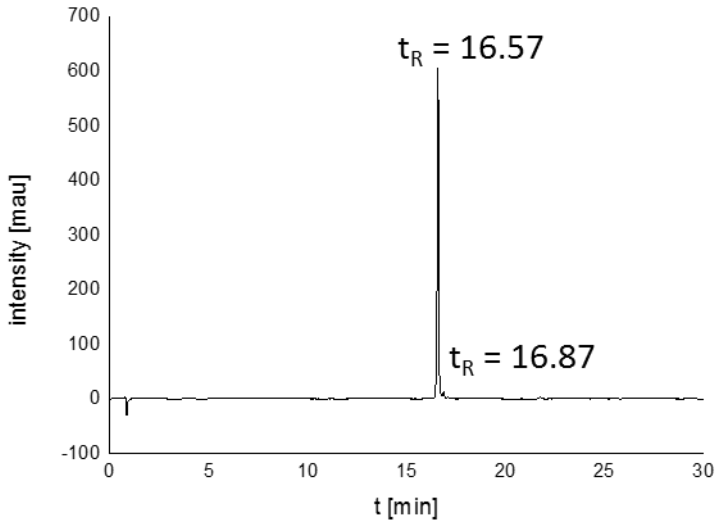

Figure 75. RP-HPLC of APG **8** (linear gradient from 5-95% acetonitrile in water in 30 min at 25°C).

5.3.3 Light scattering experiments

5.3.3.1 Dynamic light scattering

DLS measurements were performed in an angular range of 30 to 140° in 10°increments. At each angle three measurements were performed. All measurements were conducted at 25 °C. The concentration for the scattering experiments was 5 mM if not otherwise stated. Mean relaxation rates $\bar{\Gamma}$ were determined by applying the cumulant method. For the cumulant method the obtained autocorrelation functions were fitted using the equation derived by Frisken (see introduction).[225]

*Table 13. Mean relaxation rates, squared vector and standard deviations for the DLS experiment of APG **1**, Gly-TDS(Man)-HDM-C12*

Angle	q^2 [m^{-2}]	Mean relaxation rate $\bar{\Gamma}$ [s^{-1}]	Standard deviation [s^{-1}]
40	8.16×10^{13}	151	5
50	1.24×10^{14}	298	18
60	1.74×10^{14}	510	17
70	2.29×10^{14}	715	18
80	2.88×10^{14}	944	42
90	3.49×10^{14}	1244	18
100	4.09×10^{14}	1502	134
110	4.68×10^{14}	1722	25
120	5.23×10^{14}	2043	60
130	5.73×10^{14}	2211	42
140	6.16×10^{14}	2289	37

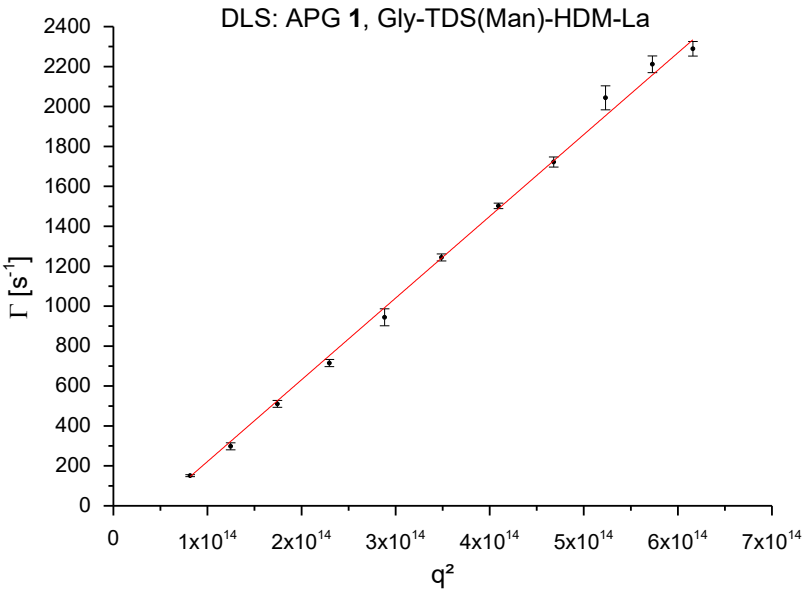

Figure 76. Linear fit of the plot from the relaxation rate against the squared scattering vector for APG **1**.

*Table 14. Mean relaxation rates, squared vector and standard deviations for the DLS experiment of APG **6**, Gly-TDS(Man)-HDS-C12*

Angle	q^2 [m^{-2}]	Mean relaxation rate $\bar{\Gamma}$ [s^{-1}]	Standard deviation [s^{-1}]
30	4.67×10^{13}	46	3
40	8.16×10^{13}	89	2
50	1.24×10^{14}	1645	17
60	1.74×10^{14}	248	10
70	2.29×10^{14}	371	16
80	2.88×10^{14}	477	13
90	3.49×10^{14}	605	245
100	4.09×10^{14}	697	3
110	4.68×10^{14}	812	15
120	5.23×10^{14}	919	19
130	5.73×10^{14}	1003	2
140	6.16×10^{14}	1051	4

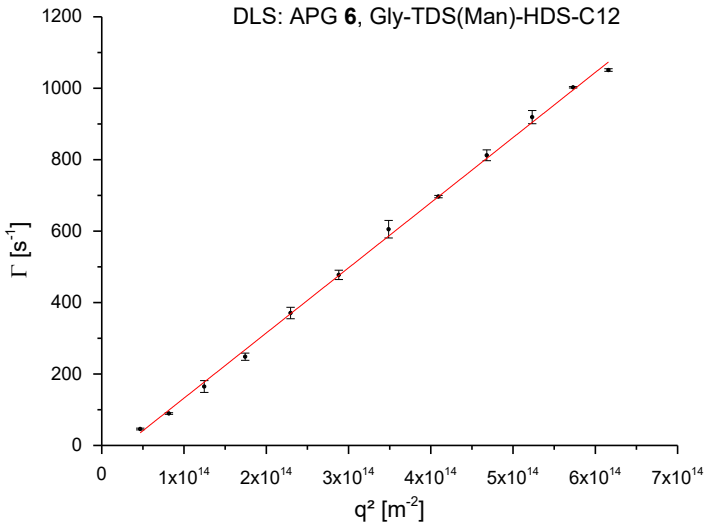

Figure 77. Linear fit of the plot from the relaxation rate against the squared scattering vector for APG **6.**

*Table 15. Mean relaxation rates, squared vector and standard deviations for the DLS experiment of APG **7**, TDS(Man)-C12.*

Angle	q^2 [m^{-2}]	Mean relaxation rate $\bar{\Gamma}$ [s^{-1}]	Standard deviation [s^{-1}]
30	4.67×10^{13}	49	5
40	8.16×10^{13}	115	11
50	1.24×10^{14}	203	19
60	1.74×10^{14}	337	28
70	2.29×10^{14}	558	9
80	2.88×10^{14}	644	18
90	3.49×10^{14}	898	43
100	4.09×10^{14}	1056	20
110	4.68×10^{14}	1194	84
120	5.23×10^{14}	1341	9
130	5.73×10^{14}	1432	43

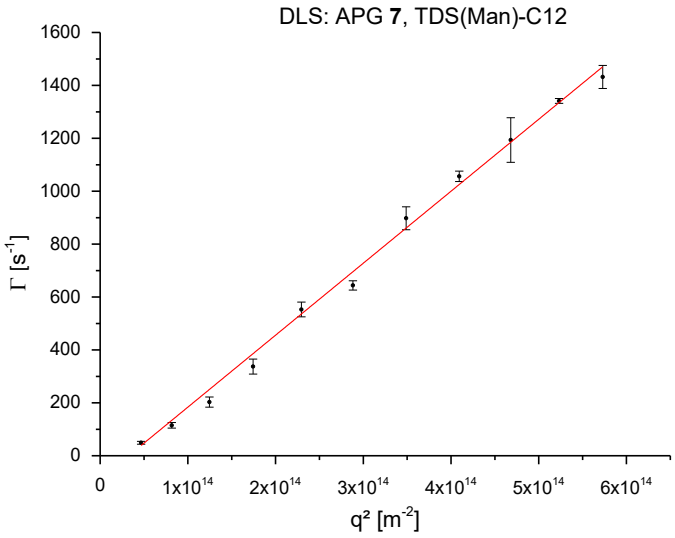

Figure 78. Linear fit of the plot from the relaxation rate against the squared scattering vector for APG **7.**

For APG **8** a concentration of 2.5 mM was used.

*Table 16. Mean relaxation rates, squared vector and standard deviations for the DLS experiment of APG **8**, Gly-BADS(Man)-HDM-C12.*

Angle	q^2 [m^{-2}]	Mean relaxation rate $\bar{\Gamma}$ [s^{-1}]	Standard deviation [s^{-1}]
40	8.16×10^{13}	186	3
50	1.24×10^{14}	286	5
60	1.74×10^{14}	432	3
70	2.29×10^{14}	589	12
80	2.88×10^{14}	789	5
90	3.49×10^{14}	969	6
100	4.09×10^{14}	1153	15
110	4.68×10^{14}	1336	19
120	5.23×10^{14}	1499	3
130	5.73×10^{14}	1615	15
140	6.16×10^{14}	1737	32

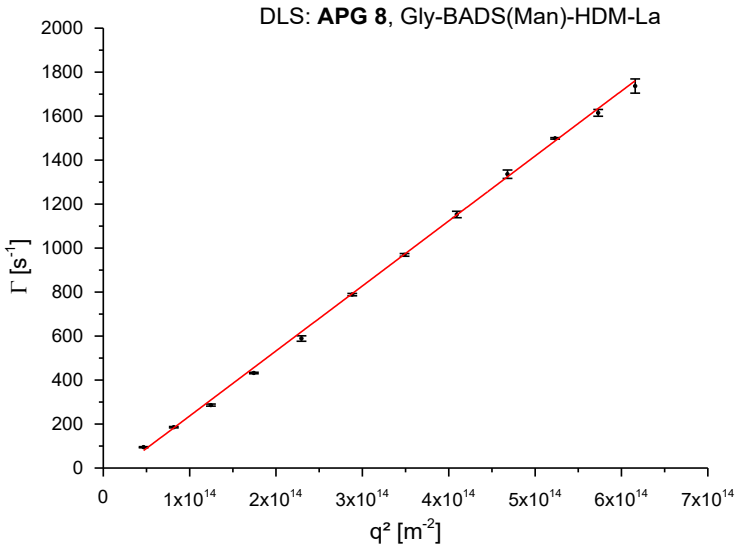

Figure 79. Linear fit of the plot from the relaxation rate against the squared scattering vector for APG **8.**

5.3.3.2 Dynamic depolarized light scattering

DDLS measurements were performed under the exact same conditions as mentioned before for DLS, except for the polarizer position in front of the detector, that was changed to crossed polarized (90°) conditions. The data obtained was processed as the DLS data and the obtained mean relaxation rates were again plotted against the square of q and the translational diffusion coefficients were obtained in the same manner as for DLS using the slopes of the respective linear fits to the data. While with the DLS data only the translational diffusion coefficient D_t could be determined, with the DDLS data the rotational diffusion coefficient D_r could be determined[79].

$$\bar{\Gamma} = D_t * q^2 + 6D_r \tag{5}$$

$$D_r = rotational\ diffusicon\ coefficient$$

Thus the intercept of the linear fit gives access to D_R. With the values for D_R and D_T at hand, the next step was the estimation of the dimensions of the micelles. Expecting cylindrical micelles, a theoretical approach from Garcia De la Torre *et al.* was followed in order to calculate the length and the radius of the micelles.[80, 81, 226] Garcia De la Torre *et al.* defined two functions of the axial ratio, which are shown in equation 10 and 11.

$$f(p) = \left(\frac{9 * \pi * \eta}{k * T}\right)^{\frac{2}{3}} * \frac{D_T}{(D_{R)})^{\frac{1}{3}}} \tag{10}$$

$$f(p) = \frac{\ln p + v}{(\ln p + \delta)^{\frac{1}{3}}} \tag{11}$$

$$with\ \eta = viscosity\ of\ the\ solvent, p = aspect\ ratio\ and$$
$$v\ and\ \delta = end - effect\ corrections\ depending\ on\ p$$

After f(p) was determined, the next step was the calculation of the axial ratio p (see Equation 12).

$$p = \frac{L}{2r} \tag{12}$$

$$with\ p = axial\ ratio, L = lenght\ and\ r = radius$$

Therefore, the numerical results for ν and δ, which have been calculated and regressed by Garcia De la Torre *et al.*, were used (see equation 13 and 14).[81, 226]

$$\upsilon = 0.312 + 0.565 * p^{-1} - 0.1 * p^{-2} \quad (13)$$

$$\delta = -0.662 + 0.917 * p^{-1} - 0.05 * p^{-2} \quad (14)$$

Equation 13 and 14 were inserted into equation 11 and the resulting final function was plotted as shown in Figure 80.

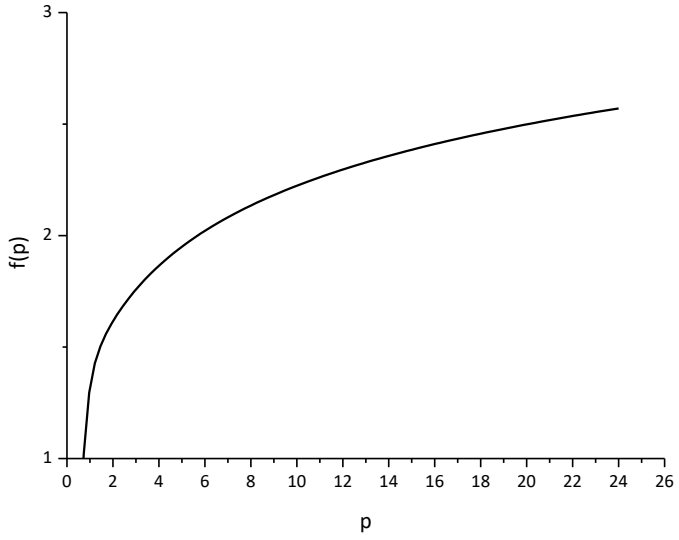

Figure 80. Plot of f(p) against the axial ratio p.

Using this plot p could be estimated. Using p and one of the equations 15 and 16, the length of the cylindrical micelles was calculated.[80]

$$L = \frac{(\ln p + 0.312 + 0.565 * p^{-1} - 0.1 * p^{-2}) * k * T}{3 * \pi * \eta * D_T} \quad (15)$$

$$L = \sqrt[3]{\frac{(\ln p - 0.662 + 0.917 * p^{-1} - 0.05 * p^{-2}) * k * T * 3}{\pi * \eta * D_R}} \quad (16)$$

$$with\ L = length\ of\ the\ rod$$

In the last step the radius of the rod was determined by using the axial ratio, which is given in equation 12.

*Table 17. Mean relaxation rates, squared vector and standard deviations for the DDLS experiment of APG **6**, Gly-TDS(Man)-HDS-C12.*

Angle	q^2 [m^{-2}]	Mean relaxation rate $\bar{\Gamma}$ [s^{-1}]	Standard deviation [s^{-1}]
30	4.67×10^{13}	143	28
40	8.16×10^{13}	215	2
50	1.24×10^{14}	269	15
60	1.74×10^{14}	341	7
70	2.29×10^{14}	376	8
80	2.88×10^{14}	470	24
90	3.49×10^{14}	534	8
100	4.09×10^{14}	705	7
110	4.68×10^{14}	733	3
120	5.23×10^{14}	827	22
130	5.73×10^{14}	872	21
140	6.16×10^{14}	884	32

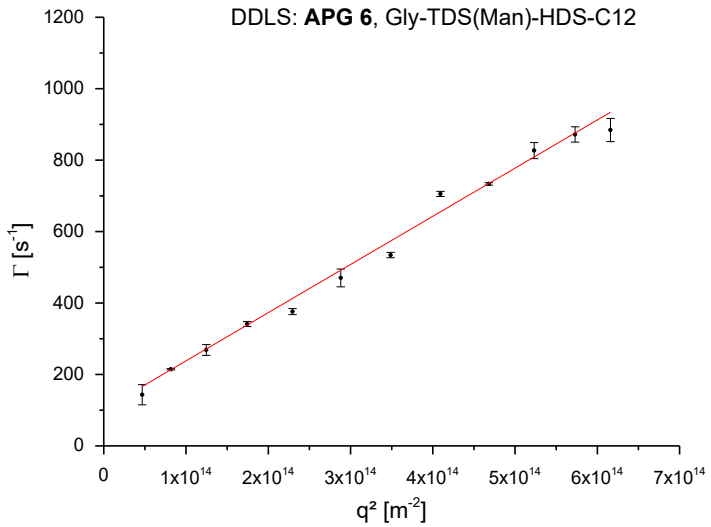

*Figure 81. Linear fit of the plot from the relaxation rate against the squared scattering vector for APG **6**.*

*Table 18. Mean relaxation rates, squared vector and standard deviations for the DDLS experiment of APG **8**, Gly-BADS(Man)-HDM-C12.*

Angle	q^2 [m^{-2}]	Mean relaxation rate $\bar{\Gamma}$ [s^{-1}]	Standard deviation [s^{-1}]
30	4.67×10^{13}	536	5
40	8.16×10^{13}	728	15
50	1.24×10^{14}	858	9
60	1.74×10^{14}	1027	46
70	2.29×10^{14}	1149	167
80	2.88×10^{14}	1238	42
90	3.49×10^{14}	1393	20
100	4.09×10^{14}	1476	49
110	4.68×10^{14}	1676	50
120	5.23×10^{14}	1691	46
130	5.73×10^{14}	1802	53
140	6.16×10^{14}	1806	32

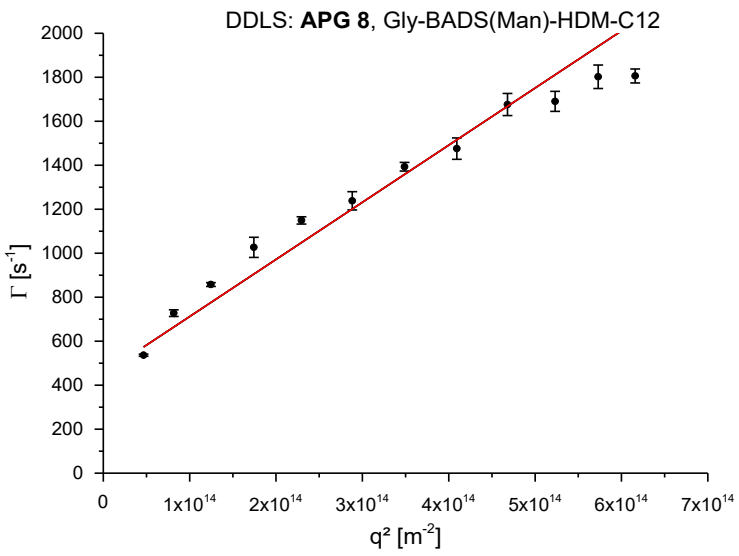

Figure 82. Linear fit of the plot from the relaxation rate against the squared scattering vector for APG **8.**

*Table 19. Overview of the calculated values from the DLS and DDLS experiments for APG **6** and APG **8**.*

Structure	D_T [m^2s^{-1}]	R_H [nm]	D_r [s^{-1}]	L [nm]	r [nm]
APG 6	$1.59x10^{-12}$	160.5	15.5	888	56
APG 8	$2.78x10^{-12}$	88.3	75.4	460	24

For TDS(Man)-C12 no signal could be detected in the depolarized setup, which indicates that isotropic (spherical) aggregates are formed.

For GLY-TDS(MAN)-HDM-C12 a signal was detected but the data could not be fitted, which indicates a high polydispersity.

5.3.4 Fluorescence spectroscopy

5.3.4.1 CMC determination with pyrene

For the fluorescence experiments a concentration series of the oligomers was prepared with a pyrene concentration of $2x10^{-6}$ mol/L in each sample. For that an acetone stock solution of pyrene was prepared with a concentration of $1.24x10^{-4}$ mol/L. In each vial 32.36 µl was pipetted and the acetone was allowed to evaporate. Then stock solutions of the oligomers were prepared and pipetted to the vials. Resulting in a concentration series with a constant pyrene concentration of $2x10^{-6}$ mol/l. The series was measured with a FLS980 Fluorometer from Edinburgh Instruments using following experimental conditions. Each sample was excited at 320 nm with a slit width of 5 mm and the fluorescence signal was collected between 350 and 450 nm in 0.4 nm steps. Every measurement was repeated 10 times to minimize errors.

*Table 20. Results of the fluorescence pyrene probe experiment for APG **8**, Gly-BADS(Man)-HDM-C12.*

Concentration APG 8 [mmol/l]	I_1 at 372.5 nm	I_3 at 383 nm	I_3/I_1
0	8.58×10^{11}	4.44×10^{11}	0.52
0.10037	1.24×10^{12}	6.44×10^{11}	0.52
0.15056	1.12×10^{12}	6.17×10^{11}	0.55
0.20075	1.30×10^{12}	7.53×10^{11}	0.58
0.25093	1.08×10^{12}	6.33×10^{11}	0.59
0.30112	1.06×10^{12}	6.24×10^{11}	0.59
0.50187	1.12×10^{12}	7.46×10^{11}	0.67
0.7528	7.74×10^{11}	5.52×10^{11}	0.71
1.00374	8.93×10^{11}	6.92×10^{11}	0.78

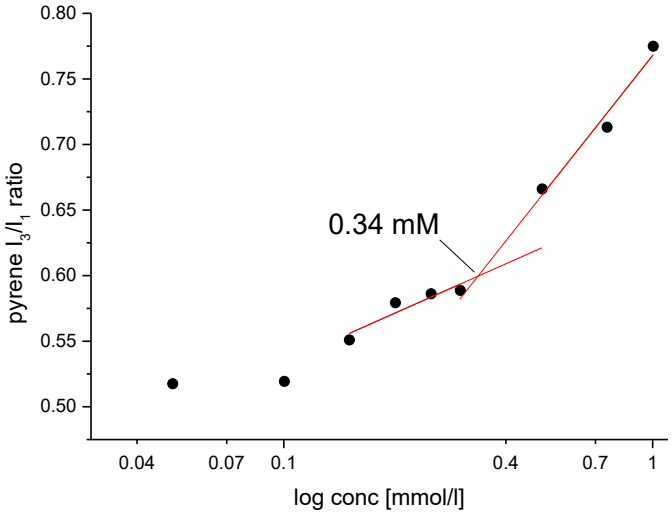

Figure 83. Pyrene I_3/I_1 ratio plotted against the logarithmic concentration of APG **8**.

*Table 21. Results of the fluorescence pyrene probe experiment for APG **1**, Gly-TDS(Man)-HDM-C12.*

Concentration APG 1 [mmol/l]	I_1 at 372.5 nm	I_3 at 383 nm	I_3/I_1
0	$1.52x10^{12}$	$8.2x10^{11}$	0.54
0.28	$4.84x10^{12}$	$2.6x10^{12}$	0.54
0.31	$3.6x10^{12}$	$1.93x10^{12}$	0.54
0.34	$5.13x10^{12}$	$2.76x10^{12}$	0.54
0.52	$4.22x10^{12}$	$2.27x10^{12}$	0.54
0.69	$1.66x10^{12}$	$9.66x10^{11}$	0.58
0.86	$2.63x10^{12}$	$1.48x10^{12}$	0.56
1.03	$2.25x10^{12}$	$1.27x10^{12}$	0.56
1.72	$2.16x10^{12}$	$1.57x10^{12}$	0.73
3.45	$7.45x10^{11}$	$5.42x10^{11}$	0.73

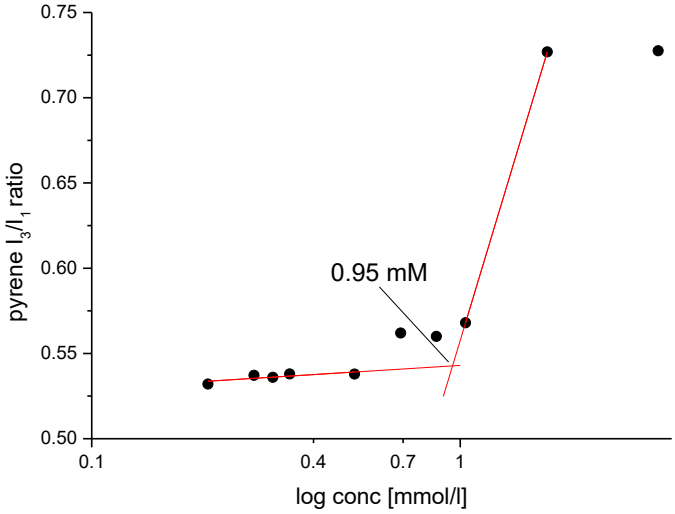

Figure 84. Pyrene I_3/I_1 ratio plotted against the logarithmic concentration of APG **1**.

*Table 22. Results of the fluorescence pyrene probe experiment for APG **4**, Gly-TDS(Gal)-HDM-C12.*

Concentration APG 4 [mol/l]	I_1 at 372.5 nm	I_3 at 383 nm	I_3/I_1
0.16	33716	18614	0.55
0.19	31432	18079	0.58
0.28	36492	21357	0.59
0.31	42307	24568	0.58
0.47	37357	22485	0.60
0.62	28899	18575	0.64
0.78	35314	22565	0.64
1.55	18835	16461	0.87
3.1	16624	14054	0.85

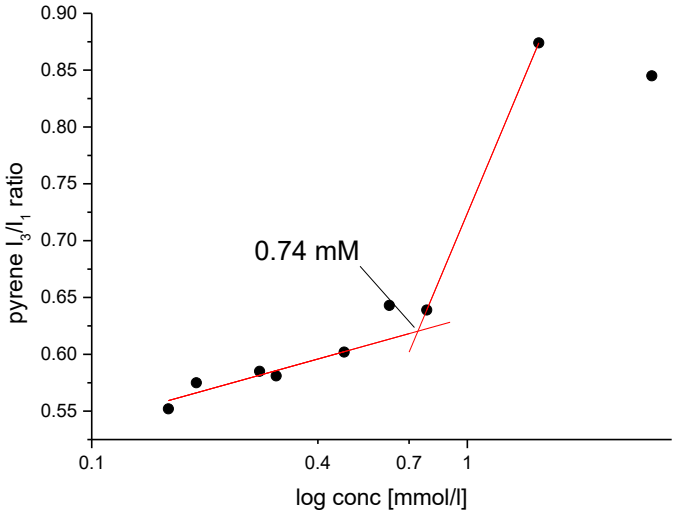

Figure 85. Pyrene I_3/I_1 ratio plotted against the logarithmic concentration of APG **4**.

5.3.4.1.1 Fluorescence overlap of APGs and pyrene

As stated in the article the fluorescence emission of pyrene and the oligomers overlap and requires background corrections. Here are we provide additional information on this matter and show one exemplary background correction.

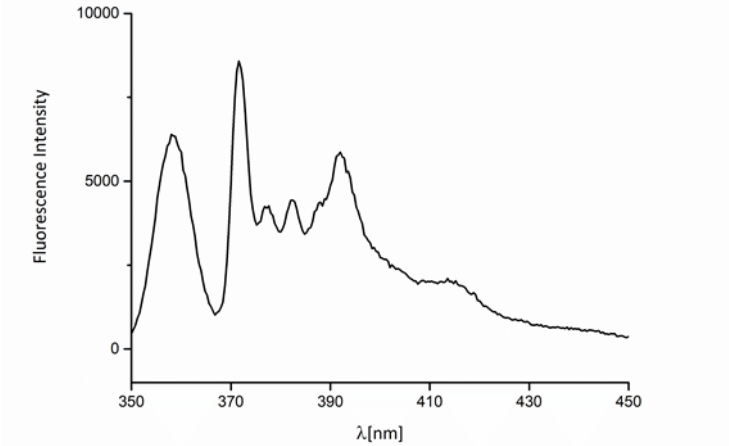

Figure 86. Pyrene fluorescence emission spectrum (ex. 320 nm).

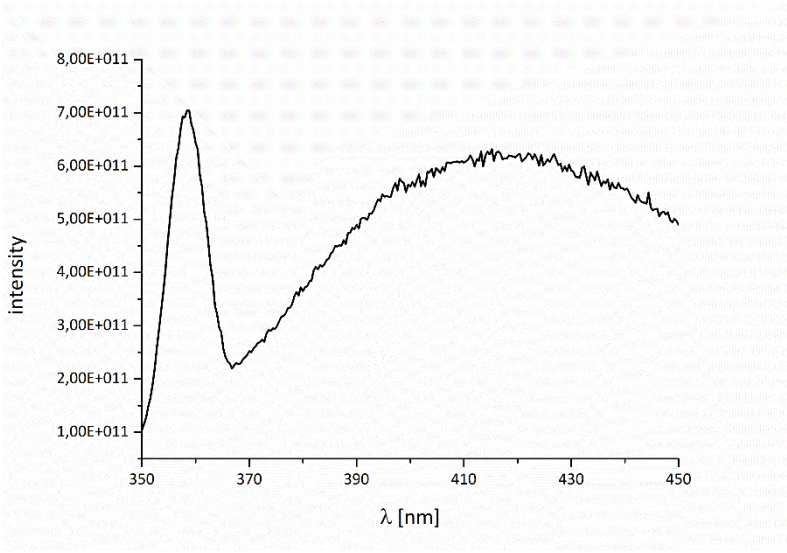

Figure 87. APG **8** fluorescence emission spectrum (ex. 320 nm).

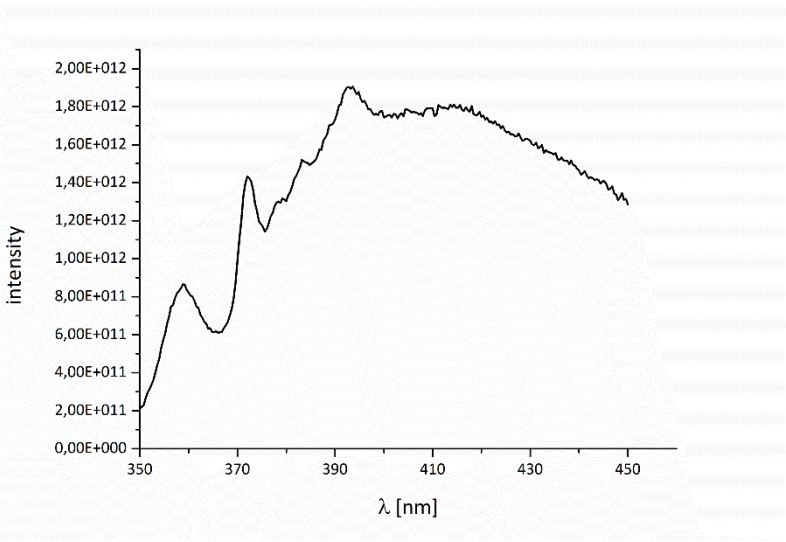

Figure 88. Combined APG **8** and pyrene fluorescence emission spectrum.

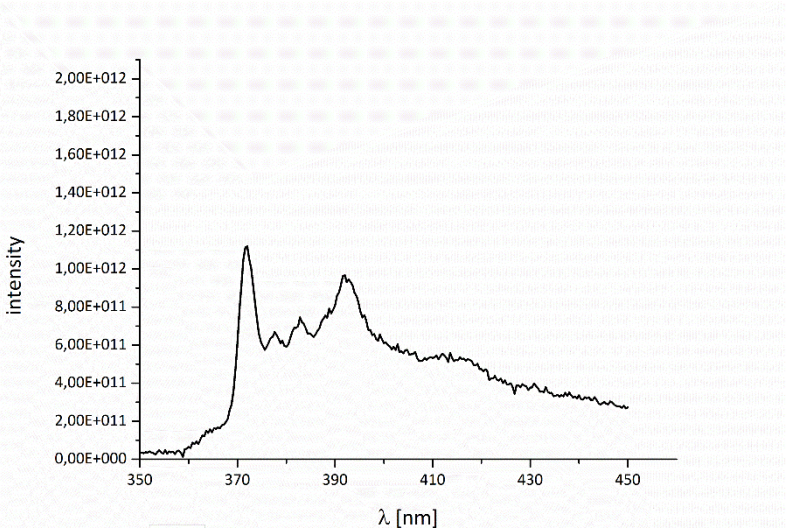

*Figure 89. Fluorescence spectrum corrected against APG **8** emission*

5.3.4.2 CMC determination with Nile red

To avoid extensive background corrections, we switched to the Nile red method. Nile red is not only highly solvatochromic but also excited at 550 nm. At this excitation wavelength the emission of the APGs is close to zero.

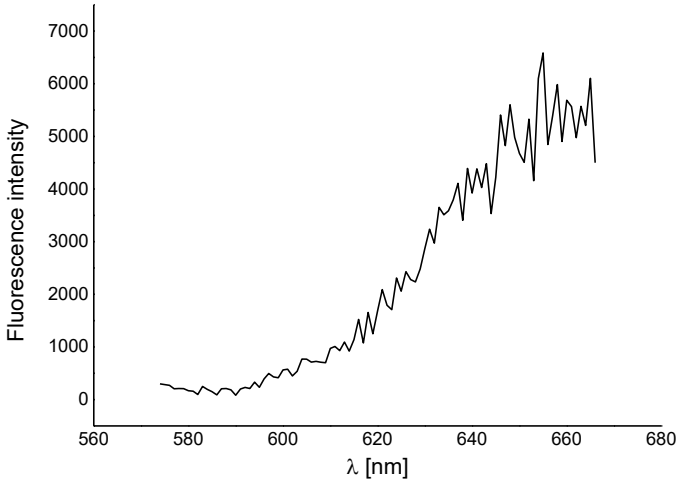

Figure 90. Fluorescence emission spectrum of Nile red in water (ex. 550 nm).

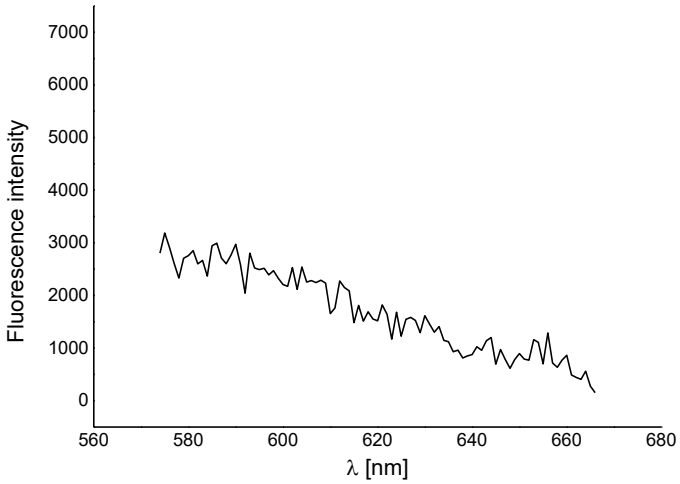

Figure 91. Fluorescence emission spectrum of APG 8 in water (ex. 550 nm).

For the fluorescence experiments a concentration series of the oligomers was prepared with a Nile red concentration of $1x10^{-6}$ mol/L in each sample. For that a dioxane stock solution of Nile red was prepared with a concentration of 0.129 mg/ml. Then in a glass tube 50 µl of the stock solution was pipetted into 10 ml of ultrapure water. A concentration series was prepared with a total volume of 100 µl in well plates. The series was measured with a

Clariostar plate reader reader from BMG Labtech. Each sample was excited at λ_{ex} = 550 nm and data was collected at 635 nm. The measurements were performed in triplicates.

*Table 23. CMC with Nile red of APG **2**, GLY-TDS(MAN)-HDM-C10 CMC.*

Concentration [mM]	Ø Counts @635 nm	Standard deviation
0.5	18323	2736
1	20687	1066
2	21483	2497
4	47618	1954
6	95131	7929
8	147263	12496
10	185969	6554

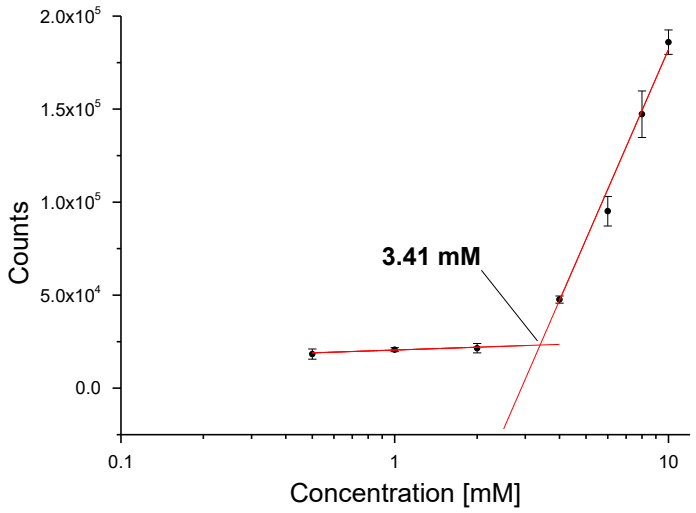

*Figure 92. Counts plotted against the logarithmic concentration of APG **2**.*

*Table 24. CMC with Nile red of APG **1**, GLY-TDS(MAN)-HDM-C12.*

Concentration [mM]	Ø Counts @635 nm	Standard deviation
0	1753	491
0.1	2999	138
0.15	3290	291
0.25	5339	67
0.5	9869	12
0.75	18303	531
1	25358	1493
1.5	39092	487
2	52740	347
3	68528	218
4	72443	180

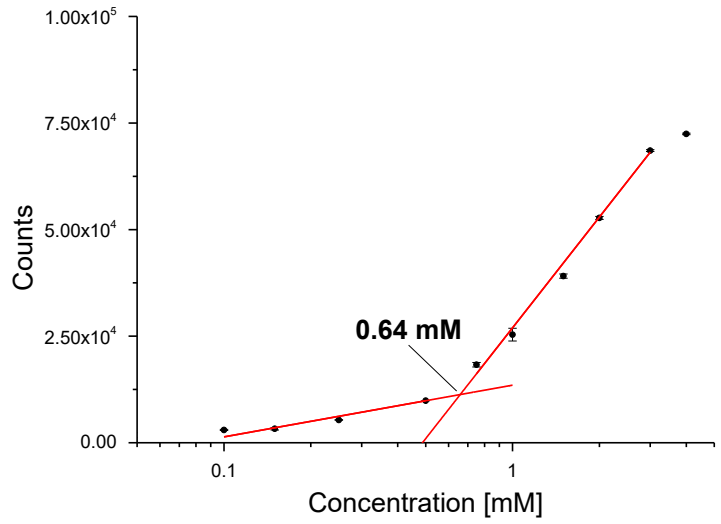

Figure 93. Counts plotted against the logarithmic concentration of APG **1**.

*Table 25. CMC with Nile red of APG **3**, GLY-TDS(MAN)-HDM-C15.*

Concentration [mM]	Ø Counts @635 nm	Standard deviation
0	3407	578
0.02	4230	125
0.04	5933	1.5
0.06	7373	409
0.08	8923	714
0.1	12809	472
0.15	15966	3108
0.25	47026	1311
0.5	135363	12758
0.75	185388	8189
1	197668	11227
1.5	208685	605
2	226966	5175
3	229697	424
4	235331	343

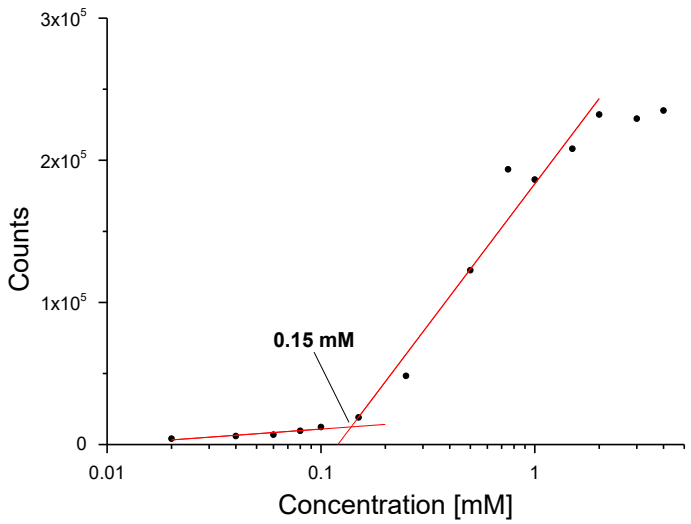

*Figure 94. Counts plotted against the logarithmic concentration of APG **3***

*Table 26. CMC with Nile red of APG **4**, GLY-TDS(Gal)-HDM-C12.*

Concentration [mM]	Ø Counts @635 nm	Standard deviation
0	1160	23
0.1	2383	63
0.15	2268	111
0.25	3093	49
0.5	5077	69
0.75	9882	17
1	12691	73
1.5	21462	5
2	29667	149
3	45193	1379

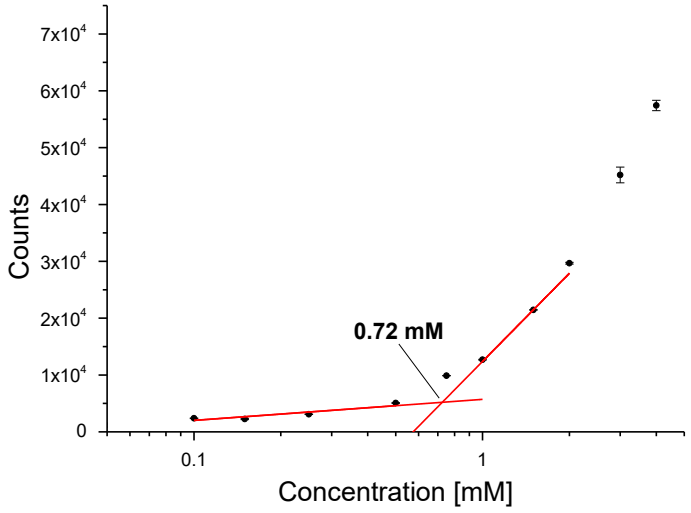

Figure 95. Counts plotted against the logarithmic concentration of APG **4**.

*Table 27. CMC with Nile red of APG **6**, Gly-TDS(Man)-HDS-C12.*

Concentration [mM]	Ø Counts @635 nm	Standard deviation
0.1	5514	272
0.15	5422	201
0.25	6346	512
0.5	8667	143
0.75	10312	73
1	14580	199
1.5	22448	1235
2	39316	440
3	181688	868
4	239964	10647

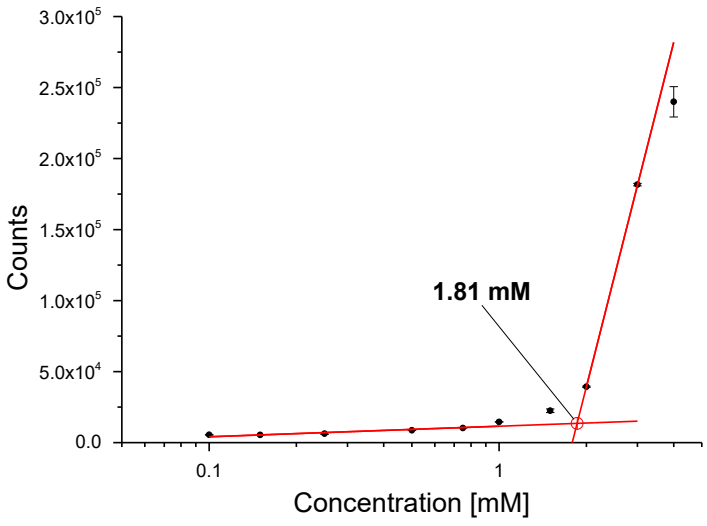

Figure 96. Counts plotted against the logarithmic concentration of APG **6**.

*Table 28. CMC with Nile red of APG **7**, TDS(Man)-C12.*

Concentration [mM]	Ø Counts @635 nm	Standard deviation
0.1	5341	160
0.15	4906	67
0.25	5921	348
0.5	5913	89
0.75	7894	216
1	10280	200
1.5	21786	5236
2	36347	7196
3	75543	7068
4	153909	768

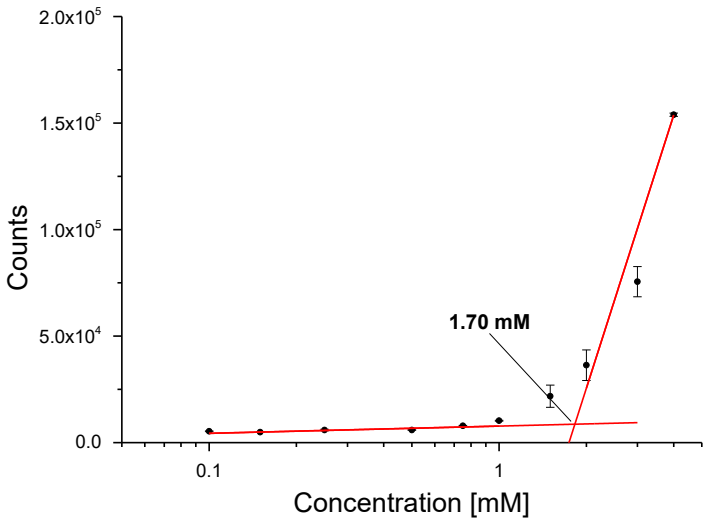

Figure 97. Counts plotted against the logarithmic concentration of APG **7**.

*Table 29. CMC with Nile red of APG **8**, Gly-BADS(Man)-HDM-C12.*

Concentration [mM]	Ø Counts @635 nm	Standard deviation
0.1	5720	199
0.15	7760	547
0.25	12490	589
0.5	23920	503
0.75	38329	1339
1	45277	104
1.5	59144	1073
2	66831	1627
3	75281	699
4	75146	5

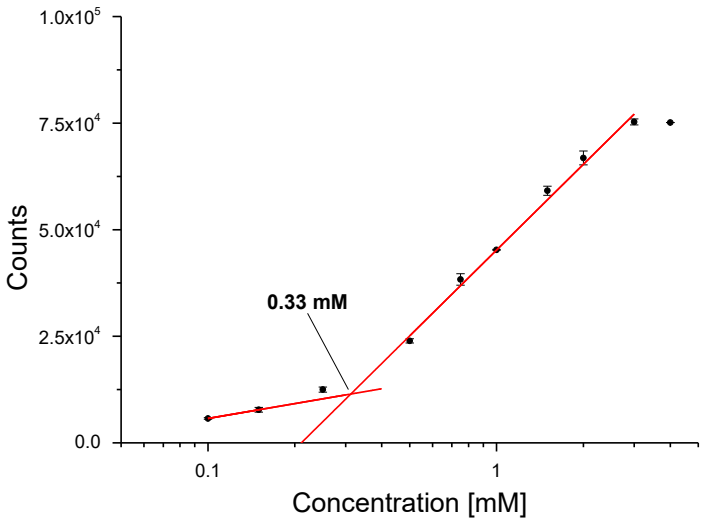

*Figure 98. Counts plotted against the logarithmic concentration of APG **8**.*

5.3.5 Crosslinking verification

To further verify the crosslinking both samples crosslinked and non-crosslinked were dispersed at the same concentration in ethanol/water 1:1 mixture and the scattered light intensity (count rate) of the DLS was measured. In this solvent mixture all non-crosslinked micelles will be dissolved and only the crosslinked micelles remain intact. In Figure 99 the count rates and the respective correlation functions are displayed. The count rate for the crosslinked sample is about 5 times higher and the respective correlation cruve shows a typical progression. For the non-crosslinked sample, the count rate is really low and the correlation function is shifted towards smaller tau, which indicates that only unimers are present in solution.

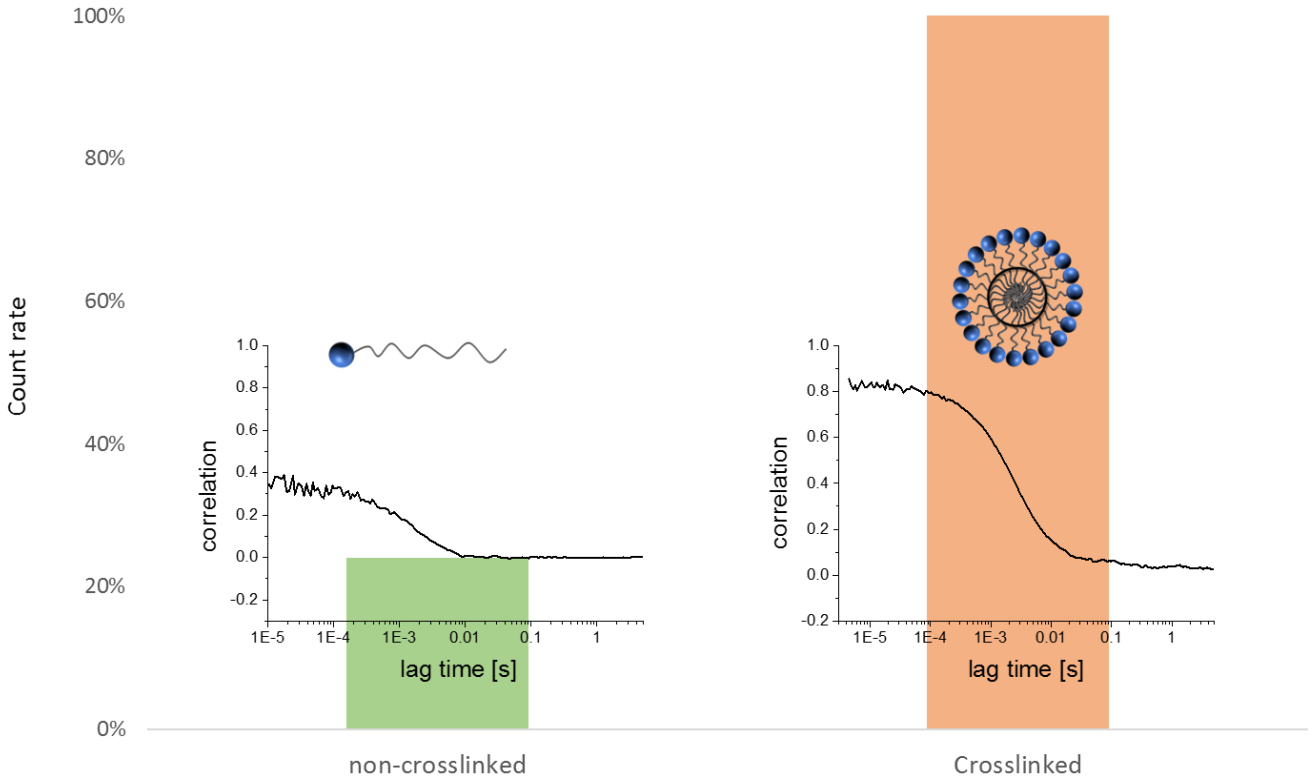

Figure 99. Comparison of the Count rate and correlation curve of non-crosslinked and crosslinked APG **8** micelles in ethanol/water mixture 1:1.

5.3.6 Clustering experiments with rhodamine labeled Con A and APG 8

A rhodamine labeled Con A stock solution of 1mg/ml was prepared in lectin binding buffer (10 mM Hepes, 50 mM NaCl, 1 mM $MnCl_2$, 1 mM $CaCl_2$, pH 7.4). 1 µL of this solution was added to a solution of 5 mM APG **8** also in LBB. This mixture was incubated for 30 minutes and afterwards directly measured with a fluorescence Microscope.

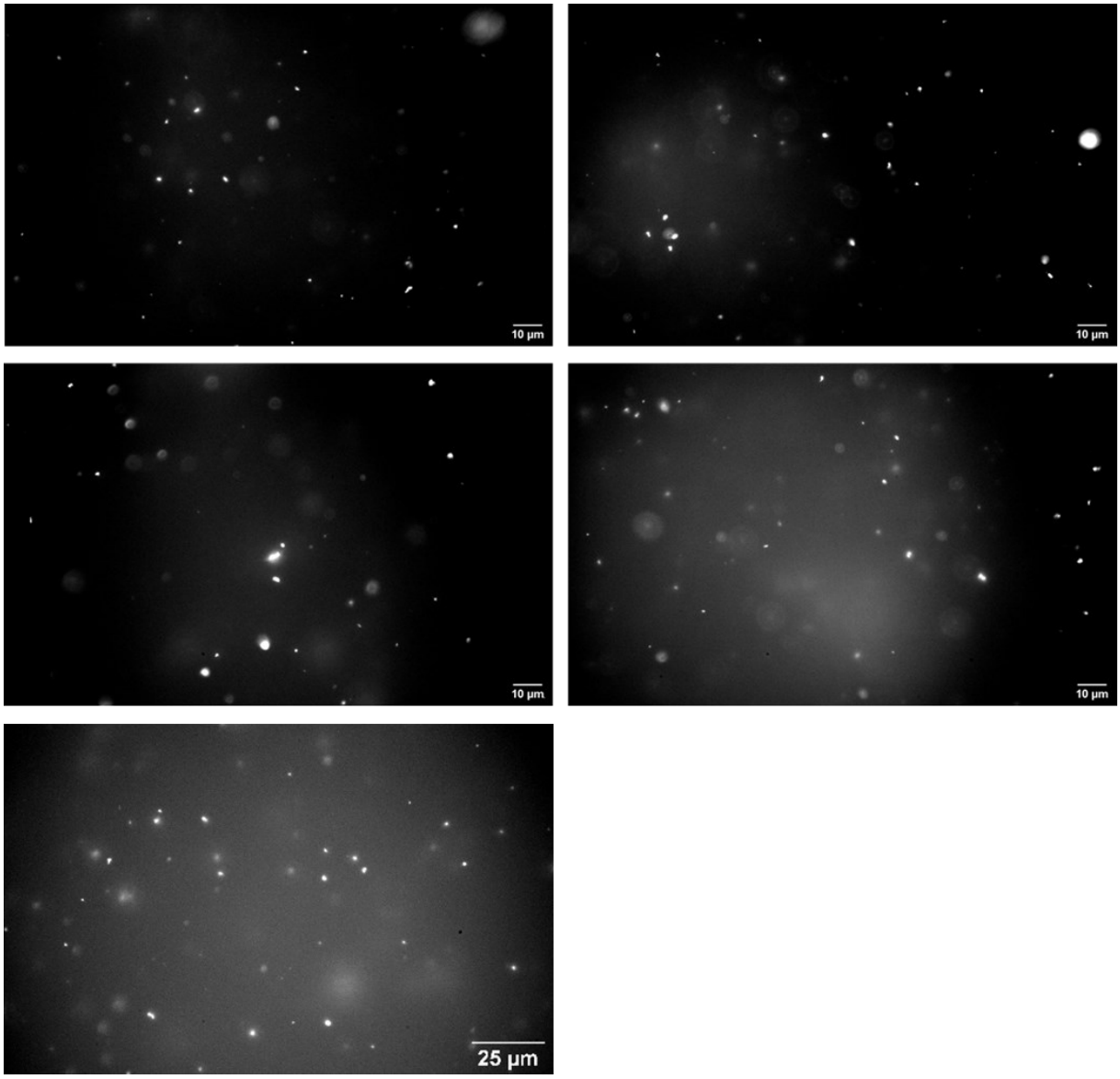

Figure 100. Fluorescence microscope image of APG **8** incubated with rhodamine conjugated Con A (post edited with ImageJ).

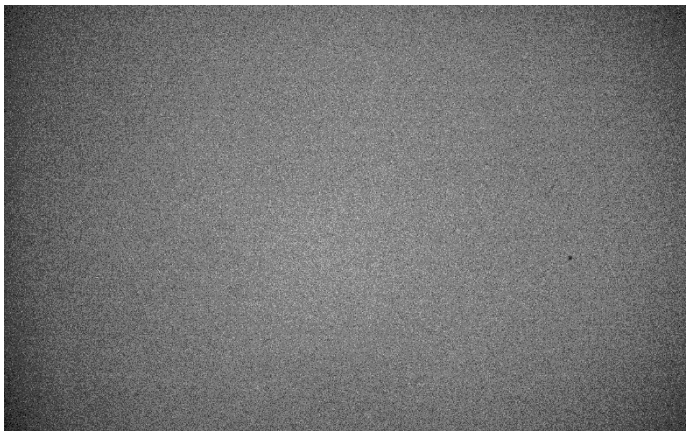

Figure 101. Picture of only APG **8** in solution under fluorescence microscope.

Figure 102. Fluorescence microscope image of rhodamine conjugated Con A in solution.

5.3.7 Micelle stability in PBS

CMC in PBS

APGs were dissolved in MQ water and CMCs were measured following the Nile red CMC protocol. Subsequently, 10 µL of ten times concentrated PBS solution were added to each well. Wellplates were shaken and subsequently the CMC measurement was repeated.

Table 30. Overview of the CMCs in PBS

Structure	CMC	Deviation
APG_1	0.59	0.01
APG_3	0.06	0.004
APG_4	0.63	0.07
APG_6	0.49	0.001
APG_7	1.98	0.02
APG_8	0.3	0.01

TEM images of APGs in PBS

APG **1** and **8** were dissolved in PBS with a final concentration of 4 mM. TEM samples were prepared following the standard TEM staining protocol. Micelles were observed for APG **1** and APG **8** in PBS.

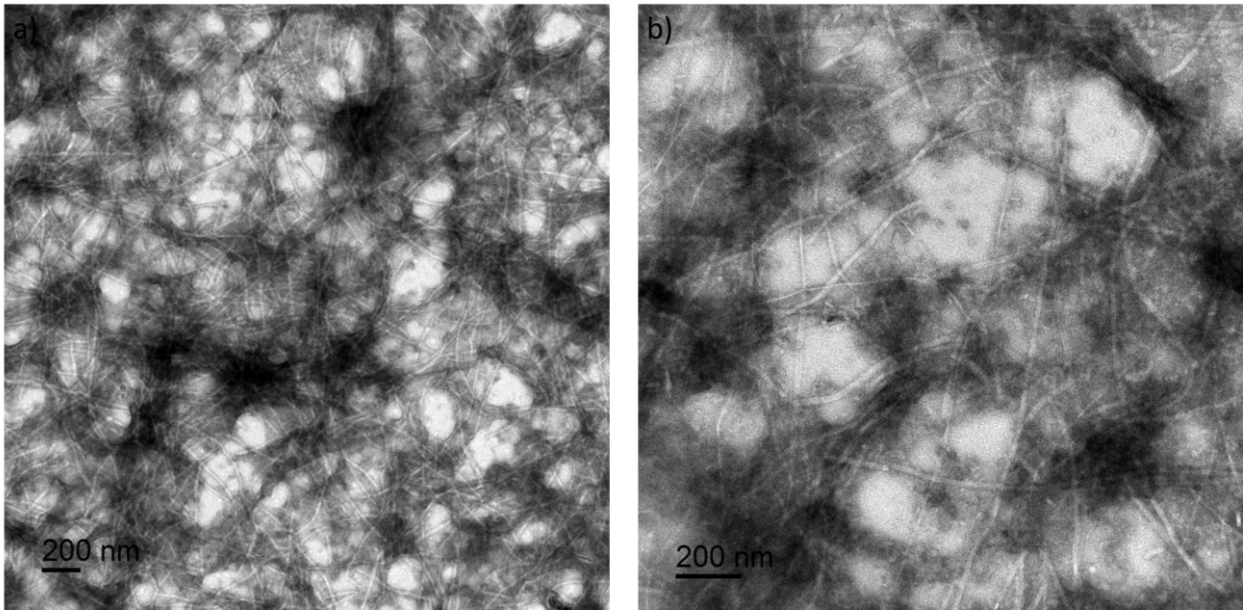

Figure 103. TEM images of a) APG **1** in PBS and b) APG **8** in PBS.

5.3.8 Bacteria adhesion assay

Experiments were conducted as described in the general methods section. All data points were averaged, corrected against the Blank (PBS) and then relative values are calculated by dividing the data against the Blank (Bacteria). APG **4** was used as negative control in all measurements.

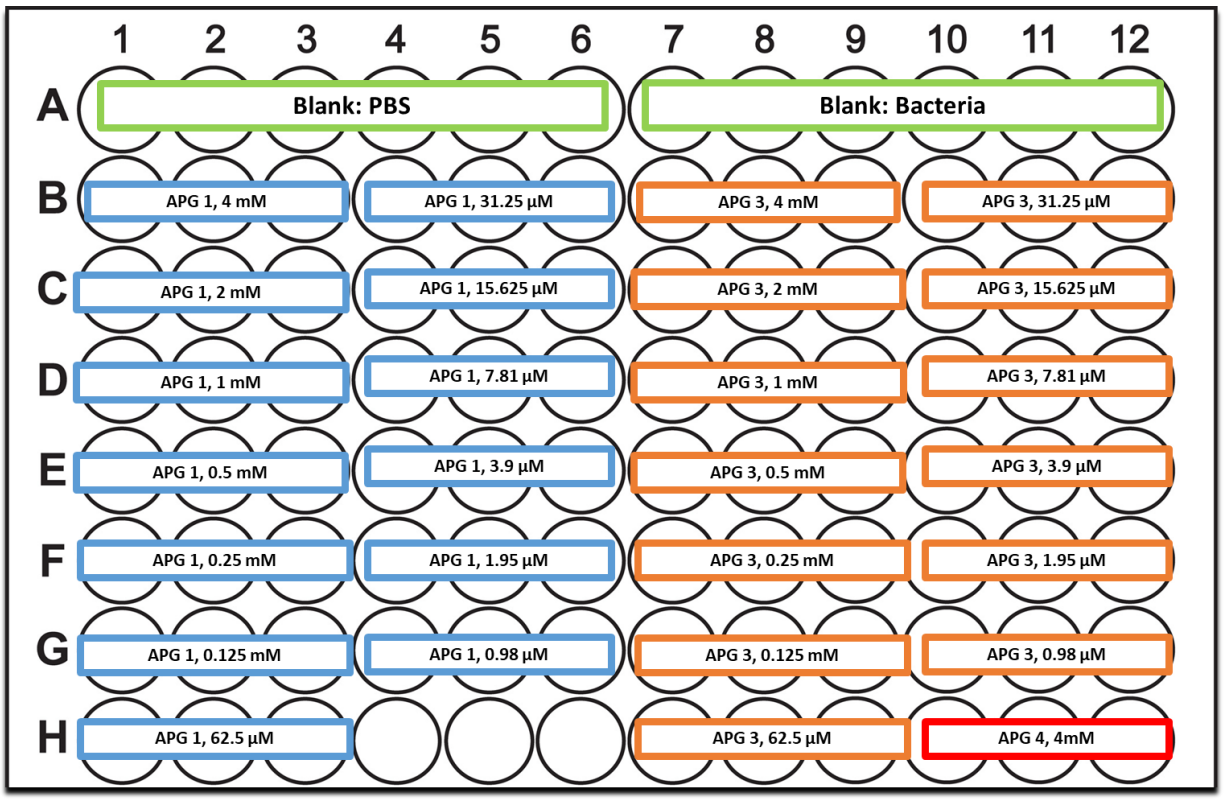

Figure 104. Standard 96-wellplate setup for the bacteria adhesion assay.

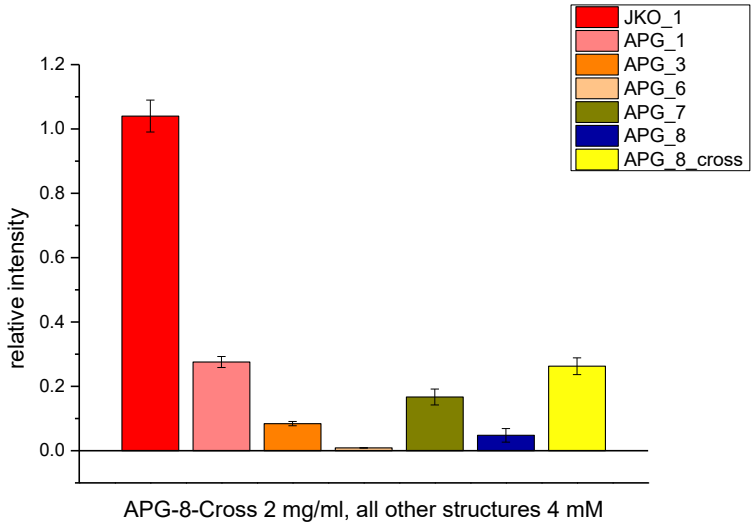

Figure 105. Inhibition of *E. coli* surface adhesion after 4.5 hour of incubation at the highest concentration of APGs.

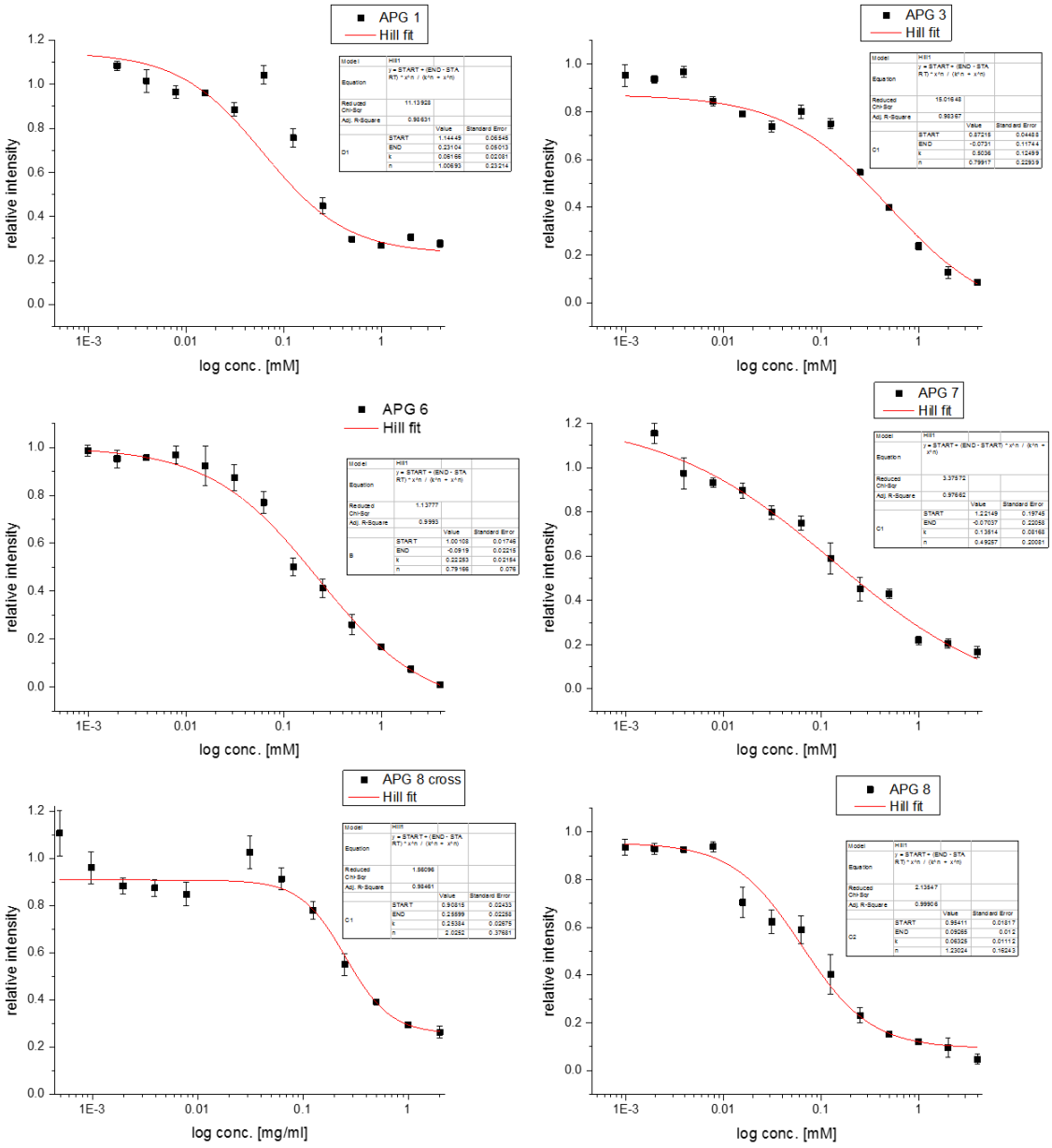

Figure 106. Inhibition curves and hill fit of APG **1**, **3**, **6, 7**, **8** and APG **8** crosslinked after 4.5 hours of incubation.

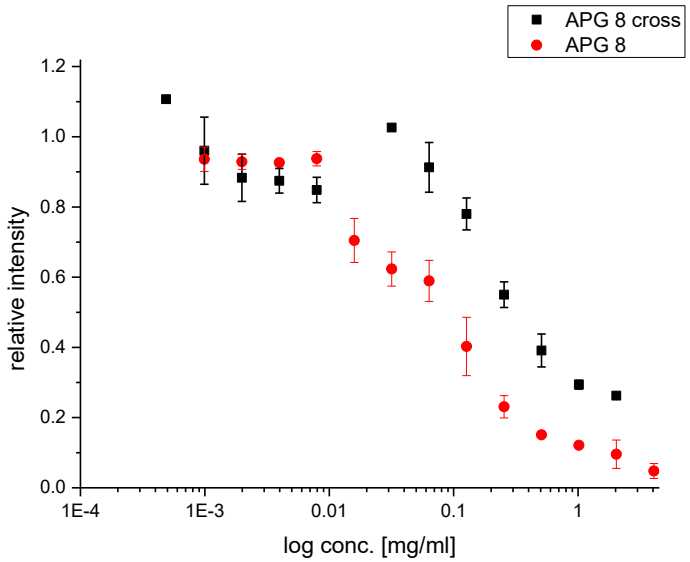

*Figure 107. Comparison of the inhibitory potential in mg/ml of APG **8** crosslinked and APG*

5.3.9 Reduction of 3,4,6-tri-O-acetyl-β-D-GlcNAc azide

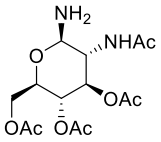

*Scheme 10. 3,4,6-tri-O-acetyl-β-D-GlcNAc amine **17** derived from the respective azide.*

The reaction procedure was adapted from Liu et al.[215] 3,4,6-tri-O-acetyl-β-D-GlcNAc azide 12 (1 g, 2. 68 mmol) was added to a suspension of 10% Pd/C in 15 ml methanol. The reaction vessel was charged with hydrogen using a hydrogen balloon and subsequently stirred overnight. The crude mixture was then filtered using a 5 µM Teflon syringe filter, which resulted in a clear slightly yellow solution. Following, the filtrate was concentrated under reduced pressure, which yielded an off-white solid with an overall yield of 70%. This crude product was used without further purifications.

5.3.10 Synthesis of the novel CTA compound 8

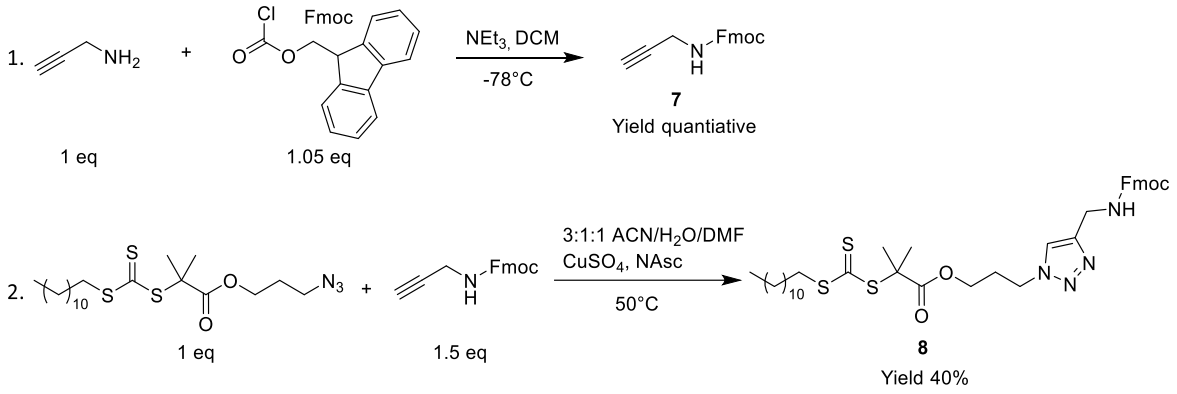

*Scheme 11. Synthetic scheme of two step synthesis of the novel RAFT CTA **8**.*

A solution of Fmoc chloride in 50 ml DCM was added dropwise to a solution of propargylamin and TEA in 70 DCM at -78 °C. The solution was allowed to reach room temperature and let stir overnight. Subsequently, the solution was washed with citric acid 0.1 M and saturated $NHCO_3$ and Brine. Organic phase was dried over $MgSO_4$ and concentrated under reduced pressure. Sonication in Hexane, followed by filtration leads to a white powder (**7**).

7 and the commercially available azide containing CTA are dissolved in 6 ml ACN. Followed by the addition of 10 mg of $CuSO_4$ and 10 mg of NaAsc both dissolved in 1 ml of H_2O each. The cloudy solution is then stirred for 16h at 50 °C. Subsequently, 3 ml of DMF are added and the reaction is stirred again for 16h.-Reagents precipated therefore 3ml of DMF were added and

the solution was kept at 50°C. Afterwards, the reaction mixture was cleaned using column chromatography. First a mixture of 5/95 EE/Hex is used and one side product as well as unreacted raft agent is isolated. Second the solvent is changed to DCM, which allows to isolate unreacted compound **7.** Lastly, the acetone is used to wash down the clean product (**8**) from the column.

^{1}H-NMR (600 MHz, DMSO-D_6): δ (ppm) 7.94 – 7.78 (m, 3H), 7.74 – 7.52 (m, 2H), 7.48 – 7.27 (m, 4H), 4.47 – 3.98 (m, 8H), 3.33 – 3.22 (m, 2H), 2.20 – 2.04 (m, 2H), 1.70 – 1.48 (m, 8H), 1.37 – 1.11 (m, 18H), 0.83 (t, 3H).

HR-ESI-MS for $C_{38}H_{52}N_4O_4S_3$ (Exact monoisotopic mass: 724.3151. g/mol): Found $[M+H]^+$ 725.3216 g/mol, mass accuracy 1 ppm.

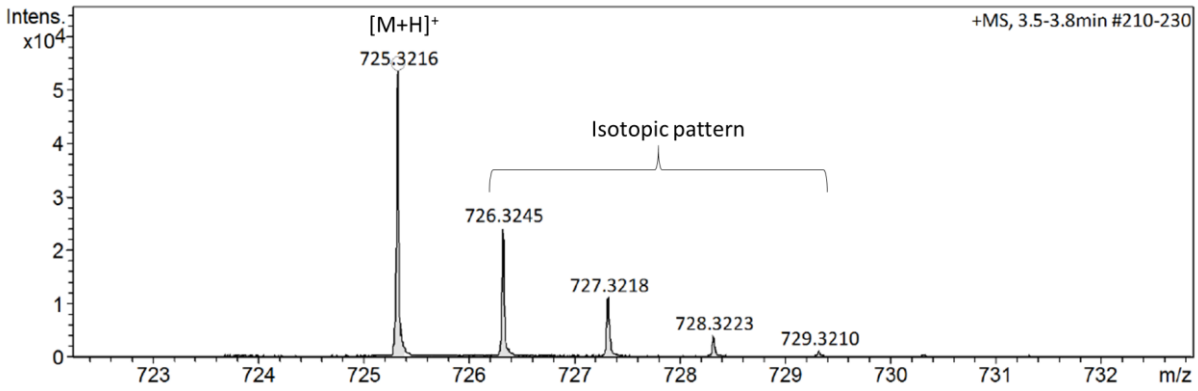

Figure 108. HR-ESI spectrum of the novel CTA-prot, recorded in positive mode.

5.3.11 General Raft protocol for the synthesis of compound 9

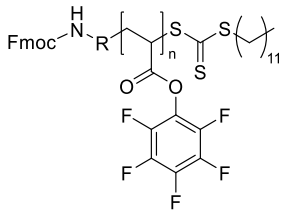

*Scheme 12. Final structure of compound **9** derived from RAFT polymerization of **5** and **6**.*

For M : CTA : I (50 : 1 : 0.1): 1 mL (6.0728 mmol) of PFPA **5**, with 87 mg (0.12 mmol) of **8** and 2 mg (0.012 mmol) AIBN.

For M : CTA : I (100 : 1 : 0.1): 1 mL (6.0728 mmol) of PFPA **5**, with 43.5 mg (0.06 mmol) of **8** and 1 mg (0.006 mmol) AIBN.

The mixture was dissolved in 8 ml benzene and degassed for 45 min using argon. Following the reaction mixture was tightly sealed and heated to 70°C for 6 or 18 hours. Subsequently, the reaction was quenched by exposing it to air, precipitated in hexane and dried under high vacuum yielding a yellow powder. Finally, the product was dialyzed using a Readylyzer (MWCO 3.5 kDa) against THF for three solvent changes, precipitated and dried again in high vacuo yielding an off-white powder with an overall yield of 59%.

^{1}H-NMR (600 MHz, $CDCl_3$): δ 7.74 (d, *J* = 7.6 Hz, 2H), 7.59 – 7.48 (m, 3H), 7.38 (t, *J* = 7.5 Hz, 2H), 7.31 – 7.26 (m, 2H), 4.52 – 4.32 (m, 5H), 4.25 – 4.02 (m, 4H), 3.47 – 3.29 (m, 2H), 3.25 – 2.70 (m, 33H), 2.50 (d, *J* = 15.7 Hz, 13H), 2.33 – 1.79 (m, 56H), 1.78 – 1.59 (m, 6H), 1.47 – 1.34 (m, 2H), 1.35 – 1.13 (m, 20H).

^{19}F-NMR (600 MHz, $CDCl_3$): δ (ppm) = -153.16 (s, 2F), -156.72 (s, 1F), -162.17 (s, 2F)

5.3.12 Synthesis of P-AE

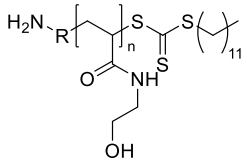

*Scheme 13. Final structure of P-AE, **14***

0.1 g of **9** was dissolved in 1 ml DMF and a few drops of trimethylamine were added. Following, 5 eq of aminoethanol were added and the solution was stirred for 18 hours. Next, 0.25 ml piperidine was added that the overall piperidine concentration was 25% and the solution was stirred for additional 3h. Finally, the solution was precipitated in Acetone, dialyzed using a Readylyzer (MWCO 3.5 kDa) against water and lastly freeze dried. A white powder was obtained with an overall yield of 30%.

^{1}H-NMR (600 MHz, D_2O): δ 8.07 (s, 1H), 3.74 – 3.48 (m, 47H), 3.42 – 3.08 (m, 47H), 2.27 – 1.81 (m, 25H), 1.77 – 1.30 (m, 48H). Signals for the carbon tail of the CTA could not be assigned.

^{19}F-NMR (600 MHz, $CDCl_3$): No signals – Full conversion of the active ester

5.3.13 Synthesis of P-AG

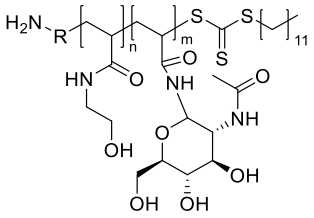

*Scheme 14. Final structure of P-AG, **15**.*

0.1 g of **9** was dissolved in 1 ml DMF and a few drops of trimethylamine were added. Following, 1.1 eq of 3,4,6-tri-O-acetyl-β-D-GlcNAc amine were added and the solution was stirred for 18 hours. Next, 0.25 ml piperidine was added that the overall piperidine concentration was 25% and the solution was stirred for additional 3 h. Afterwards, 1 ml of 0.1 M sodium methoxide solution in methanol was added and again stirred for 2 h. Finally, the solution was precipitated in Acetone, dialyzed using a Readylyzer (MWCO 3.5 kDa) against water and lastly freeze dried. A white powder was obtained with an overall yield of 20%.

^{1}H-NMR (600 MHz, D_2O): Signals could not be assigned due to strong baseline distortion.

^{19}F-NMR (600 MHz, $CDCl_3$): No signals – Full conversion of the active ester

6 Appendix

6.1 List of figures

6.2 List of schemes

6.3 List of tables

6.4 List of abbreviations

azide-functionalized diethylenetriamine coupled with succinic anhydride	ADS
atomic force microscopy	AFM
aggregation induced emission dyes	AIE
allyloxycarbonyl	Alloc
amphiphilic precision glycomacromolecules	APGs
benzyl azide functionalized diethylenetriamine coupled with succinic anhydride	BADS
tert-butyloxycarbonyl	Boc
aggregation concentrations	CA
carboxylated aromatic thioether luminophore	CATE
critical micelle concentration	CM
cellulose nanocrystals	CNCs
concanavalin A	Con A
carbohydrate binding domains	CR
transmission electron cryomicroscopy	cryo-TEM
copper(I)-catalyzed azide-alkyne cycloaddition	CuAAC
diffusion coefficient	D
1,8-Diazabicyclo[5.4.0]undec-7-ene	DBU
N,N'- dicyclohexylcarbodiimide	DCC
depolarized dynamic light scattering	DDLS
N - Diisopropylethylamine	DIPEA
dynamic light scattering	DL
dimethyl formamide	DM
2,2-dimethoxy-2-phenylacetophenone	DMPA
dimethyl sulfoxide	DMSO
dibenzoyl peroxide	DPBO
rotational diffusion coefficient	D_r
translational diffusion coefficient	D_t
divinylbenzene	DVB
extracellular matrix	ECM

succinylated 2,2'-(ethylenedi-oxy)bis(ethylamine)	EDS
fluorenyl methoxycarbonyl	Fmoc
glycosaminoglycans	GAGs
galactose	Gal
acetyl-D-glucosamine	GlcNAc
tetrameric Galanthus nivalis lectin	GNA
hyaluronic acid	HA
uronium salt 2-(1H-Benzotriazol-1-yl)-1,1,3,3-tetramethyluronium-hexafluorophosphat	HBTU
hexamethylenediamine coupled with maleic anhydride	HDM
hexamethylenediamine coupled with succinic anhydride	HDS
4-(Hydroxymethyl)phenoxy aceamidomethyl	HMPA
lectin binding buffer	LBB
dimeric Lens culinaris lectin or agglutinin	LCA
multi-angle light scattering	MALS
mannose	Man
Nuclear magnetic resonance	NMR
4-((8-aminooctyl)amino)-4-oxobutanoic acid	ODS
poly(pentafluorophenyl acrylate)	p(PFPA)
poly(amidoamine)s	PAAs
peptide amphiphiles	PAs
phosphate-buffered saline	PBS
polyethylene	PE
polyethyleneglycol	PE
protecting groups	PGs
polymerization induced self-assembly	PISA
polymeric micelles	PMs
polystyrene	PS
benzotriazol-1-yl-oxy-tris-(pyrrolidino)-phosphonium hexafluorophosphate	PyBOP
hydrodynamic radius	R
reversible addition–fragmentation chain-transfer	RAFT

Arg-Gly-Asp	RGD
reverse phase high-performance liquid chromatography	RP-HPLC
sodium dodecyl sulphate	SDS
static light scattering	SLS
solid phase polymer synthesis	SPPoS
solid phase peptide synthesis	SPPS
tert-butyl	tBu
10,12-tricosadiynoic acid	TCDA
triple bond functionalized diethylenetriamine coupled with succinic anhydride	TDS
transmission electron microscopy	TEM
trifluoroacetic acid	TF
thin layer chromatography	TLC
tetraphenylethylene	TPE
tritylchloride	Trt-Cl

6.5 Experimental appendix

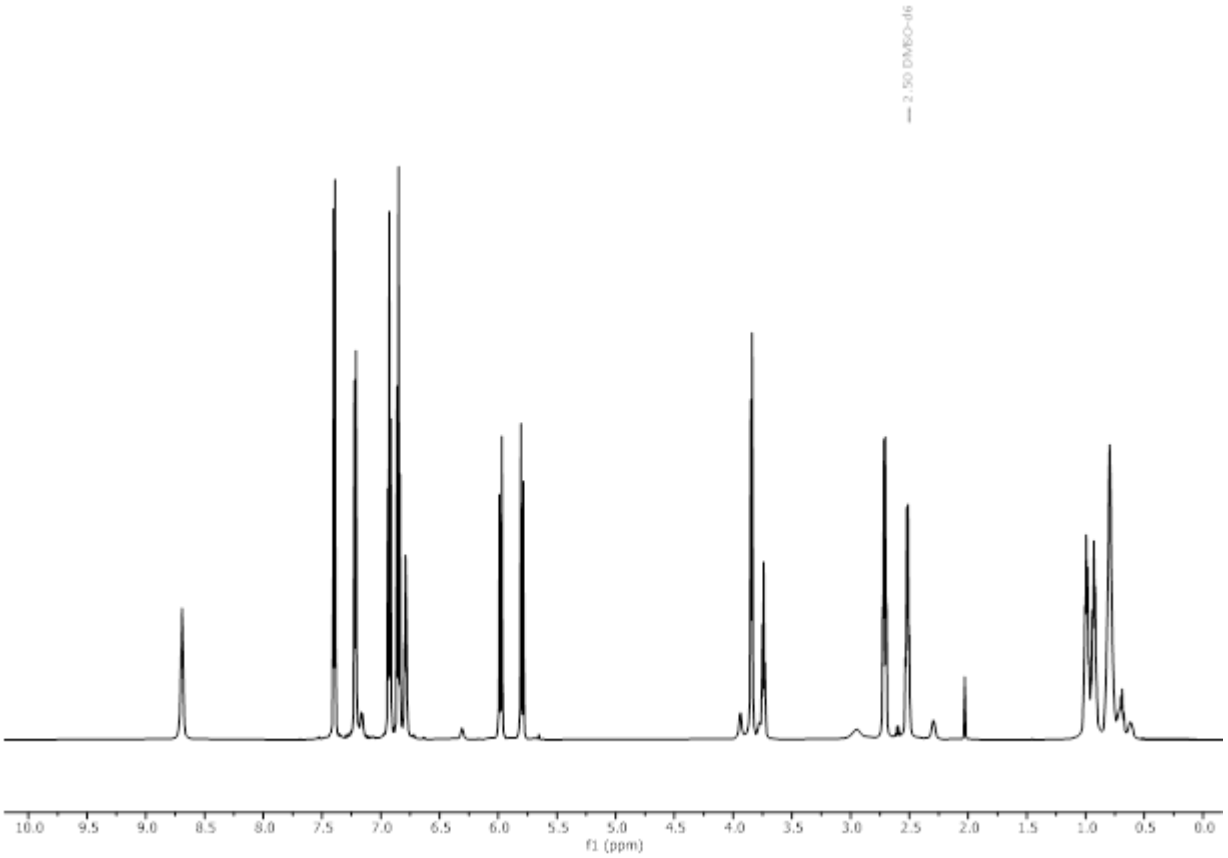

Appendix 1. ^{1}H-NMR (600 MHz, DMSO-d_6) of the maleic acid/anhydride polymer.

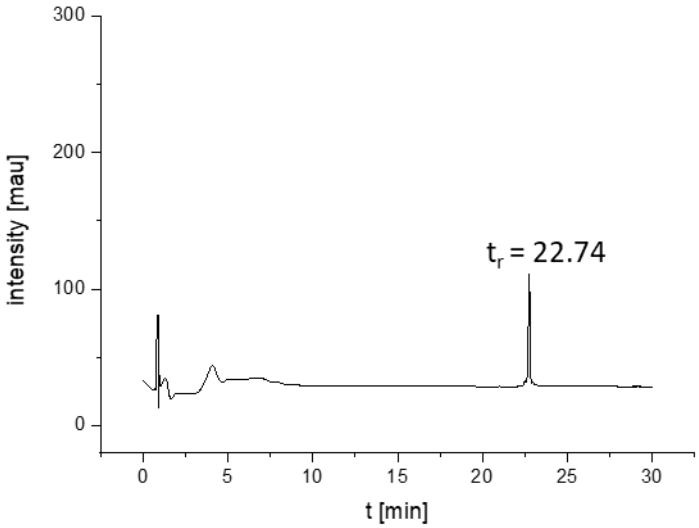

*Appendix 2. RP-HPLC of **APG-G** (linear gradient from 5-95% acetonitrile in water in 30 min): t_R = 22.74 min. Determined relative purity: >90%.*

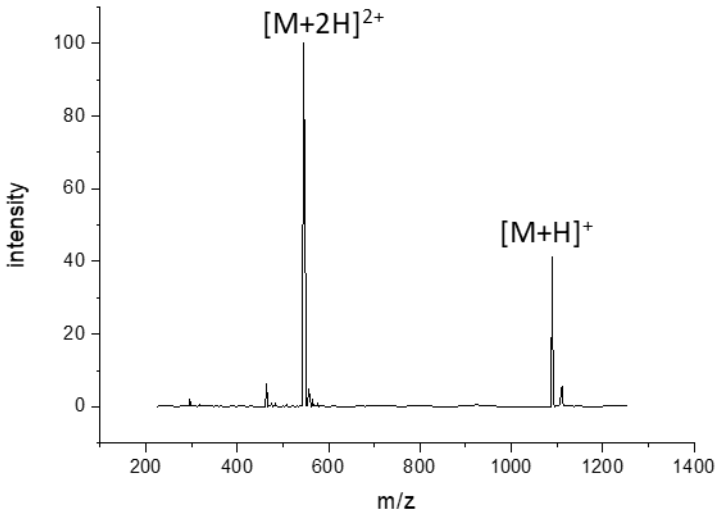

*Appendix 3. ESI-MS of **APG-G** masses found for $[M+H]^+$ and $[M+H]^{2+}$.*

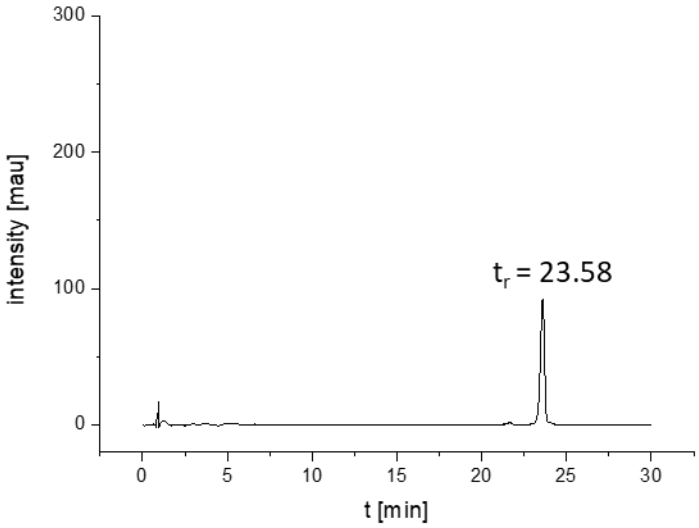

*Appendix 4. RP-HPLC of **APG-S** (linear gradient from 5-95% acetonitrile in water in 30 min): t_R = 23.58 min. Determined relative purity: >90%.*

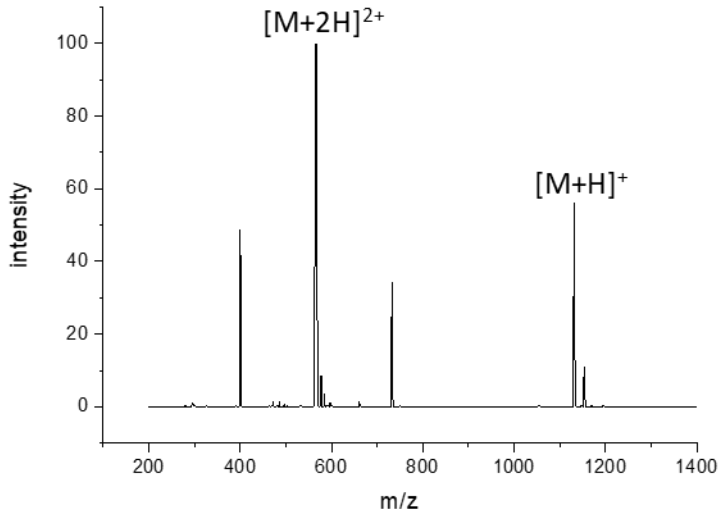

*Appendix 5. ESI-MS of **APG-S** masses found for $[M+H]^+$ and $[M+H]^{2+}$.*

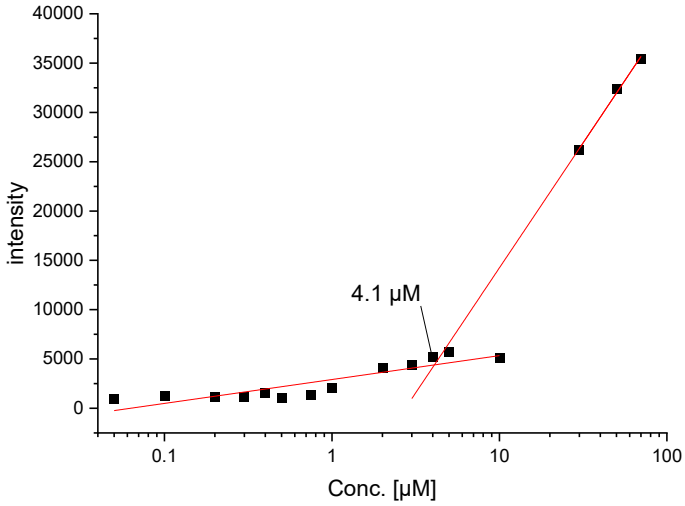

*Appendix 6. Counts plotted against the logarithmic concentration of **APG-G** (measured with 1 µM Nile red).*

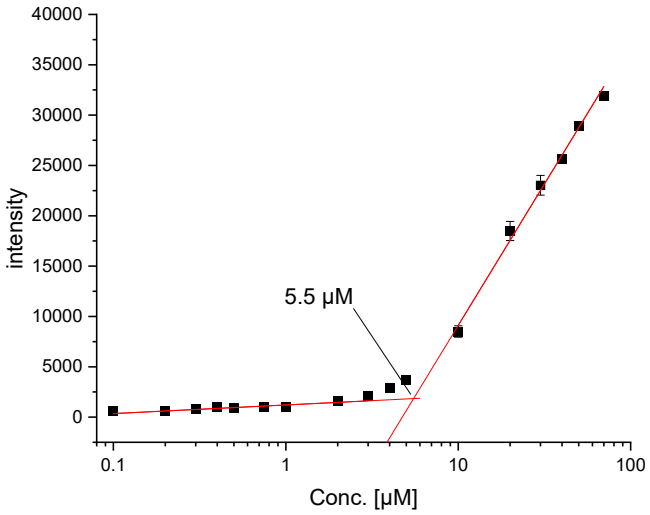

*Appendix 7. Counts plotted against the logarithmic concentration of **APG-S** (measured with 1 µM Nile red).*

1

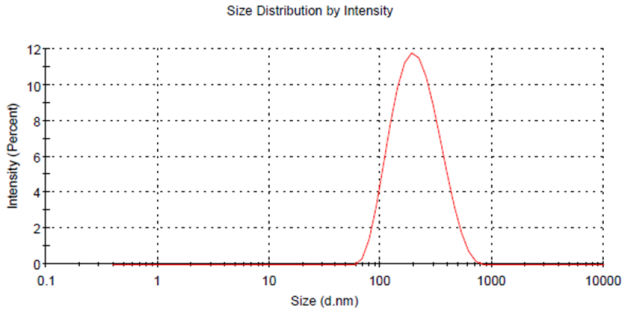

2

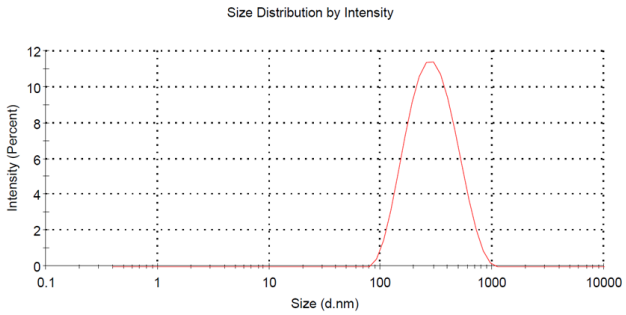

*Appendix 8. DLS size distribution for **APG-G** crosslinked in water (1) and in Ethanol (2).*

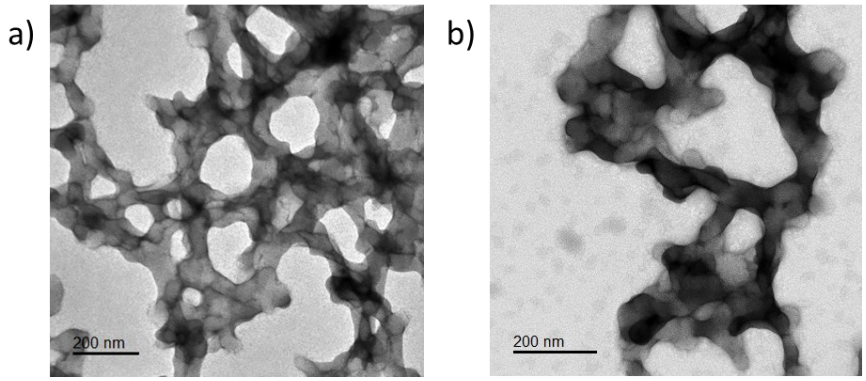

*Appendix 9. TEM images in water of a) pure **MTO** micelles and b) mixed micelles (**MTO** + **GLO**) showing big clustered aggregates.*

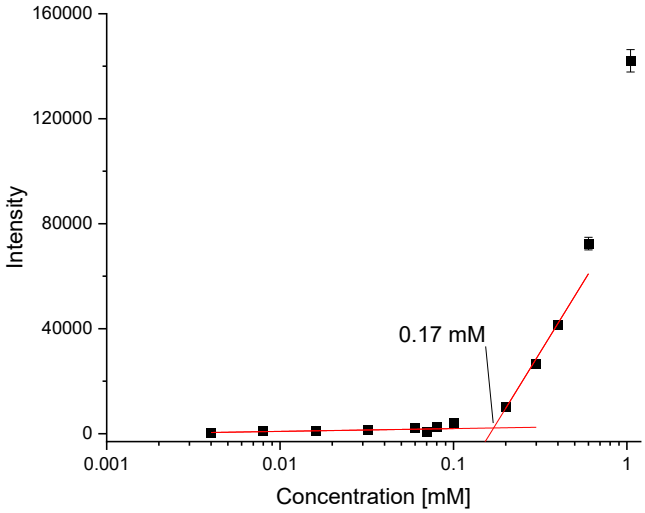

Appendix 10. Exemplary CMC fit of mixed micelles (ratio 1 TPE : 20 GLO) in MQ (λ_{ex} = 340 nm, λ_{em} = 483 nm).

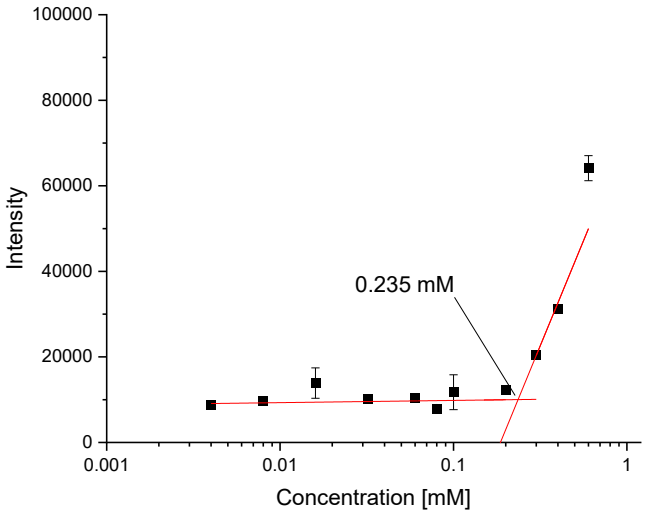

Appendix 11. Exemplary CMC fit of mixed micelles (ratio 1 TPE : 20 GLO) in MQ using Nile red as fluorescence reporter (λ_{ex} = 550 nm, λ_{em} = 635 nm).

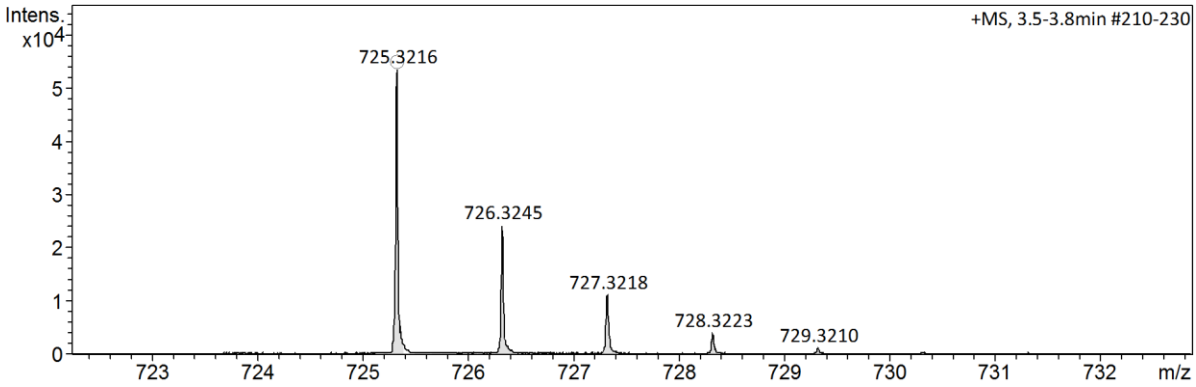

*Appendix 12. HR-ESI-MS of the CTA **8**, recorded in positive mode.*

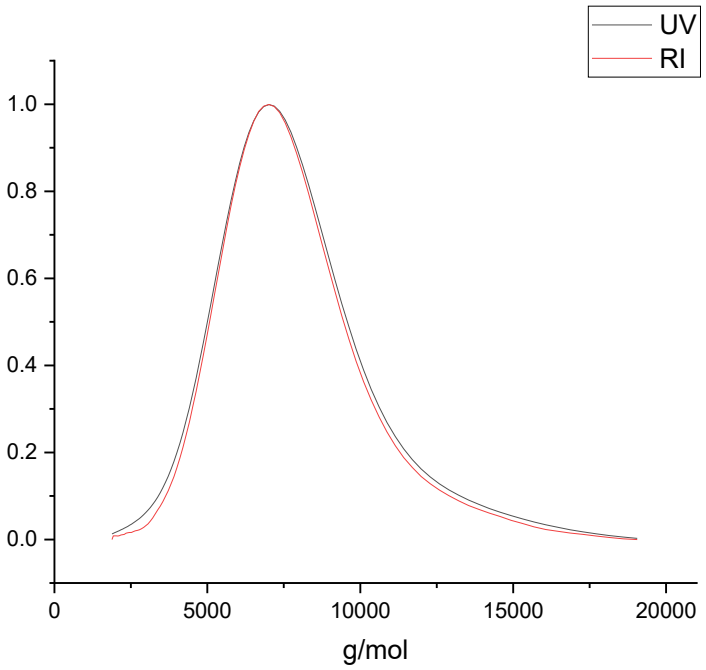

*Appendix 13. THF-GPC Data for the molar mass distribution of sample **10** detected using a UV and RI detector.*

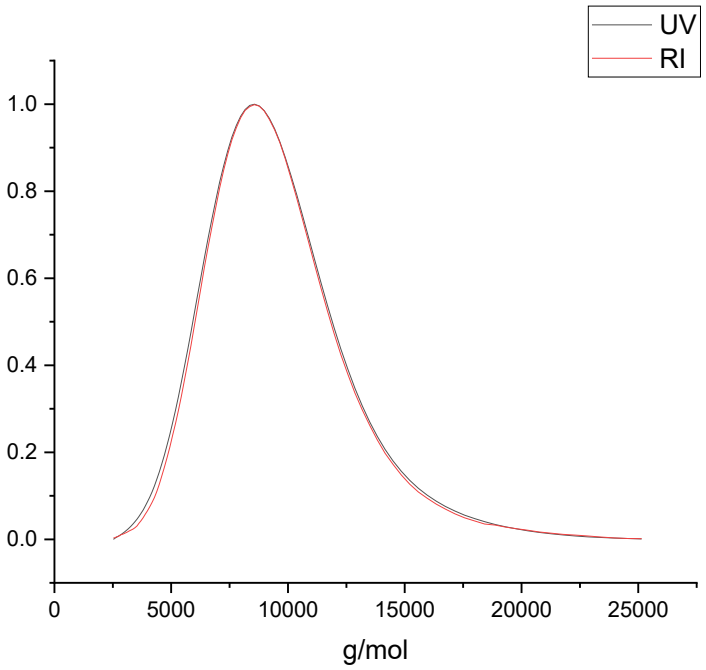

*Appendix 14. THF-GPC Data for the molar mass distribution of sample **11** detected using a UV and RI detector.*

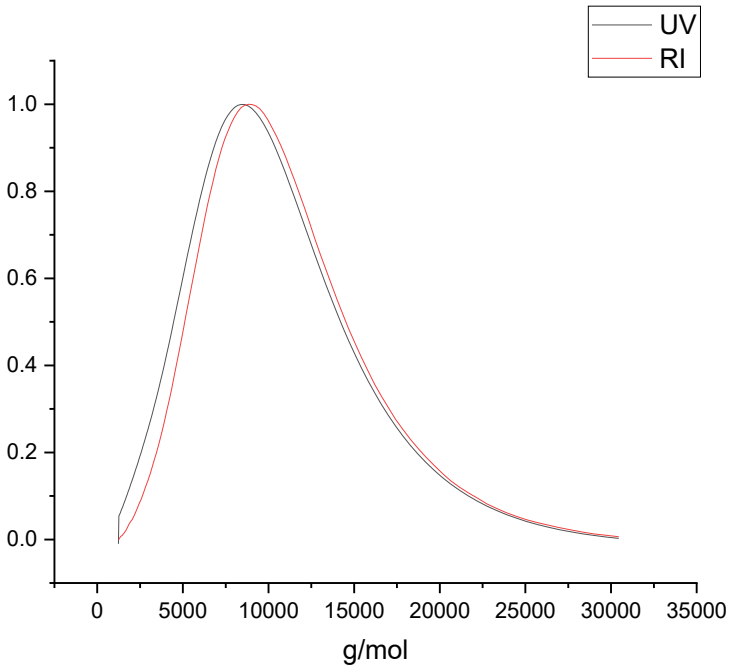

*Appendix 15. THF-GPC Data for the molar mass distribution of sample **12** detected using a UV and RI detector.*

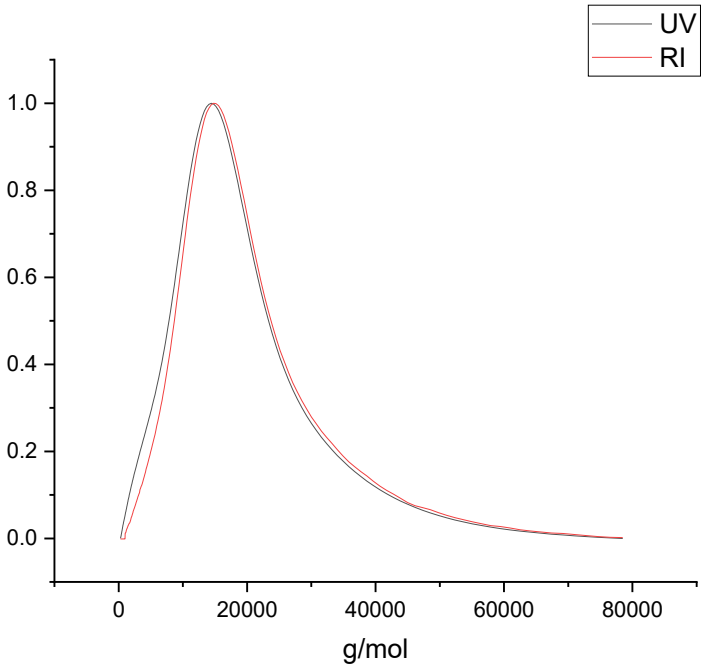

*Appendix 16. THF-GPC Data for the molar mass distribution of sample **13** detected using a UV and RI detector.*

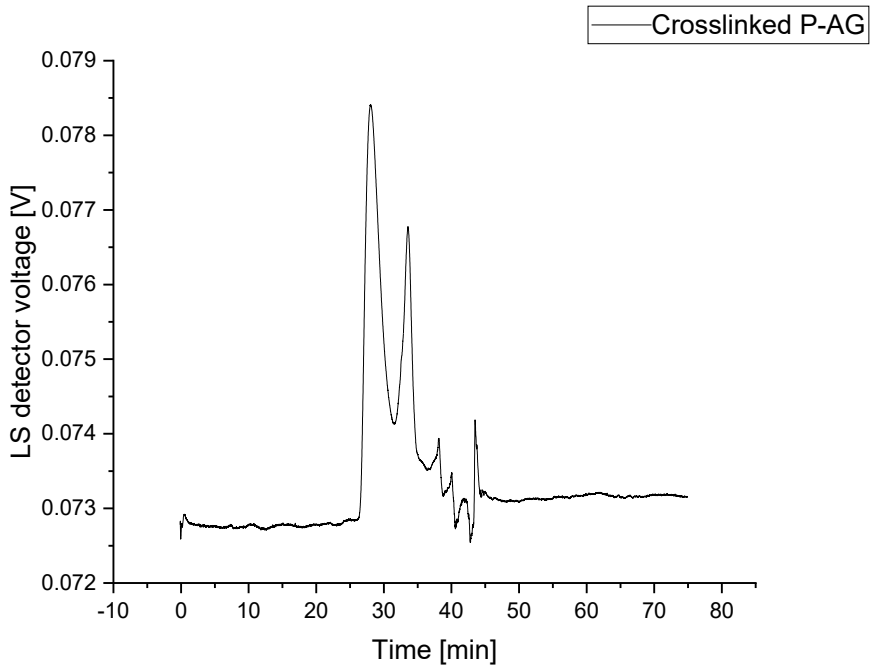

Appendix 17. GPC-RI-LS of crosslinked P-AG (LS y-axis). Column: GE Healthcare Superdex (75 10/300). Aqueous buffer: 50 mM NaH_2PO_4, 150 mM NaCl, 250 ppm NaN_3 at pH 7. Flow rate: 0.8 mL/min.

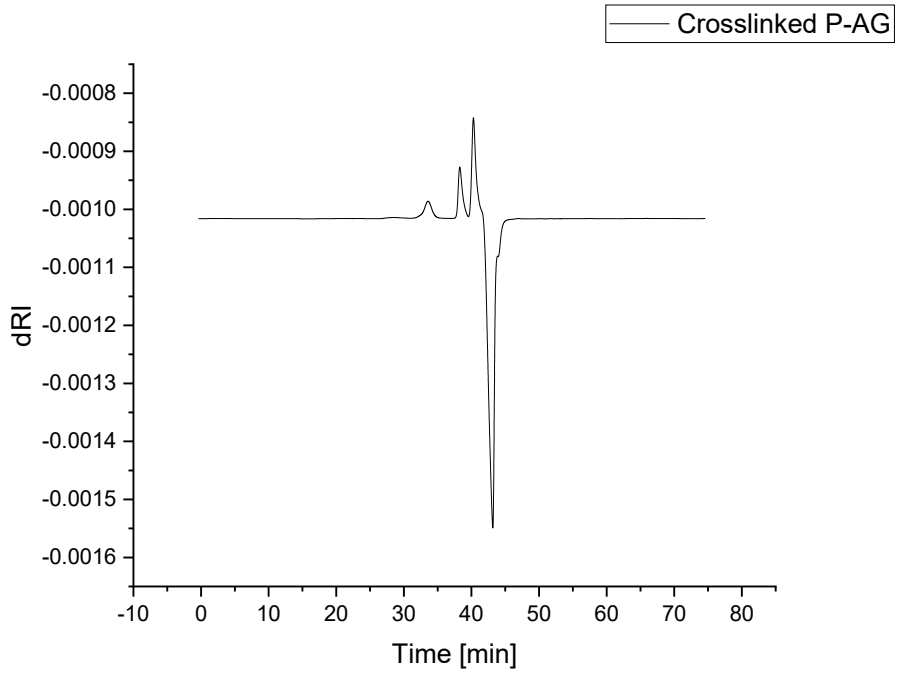

Appendix 18. GPC-RI-LS of crosslinked P-AG (RI y-axis). Column: GE Healthcare Superdex (75 10/300). Aqueous buffer: 50 mM NaH_2PO_4, 150 mM NaCl, 250 ppm NaN_3 at pH 7. Flow rate: 0.8 mL/min.

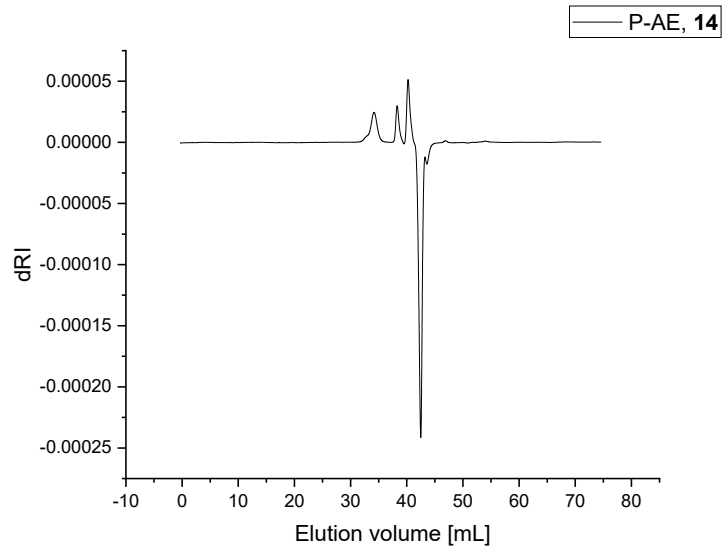

*Appendix 19. GPC-RI-LS of P-AE (**14**) (RI y-axis). Column: GE Healthcare Superdex (75 10/300). Aqueous buffer: 50 mM NaH_2PO_4, 150 mM NaCl, 250 ppm NaN_3 at pH 7. Flow rate: 0.8 mL/min.*

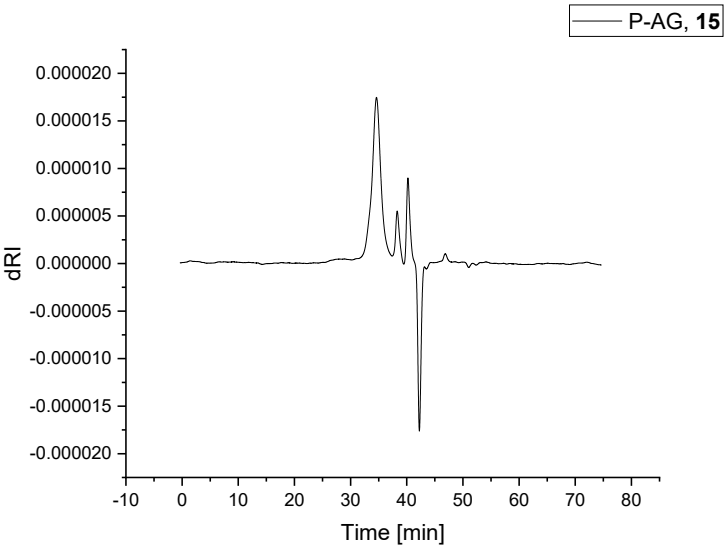

*Appendix 20. GPC-RI-LS of P-AG (**15**) (RI y-axis). Column: GE Healthcare Superdex (75 10/300). Aqueous buffer: 50 mM NaH_2PO_4, 150 mM NaCl, 250 ppm NaN_3 at pH 7. Flow rate: 0.8 mL/min.*

7 Acknowledgement

To begin with I would like to thank my mentor and supervisor Prof. Dr. Hartmann who not only gave me the chance to conduct my PhD thesis at her working group but also supported me with great ideas and feedback throughout my whole time at her working group. Her continuous support and motivation were essential for the successful completion of my PhD thesis.

Also, I would like to thank Prof. Dr. Karg for agreeing to be the second assessor of this thesis and also for many fruitful discussions and support regarding all the light scattering experiments conducted in this thesis.

Furthermore, I would like to thank the whole working group for the helpful and nice atmosphere in the lab and in the office. I really enjoyed working with all of you and spending time together during our parties or during our annual “Klassenfahrt”.
Especially, I would like to thank Dr. Monir Tabatabai, Michaela Kitza and Stephanie Scheelen for being the kind souls of the working group. You really make a difference!

I also would like to thank my collaboration partners Julian Sindram, Marius Otten, Dimitri Wilms, Alexander Strzelczyk, Sean Miletic and Thomas C. Marlovits.

A special thanks goes to my former colleagues and now dear friends Özgür, Peter, Fadi and Josip. You made my PhD time memorable through long lasting coffee sessions, golfing adventures and business ideations. I look forward making the next steps together with you guys!

Lastly, I would like to express my gratitude to my family. Thank you, Annette and Oma, for being always there for me and supporting me since I was a toddler. Thank you, Lea, for being the best little sister I can imagine although I have not always made it easy for you. Thank you, Mama and Papa, for your unconditional love and support throughout my whole life. You have given me the chance to become the person I am today. Thank you, Elena, for sticking with me for now more than 13 years. Marrying a woman like you makes me really proud.

8 References

1. H. S. Bennett, *Journal of histochemistry & cytochemistry*, 1963, **11**, 14-23.
2. H.-J. Gabius and J. Roth, *Journal*, 2017.
3. P. Winterburn and C. Phelps, *Nature*, 1972, **236**, 147-151.
4. B. K. Brandley and R. L. Schnaar, *Journal of leukocyte biology*, 1986, **40**, 97-111.
5. S. Califice, V. Castronovo and F. Van Den Brûle, *Int. J. Oncol.*, 2004, **25**, 983-1075.
6. J. N. Varghese, P. M. Colman, A. Van Donkelaar, T. J. Blick, A. Sahasrabudhe and J. L. McKimm-Breschkin, *Proceedings of the National Academy of Sciences*, 1997, **94**, 11808-11812.
7. G. R. Vasta, *Nature Reviews Microbiology*, 2009, **7**, 424-438.
8. R. Kannagi, M. Izawa, T. Koike, K. Miyazaki and N. Kimura, *Cancer science*, 2004, **95**, 377-384.
9. J. B. Sumner and S. F. Howell, *J. Bacteriol.*, 1936, **32**, 227.
10. I. Goldstein and R. D. Poretz, *The lectins. Properties, functions, and applications in biology and medicine*, 2012, 233-247.
11. I. Goldstein, C. Hollerman and E. Smith, *Biochemistry*, 1965, **4**, 876-883.
12. T. Rademacher, R. Parekh and R. Dwek, *Annu. Rev. Biochem*, 1988, **57**, 785-838.
13. N. Sharon, *Biochimica et Biophysica Acta (BBA)-General Subjects*, 2006, **1760**, 527-537.
14. R. A. Flynn, K. Pedram, S. A. Malaker, P. J. Batista, B. A. Smith, A. G. Johnson, B. M. George, K. Majzoub, P. W. Villalta and J. E. Carette, *Cell*, 2021, **184**, 3109-3124. e3122.
15. R. V. Iozzo and L. Schaefer, *Matrix Biol.*, 2015, **42**, 11-55.
16. A. Varki, R. D. Cummings, J. D. Esko, P. Stanley, G. W. Hart, M. Aebi, A. G. Darvill, T. Kinoshita, N. H. Packer and J. H. Prestegard, 2015.
17. P. H. Seeberger, 2017.
18. B. Ernst and J. L. Magnani, *Nature Reviews Drug Discovery*, 2009, **8**, 661-677.
19. Y. K. Gupta, M. Meenu and P. Mohan, *Indian journal of pharmacology*, 2015, **47**, 11.
20. P. Ward, I. Small, J. Smith, P. Suter and R. Dutkowski, *J. Antimicrob. Chemother.*, 2005, **55**, i5-i21.
21. J. M. Gargano, T. Ngo, J. Y. Kim, D. W. Acheson and W. J. Lees, *J. Am. Chem. Soc.*, 2001, **123**, 12909-12910.
22. D. Ponader, F. Wojcik, F. Beceren-Braun, J. Dernedde and L. Hartmann, *Biomacromolecules*, 2012, **13**, 1845-1852.
23. Y.-b. Lim and M. Lee, *Organic & biomolecular chemistry*, 2007, **5**, 401-405.
24. M. Mammen, S. K. Choi and G. M. Whitesides, *Angew. Chem. Int. Ed.*, 1998, **37**, 2754-2794.
25. F. Shamout, A. Monaco, G. Yilmaz, C. R. Becer and L. Hartmann, *Macromol. Rapid Commun.*, 2020, **41**, 1900459.
26. A. Imberty, Y. M. Chabre and R. Roy, *Chem. Eur. J.*, 2008, **14**, 7490-7499.
27. N. Röckendorf and T. K. Lindhorst, *Dendrimers IV*, 2001, 201-238.
28. A. Monaco, V. P. Beyer, R. Napier and C. R. Becer, *Biomacromolecules*, 2020, **21**, 3736-3744.
29. S. Boden, F. Reise, J. Kania, T. K. Lindhorst and L. Hartmann, *Macromol. Biosci.*, 2019, **19**, 1800425.
30. S. Ordanini, N. Varga, V. Porkolab, M. Thépaut, L. Belvisi, A. Bertaglia, A. Palmioli, A. Berzi, D. Trabattoni and M. Clerici, *Chem. Commun.*, 2015, **51**, 3816-3819.
31. H. H. Abdu-Allah, K. Watanabe, G. C. Completo, M. Sadagopan, K. Hayashizaki, C. Takaku, T. Tamanaka, H. Takematsu, Y. Kozutsumi and J. C. Paulson, *Biorg. Med. Chem.*, 2011, **19**, 1966-1971.
32. S. Boden, K. G. Wagner, M. Karg and L. Hartmann, *Polymers*, 2017, **9**, 716.
33. F. Jacobi, A. Camaleño de la Calle, S. Boden, A. Grafmüller, L. Hartmann and S. Schmidt, *Biomacromolecules*, 2018, **19**, 3479-3488.
34. X. Li and G. Chen, *Polym. Chem.*, 2015, **6**, 1417-1430.
35. L. Wu, Y. Zhang, Z. Li, G. Yang, Z. Kochovski, G. Chen and M. Jiang, *J. Am. Chem. Soc.*, 2017, **139**, 14684-14692.
36. L. Bes, S. Angot, A. Limer and D. M. Haddleton, *Macromolecules*, 2003, **36**, 2493-2499.

37. Z. Ma and X. Zhu, *Journal of Materials Chemistry B*, 2019, **7**, 1361-1378.
38. N. Jayaraman, K. Maiti and K. Naresh, *Chem. Soc. Rev.*, 2013, **42**, 4640-4656.
39. N. K. Sauter, M. D. Bednarski, B. A. Wurzburg, J. E. Hanson, G. M. Whitesides, J. J. Skehel and D. C. Wiley, *Biochemistry*, 1989, **28**, 8388-8396.
40. L. L. Kiessling, T. Young, T. D. Gruber and K. H. Mortell, *Glycoscience*, 2008, 2483.
41. C. Fasting, C. A. Schalley, M. Weber, O. Seitz, S. Hecht, B. Koksch, J. Dernedde, C. Graf, E. W. Knapp and R. Haag, *Angew. Chem. Int. Ed.*, 2012, **51**, 10472-10498.
42. J. J. Lundquist and E. J. Toone, *Chem. Rev.*, 2002, **102**, 555-578.
43. C.-H. Heldin, *Cell*, 1995, **80**, 213-223.
44. J. I. Healy and C. C. Goodnow, *Annual review of immunology*, 1998, **16**, 645-670.
45. M. I. Page and W. P. Jencks, *Proceedings of the National Academy of Sciences*, 1971, **68**, 1678-1683.
46. L. L. Kiessling, J. E. Gestwicki and L. E. Strong, *Angew. Chem. Int. Ed.*, 2006, **45**, 2348-2368.
47. J. E. Gestwicki, C. W. Cairo, L. E. Strong, K. A. Oetjen and L. L. Kiessling, *J. Am. Chem. Soc.*, 2002, **124**, 14922-14933.
48. W. J. Lees, A. Spaltenstein, J. E. Kingery-Wood and G. M. Whitesides, *J. Med. Chem.*, 1994, **37**, 3419-3433.
49. F. Jacobi, D. Wilms, T. Seiler, T. Queckbörner, M. Tabatabai, L. Hartmann and S. Schmidt, *Biomacromolecules*, 2020, **21**, 4850-4856.
50. G. M. Whitesides and B. Grzybowski, *Science*, 2002, **295**, 2418-2421.
51. F. S. Bates, M. A. Hillmyer, T. P. Lodge, C. M. Bates, K. T. Delaney and G. H. Fredrickson, *Science*, 2012, **336**, 434-440.
52. G. R. Desiraju and G. W. Parshall, *Materials science monographs*, 1989, **54**.
53. K. Thorkelsson, P. Bai and T. Xu, *Nano Today*, 2015, **10**, 48-66.
54. H. Sirringhaus, L. Bürgi, T. Kawase and R. Friend, *Thin Film Transistors*, 2003, 427-474.
55. A. Rösler, G. W. Vandermeulen and H.-A. Klok, *Advanced drug delivery reviews*, 2012, **64**, 270-279.
56. C. J. Drummond and C. Fong, *Current opinion in colloid & interface science*, 1999, **4**, 449-456.
57. C. Tanford, *The Hydrophobic Effect: Formation of Micelles and Biological Membranes 2d Ed*, J. Wiley., 1980.
58. L. R. Pratt and D. Chandler, *J. Chem. Phys.*, 1977, **67**, 3683-3704.
59. D. Chandler, *Nature*, 2005, **437**, 640-647.
60. J. W. Gibbs, *The collected works of J. Willard Gibbs*, Yale Univ. Press, 1948.
61. J. N. Israelachvili, D. J. Mitchell and B. W. Ninham, *J. Chem. Soc., Faraday Trans.*, 1976, **72**, 1525-1568.
62. A. Samad, Y. Sultana and M. Aqil, *Current drug delivery*, 2007, **4**, 297-305.
63. R. Nagarajan, *Langmuir*, 2002, **18**, 31-38.
64. Ö. Topel, B. A. Çakır, L. Budama and N. Hoda, *J. Mol. Liq.*, 2013, **177**, 40-43.
65. T. Chakraborty, I. Chakraborty and S. Ghosh, *Arabian Journal of Chemistry*, 2011, **4**, 265-270.
66. P. L. Du Nouy, *The Journal of general physiology*, 1925, **7**, 625-631.
67. J. Stetefeld, S. A. McKenna and T. R. Patel, *Biophysical reviews*, 2016, **8**, 409-427.
68. H. Ruf, *Langmuir*, 2002, **18**, 3804-3814.
69. A. Nakajima, *Bull. Chem. Soc. Jpn.*, 1971, **44**, 3272-3277.
70. G. B. Ray, I. Chakraborty and S. P. Moulik, *J. Colloid Interface Sci.*, 2006, **294**, 248-254.
71. H. Xu, Y. Wang, X. Ge, S. Han, S. Wang, P. Zhou, H. Shan, X. Zhao and J. R. Lu, *Chem. Mater.*, 2010, **22**, 5165-5173.
72. K. Kalyanasundaram and J. Thomas, *J. Am. Chem. Soc.*, 1977, **99**, 2039-2044.
73. M. C. Stuart, J. C. van de Pas and J. B. Engberts, *J. Phys. Org. Chem.*, 2005, **18**, 929-934.
74. I. N. Kurniasih, H. Liang, P. C. Mohr, G. Khot, J. r. P. Rabe and A. Mohr, *Langmuir*, 2015, **31**, 2639-2648.
75. P. Greenspan, E. P. Mayer and S. D. Fowler, *J. Cell Biol.*, 1985, **100**, 965-973.
76. B. J. Berne and R. Pecora, *Dynamic light scattering: with applications to chemistry, biology, and physics*, Courier Corporation, 2000.

77. R. Pecora, *Dynamic light scattering: applications of photon correlation spectroscopy*, Springer Science & Business Media, 2013.
78. P. W. Atkins and J. De Paula, *Physikalische chemie*, John Wiley & Sons, 2013.
79. M. Hoffmann, Y. Lu, M. Schrinner, M. Ballauff and L. Harnau, *The Journal of Physical Chemistry B*, 2008, **112**, 14843-14850.
80. D. La Torre, J. García, M. C. L. Martinez and M. M. Tirado, *Biopolymers*, 1984, **23**, 611-615.
81. M. M. Tirado and J. G. de la Torre, *J. Chem. Phys.*, 1979, **71**, 2581-2587.
82. Z. Tuzar and P. Kratochvil, *Adv. Colloid Interface Sci.*, 1976, **6**, 201-232.
83. B. H. Zimm, *J. Chem. Phys.*, 1948, **16**, 1099-1116.
84. L. Muus and F. Billmeyer Jr, *J. Am. Chem. Soc.*, 1957, **79**, 5079-5082.
85. G. Binnig, C. F. Quate and C. Gerber, *Phys. Rev. Lett.*, 1986, **56**, 930.
86. E. Ruska, *Zeitschrift für Physik*, 1934, **87**, 580-602.
87. S. D. Connell, S. Collins, J. Fundin, Z. Yang and I. W. Hamley, *Langmuir*, 2003, **19**, 10449-10453.
88. Y.-Y. Won, A. K. Brannan, H. T. Davis and F. S. Bates, *The Journal of Physical Chemistry B*, 2002, **106**, 3354-3364.
89. D. Kushner, *Bacteriological reviews*, 1969, **33**, 302.
90. G. L. Hasenhuettl and R. W. Hartel, *Food emulsifiers and their applications*, Springer, 2008.
91. S.-W. Lee, Y.-M. Kim, C. H. Cho, Y. T. Kim, S. M. Kim, S. Y. Hur, J.-H. Kim, B.-G. Kim, S.-C. Kim and H.-S. Ryu, *Cancer research and treatment: official journal of Korean Cancer Association*, 2018, **50**, 195.
92. Y. Zou, X. Zhou, J. Ma, X. Yang and Y. Deng, *Chem. Soc. Rev.*, 2020, **49**, 1173-1208.
93. M. Szwarc, M. Levy and R. Milkovich, *J. Am. Chem. Soc.*, 1956, **78**, 2656-2657.
94. S. Krause, *J. Phys. Chem.*, 1964, **68**, 1948-1955.
95. M.-C. Jones and J.-C. Leroux, *European journal of pharmaceutics and biopharmaceutics*, 1999, **48**, 101-111.
96. R. Nagarajan, in *Solvents and Self-organization of Polymers*, Springer, 1996, pp. 121-165.
97. N. J. Warren and S. P. Armes, *J. Am. Chem. Soc.*, 2014, **136**, 10174-10185.
98. C. J. Ferguson, R. J. Hughes, D. Nguyen, B. T. Pham, R. G. Gilbert, A. K. Serelis, C. H. Such and B. S. Hawkett, *Macromolecules*, 2005, **38**, 2191-2204.
99. Y. Pei and A. B. Lowe, *Polym. Chem.*, 2014, **5**, 2342-2351.
100. L. Zhang and A. Eisenberg, *Science*, 1995, **268**, 1728-1731.
101. S. Jain and F. S. Bates, *Science*, 2003, **300**, 460-464.
102. M. Antonietti and S. Förster, *Adv. Mater.*, 2003, **15**, 1323-1333.
103. S. J. Holder and N. A. Sommerdijk, *Polym. Chem.*, 2011, **2**, 1018-1028.
104. I. Hamley, *Angew. Chem. Int. Ed.*, 2003, **42**, 1692-1712.
105. K. Kataoka, A. Harada and Y. Nagasaki, *Advanced drug delivery reviews*, 2001, **47**, 113-131.
106. H. Cabral, K. Miyata, K. Osada and K. Kataoka, *Chem. Rev.*, 2018, **118**, 6844-6892.
107. T.-Y. Kim, D.-W. Kim, J.-Y. Chung, S. G. Shin, S.-C. Kim, D. S. Heo, N. K. Kim and Y.-J. Bang, *Clinical cancer research*, 2004, **10**, 3708-3716.
108. P. Berndt, G. B. Fields and M. Tirrell, *J. Am. Chem. Soc.*, 1995, **117**, 9515-9522.
109. J. D. Hartgerink, E. Beniash and S. I. Stupp, *Science*, 2001, **294**, 1684-1688.
110. S. E. Paramonov, H.-W. Jun and J. D. Hartgerink, *J. Am. Chem. Soc.*, 2006, **128**, 7291-7298.
111. F. Tantakitti, J. Boekhoven, X. Wang, R. V. Kazantsev, T. Yu, J. Li, E. Zhuang, R. Zandi, J. H. Ortony and C. J. Newcomb, *Nature materials*, 2016, **15**, 469-476.
112. N. Singha, P. Gupta, B. Pramanik, S. Ahmed, A. Dasgupta, A. Ukil and D. Das, *Biomacromolecules*, 2017, **18**, 3630-3641.
113. S. Ghanaati, M. J. Webber, R. E. Unger, C. Orth, J. F. Hulvat, S. E. Kiehna, M. Barbeck, A. Rasic, S. I. Stupp and C. J. Kirkpatrick, *Biomaterials*, 2009, **30**, 6202-6212.
114. S. Soukasene, D. J. Toft, T. J. Moyer, H. Lu, H.-K. Lee, S. M. Standley, V. L. Cryns and S. I. Stupp, *ACS nano*, 2011, **5**, 9113-9121.
115. R. Zhang, J. D. Smith, B. N. Allen, J. S. Kramer, M. Schauflinger and B. D. Ulery, *ACS Biomaterials Science & Engineering*, 2018, **4**, 2463-2472.
116. M. J. Sis and M. J. Webber, *Trends in pharmacological sciences*, 2019, **40**, 747-762.

117. N. Habibi, N. Kamaly, A. Memic and H. Shafiee, *Nano today*, 2016, **11**, 41-60.
118. E. Fischer and E. Fourneau, in *Untersuchungen über Aminosäuren, Polypeptide und Proteïne (1899–1906)*, Springer, 1906, pp. 279-289.
119. R. B. Merrifield, *J. Am. Chem. Soc.*, 1963, **85**, 2149-2154.
120. R. B. Merrifield, *Science*, 1986, **232**, 341-348.
121. E. Bayer and W. Rapp, in *Poly (Ethylene Glycol) Chemistry*, Springer, 1992, pp. 325-345.
122. E. Bayer, *Angew. Chem.*, 1991, **103**, 117-133.
123. G. Jung, *Combinatorial peptide and nonpeptide libraries: a handbook*, John Wiley & Sons, 2008.
124. M. Meldal, *Methods Enzymol.*, 1997, **289**, 83-104.
125. E. Bayer, K. Albert, H. Willisch, W. Rapp and B. Hemmasi, *Macromolecules*, 1990, **23**, 1937-1940.
126. J. Rademann, M. Grøtli, M. Meldal and K. Bock, *J. Am. Chem. Soc.*, 1999, **121**, 5459-5466.
127. S. Côté, *WO*, **2005012277**, A1.
128. F. García-Martín, M. Quintanar-Audelo, Y. García-Ramos, L. J. Cruz, C. Gravel, R. Furic, S. Côté, J. Tulla-Puche and F. Albericio, *J. Comb. Chem.*, 2006, **8**, 213-220.
129. B. Bacsa, S. Bősze and C. O. Kappe, *The Journal of organic chemistry*, 2010, **75**, 2103-2106.
130. W. Rapp, *PEG grafted polystyrene tentacle polymers: Physicochemical properties and application in chemical synthesis*, VCH: Weinheim, 1996.
131. A. Banger, J. Sindram, M. Otten, J. Kania, A. Strzelczyk, D. Wilms, S. Miletic, T. Marlovits, M. Karg and L. Hartmann, *Polym. Chem.*, 2021.
132. C. G. Bochet, *J. Chem. Soc., Perkin Trans. 1*, 2002, 125-142.
133. F. Stieber, U. Grether and H. Waldmann, *Angew. Chem. Int. Ed.*, 1999, **38**, 1073-1077.
134. S. Jin, D. P. Holub and D. J. Wustrow, *Tetrahedron letters*, 1998, **39**, 3651-3654.
135. J. C. Sheehan and G. P. Hess, *J. Am. Chem. Soc.*, 1955, **77**, 1067-1068.
136. C. A. Montalbetti and V. Falque, *Tetrahedron*, 2005, **61**, 10827-10852.
137. E. Valeur and M. Bradley, *Chem. Soc. Rev.*, 2009, **38**, 606-631.
138. R. Knorr, A. Trzeciak, W. Bannwarth and D. Gillessen, *Tetrahedron Letters*, 1989, **30**, 1927-1930.
139. F. Albericio, *Peptide Science*, 2000, **55**, 123-139.
140. P. G. Wuts and T. W. Greene, *Greene's protective groups in organic synthesis*, John Wiley & Sons, 2006.
141. M. Bergmann and L. Zervas, *Berichte der deutschen chemischen Gesellschaft (A and B Series)*, 1932, **65**, 1192-1201.
142. O. Dangles, F. Guibe, G. Balavoine, S. Lavielle and A. Marquet, *The Journal of Organic Chemistry*, 1987, **52**, 4984-4993.
143. R. L. Letsinger and V. Mahadevan, *J. Am. Chem. Soc.*, 1965, **87**, 3526-3527.
144. S. J. Danishefsky, K. F. McClure, J. T. Randolph and R. B. Ruggeri, *Science*, 1993, **260**, 1307-1309.
145. O. J. Plante, E. R. Palmacci and P. H. Seeberger, *Science*, 2001, **291**, 1523-1527.
146. L. Hartmann, E. Krause, M. Antonietti and H. G. Börner, *Biomacromolecules*, 2006, **7**, 1239-1244.
147. F. Wojcik, S. Mosca and L. Hartmann, *The Journal of organic chemistry*, 2012, **77**, 4226-4234.
148. M. Baier, M. Giesler and L. Hartmann, *Chem. Eur. J.*, 2018, **24**, 1619-1630.
149. F. Shamout, L. Fischer, N. L. Snyder and L. Hartmann, *Macromol. Rapid Commun.*, 2020, **41**, 1900473.
150. S. A. Hill, C. Gerke and L. Hartmann, *Chemistry–An Asian Journal*, 2018, **13**, 3611-3622.
151. C. W. Tornøe, C. Christensen and M. Meldal, *The Journal of organic chemistry*, 2002, **67**, 3057-3064.
152. R. Huisgen, *Angew. Chem.*, 1963, **75**, 604-637.
153. H. C. Kolb, M. Finn and K. B. Sharpless, *Angew. Chem. Int. Ed.*, 2001, **40**, 2004-2021.
154. H. Ghazarian, B. Idoni and S. B. Oppenheimer, *Acta histochemica*, 2011, **113**, 236-247.
155. N. R. Mantuano, M. Natoli, A. Zippelius and H. Läubli, *Journal for Immunotherapy of Cancer*, 2020, **8**.

156. G. Zhou, W.-J. Mo, P. Sebbel, G. Min, T. A. Neubert, R. Glockshuber, X.-R. Wu, T.-T. Sun and X.-P. Kong, *J. Cell Sci.*, 2001, **114**, 4095-4103.
157. J. Stelzer, C. Vallet, A. Sowa, D. Gonzalez-Abradelo, S. Riebe, C. G. Daniliuc, M. Ehlers, C. A. Strassert, S. K. Knauer and J. Voskuhl, *ChemistrySelect*, 2018, **3**, 985-991.
158. L. Wu and N. S. Sampson, *ACS Chem. Biol.*, 2014, **9**, 468-475.
159. A. Mahler, M. Reches, M. Rechter, S. Cohen and E. Gazit, *Adv. Mater.*, 2006, **18**, 1365-1370.
160. T. Nishikawa, H. Narita, S. Ogi, Y. Sato and S. Yamaguchi, *Chem. Commun.*, 2019, **55**, 14950-14953.
161. R. Hu, N. L. Leung and B. Z. Tang, *Chem. Soc. Rev.*, 2014, **43**, 4494-4562.
162. J. Luo, Z. Xie, J. W. Lam, L. Cheng, H. Chen, C. Qiu, H. S. Kwok, X. Zhan, Y. Liu, D. Zhu and B. Z. Tang, *Chem. Commun.*, 2001, 1740-1741.
163. S. Boden, 2020.
164. D. P. Nair, M. Podgorski, S. Chatani, T. Gong, W. Xi, C. R. Fenoli and C. N. Bowman, *Chem. Mater.*, 2014, **26**, 724-744.
165. M. Talelli, M. Barz, C. J. Rijcken, F. Kiessling, W. E. Hennink and T. Lammers, *Nano today*, 2015, **10**, 93-117.
166. T. Willke and K.-D. Vorlop, *Appl. Microbiol. Biotechnol.*, 2001, **56**, 289-295.
167. D. Braun and J. Pomakis, *Macromol. Chem. Phys.*, 1974, **175**, 1411-1425.
168. J. Kania, 2018.
169. Q. Meng, Y. Kou, X. Ma, L. Guo and K. Liu, *J. Pept. Sci.*, 2014, **20**, 223-228.
170. D. J. Welsh, P. Posocco, S. Pricl and D. K. Smith, *Organic & biomolecular chemistry*, 2013, **11**, 3177-3186.
171. N. M. Javali, A. Raj, P. Saraf, X. Li and B. Jasti, *Pharmaceutical research*, 2012, **29**, 3347-3361.
172. R. J. M. Tausk, J. Karmiggelt, C. Oudshoorn and J. T. G. Overbeek, *Biophys. Chem.*, 1974, **1**, 175-183.
173. E. Fuguet, C. Ràfols, M. Rosés and E. Bosch, *Anal. Chim. Acta*, 2005, **548**, 95-100.
174. S. Hayashi and S. Ikeda, *J. Phys. Chem.*, 1980, **84**, 744-751.
175. G. Duplâtre, M. Ferreira Marques and M. da Graça Miguel, *J. Phys. Chem.*, 1996, **100**, 16608-16612.
176. B. Song, Z. Wang, S. Chen, X. Zhang, Y. Fu, M. Smet and W. Dehaen, *Angew. Chem. Int. Ed.*, 2005, **44**, 4731-4735.
177. T. K. Dam, B. S. Cavada, T. B. Grangeiro, C. F. Santos, F. A. De Sousa, S. Oscarson and C. F. Brewer, *J. Biol. Chem.*, 1998, **273**, 12082-12088.
178. C. Gerke, M. F. Ebbesen, D. Jansen, S. Boden, T. Freichel and L. Hartmann, *Biomacromolecules*, 2017, **18**, 787-796.
179. F. K. Bahrani-Mougeot, E. L. Buckles, C. Lockatell, J. Hebel, D. Johnson, C. Tang and M. Donnenberg, *Mol. Microbiol.*, 2002, **45**, 1079-1093.
180. F. G. Sauer, M. Barnhart, D. Choudhury, S. D. Knight, G. Waksman and S. J. Hultgren, *Curr. Opin. Struct. Biol.*, 2000, **10**, 548-556.
181. E. H. Beachey, *J. Infect. Dis.*, 1981, **143**, 325-345.
182. M. Hartmann, A. K. Horst, P. Klemm and T. K. Lindhorst, *Chem. Commun.*, 2010, **46**, 330-332.
183. M. M. Sauer, R. P. Jakob, T. Luber, F. Canonica, G. Navarra, B. Ernst, C. Unverzagt, T. Maier and R. Glockshuber, *J. Am. Chem. Soc.*, 2018, **141**, 936-944.
184. S. M. Dimick, S. C. Powell, S. A. McMahon, D. N. Moothoo, J. H. Naismith and E. J. Toone, *J. Am. Chem. Soc.*, 1999, **121**, 10286-10296.
185. M. W. Freyer, R. Buscaglia, B. Nguyen, W. D. Wilson and E. A. Lewis, *Anal. Biochem.*, 2006, **355**, 259-266.
186. J. Li, J. Wang, H. Li, N. Song, D. Wang and B. Z. Tang, *Chem. Soc. Rev.*, 2020, **49**, 1144-1172.
187. M. Gao and B. Z. Tang, *ACS sensors*, 2017, **2**, 1382-1399.
188. R. M. Da Silva, D. Van Der Zwaag, L. Albertazzi, S. S. Lee, E. Meijer and S. I. Stupp, *Nat. Commun.*, 2016, **7**, 1-10.
189. Y. Hong, J. W. Lam and B. Z. Tang, *Chem. Soc. Rev.*, 2011, **40**, 5361-5388.
190. P. K. Jana and S. P. Moulik, *J. Phys. Chem.*, 1991, **95**, 9525-9532.

191. B. Liu, P.-J. J. Huang, X. Zhang, F. Wang, R. Pautler, A. C. F. Ip and J. Liu, *Anal. Chem.*, 2013, **85**, 10045-10050.
192. Y. Li, N. Khuu, A. Gevorkian, S. Sarjinsky, H. Therien-Aubin, Y. Wang, S. Cho and E. Kumacheva, *Angew. Chem. Int. Ed.*, 2017, **56**, 6083-6087.
193. E. Prince, M. Alizadehgiashi, M. Campbell, N. Khuu, A. Albulescu, K. De France, D. Ratkov, Y. Li, T. Hoare and E. Kumacheva, *Biomacromolecules*, 2018, **19**, 1276-1284.
194. Y. Li and E. Kumacheva, *Science advances*, 2018, **4**, eaas8998.
195. A. Gevorkian, S. M. Morozova, S. Kheiri, N. Khuu, H. Chen, E. Young, N. Yan and E. Kumacheva, *Adv. Funct. Mater.*, 2021, **31**, 2010743.
196. E. Prince, Z. Chen, N. Khuu and E. Kumacheva, *Biomacromolecules*, 2021.
197. R. Dash, M. Foston and A. J. Ragauskas, *Carbohydr. Polym.*, 2013, **91**, 638-645.
198. S. E. D'Souza, M. H. Ginsberg and E. F. Plow, *Trends Biochem. Sci*, 1991, **16**, 246-250.
199. E. Ruoslahti and M. D. Pierschbacher, *Science*, 1987, **238**, 491-497.
200. M. Eberhardt, R. Mruk, R. Zentel and P. Théato, *Eur. Polym. J.*, 2005, **41**, 1569-1575.
201. P. J. Roth, F. D. Jochum, R. Zentel and P. Theato, *Biomacromolecules*, 2010, **11**, 238-244.
202. P. Theato, *J. Polym. Sci., Part A: Polym. Chem.*, 2008, **46**, 6677-6687.
203. C. Boyer and T. P. Davis, *Chem. Commun.*, 2009, 6029-6031.
204. P. A. Woodfield, Y. Zhu, Y. Pei and P. J. Roth, *Macromolecules*, 2014, **47**, 750-762.
205. A. Balasini, Master of Science, Heinrich-Heine-University, 2021.
206. F. Sebest, L. Casarrubios, H. S. Rzepa, A. J. White and S. Díez-González, *Green Chemistry*, 2018, **20**, 4023-4035.
207. S. Perrier, *Macromolecules*, 2017, **50**, 7433-7447.
208. S. Höck, R. Marti, R. Riedl and M. Simeunovic, *CHIMIA International Journal for Chemistry*, 2010, **64**, 200-202.
209. M. Höök, L. Kjellén, S. Johansson and J. Robinson, *Annu. Rev. Biochem*, 1984, **53**, 847-869.
210. M. Inoue and C. Katakami, *Investigative ophthalmology & visual science*, 1993, **34**, 2313-2315.
211. Y. Lei, S. Gojgini, J. Lam and T. Segura, *Biomaterials*, 2011, **32**, 39-47.
212. J. R. E. Fraser, T. C. Laurent and U. Laurent, *Journal of internal medicine*, 1997, **242**, 27-33.
213. L. Soria-Martinez, S. Bauer, M. Giesler, S. Schelhaas, J. Materlik, K. Janus, P. Pierzyna, M. Becker, N. L. Snyder and L. Hartmann, *J. Am. Chem. Soc.*, 2020, **142**, 5252-5265.
214. F. Shamout, Universitäts-und Landesbibliothek der Heinrich-Heine-Universität Düsseldorf, 2020.
215. H. Chai, K. Le Mai Hoang, M. D. Vu, K. Pasunooti, C. F. Liu and X. W. Liu, *Angew. Chem.*, 2016, **128**, 10519-10523.
216. Y. Hrynets, M. Ndagijimana and M. Betti, *J. Agric. Food. Chem.*, 2015, **63**, 6249-6261.
217. M. van den Heuvel, D. W. Löwik and J. C. van Hest, *Biomacromolecules*, 2008, **9**, 2727-2734.
218. Y. Shi, G. Yin, Z. Yan, P. Sang, M. Wang, R. Brzozowski, P. Eswara, L. Wojtas, Y. Zheng and X. Li, *J. Am. Chem. Soc.*, 2019, **141**, 12697-12706.
219. J. L. Asensio, A. Ardá, F. J. Cañada and J. Jimenez-Barbero, *Acc. Chem. Res.*, 2013, **46**, 946-954.
220. S. Hossen, M. K. Hossain, M. Basher, M. Mia, M. Rahman and M. J. Uddin, *Journal of advanced research*, 2019, **15**, 1-18.
221. T. Freichel, V. Heine, D. Laaf, E. E. Mackintosh, S. Sarafova, L. Elling, N. L. Snyder and L. Hartmann, *Macromol. Biosci.*, 2020, **20**, 2000163.
222. P. Ferruti, M. A. Marchisio and R. Duncan, *Macromol. Rapid Commun.*, 2002, **23**, 332-355.
223. J. L. J. Blanco, C. O. Mellet and J. M. G. Fernández, *Chem. Soc. Rev.*, 2013, **42**, 4518-4531.
224. N. Murthy, Y. X. Thng, S. Schuck, M. C. Xu and J. M. Fréchet, *J. Am. Chem. Soc.*, 2002, **124**, 12398-12399.
225. B. J. Frisken, *Applied optics*, 2001, **40**, 4087-4091.
226. M. M. Tirado and J. G. de la Torre, *The Journal of Chemical Physics*, 1980, **73**, 1986-1993.